

University of Warwick institutional repository: <http://go.warwick.ac.uk/wrap>

**A Thesis Submitted for the Degree of PhD at the University of Warwick**

<http://go.warwick.ac.uk/wrap/77856>

This thesis is made available online and is protected by original copyright.

Please scroll down to view the document itself.

Please refer to the repository record for this item for information to help you to cite it. Our policy information is available from the repository home page.

MBE Growth and Characterization of lattice  
mismatched III-Antimonide semiconductors

By

Huiping Shen

A thesis submitted to the University of Warwick for the degree  
of Doctor of Philosophy in Engineering

University of Warwick, Department of Engineering

February 2015

## **Table of Contents**

<b>List of Tables.....</b>	<b>VIII</b>
<b>List of Figures.....</b>	<b>IX</b>
<b>Acknowledgements.....</b>	<b>XX</b>
<b>Declaration.....</b>	<b>XXI</b>
<b>Related Publications.....</b>	<b>II</b>
<b>Abstract.....</b>	<b>III</b>
<b>Abbreviations.....</b>	<b>XXIV</b>
<b>Chapter 1 Introduction.....</b>	<b>1</b>
1.1 Motivation.....	1
1.2 Properties of semiconductors.....	2
1.2.1 Crystal structures.....	3
1.2.1.1 The diamond crystal structure.....	3
1.2.1.2 The zinc blende crystal structure.....	4
1.2.2 Lattice mismatch.....	5
1.2.3 Crystalline imperfections.....	5
1.2.3.1 Point-like defects.....	6
1.2.3.2 Line defects.....	7
1.3 Properties of Low dimensional antimonide semiconductors.....	8
1.4 Heteroepitaxial growth of thin films.....	11
1.5 Outline of the thesis.....	17

## **Chapter 2 MBE and characterization techniques.....21**

2.1 MBE.....	21
2.1.1 The growth chamber.....	23
2.1.2 SUMO cell.....	24
2.2 RHEED .....	26
2.2.1 Interpretation of several typical RHEED patterns .....	27
2.2.2 The intensity oscillations.....	29
2.3 AFM .....	30
2.3.1 Contact mode.....	33
2.3.2 Tapping mode.....	34
2.4 TEM.....	34
2.5 Photoluminescence.....	36
2.6 Hall Measurement.....	37
2.6.1 Sample preparation and mounting .....	37
2.6.2 Measurement.....	38

## **Chapter 3 MBE growth and characterization of single layers of InSb dots.....40**

3.1 Introduction.....	40
3.2 Experimental.....	43
3.3 Results and discussion .....	44

3.3.1 RHEED patterns and AFM analysis of samples grown at 320 °C.....	44
3.3.1.1 RHEED patterns.....	44
3.3.1.2 AFM analysis.....	46
3.3.2 RHEED patterns and AFM analysis of samples grown at 275 °C.....	52
3.3.2.1 RHEED patterns.....	53
3.3.2.2 AFM analysis.....	54
3.3.3 Analysis of samples grown at 250 °C.....	64
3.3.3.1 RHEED patterns.....	64
3.3.3.2 AFM analysis.....	65
3.3.4 Comparison of dots properties for three sets of samples.....	69
3.3.5 Analysis of the material balance.....	72
3.3.6 Analysis the critical size and relaxation mechanism of InSb/GaSb QDs.....	77
3.3.7 The electrical properties of InSb/GaSb QDs.....	81
3.4	
Conclusions.....	82
<b>Chapter 4 MBE growth and characterization of buried layers of InSb dots.....</b>	<b>85</b>
4.1 Introduction.....	85
4.2 Experimental.....	86

4.3 Results and analysis.....	87
4.3.1 Structural properties of the InSb SQDs.....	87
4.3.2 TEM images of sample (before etching).....	91
4.3.3 Electrical properties of sample (before etching).....	93
4.3.4 Etching of InSb surface.....	97
4.3.5 Structural and electrical properties of BQDs.....	99
4.4 Conclusions.....	102
<b>Chapter 5 Investigation the growth of III-Sb on GaAs (001)....</b>	<b>104</b>
5.1 Analysis of the deposition of GaSb on GaAs (001).....	104
5.1.1 Introduction.....	104
5.1.2 Experimental.....	107
5.1.3 Results and analysis.....	108
5.1.3.1 Analysis of 5 nm GaSb on GaAs (001) .....	108
5.1.3.2 Analysis of 250 nm GaSb on GaAs (001).....	112
5.1.3.3 Analysis of 500 nm GaSb on GaAs (001).....	114
5.1.3.3.1 TEM results.....	115
5.1.3.4.2 AFM analysis of 500 nm GaSb on GaAs (001) .....	116
5.1.3.4 Analysis of 0.5 $\mu$ m GaSb on GaAs (001) grown at 400 $^{\circ}$ C.....	117
5.1.3.5 Analysis of 1 $\mu$ m GaSb on GaAs (001).....	121
5.1.3.6 Analysis the dependence of the structural and electrical properties of samples on growth temperature.....	124
5.1.3.7 Analysis GaSb/GaAs with an insertion of AlSb buffer.....	129

5.1.4 Analysis the deposition of $\text{Al}_{1-x}\text{Ga}_x\text{Sb}$ on GaAs.....	135
5.1.5 Conclusions.....	139
5.2 Analysis the deposition of InSb on GaAs (001).....	140
5.2.1 Introduction.....	141
5.2.2 Experimental.....	141
5.2.3 Results and analysis.....	142
5.2.3.1 Analysis of 0.5 $\mu\text{m}$ InSb grown on GaAs (001).....	143
5.2.3.2 Analysis of 2 $\mu\text{m}$ InSb grown on GaAs (001).....	150
5.2.3.3 Analysis of 5 $\mu\text{m}$ InSb grown on GaAs (001).....	153
5.2.4 Conclusions.....	155

## **Chapter 6 Theoretical and experimental analysis the optical properties of III-Sb thin films.....158**

6.1 Introduction.....	158
6.2 Theoretical analysis of the optical properties, electrical properties, and their transformation.....	158
6.2.1 Analysis of optical propagation and energy dissipation inside homogeneous structures .....	159
6.2.2 Relationships between optical and electrical properties.....	162
6.3 Experimental .....	165
6.4 Results and discussion.....	165
6.4.1 Results for GaSb and analysis.....	165

6.4.2 Results for InSb and analysis.....	165
6.5 Conclusions.....	168
<b>Chapter 7 Conclusions and future work.....</b>	<b>169</b>
7.1 Conclusions.....	169
7.2 Future work.....	170
<b>References.....</b>	<b>172</b>



## List of Tables

Table 1.1 Lattice Constants and Crystal Structures of some technologically important semiconductors.....	5
Table 2.1 parameters measured by Hall measurement.....	39
Table 3.1 Dot densities and total dots volume at various InSb coverages.....	48
Table 3.2 Dots volume versus total amount of deposited InSb.....	62
Table 3.3 Comparison of properties of InSb/GaSb QDs grown under different techniques.....	69
Table 5.1 A summary of growth parameters of samples.....	124
Table 5.2 Experimental results of RMS surface roughness, number density of threading dislocation, and mobility.....	125
Table 5.3 A summary of sample parameter and experimental results.....	133
Table 6.1 Parameters obtained from infrared reflectivity (r) and Hall measurements (h) on sample tmw05057.....	166
Table 6.2 Parameters obtained from infrared reflectivity (r) and Hall measurements (h) on Sample tmw05083.....	168

## List of Figures

Fig.1.1 Semiconductor energy gap as a function of crystal lattice constant for several cubic structures (blue lines indicate a direct band gap and red lines indicate an indirect band gap, values were given at room temperature)[1].....	1
Fig.1.2 A unit cell* of the diamond structure (* A unit cell is a volume in the lattice that is representative of the entire lattice and repeated regularly throughout the crystal. The smallest parallelepiped that satisfies the definition is always chosen as the unit cell).....	3
Fig.1.3 The zinc blende structure of GaSb (the purple and green atoms at the face-centered cubic lattice point are of two different types, e.g. Ga and Sb).....	4
Fig.1.4 2-D representation of crystal structure with point defects.....	6
Fig.1.5 Representations of crystal structure with line defects.....	8
Fig.1.6 Schematic representations (top) and density of electronic states (bottom) of 0D, 1D, 2D, and 3D heterostructures[11].....	10
Fig.1.7 Schematic representations of Frank-vander Merwe (FM), Stranski-Krastanov (SK), and Volmer-Weber (VW) growth mode.....	13
Fig.1.8 Equilibrium phase diagram of heteroepitaxial growth epilayers on a substrate. Where $f$ is the lattice mismatch strain, $T$ is the epilayer thickness in monolayer. The top insets illustrate the morphology of the surface in the corresponding phase regions. The large black triangles represent ripened 3-D islands and the small triangles denote stable 3-D dots (The phase diagram is reprinted from reference[24]) Daruka, I. and Barabási established an equilibrium diagram quantitatively describes the effect of lattice mismatch strain and epilayer thickness on the growth mode).....	16
Fig.2.1 A top-view schematic of the GEN II MBE equipment used in this study. Some important components are displayed in this representation.....	22
Fig.2.2 RHEED patterns performed on an (a) amorphous/polycrystalline surface, (b) rough surface, (c) smooth surface and (d) dots surface.....	28

Fig.2.3 RHEED intensity oscillation in the deposition of 5 ML InSb on GaSb (001) at 320 °C, the oscillation period is ~ 10s that indicates the completion of 1 ML and the calibrated growth rate is ~ 0.1 ML/s.....	29
Fig.2.4 A schematic diagram of atomic force microscopy. The z piezoelectric element is collected in an actuator installed apart from x and y piezo stage to prevent cross talk.....	31
Fig.2.5 The vander Waals force curve between the tip and the specimen under examination. The blue curve indicates the repulsive force region (contact mode) and the red curve represents the attractive force region (non-contact mode).....	32
Fig. 2.6 A representation of contact mode.....	33
Fig. 2.7 A representation of tapping mode.....	34
Fig.2.8 A TEM image taken from a 500nm GaSb grown on GaAs (001) under 220 bright field. It is clear that the misfit arrays formed on the interface, the dislocations originate from the interface and propagate to the GaSb epilayer.....	34
Fig.2.9 A representation of PL measurement set-up.....	36
Figure 2.10 (a) Sample with scratched corners, (b) Sample mounted on sample holder. Wires are attached in a clockwise ‘rainbow’ manner.....	37
Fig.3.1 RHEED patterns taken (a) after growth of the 0.1um GaSb buffer layer, (b) –(f) after deposition of 1ML, 1.5ML, 2ML, 3ML and 4ML of InSb at 320 °C, respectively.....	45
Fig.3.2 AFM images of surface morphology and histograms of InSb QDs height distribution at the coverage of (a) 2.5ML, (b) 3.5 ML, and (c) 4ML of InSb grown at 320 °C.....	46

Fig.3.3 Densities of small and large dots as a function of InSb coverage ( $\Theta$ ) for epilayer grown at a temperature of 320 °C and growth rate of ~ 0.11 ML/s. The full lines join the data for an eye guide.....	50
Fig.3.4 The height (top) and base diameter (bottom) of large dots as a function of InSb coverage ( $\Theta$ ) for epilayer grown at the growth temperature of 320 °C. The full lines join the data for an eye guide. The almost parallel phenomenon of these two guided lines indicated the aspect ratio of dots keeps stable.....	52
Fig.3.5 RHEED patterns taken from samples grown at 275 °C during the cooling down process.....	53
Fig.3.6 RHEED patterns (a) –(f) taken after deposition of 1ML, 1.5ML, 2ML, 3ML, 4ML and 5ML of InSb at 275 °C, respectively.....	54
Fig.3.7 AFM images and cross-section area scan of (a) 1ML and (b) 1.5ML InSb grown at 275 °C, respectively.....	55
Fig.3.8 A set of AFM images and cross-section scan of a range of InSb coverage from 2ML upto 5ML grown at 275 °C.....	57
Fig.3.9 AFM topograph of 2.5 ML InSb on GaSb(001) with insertion of a 0.1 $\mu$ m GaSb buffer layer, growth temperature of 275 °C, growth rate of 0.11 ML/s. Terraces with monolayer height step were observed. Several typical morphologies emerged on surface, there were small 3D dots with height below 1ML (marked as A), large 3D dots with height above 1ML (marked as B), only these two types of fully strained dots can be considered to be QDs. In addition, large 2D islands were observed on the surface (marked as C).....	61
Fig. 3.10 Number densities of small and large dots as a function of InSb coverage ( $\Theta$ ) at a temperature of 275°C. The full lines join the data for an eye guide.....	63

Fig.3.11 RHEED patterns (a)–(f) taken after deposition of 1.5ML, 2ML, 2.5ML, 3ML, 3.5ML and 4ML of InSb at 250°C, respectively.....	64
Fig.3.12 AFM images of 1.5ML InSb on GaSb (001) with a 0.1 $\mu$ m GaSb buffer layer. The epilayer growth temperature was 250 °C and the growth rate was 0.11ML/s.....	67
Fig.3.13 Densities of small and large dots as a function of InSb coverage ( $\Theta$ ) at a temperature of 250 °C. The full lines join the data for an eye guide.....	68
Fig.3.14 Average dot height (up) and density (bottom) shown as a function of temperature for different growth rate, InSb coverage, and aspect ratio. The symbols represented experimental data: part from this work, part from Refs [61, 68, 69].....	71
Fig.3.15 The aspect ratio of dots as a function of deposited InSb amount. The symbols represented the experimental aspect ratio data of dots grown at 320 °C (rhombus), 275 °C (square) and 250 °C (triangle).....	72
Fig.3.16 Number densities of dots with height above 1ML as a function of InSb coverage. The symbols corresponded to the experimental number density data of InSb/GaSb(001) QDs grown at 320 °C (rhombus), 275 °C (square) and 250 °C (triangle).....	72
Fig.3.17 Total volume of 3D dots and thick islands as a function of InSb coverage per unit surface. Three sets of samples were grown at 320 °C, 275 °C and 250 °C, respectively, with a same growth rate of 0.1ML/s. The dashed line (black) corresponds to the deposited amount of InSb. The dash line (red) indicates the thickness of the wetting layer beneath the 3D features. All the data obtained from AFM particle analysing program. The full lines join the data for an eye guide.....	74

Fig.3.18 The calculated large 3D dots volume according the segment of sphere model as a function of InSb coverage per unit surface. Three sets of samples were grown at 320 °C (rhombus), 275 °C (square) and 250 °C(triangle), respectively, with a same growth rate of 0.1ML/s. The interpolations of dots volume data indicate the estimated thickness of wetting layer of sample grown at 320 °C, 275 °C and 250 °C is about 1.9 ML, 1.8ML and 2.2ML, respectively. All the data obtained from calculation of large 3D dots volume according the segment of sphere model.....75

Fig.3.19 Dots size distribution of sample A2.5 and B2.5 for 2.5ML InSb grown at 320 °C and 275 °C, respectively. The dash line is a smooth fit to guide the eye.....76

Fig.3.20 Size and shape evolution of the InSb/GaSb QD ensemble, left images are obtained by cross-section HRTEM and right figure was a schematic representation of the Size and shape evolution of the QD[66].....77

Fig.3.21 High-resolution TEM image of 2.5 ML buried InSb QDs in a GaSb matrix. Two pairs of 60 °dislocations were marked as A and B, respectively.....79

Fig.3.22The strain components in the x (a) and y (b) axis direction, a hint of  $\sqrt{3}$  (c), and  $\sqrt{3}$  (d) structured long chain of loops using peak-pairs algorithm.....80

Fig. 3.23 Photoluminescence spectra recorded at 10 K from (sample tmw05066) 2.5 ML InSb capped with 100 ML GaSb. The laser excitation density taken for this measurement was 3 W/cm<sup>2</sup>.....82

Fig.4.1 RHEED pattern (a) taken prior to initial deposition of InSb in [110] azimuthal, (b) taken after deposition of 2.5 ML InSb on GaSb (001) wafer in [1  $\bar{1}$  0] amimuthal, (c) taken after deposition of the 0.1  $\mu$ m GaSb spacer layer, (d) taken after the final 2.5 ML InSb on GaSb spacer layer in [110] azimuthal. All the samples were grown with rotation only during the growth of spacer and

buffer, the growth temperature was 275 °C, the growth rate was 0.11 ML/s and rotation rate was 13.0 rpm.....88

Fig.4.2 (a) growth structure, (b) 500nm ×500 nm AFM images, (c)cross-section of surface QDs, (d) height histogram of InSb SQDs.....90

Fig.4.3 (top) Bright-field TEM image of the InSb (QDs)/ GaSb/InSb(QDs)/GaSb heterostructure, obtained under actual diffraction vector  $g(002)$  in two-ray conditions. Dark spots were suspected to be drops of atomic Indium at the InSb/GaSb interface. Arrows near the position 1 indicated InSb QDs/GaSb (spacer) interface and arrow 2 illustrated the InSb QDs/ GaSb (buffer) interface, (bottom) dark field TEM image of the InSb(QDs)/ GaSb and InSb(QDs)/GaSb interfaces, obtained under actual diffraction vector  $g(002)$ , in two-ray conditions, dark arrows indicated the existence of the wetting layers.....91

Fig.4.4 PL intensity measured at sample before etching, the operating temperature was 300 K.....93

Fig.4.5 Temperature dependence of (top) peak energy and (bottom) FWHM of surface QDs and buried QDs, square represented SQDs and circle represented BQDs.....94

Fig.4.6 AFM image and cross section of the surface after 30 Sec etching in the  $H_3PO_4/H_2O_2/C_6H_8O_7$  (2 M/0.5 M/0.5 M) solution.....98

Fig.4.7(a)Dark-field TEM image of the GaSb/InSb (QDs layer)/GaSb heterostructure with diffraction vector  $g(002)$ . Dark arrow indicated the existence of a wetting layer at the interface. (b) bright-field TEM image of the GaSb/InSb (QDs layer)/GaSb heterostructure with diffraction vectors  $g(004)$  and  $g(002)$ .....99

Fig.4.7 Dots size distribution of 2.3ML, 3ML, 3.5ML and 4.5ML buried InSb on GaSb (001). All the samples were grown with rotation only during the growth of spacer and buffer, the growth temperature was 320 °C, the growth rate was 0.11

ML/s and rotation rate was 13.0 rpm. The full lines join the data for an eye guide.....	99
Fig.4.8 Normalized PL intensity of InSb BQDs at the excitation power of 1, 10 and 100 mW under the temperature of 10 K.....	100
Fig.5.1 RHEED pattern taken (a)after deposition of 5 nm GaSb for sample tmw04083 with the beam incident in the [110] direction (b) during cooling down of sample tmw04083 in with the beam incident in the [110] direction (c) during cooling down of sample tmw04083 in with the beam incident in the $\bar{1}10$ direction (d) after deposition of 5 nm GaSb for sample tmw04085 with the beam incident in [110] direction (e) for sample tmw04085 with the beam incident in incident in $\bar{1}10$ direction (f) during cooling down of sample tmw04085 with a bright transition from $\times 3$ to $\times 5$ reconstruction.....	108
Fig.5.2 AFM images of 5ML GaSb grown on GaAs (001) (a) without annealing, (b) after annealing under Sb flux for 30 mins. The growth temperature was 500 °C and the growth rate was 0.5 $\mu\text{m/h}$ .....	109
Fig.5.3 AFM images and cross-section scan of 250nm GaSb on GaAs(001) grown at 500 °C (a) without annealing, (b) after annealing under Sb flux at 580 °C for 30 mins. The growth temperature was 500 °C and the growth rate was 0.55 $\mu\text{m/h}$ .....	111
Fig.5.4. Cross-section TEM image of unannealed 500nm GaSb on GaAs showing a highly periodic array of misfit dislocations at the GaSb/GaAs interface. Images measured under bright field 220 conditions. The top (200nm-scale) image manifested that threading dislocations induced by lattice mismatch originated at the GaSb/GaAs interface and propagated through the epitaxial GaSb film. The bottom (50nm-scale) image clearly illustrated that those threading dislocations	



arised from the misfit array at the interface and propagated to the GaSb epilayer.....	114
Fig.5.5 Cross-section TEM micrograph taken from different regions from the interface of the unannealed sample1 clearly show a highly periodic array of misfit dislocations at the GaSb/GaAs interface. Images were taken under bright field 220 and dark field 002 conditions.....	116
Fig.5.6 RHEED pattern(a) taken after oxide removal, (b) taken after growth of 0.5 $\mu\text{m}$ GaSb on GaAs(001) for sample tmw05033, good $\times 5$ symmetry observed at the end of growth, (c) taken after oxide removal, (d) taken after growth of 0.5 $\mu\text{m}$ GaSb on GaAs(001) for sample tmw05032, $\times 3$ symmetry observed at the end of growth. The growth temperature was 400 $^{\circ}\text{C}$ and the growth rate was 0.55 $\mu\text{m}/\text{h}$ .....	117
Fig.5.7 AFM images and cross-section scan of 0.5 $\mu\text{m}$ GaSb grown on GaAs (001) at 400 $^{\circ}\text{C}$ under growth rate of (a) 1 $\mu\text{m}/\text{h}$ , sample tmw05033, and (b) 0.5 $\mu\text{m}/\text{h}$ , sample tmw05032.....	118
Fig.5.8 (a) 20 $\mu\text{m} \times 20\mu\text{m}$ AFM image (top), cross-section scan (middle ) and 3D-rendering (bottom) (b) 2 $\mu\text{m} \times 2\mu\text{m}$ AFM image (top), cross-section scan (middle ) and 3D-rendering (bottom) of 1 $\mu\text{m}$ GaSb on GaAs(001) grown at 500 $^{\circ}\text{C}$ with a nominal growth rate of 0.5 $\mu\text{m}/\text{h}$ .....	122
Fig.5.9 The dependence of RMS surface roughness over 20 $\mu\text{m} \times 20\mu\text{m}$ area and carrier mobility on the GaSb epilayer thickness. The full lines join the data for an eye guide.....	126
Fig.5.10 The dependence of RMS surface roughness over 20 $\mu\text{m} \times 20 \mu\text{m}$ area and number density of threading dislocations on the GaSb epilayer thickness. The full lines join the data for an eye guide.....	128

Fig.5.11 The dependence of RT mobility and number density of threading dislocations on the GaSb epilayer thickness for samples deposition at the optimum growth condition, 500 °C and 0.5 μm/h. The full lines join the data for an eye guide.....	129
Fig.5.12 RHEED pattern (a) taken at the initial GaAs surface prior to AlSb deposition, a elongated spotty pattern indicted a rough surface after the removal of oxide, (b) taken after 14 -s AlSb deposition, good x3 symmetry streaky pattern indicated a smooth surface at that moment, (c) taken at the end of GaSb epilayer growth, a mixed 4 x 4 and x 3 surface reconstruction was observed at 305 °.....	130
Fig.5.13 AFM images and cross-section scan of 0.1μm GaSb on GaAs(001) with (a) 10 nm (tmw05079), (b) 50 nm ( tmw05081), (c) 0.1 μm (tmw05080) and (d) 0.5 μm (tmw05075) AlSb buffer layer grown at 550 °C with a nominal growth rate of 1 μm/h.....	133
Fig.5.14 The dependence of RMS surface roughness over 20 μm×20 μm area and number density of threading dislocations on the AlSb buffer layer thickness. The full lines join the data for an eye guide.....	134
Fig.5.15 The dependence of number density of threading dislocations and mobility (RT) on the AlSb buffer layer thickness. The full lines join the data for an eye guide.....	135
Fig.5.16 20 μm x 20 μm and 500 nm x 500 nm AFM topographs and cross sections of 0.5 μm Al <sub>1-x</sub> Ga <sub>x</sub> Sb grown on GaAs(001) at 550 °C , under the growth rate of 0.5 μm/h (a) sample tmw05076 , x = 0.2 and (b) tmw05078, x= 0.1, respectively.....	137
Fig.5.17 20 μm x 20 μm and 500 nm x 500 nm AFM topographs and cross sections of (a) 0.1μm GaSb on GaSb (001) substrate with a 0.5 μm Al <sub>1-x</sub> Ga <sub>x</sub> Sb (x=0.2) buffer and (b) 0.1μm GaSb homoepitaxial on GaSb (001) substrate at 520 °C.....	139
Fig.5.18 RHEED pattern of sample tmw05035 (a) taken after oxide removal, an	

elongated spotty pattern indicated rough surface (b) taken after initial 33 s of InSb growth on GaAs (001), spotty pattern indicated large number of 3D dots formed on the surface at that moment (c) after 0.5  $\mu\text{m}$  InSb grown on GaAs(001), good  $\times 3$  symmetry observed at the end of growth, indicated flat surface; RHEED pattern of sample tmw05034 (d) taken after oxide removal, a streaky pattern with elongated spots indicated rough surface (e) taken after initial 33 s of InSb growth on GaAs (001), spotty pattern indicated large number of 3D dots formed on the surface at that moment , (f) taken after growth of 0.5  $\mu\text{m}$  GaSb on GaAs(001),  $\times 3$  symmetry observed at the end of growth, indicated flat surface.....144

Fig.5.19 (a) and (b): 20  $\mu\text{m}$  x 20  $\mu\text{m}$  and 500 nm x 500 nm AFM topographs and cross sections of the surfaces of 500 nm InSb hetero-growth at 400  $^{\circ}\text{C}$  , growth rate of 1  $\mu\text{m}/\text{h}$  and 0.5  $\mu\text{m}/\text{h}$ , respectively .....146

Fig. 5.20 A 2  $\mu\text{m}$  x 2  $\mu\text{m}$  zoom-in AFM image and cross sections of the mounds on sample tmw05034. AFM topograph shows a four lobed spiral corresponding to four threading dislocations at the center of the mound and the spiral step edge emanating from a threading dislocation.....147

Fig.5.21 The dependence of Carrier density(top) and mobility (bottom) versus the reciprocal of temperature for sample tmw05035 and tmw05034 with 0.5  $\mu\text{m}$  InSb grown on GaAs(001) at 400  $^{\circ}\text{C}$ , under growth rate of 1  $\mu\text{m}/\text{h}$  and 0.5  $\mu\text{m}/\text{h}$ , respectively. The full lines join the data for an eye guide.....149

Fig.5.22 20  $\mu\text{m}$  x 20  $\mu\text{m}$  and 500 nm x 500 nm AFM topographs and cross sections of sample tmw05056, 2  $\mu\text{m}$  InSb grown on GaAs (001) at 420  $^{\circ}\text{C}$ , growth rate of 0.5  $\mu\text{m}/\text{h}$ .....151

Fig.5.23 Carrier density and mobility versus the reciprocal of temperature for sample tmw05056 with 2  $\mu\text{m}$  InSb grown on GaAs (001) under temperature of 420  $^{\circ}\text{C}$ , under growth rate of 0.5  $\mu\text{m}/\text{h}$ . The full lines join the data for an eye guide.....152

Fig.5.24 A 20  $\mu\text{m}$  x 20  $\mu\text{m}$  and a 500 nm x 500 nm AFM topographs and cross sections of the surfaces of 5  $\mu\text{m}$  InSb grown on GaAs(001) at 420  $^{\circ}\text{C}$ , under

growth rate of 0.5 $\mu\text{m/h}$ .....	153
Fig.5.25 Carrier density and mobility versus the reciprocal of temperature for sample tmw05083 with 5 $\mu\text{m}$ InSb grown on GaAs (001) under temperature of 420 $^{\circ}\text{C}$ , under growth rate of 0.5 $\mu\text{m/h}$ . The full lines join the data for an eye guide.....	154
Fig.5.26 The dependence of RT mobility and carrier density versus insb thickness for InSb layers with various thickness on GaAs (001) substrates at the optimum growth temperature of 420 $^{\circ}\text{C}$ and growth rate of 0.5 $\mu\text{m/h}$ . The full lines join the data for an eye guide.....	155
Fig.5.27 Electron mobility and number density of threading dislocations for InSb layers with various thickness on GaAs (001) substrates grown at 420 $^{\circ}\text{C}$ and 0.5 $\mu\text{m/h}$ . The full lines join the data for an eye guide.....	156
Fig.6.1 Light propagation through a single layer homogeneous film.....	159
Fig.6.2 RT Band structure and carrier concentration of undoped GaSb [145]..	164
Fig.6.3 Reflectivity of sample tmw05057 at room temperature, experimental (full curve with square symbols) and theoretical (dash curve with triangle symbols). The spectral range 20-250 $\text{cm}^{-1}$ . Sample tmw05057 was 1 $\mu\text{m}$ GaSb on GaAs (001) substrate grown at temperature of 500 $^{\circ}\text{C}$ and growth rate of 0.5 $\mu\text{m/h}$ ...	166
Fig.6.4 Reflectivity of sample tmw05083 at room temperature, experimental (full curve with square symbols) and theoretical (dash curve with triangle symbols). The spectral range 20-250 $\text{cm}^{-1}$ . Sample tmw05083 was 5 $\mu\text{m}$ InSb on GaAs (001) substrate grown at temperature of 420 $^{\circ}\text{C}$ and growth rate of 0.5 $\mu\text{m/h}$ .....	167

## **Acknowledgements**

I need to express deep gratitude to many people who have contributed to the completion of my PhD research. First and foremost, I must thank my supervisor Dr. CY Zhao providing me the opportunity to start a PhD research in his group. His continuous support during the entire PhD study, his patience and enthusiasm in semiconductor research, and many detailed discussions about my research result have deeply impressed me. Gratitude is extended to Prof. Tim Jones for his support me in doing collaborated research of narrow band gap III-Sb semiconductors in his lab. Special thanks belong to Dr. Mark Ashwin for the detailed guidance in the growth of semiconductor by molecular beam epitaxy. He takes me to the world of MBE. His knowledge and experience in Sb-based materials and manipulating MBE are an invaluable resource to assist me finish my PhD research in III-Sb semiconductors. His suggestions are also valuable in my future exploring the research in narrow band gap semiconductors. In particular, Mark is more than an expert in MBE wisdom, he is also a great friend and an extraordinary great mentor on life.

I further want to thank Patel, Sanchez, and Beanland for assistance in TEM characterization. Even more, I am grateful to Dr. Vishal Shah who gives me a lot of guidance during the Hall measurement. I also would like to thank Dr. XiaoJun Ji and Prof. Yan Lan in Shanghaijiaotong University, their great knowledge in semiconductors especially in quantum dots gives me a lot of help in doing the PL measurement. Special thanks to Prof. Wang Xiao and Dr. Liu Li who gave me a lot support during the TEM and PL test in Physics department in university of NanJing. Many thanks to Dr. Hu Yang who helped me a lot during the InSb etching.

To Ian, Nat, Guanhua, JY, and all my colleagues in department of Engineering and Chemistry, your support and companionship make my PhD life in Warwick more colourful.

## **Declaration**

This thesis is submitted to the University of Warwick in support of my application for the degree of Doctor of Philosophy.

The development of all experimental data, theoretical analysis, proposal and construction of the new models in this thesis were carried out by the author. I declare that this document, or any part thereof, has not been submitted for the consideration of any other degree, at any institution. I confirm the work described herein to have been undertaken by me, except where acknowledged and in the cases of TEM characterisation (RK Patel and AM Sanchez, Department of Physics in Warwick).

## **Related Publications**

[1]HP Shen, M J Ashwin, CY Zhao, T S Jones, Molecular-beam epitaxy of InSb nano-scale dots on GaSb at low temperatures, MRS Spring Conference, April, 2012 (Published).

[2]HP Shen and CY Zhao, Analytical considerations of light transport in nanostructured homogeneous/inhomogeneous thin films, Thin Solid Films (2013), <http://dx.doi.org/10.1016/j.tsf.2013.06.066> (Published).

[3]HP Shen, M J Ashwin, RK Patel, CY Zhao, T S Jones, MBE of high-density InSb/GaSb QDs and characterization, Journal of Applied Physics, 2014 (Submitted).

[4]HP Shen, M J Ashwin, CY Zhao, T S Jones, MBE of buried InSb QDs and evaluating the emissive properties in infrared region, Journal of Applied Physics (To be submitted).

## Abstract

In recent years, there emerges intense research on heteroepitaxial growth of semiconductors, especially towards the material systems with interesting optical and physical properties. In particular, as the invention and advancement of modern growth techniques such as MOCVD and MBE, the research in microstructures and quantum devices has been largely promoted.

The thesis was focused on the fundamental research on the heteroepitaxial growth of III-Sb semiconductors, particularly on the InSb/GaSb (001) QD ensembles and III-Sb / GaAs (001) heterostructures. The growth was undertaken on GEN II MBE apparatus and the optimum growth parameters were obtained for the growth of the materials in the lab. After the growth, the structural and electrical properties of the corresponding samples were investigated by AFM, TEM, PL and Hall measurement. Large work has been undertaken to assess the effect of growth parameters such as growth temperature, growth rate and III/V ratio on the structural and electrical properties of QDs. InSb/GaSb QDs with high number density ( $\sim 10^{11} \text{ cm}^{-2}$ ) and narrow size distribution have been obtained. To evaluate the quantum effect of these dots, the PL measurements taken from 2.5ML buried InSb layer grown at 275 °C manifested QDs emitted at 3.4  $\mu\text{m}$  upto room temperature. In addition to the QDs research, primary investigations of the surface morphologies, defects, and the electrical properties were presented for the III-Sb/GaAs heterostructures. In the end, the theoretical and experimental analysis of the optical properties of InSb/GaAs and GaSb/GaAs have been presented.



## Abbreviations

$E$	Electric field intensity
$B$	Magnetic field intensity
$\phi_0$	Angle of incident light
$\phi_1$	Angle of refraction
$\phi_2$	Angle of emergence in substrate
$\epsilon_0$	Permittivity of free space (an electric constant)
$\mu_0$	Permeability of free space (a magnetic constant)
$n$	Refractive index
$k$	Absorption index
$\tilde{\epsilon}(\nu)$	Complex permittivity
$\epsilon_\infty$	High frequency dielectric constant
$\epsilon_s$	Static dielectric constant
$\nu_L$	LO phonon frequency
$\nu_P$	Plasma frequency
$\gamma$	Damping constant of phonon
$\tau$	Carrier scattering time
$n_c$	Carrier concentration
$\mu$	Carrier mobility
$m_{Hh}$	Mass of heavy hole
$m_{Lh}$	Mass of light hole
$n_r$	Carrier concentration obtained from reflectivity measurement
$n_h$	Carrier concentration obtained from Hall measurement
$\mu_r$	Mobility obtained from reflectivity measurement
$\mu_h$	Mobility obtained from Hall measurement

## Chapter 1 Introduction

### 1.1 Motivation

For the development of novel semiconductor materials and devices, heteroepitaxial growth of one semiconductor on another with precise control of the composition and the structure is of significant importance. The motivations for heteroepitaxy of semiconductors include two aspects, one is the fabrication of substrates in form of high quality, large area and single crystal wafers with interesting optical and electrical properties, the other one focuses on hetero-junction devices. Figure 1 illustrates some widely used semiconductors, all having unique properties that make them appealing in device applications. Among all the properties of semiconductors, of special importance is the energy gap which determines the emission wavelength in light-emitting diodes and lasers, as well as the suitability for other device applications. In most cases, the combination of materials with different energy gaps will require mismatched heteroepitaxy due to the different lattice constants.

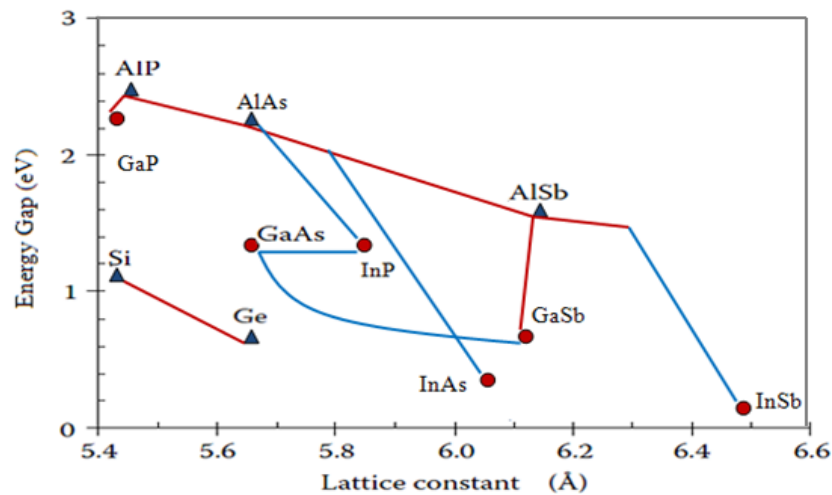


Fig.1.1 Semiconductor energy gap as a function of crystal lattice constant for several cubic structures (blue lines indicate a direct band gap and red lines indicate an indirect band gap, values were given at room temperature) [1].

Figure 1.1 shows some widely used semiconductors with unique crystal and band structures. The unique properties of semiconductors make them becoming promising candidates in the device fabrication. For instance, in the lasers and light-emitting diodes application, the band gaps of semiconductors used in the active region determine the emission wavelengths of the devices. In practical usage, the combination of semiconductors with different band gaps is quite desirable that will require the technique of heteroepitaxial growth.

The primary but crucial challenges in epitaxial growth of mismatched semiconductors are the control of growth mode, manipulation of the growth condition in order to tailor the surface morphology, stress, and crystal defects. Thus, it is necessary to review the properties of semiconductors, with special emphasis on the crystallographic properties, chemical and surface properties, and defects.

## 1.2 Properties of semiconductors

A Semiconductor is a material composed of a chemical element or compound that owns electrical conductivity between a metal and an insulator. The capability of conducting electricity under some typical conditions makes it as the foundation of modern electronics. The properties of a semiconductor are largely based on the nature of its band structure.

In a semiconductor, the highest occupied bands are completely filled and the next unoccupied band is at a higher energy. The conduction won't work until it overcomes the inter-band energy barrier. That inter-band energy barrier is the band gap.

A crystal is a solid that contains a periodically repeated arrangement of atoms in 3-D space. The manner of the arrangement of atoms in a crystal is noted as crystal structure. The crystal structure is composed by a space lattice and a basis. In 1845, the French physicist Auguste Bravais pointed out there exist fourteen uniquespace

lattice in three dimensional crystalline systems [2, 3]. Different semiconductors exhibit various crystal structures.

### 1.2.1 Crystal structures

#### 1.2.1.1 The diamond crystal structure

The diamond crystal structure consists of a face-centered cubic (FCC) lattice and a basis with two identical atoms at each lattice point. The lattice constant equals one quarter of the unit cell diagonal. Semiconductors such as Silicon, Germanium, and Si-Ge alloys exhibit the diamond crystal structure.

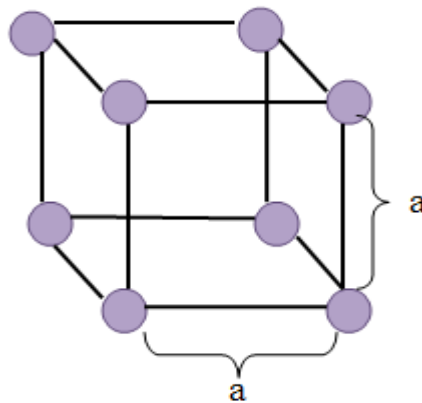


Fig.1.2 A unit cell\* of the diamond structure (\* A unit cell is a volume in the lattice that is representative of the entire lattice and repeated regularly throughout the crystal. The smallest parallelepiped that satisfies the definition is always chosen as the unit cell).

Figure 1.2 illustrates the face-centered cubic diamond crystal structure. Atoms at the face-centered cubic lattice point are of the same type. Atoms in the diamond structure are tetrahedrally bonded by covalent bonds.

#### 1.2.1.2 The zinc blende crystal structure

The zinc blende crystal structure consists of a face-centered cubic (FCC) lattice and a basis with two different atoms at each lattice point. The lattice constant is one

quarter of the unit cell diagonal. A number of semiconductors such as gallium arsenide (GaAs), gallium antimonide (GaSb), indium phosphide (InP), indium antimonide (InSb), other group III-V compound semiconductor, some group II-VI semiconductors, cubic gallium nitride, and cubic silicon carbide have the zinc blende (ZB) crystal structure.

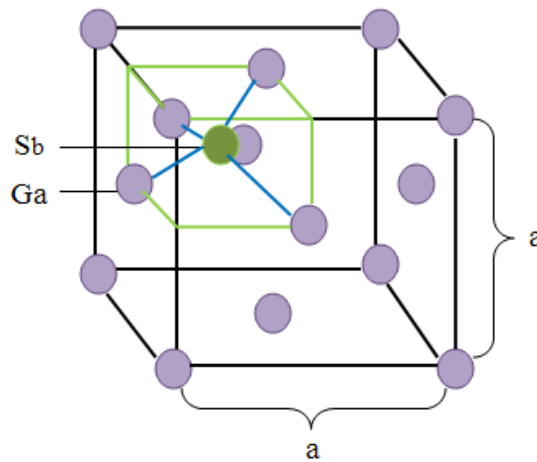


Fig.1.3 The zinc blende structure of GaSb (the purple and green atoms at the face-centered cubic lattice point are of two different types, e.g. Ga and Sb).

The zinc blende crystal structure is quite similar to the diamond structure except that its Bravais lattice point contains two different types of atoms as shown in figure 1.3. The length of the edges of the unit cell is lattice constant. Lattice constant is an important parameter which determines the crystal's physical and electrical properties. Table 1.1 illustrates the lattice constants and crystal structures of some technologically important semiconductors. The lattice constant and crystal structure are two crucial properties relevant to heteroepitaxial growth. In addition, the anisotropic behaviours such as nucleation, cleavage and etching of semiconductor are also relevant to heteroepitaxy.

Table 1.1 Lattice Constants and Crystal Structures of some technologically important semiconductors.

<b>Compound</b>	<b>Crystal structure</b>	<b>Name</b>	<b>Type</b>	<b>Lattice constant</b>
InSb	Zincblende	Indium antimonide	III-V	6.4794
GaSb	Zincblende	Gallium antimonide	III-V	6.0959
AlSb	Zincblende	Aluminium antimonide	III-V	6.1355
InAs	Zincblende	Indium arsenide	III-V	6.0584
GaAs	Zincblende	Gallium arsenide	III-V	5.6533
AlAs	Zincblende	Aluminium arsenide	III-V	5.6605

Different semiconductors have different crystal structures. Among these different types of Bravais lattices, the cubic space lattice is most relevant in this thesis since most of III-V semiconductors are face-centered cubic crystals.

### 1.2.2 Lattice mismatch

The drawbacks of heteroepitaxial are the inevitable misfit dislocations induced by the strain caused by large lattice mismatch. These misfits and threading dislocations degrade the carrier mobility commonly near the interface of the heterostructure.

### 1.2.3 Crystalline imperfections

For mass production, it is necessary to form a crystal with a high degree of crystalline perfection. In practice however, faults such as vacancy defects and dislocations break the symmetry of a perfect crystal lattice in semiconductors. The faults commonly include point-like defects such as vacancy, interstitial, and

substitutional atom and extended defects such as line defect, bulk defect and planar defect. These imperfections are usually caused by the incorporation of contaminations into the desirable materials during the growth, resulting imperfections in structures or the unexpected species situated at the regular atomic site. In heteroepitaxial growth, the strain induced by the lattice mismatch always leads to the formation of line defects such as dislocations in crystal structure. Those structural defects affect the behaviour of free carriers, may acting as scattering/recombination centers or traps in semiconductors [5, 6]. In consequence, it is better to clearly understand the main types of crystallographic defects which largely determine the optical and electrical performance of semiconductors.

There exists 4 types of defects covered most of the imperfections in crystal, interrupted as point-like defects and extended defects including line defects, bulk defects, and planar defects.

#### 1.2.3.1 Point-like defects

Point defects usually involve an extra or missing atom settle at a single lattice point. For a single element crystal, an exclusion of an atom from the lattice is called vacancy defect while the extra inclusion of one or more atoms are interstitial defects.

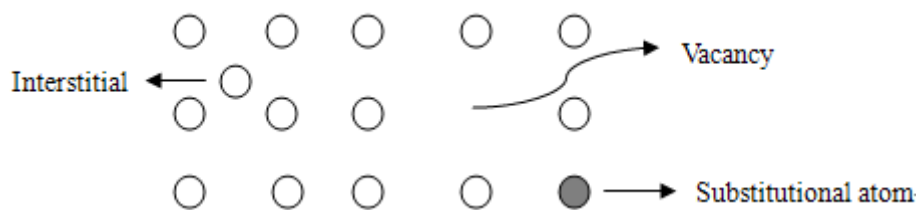


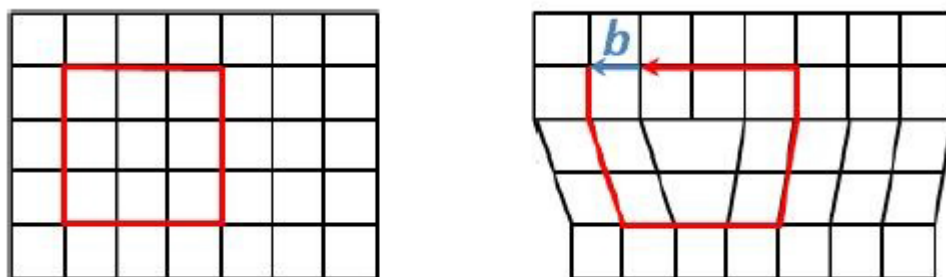
Fig.1.4 2-D representation of crystal structure with point defects.

Point defects described above are commonly unavoidable, however, the energetically favourable feature of defects make them within limits. If the impurities are incorporated into the native atomic site, these defects are substitutional defects [7]. And for the crystal comprising more than one chemical element, the exchange of

different type of atoms in the lattice is called antisite defect. As the presence of impurities even in a small proportion may largely alter the physical or electrical properties of the crystal. In semiconductor fabrication, the intentional introduction of extrinsic chemical element to the native crystal is a method called doping. And this is an efficient way to alter the properties of semiconductor into the desirable characteristics.

#### 1.2.3.2 Line defects

Dislocation is a line defect in a lattice around which some atoms are misaligned [8]. The presence of dislocation results in distortion of lattice called strain. The lattice strain is usually expressed in terms of a Burgers vector ( $b$ ). The Burgers vector  $b$  describes the propagation of the distortion through the lattice. If  $b$  is normal to the dislocation line, it forms an edge dislocation resulting in the lattice deformation. In heteroepitaxial growth of lattice mismatched semiconductors, edge dislocations are commonly formed and the strain energy deduced by the lattice mismatch is usually released in the epilayers. In the case of  $b$  parallel to the dislocation line, a screw dislocation is formed. It is caused by the partial shearing of a plane. In practice, the combination of these two types called mixed dislocation is more common.





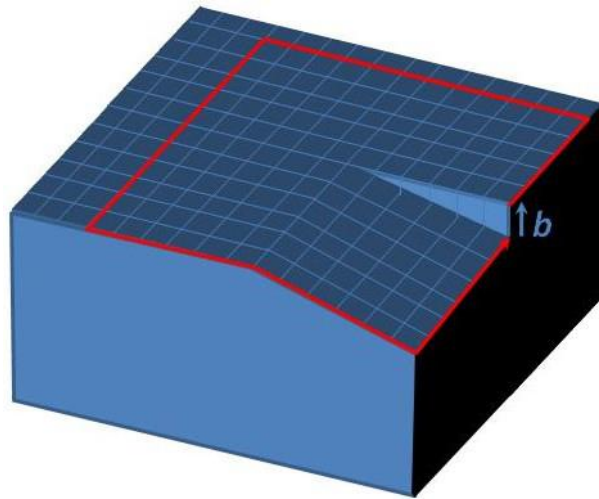


Fig.1.5 Representations of crystal structure with line defects.

If a partial shear is imposed on a plane, screw dislocations will build up and propagate into the bulk of crystal. In the long range effect, an edge dislocation may get attenuated and it is the screw dislocation leading to the subsequent layers grown upon it.

### 1.3 Properties of Low dimensional antimonide semiconductors

The III-antimonides are appealing material in the device applications such as high-electron-mobility transistors' barrier layers [9], the atmospheric window layer's (especially in the range from 3 to 5  $\mu\text{m}$ ) detector arrays, and thermophotovoltaic devices [10].

These III-antimonide materials including AlSb, GaSb and InSb could be grown by molecular beam epitaxy (MBE) and metalorganic chemical vapor deposition (MOCVD).

Due to the advancement of modern growth techniques such as MOCVD and MBE, it is possible to precisely manipulate the growth of atomic layers with atomically abrupt interfaces. Those micro-structural materials conceive large potentials in novel optical and electrical applications.

The DOS largely determines the optical and electrical properties of the quantum confined (QC) system. The degree of QC strongly alters the DOS value.

For 3D bulks, the density of states per unit volume is

$$D(E) = \frac{1}{2\pi^2} \left( \frac{2m^*}{\hbar} \right)^{3/2} \quad (1.1)$$

Where  $m^*$  is the electron effective mass,  $\hbar$  is the plank constant, and the Fermi energy is

$$E_F = \frac{\hbar^2}{2m^*} (3\pi^2 n_e)^{2/3} \quad (1.2)$$

And the Fermi wavevector of an electron in 3D is

$$k_F = (3\pi^2 n_e)^{1/3} \quad (1.3)$$

Where  $n_e$  is the electron density.

For 2D films, the density of states is

$$D(E) = \frac{m^*}{\pi \hbar^2} \quad (1.4)$$

The Fermi level energy is

$$E_F = \frac{\pi \hbar^2}{m^*} n_e \quad (1.5)$$

And the wavevector of an electron in 2D is

$$k_F = \sqrt{2\pi n_e} \quad (1.6)$$

For the 1D wires, the density of states is

$$D(E) = \frac{\sqrt{2m^*}}{\pi \hbar \sqrt{E}} \quad (1.7)$$

The Fermi lever energy is

$$E_F = \frac{\pi^2}{4m^*} n_e^2 \quad (1.8)$$

And the wavevector for an electron in 1D is

$$k_F = \frac{1}{2} \pi n_e \quad (1.9)$$

For the 0D dots, no free motion is possible. Because there is no k-space to be filled with electrons and all available states exist only at discrete energies, thus the density of states is described by the delta function.

$$D(E) = 2\delta(E - E_c) \quad (2.0)$$

Only kinetic energy is considered  $E \rightarrow E_c$ .

If the geometrical dimensions of a material is reduced below the scale of the de Broglie wavelength of a carrier (~several nanometers), it becomes a nanomaterial exhibits quantum effects. Size reducing in three, two and one directions results in quantum dots, quantum wires and quantum wells, respectively. From the basic solid physical perspective, the density of electronic states (DOS) for zero-dimensional quantum dots has been described by delta-functions. Figure 1.6 (top) illustrates the schematic representations of 0D quantum dot, 1D quantum wire, 2D quantum well and 3D bulk structures. Bottom shows the DOS of the corresponding structures

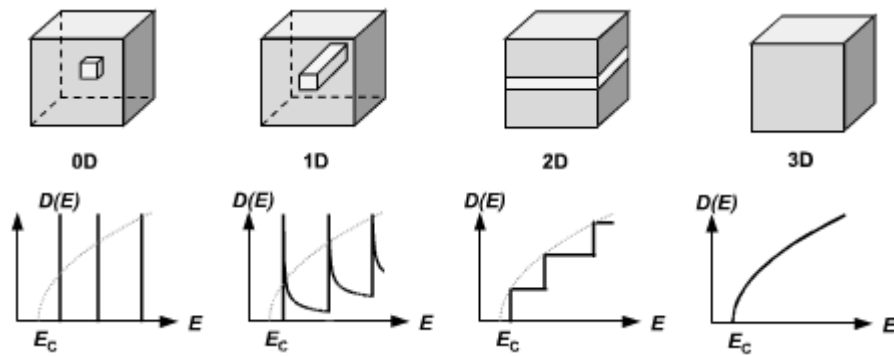


Fig.1.6 Schematic representations (top) and density of electronic states (bottom) of 0D, 1D, 2D, and 3D heterostructures [11].

The energy level of QDs resembles the single atom embedded in the dielectric surrounding rather than the classical semiconductor. In addition, the lack of commutation between the momentum and Hamilton operators provides infinite opportunities for design QD-based device with novel electrical properties.

Quantum dots are quasi-zero dimensional structures that behave quantum confinement in three dimensions. Consequently, the energy levels of QDs are discrete. The discrete energy levels make the QD materials exhibit interesting nonlinear optical behaviours. The QD materials with discrete energy states, therefore, become appealing candidates for the laser devices fabrication.

The theoretical predictions for QDs with perfect nonlinear optical features are valid for scales less than 10nm. Besides the uniformity and distribution of QDs are also significantly affect the optical performance of the structures. In practical growth techniques and devices fabrication, QDs within the scale of 100nm are of great importance since the coulomb effect among the inside electrons are still significant [12, 13]. The structural evolution of QDs is determined by the kinetic and thermodynamic factors during the heteroepitaxial growth of lattice-mismatched systems. Unlike the growth of classical defect-free hetero-structured semiconductors, slight modification of the strain in the epilayer would alter the geometrical properties and number density of QDs. Consequently heteroepitaxial growth of QDs needs more precisely control the growth process. Heteroepitaxy of different semiconductors with varied lattice constant may create different types of QDs with interesting physical and optical properties. The studies in chapter 3 and 4 mainly focus on InSb/GaSb (001) quantum dots.

#### 1.4 Heteroepitaxial growth of thin films

The advancements in the field of heteroepitaxy would not have been possible without the development of the epitaxial growth techniques such as molecular beam epitaxy (MBE) and metalorganic vapor phase epitaxy (MOVPE). These two methods

afford tremendous flexibility and the ability to deposit thin layers and complex multilayered structures with precise control and excellent uniformity. In addition, the high-vacuum environment of MBE makes it possible to employ in situ characterization tools using electron and ion beams, which provides the crystal grower with immediate feedback. For these reasons, MBE and MOVPE have been emerged as general-purpose tools for heteroepitaxial research and commercial production. Together, these two epitaxial growth methods account for virtually all production of compound semiconductor devices today [14].

The key challenges in the heteroepitaxy of semiconductors, relative to the development of useful devices, are the control of the growth morphology, strain, and crystal defects.

In real growth, fabrication of many of the devices would not be possible without the ability to form semiconductor heterojunctions such as laser diodes, high-brightness light-emitting diodes, and high-frequency transistors. Heterojunction devices are now entering mainstream electronics as well, with the development of SiGe heterojunction transistors. Hence, heteroepitaxial growth in a Stranski Krastanov or Volmer–Weber growth mode promises to enable practical quantum dot devices, including lasers and single-electron transistors [15, 16].

Heteroepitaxial growth needs the formation of a new phase on an existing substrate surface. The nucleation and growth mode greatly determine the morphology and structure of the epilayers. In its broadest sense, there are three main growth modes of heteroepitaxy: the Frank-van der Merwe (FM), Stranski-Kranstanov (SK), and Volmer-Weber (VW) mechanisms. In the case of FM growth mode, two dimensional or layer-by-layer growth dominates the deposition process. Islands of monolayer-height nucleate and coalesce to cover the substrate, followed by the formation of a next layer. In SK growth mode, the growth starts with the 2D planar growth, followed by the 3-D islanding after the growth of a certain critical thickness.

In the VW growth mode, 3-D islanding dominates the growth. The isolated 3-D islands commence on the substrate, followed by the broadening and coalescing process. This mechanism roughens the surface. Usually the root mean square roughness (rms) of the surface is close to the mean distance between islands on the surface. The FM, SK and VW mechanisms are illustrated in figure 1.7.

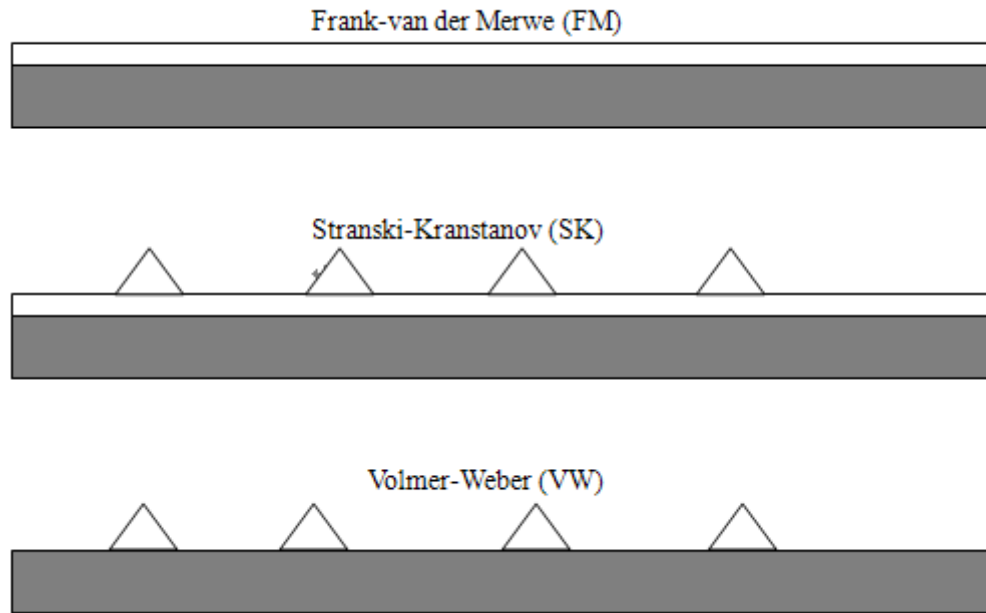


Fig.1.7 Schematic representations of Frank-vander Merwe (FM), Stranski-Krastanov (SK), and Volmer-Weber (VW) growth mode.

The growth modes are determined by the surface free energy of the substrate  $\gamma_s$ , the surface free energy of epilayer  $\gamma_e$ , and the interfacial free energy  $\gamma_i$ . The energy criterias are if the net change in free energy  $\gamma_s - \gamma_e - \gamma_i > 0$ , the growth mechanism would be 2-D F-M growth mode [17], in the reverse situation, the growth mechanism would be dominated by 3-D growth either S-K or V-W mode. Often in comparison to surface free energy, the interfacial free energy is neglectable. In the case of surface free energy of epilayer smaller than that of substrate ( $\gamma_e < \gamma_s$ ), 2-D planar growth is expected and the epilayer wets the substrate. Otherwise if  $\gamma_e > \gamma_s$ , 3-D islanding growth occurs [18]. However, in the case of growth starting with 2-D growth, as the deposition of epilayer the strain induced by the lattice mismatch

increases as increasing of the epilayer thickness. This can cause the growth of 3-D islands after the nucleation of several monolayers. From the energetic point of view, the formation of 3-D islands is one way of relieving strain caused by lattice mismatch. Therefore, in the case of heteroepitaxial layer wetting the substrate S-K growth may occur [19]. In the V-W growth mode, a wetting epilayer is not expected. For a vicinal substrate, it is not necessary to nucleate a completed layer before a new layer is commenced. The substrate surface comprises of several smooth terraces instead of a completed flat layer, therefore the epitaxial growth will proceed the step advancement (referred as step-flow growth). This phenomenon relies on the thermal energy which is sufficient for the deposited species migrating across the surface. Under the growth with a large supersaturation, the long diffusion length allows the adatoms migrate to a location with minimum energy. Step edges act as a sink for the species' diffusion, the adatoms prefer the step edge of the local terrace or the vicinal step edge down [20]. This gives rise to step edges migration instead of elimination. In the case of step-flow growth, the surface of the grown layer keeps smooth and the surface roughness doesn't change significantly for the step edges migration. Briefly, the most important kinetic factors in this growth condition could be the surface diffusivity, the growth rate, and the step barrier.

The important distinction between two-dimensional growth and the other modes is that in a two-dimensional growth mode either (1) a monolayer completes before a new one nucleates or (2) if multiple nucleation events occur on a flat substrate surface, the monolayer islands coalesce before additional growth occurs on top of them. Therefore, VW and SK growth, which involve islanding, are sometimes collectively called multilayer growth, referring to the fact that islands grow beyond one-monolayer thickness before coalescing on a flat substrate surface, the monolayer islands coalesce before additional growth occurs on top of them [21]. Therefore, VW and SK growth, which involve islanding, are sometimes collectively called

multilayer growth, referring to the fact that islands grow beyond one-monolayer thickness before coalescing.

In the case of growth of quantum-dot heterostructures (chapter 3 and 4), the S-K growth mode is desirable for the fabrication of QD assemblies. In most other device applications (chapter 5), 2-D layer by layer growth is requisite for the producing of device with flat interface and smooth surface.

With the development of epitaxial growth technique such as MOCVD and MBE, it makes the great achievements in the field of hetero-structure growth in recent years. For the requirement of producing high-quality semiconductor structures, it is necessary to control the nucleation and growth mode which determines the surface morphology and structural property of a film.

The mechanisms under the heteroepitaxial growth is commonly considered as thermo-dynamically driven [22]. Meanwhile, in the case of growth under a large supersaturation, the dominant growth mechanism is kinetically driven [23]. Growth accompanied by island ripening is commonly undesirable. From the thermodynamic point of view, the ripened islands will go through broadening in size and vanishing in number density. In a real heteroepitaxy condition, thermodynamic consideration growth of islands is also driven by kinetic factors. Therefore, the ripened islands in the real heteroepitaxial growth always involve a finite size and number density. The outstanding distinction between the stable islands and the ripened islands is that ripened islands can not retain stable as the deposition proceeds. In most device fabrication, growth of stable islands is always desirable. Although the lattice mismatch strain is fixed in a typical heterostructure, the strain in the epilayer increases with increasing amount of deposited materials.



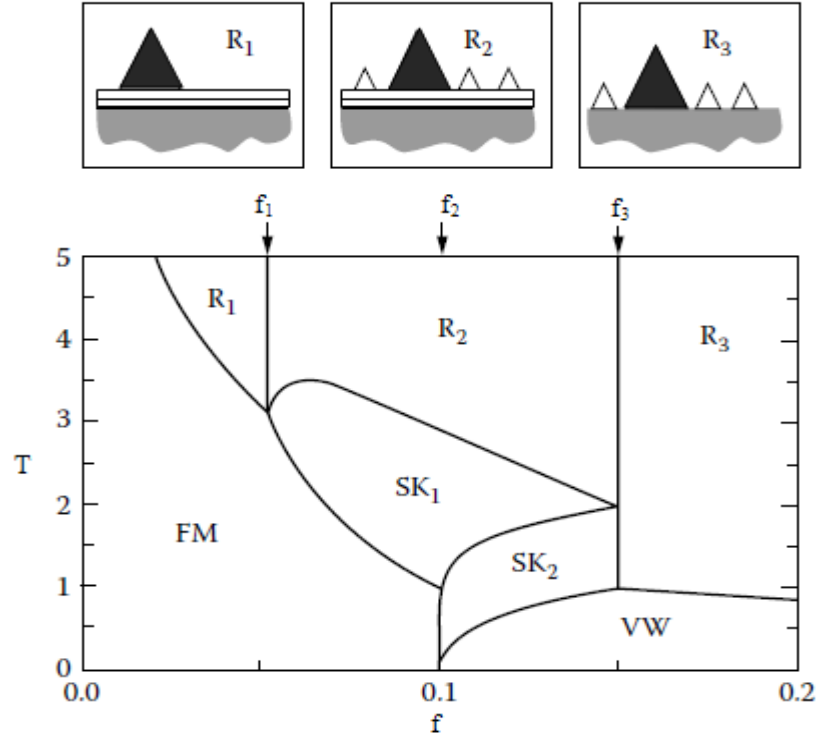


Fig.1.8 Equilibrium phase diagram of heteroepitaxial growth epilayers on a substrate. Where  $f$  is the lattice mismatch strain,  $T$  is the epilayer thickness in monolayer. The top insets illustrate the morphology of the surface in the corresponding phase regions. The large black triangles represent ripened 3-D islands and the small triangles denote stable 3-D dots (The phase diagram is reprinted from reference [24]) Daruka, I. and Barabási established an equilibrium diagram quantitatively describes the effect of lattice mismatch strain and epilayer thickness on the growth mode).

According the phase diagram established by Daruka and Barabási [24], heteroepitaxial growth with different lattice mismatch will proceed under different growth regimes. If the strain induced by lattice mismatch is small, in the regime I ( $f < f_1$ ), the growth will start with a 2D FM mode. As further deposition of epilayer on substrate to a certain thickness, the phase will be transfer to  $R_1$  region and 3D islands will form on the wetting layer. In particular, the thickness of wetting layer keeps constant and the further deposited materials only contribute to the 3D islands. In the regime II ( $f_1 < f < f_2$ ), the initial growth still occurs with a FM mode. For further

deposition of epilayer on substrate to the critical thickness, the phase will be transfer to  $SK_1$  region and the growth will change to SK mode. Stable islands with finite number density and size will form on the wetting layer [25]. Further deposition makes the phase transfer to region  $SK_2$  and increases the density of ripen and the stable islands. For the phase equilibrium consideration, the ripened islands in regime I and II will approach an infinite size and zero density while the kinetic considerations predict the islands will have a finite size and density. This makes the morphological evolution of InSb/GaSb QDs in this study complicated. Specific analysis of the QDs in different stages will be made in the forthcoming chapters.

Due to the strain in large lattice mismatched systems, the initial growth can not permit 2D FM mode and will start with 3D VW mode space in regime III, where  $f_2 < f < f_3$ . The growth will initially with the formation of 3D islands rather than a 2D wetting layer. As further deposition proceeds,  $SK_2$  mode will occur and a wetting layer may be formed after the growth of islands. The thickness of the wetting layer will increase as the continuing growth and the 3D islands will remain stable. As for the even larger lattice mismatch regime IV ( $f > f_3$ ), the initial growth will start with a 3D VW mode and the continuing growth will persist 3D islanding growth.

Based on the equilibrium theory, the four growth regimes predict the growth of ripened islands with infinite size and density. In a real growth, this will not happen due to the finite growth rate and surface diffusion process [26]. The equilibrium analysis here provides a guidance of the driven force of the growth and the direction of the growth mode. In the growth of QDs, the kinetic mechanisms determin the size and density of the QDs, and it has been demonstrated the morphology of dots could be influenced by changing the growth parameters such as growth rate and temperature [27, 28].

## 1.5 Outline of the thesis

In semiconductor industry, growth of one material on a different type of material called heteroepitaxy provides infinite variation of devices both in electronics, optics and even in quantum mechanisms. Epitaxial growth in a Stranski–Krastanov growth mode enables the fabrication of practical quantum dot devices such as lasers and single-electron transistors.

The tremendous advancements in the field of semiconductor growth would not have been possible without the advent and further development of the epitaxial growth techniques such as molecular beam epitaxy (MBE) and metalorganic chemical vapor deposition (MOCVD).

In this study, MBE is utilized to fabricate all the desirable samples. The reason for doing that is because the high-vacuum environment of MBE makes it possible to employ in situ characterization tools such as reflection high energy electron diffraction, provide immediate feedback to the crystal grower, and will further improve manipulation the growth. In particular, thanks to the capability of storage different material sources, MBE affords tremendous flexibility in growing complex multi-layers of excellent uniformity and the ability to deposit ultra thin layers (up to atomical thickness) with precise control.

The key challenges in fabrication of finest devices as well as molecular beam epitaxy of semiconductors are the control of the growth morphology, strain introduced by lattice mismatch, and crystal defects. Chapter 1 reviews the properties of semiconductors related to heteroepitaxial growth, including crystallographic properties, surface properties, and defect structures. Chapter 2 presents a brief overview of molecular beam epitaxial growth method, and some important characterization tools including in-situ reflection high electron emission diffraction (RHEED) and some ex-situ techniques such as atomic force microscopy (AFM), transmission electron microscopy (TEM), photoluminescence (PL) and Hall effect measurements. Most of the semiconductor devices are fabricated by heteroepitaxial

growth, it usually needs to nucleate a new phase on the substrate surface. Therefore, the surface and its crystal structure, play important roles in determining the usefulness of heteroepitaxial layers for the fabrication of devices. Control of the growth mode by tailoring growth conditions such growth rate, temperature and V/III ratios is critical to the development of heterostructured semiconductors. In lattice mismatched growth regime, strain relaxation and the associated creation of crystal defects are of great importance. For the development of quantum dot devices, Stranski–Krastanov (growth of a wetting layer followed by formation of islands) or Volmer–Weber (growth of 3D islands) is quite desirable. In this study, control of the QDs population, size, and distribution is critical. For this aspect, investigation of the growth and characterization of self-assembled InSb/GaSb QDs is covered in this thesis. In most cases, the flat, abrupt interfaces and surfaces, or concluded as two dimensional growth is desirable. Under the condition of moderate lattice mismatch (<2%), it is possible to grow a pseudomorphic heteroepitaxial layer, which persists coherent with the substrate crystal in the plane of the interface. But at some thickness the creation of misfit dislocations becomes energetically favorable. The initial growth is related to the growth of InSb/GaSb (001) QDs at low temperatures. Dot density of  $\sim 10^{11}$  has been obtained from sample grown at 275 °C at the InSb coverage of 2.5 ML. Further analysis of trends at 320 °C, 275 °C and 250 °C including dot densities, volumes and estimation of critical thickness have been presented in chapter 3. Growth and characterization of buried InSb dots have been presented in chapter 4. The sample with 2.5 ML buried InSb QDs with density (up to  $4 \times 10^{10} \text{ cm}^{-2}$ ) were obtained on the GaSb (001) by MBE. HRTEM cross-section images of the coherent and defect free InSb QDs buried into the GaSb spacer were observed. The estimated size of SQDs was  $\sim 26$  nm (base width) and 3 nm (height). The estimated sheet density of SQDs was  $\sim 1.2 \times 10^{10} \text{ cm}^{-2}$ . The average size of the BQDs was slightly smaller ( $\sim 22$  nm in lateral width and  $\sim 2.5$  nm in height). The experiment illustrated the possibility of the formation of InSb QDs on the GaSb matrix in SK mode. The estimated wetting layer thickness was  $\sim 0.6$  nm ( $\sim 1.7$  ML).

The electrical properties of the sample were measured by PL. The PL spectra indicated there were two energy peaks which related to the QDs. We suspected that the RT peaks at 3.4 eV and 4.6 eV were related to the SQDs and BQDs, respectively. Based on the results from the growth of InSb on GaSb, under a relatively optimized growth condition, Chapter 5 studies the heteroepitaxial growth of III-Sb layers on undoped GaAs (001) substrate. In particular, studies have been focused on the effect of growth temperature and growth rate on the surface morphology and electrical properties of III-Sb/GaAs heterostructures. Sb-based semiconductors have great potential in producing infrared devices. In chapter 6, both the theoretical and the experimental reflectivity measurement have been made on the GaSb and InSb samples. Based on the Kramers-Kronig Transform, the electrical properties can be deduced from the optical parameters. The results obtained from the reflectivity measurements are compared with the results calculated from the Hall measurements.

## **Chapter 2 MBE and characterization techniques**

Many available epitaxial growth techniques exist for the heteroepitaxy of semiconductors. Techniques such as liquid phase epitaxy (LEP) were commonly employed to the early stage growth of compound semiconductors such as GaAs. As the advent of more effective growth tools, molecular beam epitaxy (MBE) and metalorganic vapor phase epitaxy (MOVPE) are involved as more advanced techniques for heteroepitaxial growth both in experimental research and industrial production. Both MBE and MOVPE have been greatly utilized in the heteroepitaxial growth with varying degrees of success. MBE is used in the fabrication of all the samples in this thesis. The advantage of MBE lies in its great capability in the deposition of ultra-thin layers (up to monolayer thickness) with precise composition and abrupt interface. The multi-source fitted growth chamber makes it flexible and powerful in the growth of almost all kinds of compound semiconductors with various structures and superior purity. This chapter discusses the basic regimes in MBE growth and provides a brief introduction of the characterization techniques.

### **2.1 MBE**

In the late 1960s, the first MBE equipment was invented at Bell Lab by John Arthur and Alfred Cho. The MBE system is referred as ‘mega-buck’ evaporator and the structure inside it is quite sophisticated. After years of study, it was proved that the MBE growth mechanism was governed by kinetics of the surface process rather than the thermodynamic equilibrium conditions [29]. Since then, MBE technique has been further developed. Up to now almost all kinds of semiconductors including Si/Ge, group III-V and II-VI compound semiconductors [30], and diluted nitrides could be grown by MBE semiconductor materials. In addition, MBE is also used to grow various materials such as oxides, metals and magnetic alloys [31]. The structure and the mechanisms inside the MBE apparatus is sophisticated. Figure 2.1 illustrates a schematically simplified representation of the GEN II MBE apparatus.

The GEN II apparatus can equip 8 types of material sources either in Knudsen evaporation cells or gas-source crackers. For clarity, only four effusion cells are displayed in the schematic diagram. The beams inject from the effusion cells onto a heated substrate. Retractable shutters and valves are installed in the source cells to open or shut the sources very abruptly. Based on the advantages of the devices, MBE has the ability of growing thin films with monolayer thickness and atomically abrupt interfaces. In addition, the ultra-high vacuum environment allows the possibility of install a number of in situ characterization tools in the MBE apparatus, such as the RHEED equipped in the growth chamber in figure 2.1. These in situ characterization tools provide real-time feedbacks during the growth process and help to better control the growth condition. Among diverse epitaxial growth techniques, MBE is preferred to utilize in studying and inventing novel materials because of its diverse usage, precious control of material composition and its compatibility of several characterization tools.

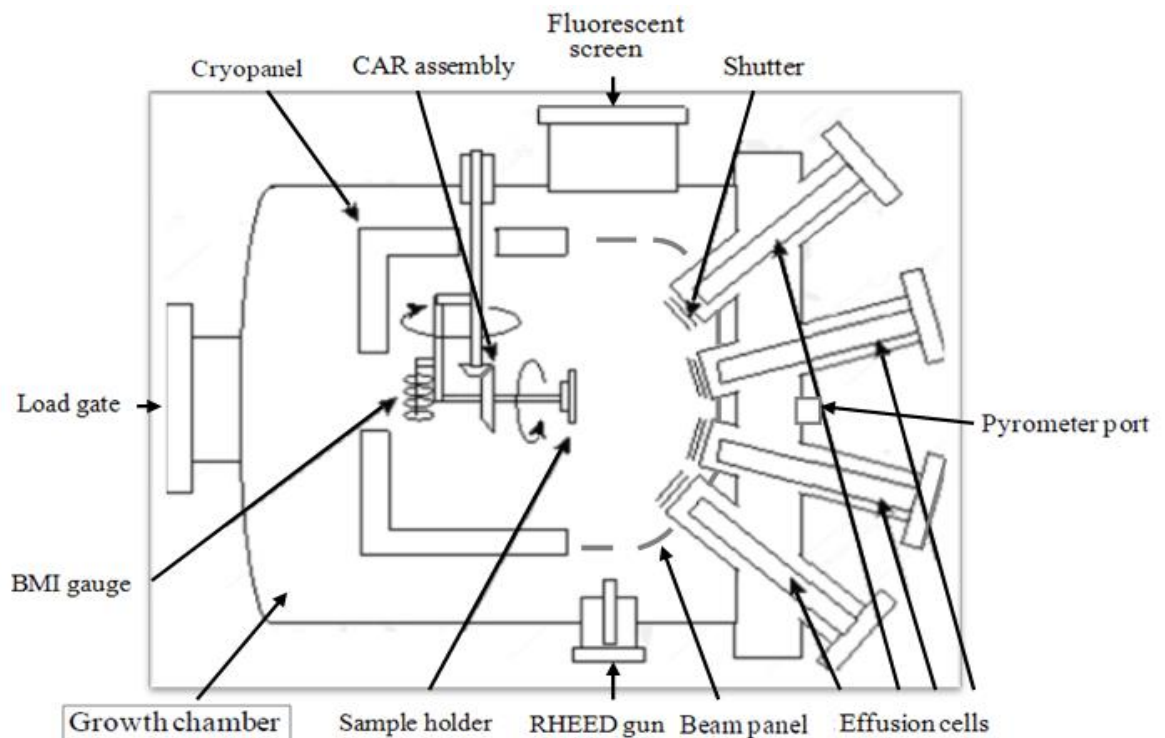


Fig.2.1 A top-view schematic of the GEN II MBE equipment used in this study. Some important components are displayed in this representation.

In this study, all the growth was conducted in the GEN II MBE chambers and equipment created by Varian and sold by Veeco. A representation of MBE growth chamber is present in figure 2.1. The system is designed to fit for epitaxy materials on wafers with diameter up to 3 inch. The outer walls of the growth chamber are surrounded by a stainless steel cryoshroud inside which liquid nitrogen is pumped. The function of the cryoshroud is not only cooling down the system but also reducing the undesirable species including the water vapour and the contaminants introduced by the hotspots such as ion gauges. Commonly eight effusion cells are installed radially around the continuous azimuthal rotation (CAR) stage, as shown in Figure 2.1. The effusion cells supply the required chemical elements for the epitaxial growth or doping of the desirable semiconductors. The protruded into the growth chamber part of the material sources are segregated by a beam panel. The beam panel may restrain the mixture of materials and the heat transfer from different sources. In addition, it also effectively prevents the liquid nitrogen evaporation from the cryopanel reservoir.

#### 2.1.1 The growth chamber

GEN II MBE Growth chamber usually installs eight material sources arranged radially around the substrate holder. Because of the multi-source chambers involving the MBE reactor, the direction of the impingement of molecular beams would not be normal to the plane of sample. Considering those samples used in this study are cleaved quarter pieces of 2'' and 3'' wafers, and the variance of effective impingement of beam flux in different region of wafer can not be neglected. Hence, for the uniformity of the coverage of beam flux, rotation of the sample during deposition process is always employed [32].

Molybdenum platen is used to affix substrate to the CAR with a Mo cover slide and a circlip. The heat unit which contains a ceramic disc inside is equipped behind the Mo platen. There is a small aperture in the center of heater unit at which affixes a



thermocouple. The thermocouple is fixed approximately 3 mm back from the wafer which gives feedback of the substrate temperature to some extent.

Sample mounting is a very important step to the growth. Different mounting methods involve difference in heat transfer mechanisms (conduction or radiation). In particular, it initially determines the types of technique that should be utilized during growth. There are two widely used methods of substrate fixation, the first one is indium bonding and the other is indium free affixing. For the mechanical and chemical consideration, the indium free mounting is employed in this study.

The growth chamber is in an ultra-high vacuum environment, under the UHV condition a flux of beam (molecule or atom) is impinged into a substrate directly. When the deposited species arrive the surface of the substrate, they will either adhere onto the substrate or desorb from the surface (in the case of inadequate bonding site in the growth crystal are unavailable). The equipped high-purity (>99.99%) material sources supply the desirable beam fluxes through evaporation or sublimation. The material sources are fixed 30-50cm from substrate platen, in the UHV environment ( $< 10^{-10}$  Torr), the mean free path of molecules (or atoms) is far greater than the distance between material source and substrate. Consequently, collisions between different molecules or atoms will be largely suppressed. Thermocouple is equipped to examine the temperature of the deposited material. Due to the sensitive beam monitoring ion gauge and temperature control, accurate growth rates control during the growth process is possible. Shutters and valves are employed during the growth. Consequently, control the amount of deposited materials becomes more precisely. In particular, abrupt interface is achievable under low growth rate due to the short shuttering time.

## 2.1. 2 SUMO cell

The original K-cell of a conical shape (with material capacity of 60 cc) has many disadvantages. First of all, the material capacity limitation, the high frequency in

source recharging leads to more opening time which needs to re-bake the system to maintain the UHV environment of the growth chamber. Secondly, due to the wide aperture of the heated cell, material wasting increases for much of the group III species adhered onto the chamber walls or shutters. It should be pointed out that due to the condensing of group III sources (Ga or In metal beads) at the crucible's lip, these condensations then drop back into the molten material sources and further spray onto substrates which has been reported as the main origins of the oval defects[33,34]. As to aluminum, although it doesn't condensed at the lip of cell because it wets the crucible, it may cause Al short-circuit of the cell. Hence, the effusion cell involved in this study is a dual filament SUMO cell (a variation of Knudsen cell sold by Veeco). Two heater coils are positioned at the tip and the bottom of the crucible. The temperature of the tip is commonly set 150-200 degree higher than the bottom. For precise control the temperature of the deposited beam flux, heat at the bottom supplies a constant portion of thermal energy to exit the bulk material and the heat at the tip provides the remaining energy for beams attaining to the desirable temperature despite the transients arising from the movement of shutter. This phenomenon indicates the smart design of growth temperature control in MBE system.

The SUMO cell with a narrow aperture results in an increased inside vapor pressure which is benefit to the flux uniformity. The narrow orifice significantly increases the capacity of the shallow upward cells and greatly reduces the introduction of undesirable species into the source cells which correspondingly prevents the formation of oval defects on the substrates. In particular, a retractable shutter is placed in front of the heated cell aperture to precisely control the amount of deposited material and effectively prevent contaminations' admission into the material source. Additionally, the SUMO cell with material capacity of 400 cc is a cylinder with straight-walled configuration instead of a conical-trumpeted shape.

One disadvantage of the SUMO cell is that it fails to precisely control the growth

rate during the deposition. Change in growth rate even in small extent requires a recalibration of the cell because even under the same temperature the beam fluxes will not always be identical. The original methods involved installing multi-cells with the same material but different growth rates. Modern MBE equipped valved effusion cells may control the growth rate more precisely [35].

Initially, Wafers are mounted on the Mo platens and transfer to the buffer chamber which is separated from the growth chamber by a valve. Then, outgassing heater would be activated to remove water vapor and other contaminants. After that but prior to admission the growth chamber, wafers are baked individually to remove the organic materials. The GEN II MBE in this study is equipped with 8 different material sources. The materials used in this study are gallium, indium, aluminum (group III) and antimony (group V).

Group III sources such as aluminum (Al), gallium (Ga) and indium (In) are impinged to the substrate through evaporation from molten material sources. The desirable material is filled in a heated crucible (pyrolytic boron nitride (PBN)). At temperatures above melting points, the group III materials have significant vapor pressure. In that case, Knudsen type evaporation is maintained instead of the Langmuir regime, then, a Knudsen cell (effusion cell) is utilized to heat these group III materials [36]. Consequently, material sources including Al, Ga and In source are commonly referred as Knudsen cells. Heating elements inside the crucible supply the necessary thermal energy to evaporate the needed depositing materials into beams.

## 2.2 RHEED

Reflection high-energy electron diffraction (RHEED) is an important in-situ diagnostic technique for MBE growth. Due to the low penetration of the electron beam and the distinct interactions between the beams and the encountered atoms, RHEED is of highly surface sensitivity. An electron beam with energy of 10-100 K eV is incident onto a surface at a glancing angle of 1-5 °. To operate a RHEED, it is

essential to reduce the elastic scattering from the bulk of sample to the greatest extent. Hence, the electrons do not greatly penetrate into the bulk and diffraction occurs on the surface which performs as diffracting from a 2D net of atoms. Besides, RHEED requires a high vacuum working condition to prevent the scattering of the electrons. When the electron fluxes incident upon the sample surface, it gets diffracted off and strikes onto a phosphorous screen. The resultant visible fluorescent pattern corresponds to the crystal structure of the surface.

Due to the high path length of incident electrons, RHEED may display a true bulk-like diffraction with electron beams penetrating a shallow surface. By analysing the separation between the streaks in RHEED patterns, lattice periodicity in the direction of perpendicular to the incidence plane can be assessed [37].

#### 2.2.1 Interpretation of several typical RHEED patterns

As a critical characterization tool, RHEED is commonly utilized to evaluate the surface of sample prior to growth and during the growth. It helps to verify the loaded substrate with a smooth and contaminant free surface which is crucial for the overgrowth of high-quality epilayer. In addition, growth parameters such as the growth mode and growth rate as well as the surface morphology are evaluated during the growth. Surface structure can be investigated by analysing the observed RHEED patterns.

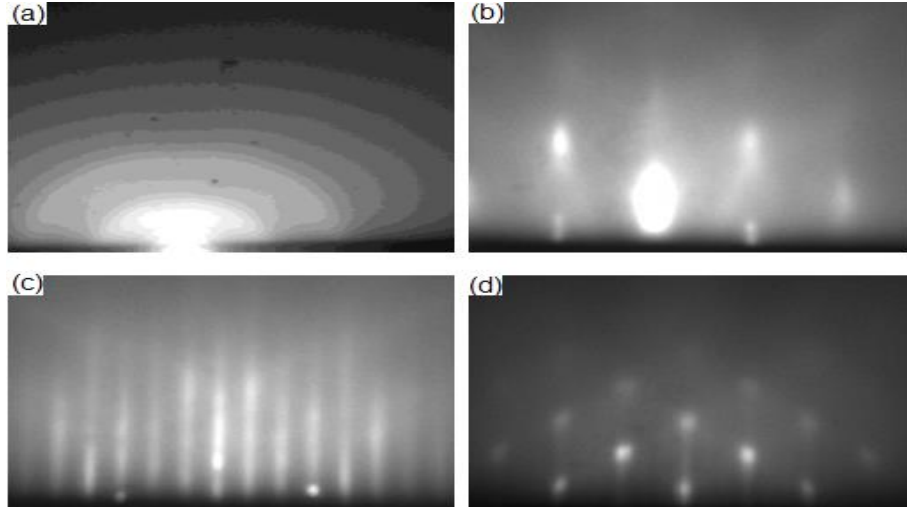


Fig.2.2 RHEED patterns performed on an (a) amorphous/polycrystalline surface, (b) rough surface in the  $[110]$  azimuthal, (c) smooth surface in the  $[\bar{1}10]$  azimuthal and (d) dots surface in the  $[\bar{1}10]$  azimuthal. Images taken under a 13 kV electron beam with a glancing angle between 1-5 ° incident in different azimuthals.

RHEED patterns display surface specificity very clearly after the incidence of electron beams in a proper glancing angle (1-5 °). For an amorphous/ polycrystalline surface, a dim haze or specular ring pattern (figure 2.2 a) is expected. For the RHEED image exhibiting an elongated spotty pattern (figure 2.2 b), a rough surface is expected. The electron diffraction from the 3D lattice is enhanced by the beam penetration through the 3D islands or other 3D structures on surface. The streaky RHEED pattern (figure 2.2 c) indicates an atomically flat surface (planar growth), and the order of streaks corresponds to surface reconstructions. Atomic reconstruction on surface commonly arises to decrease the surface free energy, otherwise only the primary streaks may be observed. Surface reconstruction displays various manners under different temperatures. Therefore, it is possible to effectively evaluate growth temperature upon the transition of the surface reconstruction. For instance, GaAs has  $2 \times 4$  surface reconstruction under a typical of arsenic overpressure condition at 580 °C [38, 39]. As to the sharp spotty pattern (figure 2.2 d), that indicates the emergence of 3D dots on the surface.

### 2.2.2 The intensity oscillations

In a planar growth dominated regime (F-M mode), RHEED intensity oscillations are commonly used to evaluate the growth rate. The time for deposition one monolayer is corresponding to one period of intensity oscillation [40].

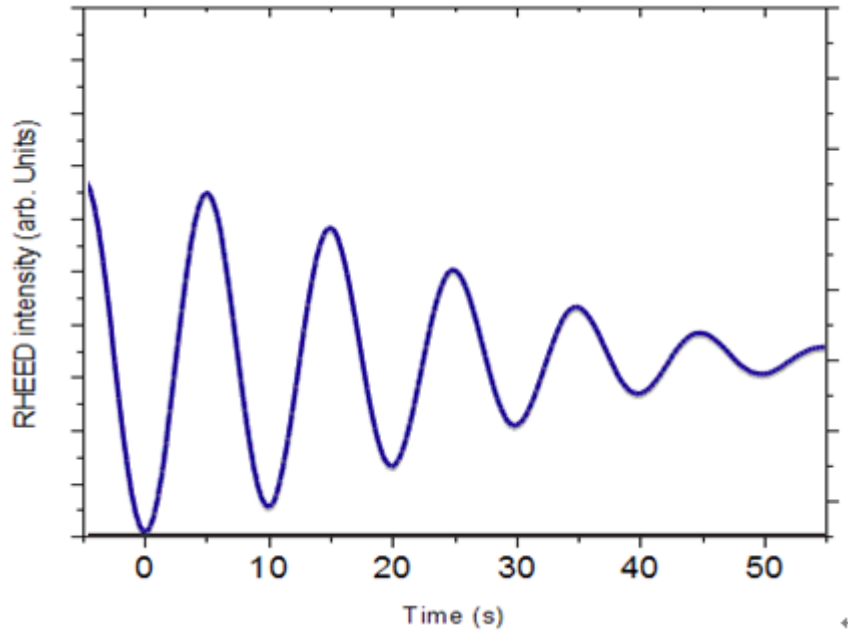


Fig.2.3 RHEED intensity oscillation in the deposition of 5 ML InSb on GaSb (001) at 320 °C, the oscillation period is ~ 10s that indicates the completion of 1 ML and the calibrated growth rate is ~ 0.1 ML/s.

It is also used to calibrate the material source by monitoring the specific intensity oscillation under different growth temperatures [41]. Figure 2.3 illustrates the RHEED intensity oscillation in the deposition of 5 ML InSb on GaSb (001) at 320 °C, the oscillation period is ~ 10s that indicates the completion of 1 ML and the calibrated growth rate is ~ 0.1 ML/s. For the growth under a stable antimony flux, the intensity oscillation curve usually exhibits a plateau region that indicates the growth is limited by the consumption of antimony [42]. This phenomenon manifests the group III material dominated depositing process. The growth in this study is all group-III limited deposition, it is very important to evaluate the flux ratio by analyzing the oscillation period. Generally speaking, through analysis of the RHEED

intensity oscillation, information including growth rate as well as material incorporation mechanisms can be evaluated.

### 2.3 AFM

Most of microscopies are utilized to study the surface morphology and analyze the growth mode. Atomic force microscopy (AFM) affords the atomic-scale resolution for imaging the surface with atomic structure.

Since the first AFM was proposed by G. Binnig and Ch. Gerber in 1986, currently AFM has become one of the most commonly used tools for scanning probe. By adhering a tiny piece of diamond onto the end of a foil of gold, AFM combines the principle of Scanning Tunneling microscopy (STM) and stylus profilometer. Compared with STM, it can be employed to examine non-conducting samples with an atomic scale resolution. AFM (offered from Asylum Research) with the MFP-3D apparatus is used in this study, information of surface morphology such as mounds, 3D islands, or quantum dots as well as defects can be observed directly.

The operation of AFM is simplified illustrated in figure 2.4. A cantilever with a diamond tip probes the surface in linear x and y direction range from 0.5 to 90  $\mu\text{m}$  with a z-direction resolution of  $\sim 0.3$  nm (one monolayer).

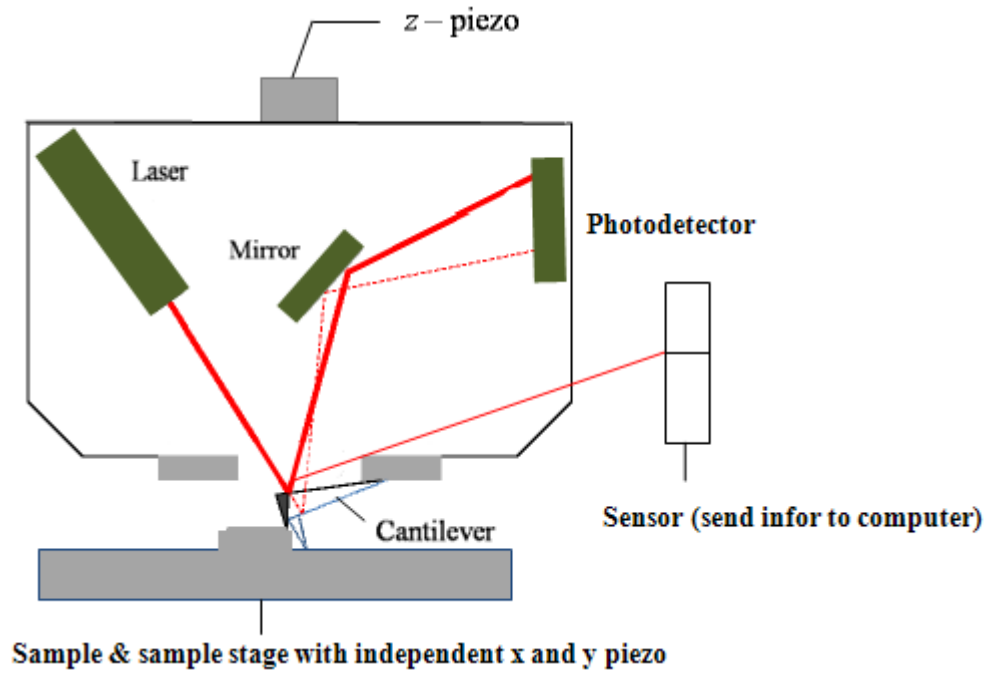


Fig.2.4 A schematic diagram of atomic force microscopy. The z piezoelectric element is collected in an actuator installed apart from x and y piezo stage to prevent cross talk.

During the imaging, a small constant force is imposed on tip of the cantilever. In particular, the z piezo electric is imposed separately to prevent the interference between the x and y stage. Different from the STM scanning regime, AFM imposes a probe close to the examined surface by physical interacting. It measures the force between the tip and the surface by deflecting the cantilever. Forces are imposed by sensing the distance between the tip and the surface of sample under observation. The Vander Waals force varies in a range from attractive (non-contact) to repulsive (contact) force as illustrated in figure 2.4. For the purpose of image with best accuracy, the scanning may be better to perform in the repulsive force region with respect to the attractive force region. Although the resolution in z-direction is precise ( $< 1 \text{ nm}$ ), the resolution in x and y direction is commonly determined by the dimension of tip used [43].



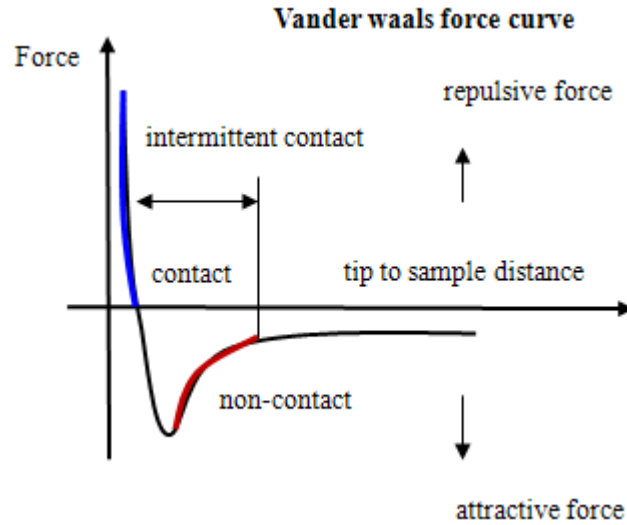


Fig.2.5 The Vander Waals force curve between the tip and the specimen under examination. The blue curve indicates the repulsive force region (contact mode) and the red curve represents the attractive force region (non-contact mode).

According to Hooke's law, the deflection is proportion to the force imposed on the catilever. The interation forces between a probe tip and a sample are measured by AFM. The force varies from no net force to a range over a strong repulsive force by going through a region of attraction. The two scanning modes are dependent on the result of z piezoelectric element as shown in figure 2.5. In operation, the force imposed on the AFM cantilever by a piezo voltage is controlled in a constant value. Similar to the tunneling current exerted in STM, the z-direction displacement of STM is corresponding to the z-direction piezo sensed by AFM regardless the specific regimes of the feedback. By measuring the position of laser reflected by cantilever, the forces in the magnification of  $10^{-11}$  N can be measured.

In addition, the scan speed of AFM is determined by the spring constant of the cantilever, its effective mass, the stiffness of the sample, and the dampling constant of the cantilever in the surrounding medium.

Both of the two scanning modes (contact and un-contact mode) involved in AFM are dependent on the requirement of z-piezo voltage. During the operation, it should control a constant position of the reflected laser onto the photodiode [44].

### 2.3.1 Contact mode

Contact mode operates in the repulsive force region as shown in the blue Vander Waals force curve (figure 2.5). During the imaging process, the diamond tip (AFM stylus) keeps in contact with the surface of the specimen under examination. The tip mounted to the cantilever commonly has a low spring constant to give sensitive feedback of the force. For the consideration of accuracy, the spring constant of tips remains at a value lower than that binding the atoms on specimen's surface. By imposing x and y piezo to the tip, it moves back and forth in a straight line across the surface. A laser beam is focused to reflect off the cantilever and onto the sensor (sends information to computer). The position of the laser spot records the deflection of the cantilever and the force between the tip and the surface of sample. The change in deflection is adjusted by a feedback loop to the z piezo and measured as a function of x and y piezos. The sensor is connected to a computer which helps to record the vertical position of tip during moving across the specimen. An AFM topographic image is built based on the data recorded by the computer.



Fig. 2.6 A representation of contact mode.

In the case of the samples with a fragile surface, contact mode could either ruin the surface or tangle onto the protruded features of the sample as shown in figure 2.6. In this case, non-contact (tapping) mode may have advantages and should be employed. A schematic representation of tapping mode is illustrated in figure 2.7

### 2.3.2 Tapping mode

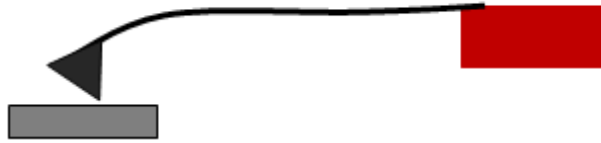


Fig. 2.7 A representation of tapping mode.

In tapping mode, a piezo driven oscillatory excitation is imposed onto the cantilever. After the probe motion is damped by the repulsive force, hence the z stage is stretched and forthcoming the lateral imaging. Each scanned point is measured by an approach cycle which effectively avoids the damage. The z-piezo driven oscillation is maintained constant by the feedback control. In computer program, the topographic information is recorded as a function of x-y position.

### 2.4 TEM

Although AFM gives the direct information of surface morphology, it is unable to inspect the defects in the bulk of material and at the interface. Transmission electron microscopy (TEM) enables the observation of dislocations and crystal defects inside the bulk of crystals. Sample preparation is a critical step in TEM characterization. The typical heteroepitaxial sample must be thinned to transmit electrons ( $< 100$  nm), provided it keeps stable under incident of high energy electron in a vacuum environment. In that case, the sample preparation may affect the bulk properties consequently alter the defects to be inspected.

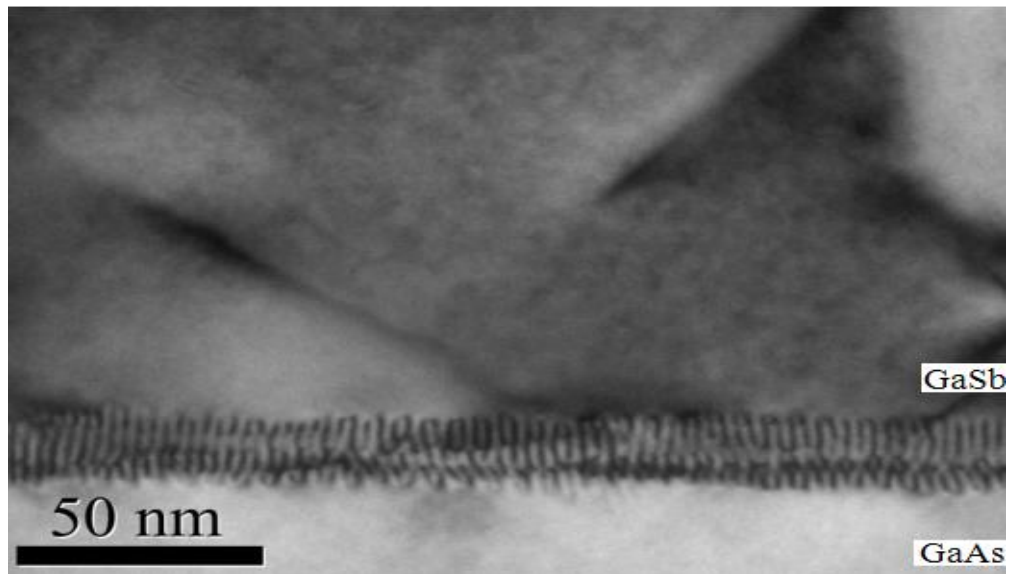


Fig.2.8 A TEM image taken from a 500nm GaSb grown on GaAs (001) under 220 bright field. It is clear that the misfit arrays formed on the interface, the dislocations originate from the interface and propagate to the GaSb epilayer. The TEM image was taken by J. Patel in Warwick university.

In the diffraction mode, the diffraction pattern comprises of an array of spots which corresponds to a particular diffraction vector [45]. In order to facilitate the selection of the diffraction spots and index the diffraction beam, the diffraction mode is used in prior to the imaging mode to ultimately form an image [46].

In the imaging mode, the aperture at the back of the objective lens is used to collect one electron beam to form the image. For the bright field imaging, images are taken from the transmissive electrons along the direction of incident electron beam. While the dark field image is collected from the electrons off the direction of the incident electron beam, that means the dark field image is created from the diffracted beam [47].

A perfect crystal will form an image with uniform diffraction intensity while crystal imperfections such as variations in composition, changes in thickness and structural defects will produce image contrast. Dislocations may displace the diffracted planes by altering the separation and orientations. Figure 2.8 displays a TEM image taken

from a 500nm GaSb grown on GaAs (001) under 220 bright field. The image contrast indicates the threading dislocations exist in the GaSb epilayer. It is clear that the misfit arrays formed on the interface, the dislocations originate from the interface and propagate to the GaSb epilayer.

## 2.5 Photoluminescence

Photoluminescence (PL) is a powerful tool to probe energy levels of semiconductors, it takes the advantage of the light emission from a material which is optically excited. The mechanism lies in the PL is that the excited electron will fall and recombine with the hole and realise a phonon to attain the available lowest energy level.

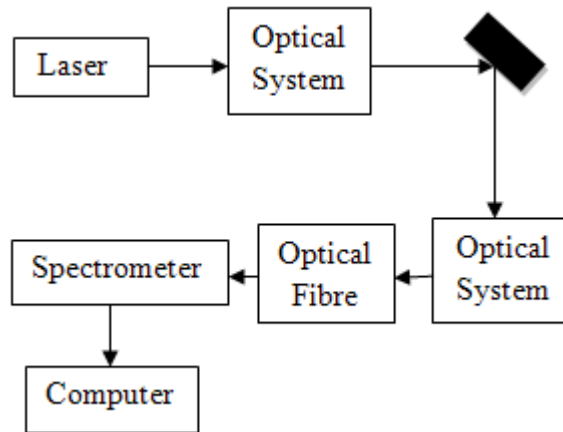


Fig.2.9 A representation of PL measurement set-up.

Figure 2.9 shows the PL experiment set-up. The laser and the optical system are used to tune the wavelength energy close to the bandgap of the semiconductor. It can be proceeded under cryostat allow the measurement of the luminescence properties at low temperatures. Photoluminescence will occur after the laser beams incident on the surface of the semiconductor, the wavelength of the emitted light is dependent on the composition of the measured material. The emitted light is incident into an optical fibre and further transferred to a spectrometer. A diffraction grating is installed inside the spectrometer and it diffracts the incident wavelengths into different directions [48]. The diffracted light wavelength intensities are measured by an array of

photo-detectors. The spectrometer is connected to a computer which puts out the digital PL information.

## 2.6 Hall Measurement

Van der Pauw method is utilized in the Hall measurement in this study. The good point of this method is that it could accurately measure the electrical properties of a sample with arbitrary shapes, as long as the sample thickness is less than its width and length [49, 50].

### 2.6.1 Sample preparation and mounting

For the purpose of accuracy in measurement, the symmetrically cleaved sample is preferable. The sample preparation procedures show below: first of all, cleave a sample to the size of 1 cm  $\times$  1 cm, in order to attain good contacts, scratch the corners with a diamond pen as shown in figure 2.10 (a). Secondly, cleave a glass slide and mount it on the copper plate holder, mount the sample on the cover glass and make sure the corners don't point to the sample holder as shown in figure 2.10 (b). Third, put some InGa onto the scratched sample corners with gloves and mount the sample plate to the cryostat. Finally, measure the resistivity of each side with a multimeter.

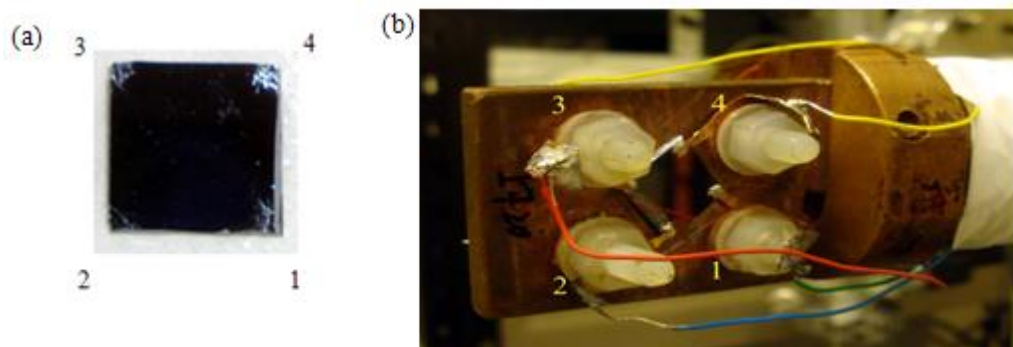


Figure 2.10 (a) Sample with scratched corners, (b) Sample mounted on sample holder. Wires are attached in a clockwise 'rainbow' manner.

After the sample preparation, sample mounting procedures display below: initially, connect both of samples with the cryostat and mount the first shell. Then, start the program ‘Cryo2012’ and measure the resistivity to check if there has contact between the sample and the first shell. After mounting the second shell, it is important to install the vacuum. Followed by closing the venting valve, starting the rotary pump, opening the valve from the vacuum system to the cryostat, and starting the turbo pump. Then, measure the diode with the ‘414-58 Semiconductor Parameter Analyzer’. Finally, turn on the water cooling, start the magnet, and start the ‘cryostat 2012’ program.

## 2.6.2 Measurement

In the ‘Cryo2012’ program, electrical parameters including resistivity, Hall coefficient, sheet density, and mobility can be obtained by the measurement.

From the resistivity measurement, the voltage  $V_{ij}$  along each edge of sample and the current  $I_{ij}$  across the opposite edge are measured. Each side resistance  $R_i$  is obtained by  $V_{ij}/I_{ij}$ , and the Van der Pauw resistance  $R_{vdP}$  is given by

$$R_{vdP} = \frac{\sum_{i=1}^4 R_i}{4} \quad (2.1)$$

The fill factor  $F_i$  is given by

$$F_i = 1 - 0.5 * \ln 2 * \left[ \frac{R_i - 1 - R_i}{R_{i+1} + R_i} \right]^2, \quad i = 1, 2, 3, 4 \quad (2.2)$$

The Sheet Resistivity  $R_s$  is given by,

$$R_s = \frac{\pi}{\ln 2} F(R_{vdP}) \quad (2.3)$$

The Hall measurement is followed by the resistivity measurement, the parameters are obtained in table 2.1 below

Table 2.1 parameters measured by Hall measurement.

	VHall+(uV)	VHall+(deg)	VHall-(uV)	VHall-(deg)	VHall(uV)
0	A <sub>0</sub>	a <sub>0</sub>	B <sub>0</sub>	b <sub>0</sub>	V <sub>0</sub>
1	A <sub>1</sub>	a <sub>1</sub>	B <sub>1</sub>	b <sub>1</sub>	V <sub>1</sub>

The Hall voltage  $V_{\text{Hall}}$  is given by

$$V_{\text{Hall}} = \frac{1}{2} \sqrt{[\bar{A} \sin \bar{a} - \bar{B} \sin \bar{b}]^2 + [\bar{A} \cos \bar{a} - \bar{B} \cos \bar{b}]^2} \quad (2.4)$$

Where  $\bar{A}$ ,  $\bar{a}$ ,  $\bar{B}$ ,  $\bar{b}$  are the average of the measured values in table 2.1, and the Hall coefficient  $H$  is defined as,

$$H = \frac{V}{B} \quad (2.5)$$

Where the magnetic field intense  $B = 0.2$  T (corrected). The sheet density  $n$  is give by

$$n = I/(q \cdot H) \quad (2.6)$$

And the mobility  $\mu$  is given by

$$\mu = (1 \times 10^6 \cdot H)/(100 \cdot R_s) \quad (2.7)$$

Where  $I = 10^{-15}$ ,  $q$  is the electron charge,  $H$  is the Hall coefficient, and  $R_s$  is the sheet resistivity.



## **Chapter 3 MBE growth and characterization of single layers of InSb dots**

A study of directly deposition of InSb on undoped GaSb (001) substrates by MBE at low temperatures is presented in this chapter. Under the growth rate of  $\sim 0.11 \text{ ML/s}$  and temperature as low as  $320^\circ \text{C}$ , self-assembled InSb quantum dots (QDs) with high density and uniform size distribution have been obtained after deposition of 2ML of InSb. The initial set of 1 to 6ML of InSb was deposited on GaSb (001) substrates at  $320^\circ \text{C}$  with a  $0.1 \mu\text{m}$  thick GaSb buffer layer grown before deposition of InSb. Surface morphology was investigated by atomic force microscopy (AFM) and the properties of QDs on the surface were statistically analysed by using the AFM particle calculation program. The AFM results indicate the total amount of deposited InSb plays an important role in determining the dot density and dots size. To further explore the dependence of dot density and dots size distribution on growth temperature, another two sets of 1 to 4.5ML of InSb were deposited on GaSb substrates under the same MBE growth procedure at the growth temperature of  $275^\circ \text{C}$  and  $250^\circ \text{C}$ . It is remarkable that the QDs grown at  $275^\circ \text{C}$  has highest dot density, the maximum dot density of  $9.8 \times 10^{10} \text{ cm}^{-2}$  was obtained after deposition of 2.5ML InSb at  $275^\circ \text{C}$ . The QDs obtained in these three sets of experiment have relatively monomodal size distribution.

### **3.1 Introduction**

The unique physical properties and narrow bandgap of InSb makes it an attractive material for the application of ultra-fast electronics [51, 52] and mid-infrared detectors [53-55]. Although the technology of Sb-based semiconductors has been well-exploited recently, problems including the high thermal sensitivity and the lack of laser source emission in the region of 3 to  $5 \mu\text{m}$  at room temperature still exist [55-58]. InSb QDs with characteristics of high material gain and low temperature sensitivity makes themselves quite promising candidates for the fabrication of novel

optoelectronic devices [59-62] and mid-infrared nanophotonic devices such as photonic sensors for environment monitoring and free-space optics [63, 64]. InSb/GaSb has a lattice mismatch of ~6.3% which is similar to the extensively studied InAs/GaAs system [65] and, in principle, the direct deposition of InSb would form 3D islands via the Stranski-Krastanov growth mode. However, reports in the literature have indicated that direct deposition leads to a low density of dots ( $\sim 4 \times 10^9 \text{ cm}^{-2}$ ) of low aspect ratio, leading to the development of methods to circumvent this problem [66]. In particular, the weaker In-Sb binding energy leads to the longer Indium adatoms' diffusion lengths on Sb-terminated surfaces makes the growth of high density InSb QDs especially on GaSb substrates more difficult. Upon this phenomena, one group grew InSb on other group V materials (such as As)-terminated surface and dots with high nucleation density has been obtained successfully [61]. Although lots of work have been done to explore the key growth parameters to tailor the properties of QDs, the basic results could be concluded as morphological features of InSb QDs are independent of the growth parameters including growth temperature range from 450 °C to 365 °C and growth rate from 1.2 ML/s to 0.3ML/s [61]. Considering all those previous growth methods and results of the InSb research [58-61], In this chapter, three sets of single layers of InSb/GaSb were grown by MBE at 320 °C, 275 °C and 250 °C respectively. Analysis of the trends for dots including quantum dot densities, volumes and estimation of critical thickness are presented. The techniques to be used are AFM, RHEED and TEM. Deposition of InSb directly on GaSb under lower growth temperatures and an ultra-low growth rate. The reason for doing that is when growth temperature drops down to a value lower than the Sb condensation temperature, not only the diffusion length of Indium adatoms decreases but also the formation of antimony solid clusters helps to further suppress the migration of In adatoms which will make the formation of high-density dots possible. The growth of the InSb was conducted in the GEN II MBE apparatus, the growth process was monitored by an in-situ RHEED. The surface morphology of sample after removal from growth chamber was examined by

atomic force microscopy (AFM). The initial set of 1 to 6ML of InSb was deposited on GaSb (001) substrates at 320 °C with a 0.1 µm thick GaSb buffer layer grown before deposition of InSb. For the deposition of 1 – 2ML of InSb, no dots were observed on the surface, which agrees with predictions for the critical thickness for InSb deposited on GaSb. Clear formation of dots was observed on the surface of sample at the InSb coverage of 2.2ML. After depositing of 3 ML InSb, dots with height of  $2 \pm 1$  nm and base diameter of  $20 \pm 10$  nm got a maximum density of  $\sim 4.7 \times 10^{10} \text{cm}^{-2}$ . Above the coverage of 3.5ML, the dot density decreased and evidence of coalescence was observed. The observed dot densities reported here are an order of magnitude greater than previously reported for direct deposition and are comparable to those achieved by post deposition annealing [56]. The second set of samples with InSb coverage range from 1 to 5ML was grown at 275 °C. The growth temperature is set to 55 °C lower than the initial set of growth to further evaluate the dependence of dot density and dot size on growth temperature. InSb QDs of higher dot density and relatively uniform size have been obtained in the second set of growth. This result indicates that under lower growth temperature the diffusion of In is further suppressed and the population of nucleation is further enhanced. After comparison of these two sets of samples, the QDs grown at 275 °C show higher dot densities than those grown at 320 °C, the maximum dot density of approximately  $10^{11} \text{cm}^{-2}$  is obtained at the InSb coverage of 2.5 ML. To assess the effect of further reduced temperature onto the properties of dots. The last set of samples with InSb coverage range from 1 to 4ML was grown at 250 °C. At the temperature of  $\sim 230$  °C, the diffusion length of In-adatom and the volatility of Sb is limited to sustain 2D layer growth and the phase segregation may occur. Surface reconstructions during the InSb growth exhibit different from the  $c(4 \times 4)$  to  $(\times 3)$  transition, the RHEED patterns get simultaneously changed along all the three azimuths. Above the coverage of 2ML InSb, a Sb-rich  $c(1 \times 1)$  surface emerges from a  $c(4 \times 4)$  less Sb-rich surface. Compared with the results of InSb/GaSb(001) QDs grown at 275 °C, It is notable that the number densities of QDs grown at a lower

temperature (250 °C) largely below those grown at 275 °C. The unique surface reconstruction at the temperature of 250 °C may suppress the nucleation of InSb. In addition, the limited volatility of Sb and diffusion length of In-atom may trigger the occurrence of phase segregation and the surface morphology is rich. Considering that 2D layer growth regime may give way to 3D island growth when further reducing the growth temperature below 230 °C [57], it is suspected that the growth mode at temperature of about 250 °C may not strictly obey the S-K growth mode. Due to the reason above, the population of dots grown at 250 °C is the smallest with largest size among the three sets of samples.

### 3.2 Experimental

Three sets of samples (cited as A1-6, B1-5 and C1-4) were grown by GEN II molecular beam epitaxy (MBE) by depositing InSb directly on GaSb (001) at 320 °C, 275 °C and 250 °C, respectively. All the substrates used in this study were cleaved quarter pieces of undoped GaSb (001) substrate (originally 2", WaferTech). The growth process was monitored by the reflection high energy electron diffraction (RHEED). GaSb substrates deoxydation under a stable  $\text{Sb}_2$  flux ( $\text{BMI} \approx 6.0 \times 10^{-7} \text{Toor}$ ) at 540-560°C (pyrometer's reading). After removal of oxide, a 0.1  $\mu\text{m}$  GaSb buffer layer was grown on the substrates prior to the InSb epilayer deposition. During growth of samples A, Good  $\times 3$  surface reconstructions were observed by the clear  $\times 3$  RHEED patterns. After the buffer layer growth, 1ML to 6ML of InSb were deposited directly on the GaSb buffer layer at the temperature of 320 °C. The growth method of group B and C samples was similar to the initial growth of samples A except dropping the growth temperature down to 275 °C and 250 °C, respectively. During the cooling down process,  $\times 3$  surface reconstruction gradually gave way to  $\times 5$  reconstruction which was clearly indicated by the RHEED patterns. Substrate rotation was not used during the entire growth process. The nominal growth rate was  $\sim 0.11 \text{ML/s}$  which is a relatively lower value compared with other InSb/GaSb research groups' growth rates [66]. The growth rate was evaluated by the RHEED

intensity oscillation. The beam flux was monitored by a beam ion gauge. After InSb growth, the substrate heating system was switched off and the continuous azimuth rotation (CAR) was set to 75°. Surface morphology of Samples was examined by atomic force microscopy (AFM) in tapping mode. Due to the nonuniformities of In flux caused by the source geometry of GEN II MBE device, there may exist InSb coverage variations at different areas of the same sample. To avoid the variation caused by the variation in InSb coverage, AFM images were taken from the areas around the center of samples. Dot density and size were statistically analysed by using of the AFM particle analysing program. Due to the closed loop and nanoparticles (nps) nature of the Asylum system, the AFM result should be accurate.

### 3.3 Results and discussion

#### 3.3.1 RHEED patterns and AFM analysis of samples grown at 320 °C

##### 3.3.1.1 RHEED patterns

RHEED patterns provided an internal calibration of the deposited quantity and provide further useful information such as surface morphology and surface reconstruction.

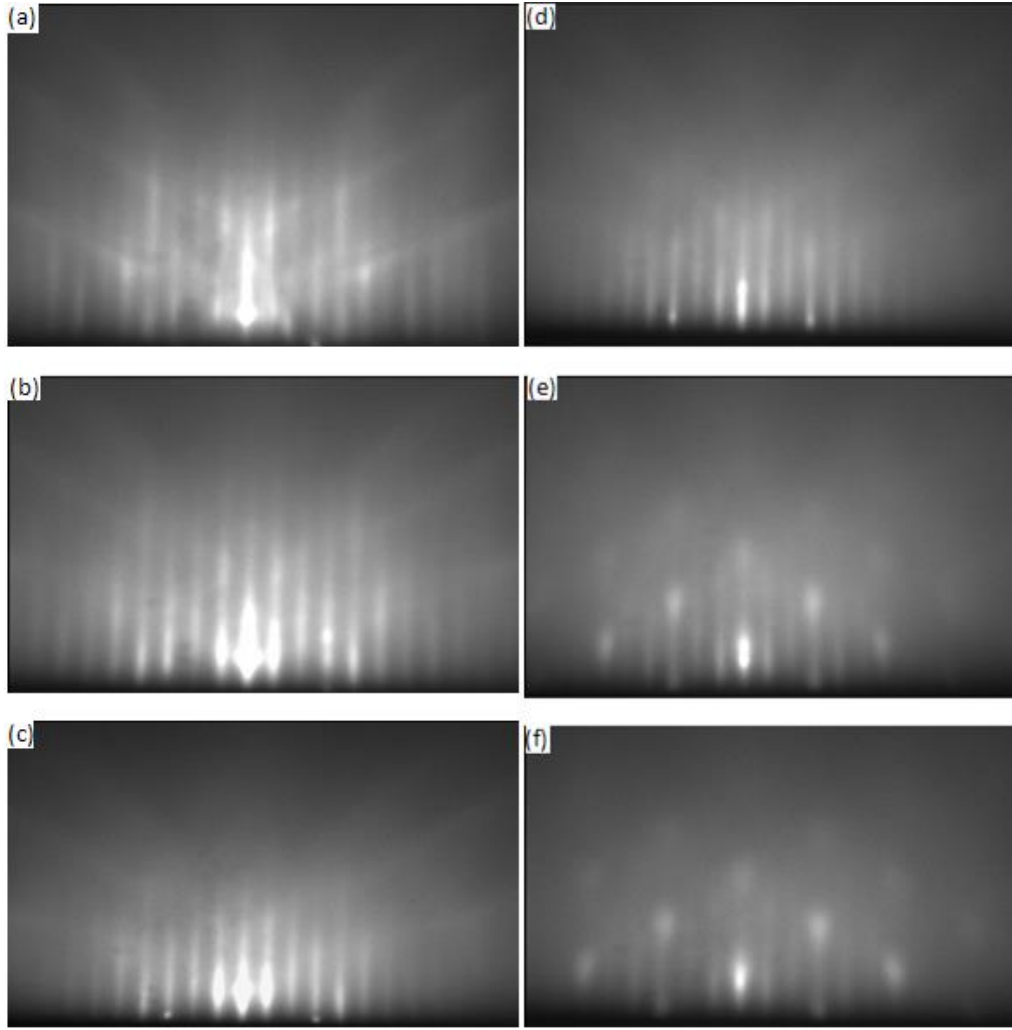


Fig.3.1 RHEED patterns taken (a) after growth of the 0.1 $\mu$ m GaSb buffer layer, (b) – (f) after deposition of 1ML, 1.5ML, 2ML, 3ML and 4ML of InSb at 320 °C, respectively, in the  $[1\bar{1}0]$  azimuthal.

The RHEED pattern in figure 3.1 (a) exhibited a streaky pattern indicating a good surface reconstruction after the 0.1  $\mu$ m GaSb buffer layer growth. Figure 3.1 (b, c) were RHEED patterns taken after depositing of 1ML and 1.5ML InSb, the streaky patterns indicate flat surfaces after the deposition of 1 to 1.5ML InSb. And this result proved the 2D growth mode dominating the initial growth of InSb wetting layer on GaSb. Spotty-like patterns as shown in figure 3.1 (e, f) indicated the formation of 3D dots above the coverage of 2.5ML InSb.

### 3.3.1.2 AFM analysis

AFM images of the uncapped samples illustrated the formation of a large number of QDs above the coverage of 2ML for all the three sets of samples. After deposition of 2ML InSb, the surface morphology became very rich. Several different types of 3D dots and 2D islands coexisted on the surface.

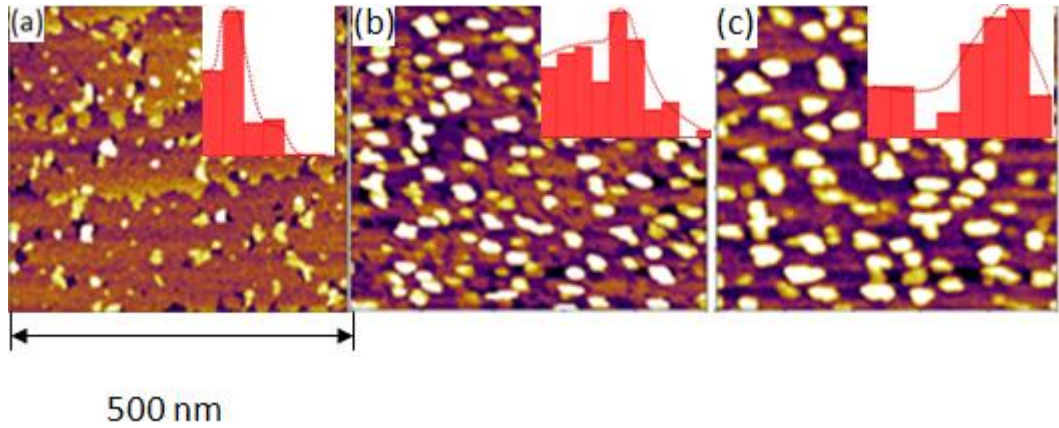


Fig.3.2 AFM images of surface morphology and histograms of InSb QDs height distribution at the coverage of (a) 2.5ML, (b) 3.5 ML, and (c) 4ML of InSb grown at 320 °C.

Three 500 nm  $\times$  500 nm AFM images in figure.3.2 (a-c) exhibited surface morphology of samples A at the InSb coverage of 2.5ML, 3.5ML and 4ML respectively. The uniform terraces suggested that at this coverage InSb layer growth under the dynamic movement of In adatoms toward step edges as shown in figure 3.2a. That was corresponding to the fact of large diffusion lengths of In adatoms on the Sb-terminated surface [72]. In particular, the estimated terrace height helped to assess the size of 3D dots formed after the deposition of the wetting layer more precisely. The large dots were about 0.65nm high with base diameter of about 15 nm. The selection of nucleation sites by those QDs could be observed directly in the 500 nm  $\times$  500 nm AFM images. Monolayer steps were also observed in figure 3.2(a), that indicated the preferential nucleation sites of QDs were step edges. It is unknown if the initial nucleation process results in the depletion of the nearby

terrace or the initial nucleation occurs at some kinks then into step [72, 73]. Invariable is that surface steps play an important role in determining QDs nucleation as well as their structural properties.

The AFM images were representative of surface morphology changing with InSb coverage. A large number of nanoscale dots were observed from the AFM images. The statistically analysis of dots properties were performed by using the AFM particle analyzing program. This computer program was able to record volume, base area and height of dots from AFM images. All the densities obtained were towards the dots with height above 1ML. The quantitative results in table 3.1 indicated a slight increase in dots size and dot density associated with increasing the InSb coverage from 2.5ML to 3.5ML. The dots with average height of  $2 \pm 1$  nm and base diameter of  $25 \pm 10$  nm had a number density of  $\sim 3.8 \times 10^{10} \text{cm}^{-2}$  at the coverage of 3.5ML. All the dot densities listed below were the mean value of several different  $500 \text{ nm} \times 500 \text{ nm}$  AFM images taken from different surface areas of the same sample. And the uniformity is  $\sim 0.9$ . The monomodal size distribution as shown in figure 3.2 (inset) indicated relatively uniform dots were obtained. A great number of large dots were formed above the coverage of 2.5ML InSb. Clearly terraces with step height of  $\sim 1\text{ML}$  were observed from the AFM topography of 2.5ML InSb on GaSb (001) (as shown in figure 3.2 a). The step edges were served as the preferred sites for the nucleation of QDs. The morphology evolution from the AFM topographies indicated the steps on the surface were mostly consumed during the deposition of 2.5 to 3.5ML InSb. This may due to the erosion between dots and step edges. The average size of dots became larger as increasing deposition of InSb. After inspection of the cross-section of dots at the InSb coverage of 4ML, the dots exhibited a flat top that indicated the fully plastic relaxation. And the size distributions of large dots were nearly monomodal.

The fully strained or partially relaxed nano-scale dots are seemed as the predecessors of QDs. In this sense, the quantitative investigation about those nano-scale dots both in



number density and size distribution are significant for the growth of high-density and uniform QDs. Table 3.1 below illustrated the dot densities and the total volume of dots at different InSb coverage. It was noticeable that from the coverage of 2.2ML to 2.5ML, the dot density increased from  $1.7 \times 10^{10} \text{ cm}^{-2}$  to  $3.0 \times 10^{10} \text{ cm}^{-2}$  while the total volume of dots slightly decreased. An increase in the dot density was associated with the reduction in the average size of dots with coverage.

Table 3.1 Dot densities and total dots volume at various InSb coverages.

InSb coverage (ML)	Dot density ( $10^{10} \text{ cm}^{-2}$ )	$\frac{\Delta V_{\text{Dots}}}{\Delta V_{\text{Deposited InSb}}}$
2	6.8	0.41
2.2	5.5	0.38
2.5	5.2	0.38
2.8	5	0.36
3	5.2	0.28
3.3	4.3	0.24
3.5	4.1	1
3.8	3.7	0.21
4	3.6	0.46
6	2.8	0.82

During the initial deposition of critical thickness upto the coverage of 2.5ML InSb, the strain induced by the added amount of InSb mainly made more new nucleation sites of InSb on GaSb. It was more likely most of the new dots were formed by the In adatoms desorption from the existed dots and stucked to the new nucleation sites since the total volume of dots got slightly decreased and the added amount of InSb was mainly incorporated into the terraces but not for the formation of dots. The other possible formation was that the added InSb created new dots and it also altered the strain in the ground of the existing dots and made those dots dissolving to some small dots or even incorporating to the beneath wetting layers. For further deposition of InSb from 2.5ML to 2.8ML, the dot density decreased from  $5.2 \times 10^{10} \text{ cm}^{-2}$  to  $5 \times 10^{10} \text{ cm}^{-2}$  and the total dots volume in an area of 1 square centimeter changed from  $0.21 \times 10^{-8} \text{ cm}^3$  to  $0.56 \times 10^{-8} \text{ cm}^3$ . This indicated the added 0.3ML of InSb made the dots size enlarge significantly with a slight increase in dot density. For the deposition of 2.8ML to 3.0ML InSb, dot density was stable while the total dots volume per square centimetre increased from  $0.56 \times 10^{-8} \text{ cm}^3$  to  $0.74 \times 10^{-8} \text{ cm}^3$ . The additional strain induced by further InSb coverage caused no further increase in dots density but made enlargement of the existing dots. For the deposition of InSb from 3ML to 3.3ML, dot density decreased from  $5.2 \times 10^{10} \text{ cm}^{-2}$  to  $4.3 \times 10^{10} \text{ cm}^{-2}$  and the total dots volume per square centimetre changed from  $0.74 \times 10^{-8} \text{ cm}^3$  to  $0.97 \times 10^{-8} \text{ cm}^3$ . This indicated the added 0.3ML of InSb resulted in an increase in the dots size, ~24% of added amount of InSb was cooperated into the formation of dots. InSb dots with average height of 3 nm and base diameter of  $30 \pm 10 \text{ nm}$  were formed at this coverage and the dot density did not increase further.

Above the coverage of 3.5ML, a slightly reduction in dot density was associated with dots size increase as further amount of InSb was deposited, evidence of dots coalescing was also observed at the coverage of 5ML. At the coverage of 6ML, a

large number of dots have coalesced together, and the dot density dropped to  $\sim 2.8 \times 10^{10} \text{ cm}^{-2}$  with average dots height decreasing to  $\sim 2 \text{ nm}$  and base diameter increasing to  $\sim 50 \text{ nm}$ . All these observations indicated the strain introduced by the further deposited InSb played a key role in altering the dot density and dots size, and the formation of dots was a kinetic driving process. In order to get a quantitative analysis of the QDs morphology, the statistical measurement of the QD dimensions has been presented.

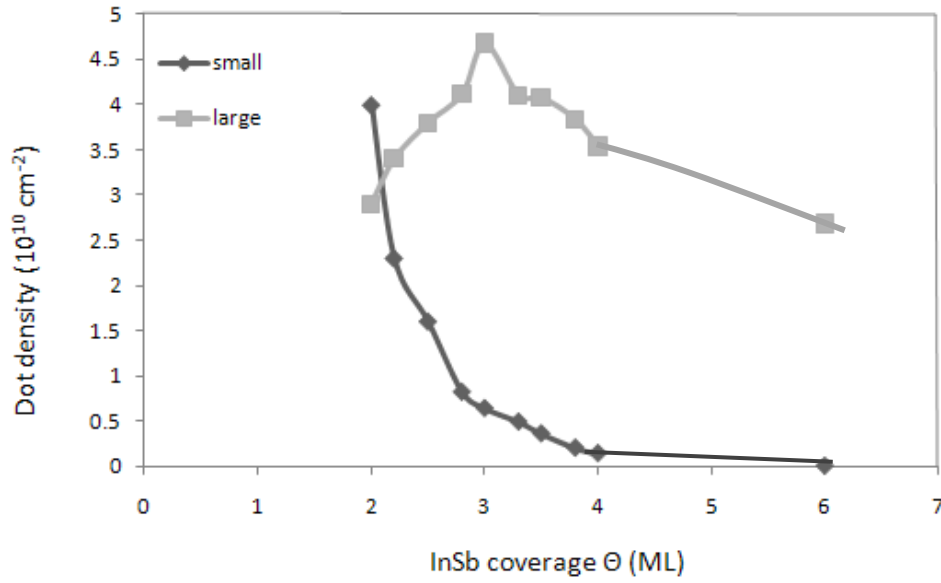


Fig.3.3 Densities of small and large dots as a function of InSb coverage ( $\Theta$ ) for epilayer grown at a temperature of  $320^\circ\text{C}$  and growth rate of  $\sim 0.11 \text{ ML/s}$ . The full lines join the data for an eye guide.

Figure 3.3 illustrated the dependence of number densities of small dots and large dots on InSb coverage for QDs grown at a temperature of  $320^\circ\text{C}$ . Nominal 2 to 6 ML InSb was deposited on GaSb (001) with an insertion of  $0.1 \mu\text{m}$  GaSb buffer layer. For the initial set of samples, a large number of dots were formed after depositing 2ML InSb. At the coverage of 2ML, the number density of small dots (height  $< 1 \text{ ML}$ ) and Large dots (height  $> 1 \text{ ML}$ ) was  $\sim 4 \times 10^{10} \text{ cm}^{-2}$  and  $\sim 2.9 \times 10^{10} \text{ cm}^{-2}$ , respectively. The average height of small dots was  $\sim 0.4 \text{ nm}$  with lateral diameter of 8

nm. For the large dots, the average height is  $\sim 0.8$  nm with lateral diameter of 14 nm. It was notable that the number density of small dots was greatly larger than the number density of large dots at the coverage below 2ML. It was suspected that a large number of 3D small dots or monolayer-high 2D islands may be formed at the initial stage of 3D island growth (when the InSb coverage was slightly above the thickness of wetting layer). These small dots should be the precursor of the QDs. with increasing deposition of InSb, the number of small dots reduced and the number of large dots increased. The added InSb material may prefer the sites of small dots and enlarge the size of small dots both in height and lateral width. For the mechanical perspective, the periphery and the apex of small dots were the sites with less strain. During the deposition of 2 to 3ML InSb, the number density of small dots dropped to  $0.7 \times 10^{10} \text{ cm}^{-2}$  and the number density of large dots increased to a maximum value of  $4.7 \times 10^{10} \text{ cm}^{-2}$ . The size of large dots at this coverage was  $\sim 2$  nm of height and  $\sim 20$  nm of base diameter with a aspect ratio (dot height divided by base diameter) of  $\sim 0.1$ . For the further deposition of 3 to 4 ML InSb, both of the number densities of large dots and small dots decreased. The trends in the experimental height and base diameter data of InSb dots grown on GaSb (001) (figure 3.3) indicated the average size of dots became large as increasing deposition of InSb. The aspect ratio (dots height/dase diameter) of large dots was between 0.07 and 0.12.

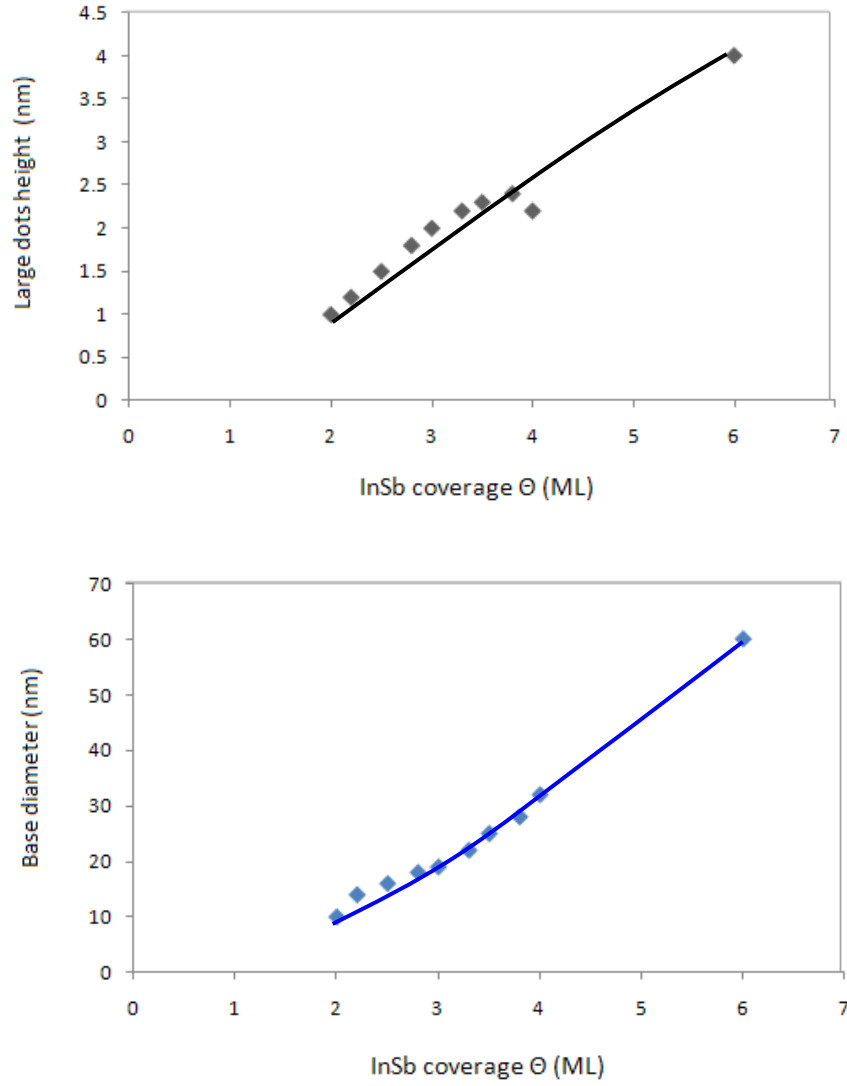


Fig.3.4 The height (top) and base diameter (bottom) of large dots as a function of InSb coverage ( $\Theta$ ) for epilayer grown at the growth temperature of 320°C. The full lines join the data for an eye guide. The almost parallel phenomenon of these two guided lines indicated the aspect ratio of dots keeps stable.

The almost parallel curves in figure 3.4 indicated the aspect ratio of those dots kept stable, although the dots properties including density, height and base width evolved a significant change during the deposition of InSb. The transition in morphology of dots could be directly observed from the AFM topographies in figure 3.2.

### 3.3.2 RHEED patterns and AFM analysis of samples grown at 275 °C

### 3.3.2.1 RHEED patterns

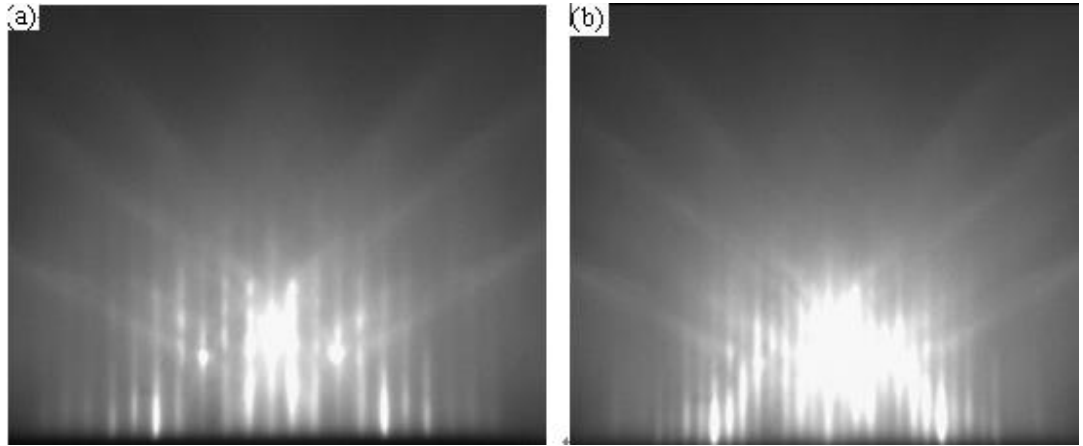


Fig.3.5 RHEED patterns taken from samples grown at 275 °C during the cooling down process, in the [110] azimuthal.

In the second set of samples growth, the substrate temperature was dropped down to 275 °C after the 0.1 $\mu$ m GaSb buffer layer growth. The RHEED patterns in figure 3.5 (a) and (b) indicated an evolution from a  $\times 3$  to  $\times 5$  reconstruction during the cooling down process in the [110] azimuthal.

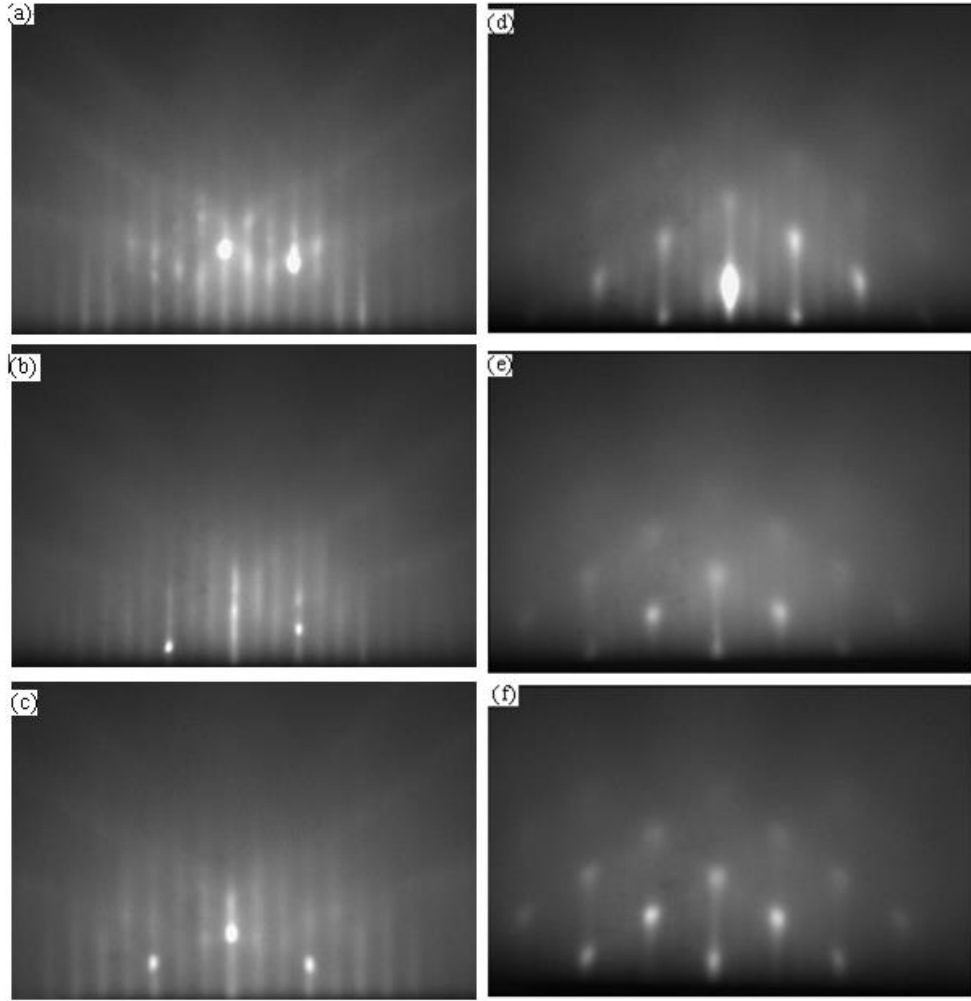


Fig.3.6 RHEED patterns (a) –(f) taken after deposition of 1ML, 1.5ML, 2ML, 3ML, 4ML and 5ML of InSb at 275 °C, respectively, both in the [110] azimuthal.

Figure 3.6 (a,b,c) were RHEED patterns taken after depositing of 1ML, 1.5ML and 2ML InSb, respectively. The x3 streaky patterns indicated relatively flat surfaces after the deposition of 1 to 1.5ML InSb in the [110] azimuthal. And this demonstrated the 2D growth mode dominating the initial growth of InSb wetting layer on GaSb. Spotty-like patterns as shown in figure 3.6 (d, e f) indicated the formation of 3D features after depositing more than 3ML InSb.

#### 3.3.2.2 AFM analysis

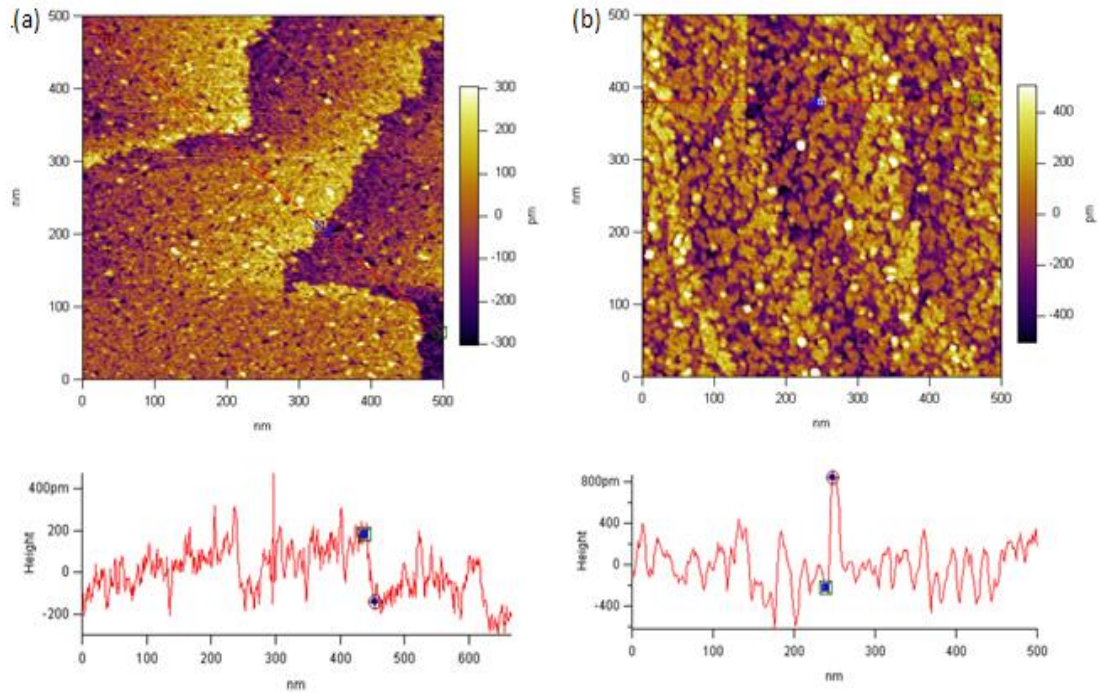
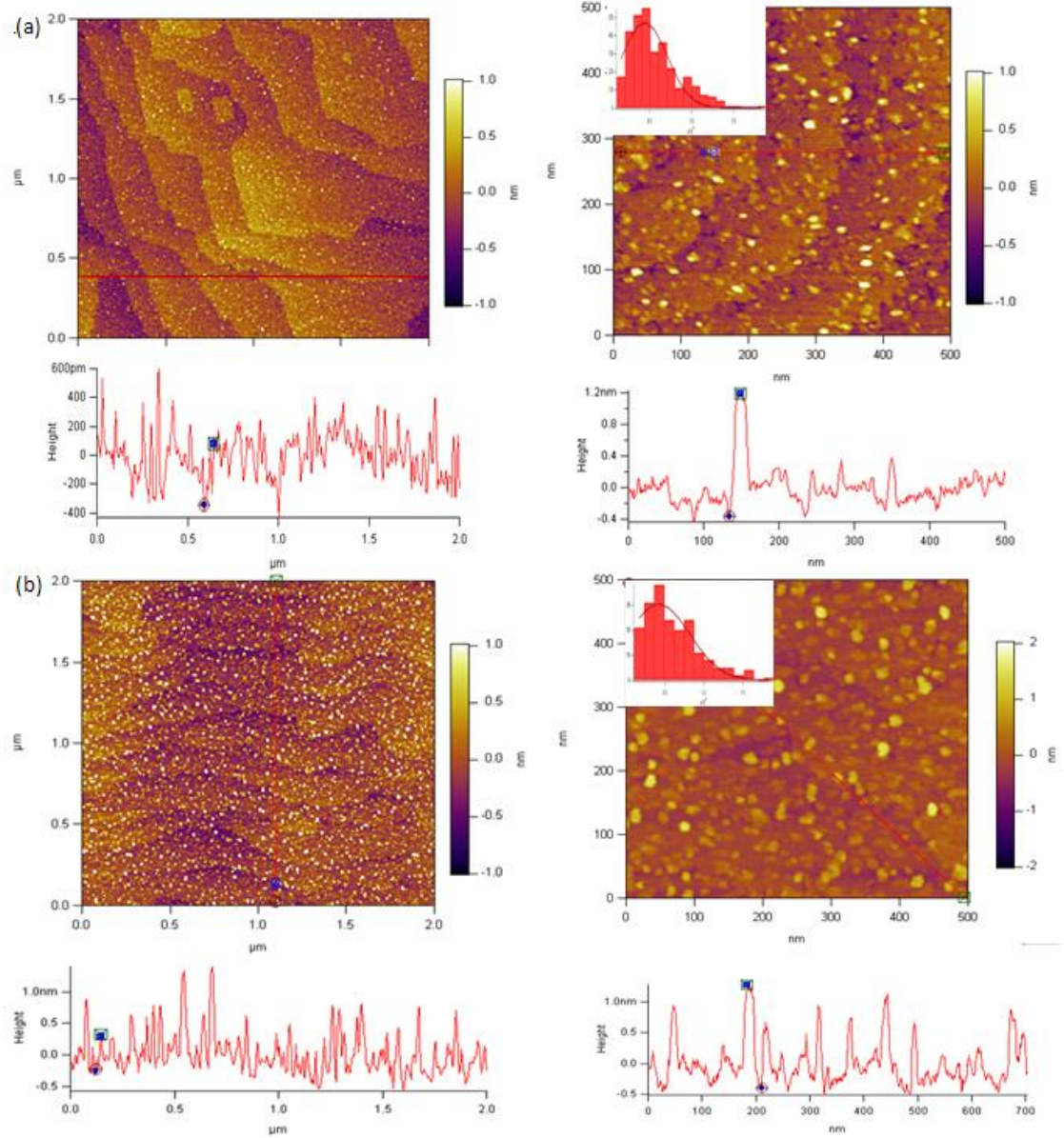


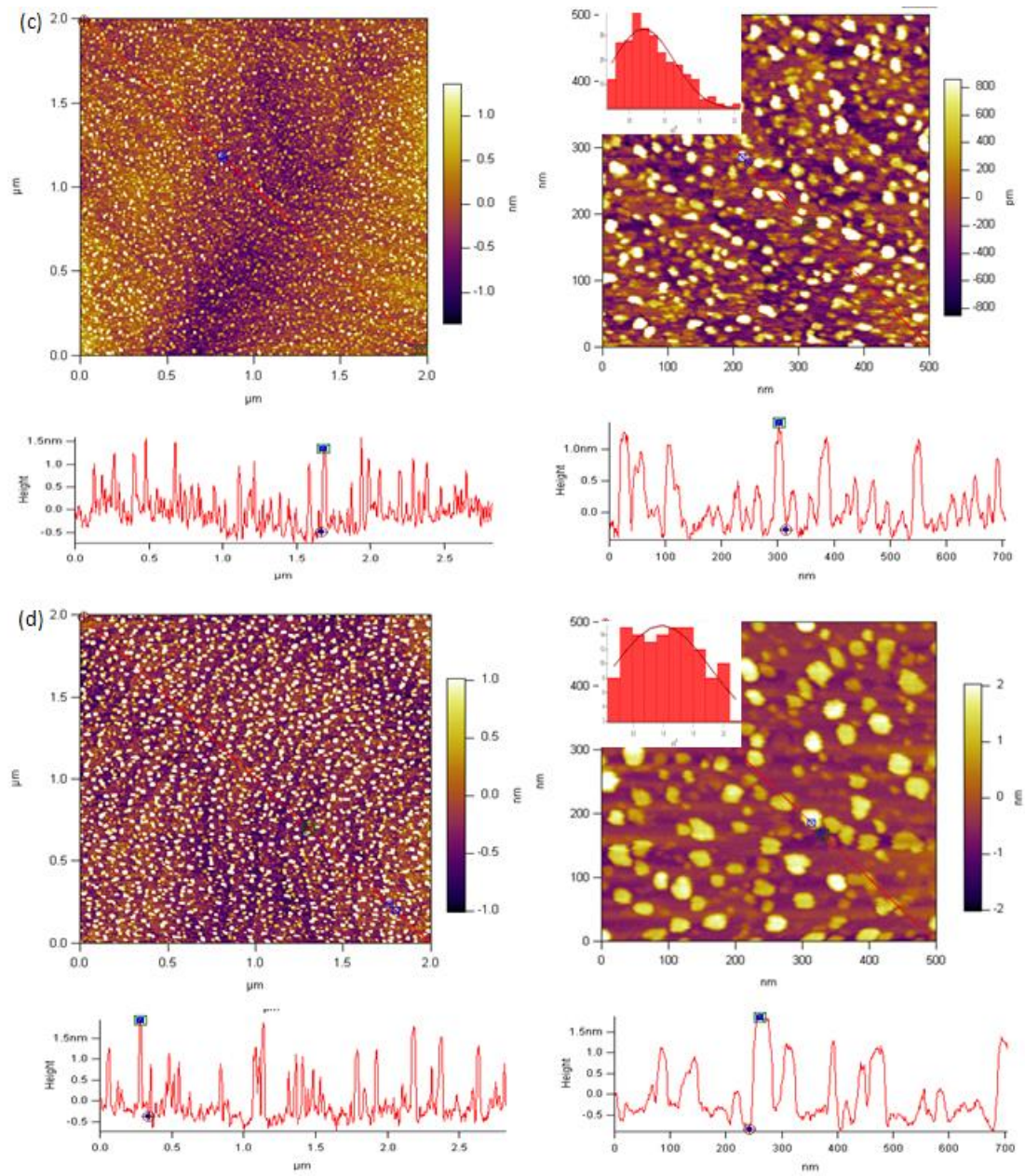
Fig.3.7 AFM images and cross-section area scan of (a) 1ML and (b) 1.5ML InSb grown at 275 °C, respectively.

Figure 3.7 (a) and (b) illustrated two 500 nm×500 nm AFM images taken from sample B1 and B1.5, where the InSb coverage was approximately 1ML and 1.5ML, respectively. At the initial stage of growth, a smooth surface was formed. Clear terraces and step edges were observed from the 500nm × 500nm AFM image as shown in figure 3.7 (a). This was also proved by the streaky RHEED pattern in figure 3.6 (a). The lateral spacing of large terrace was  $\sim 0.2 \mu\text{m}$  and the step height was  $\sim 0.33 \text{ nm}$ . After deposition of 1.5ML InSb on GaSb, several very small islands were observed from the surface as shown in the AFM images in figure 3.7 (b). The dot density was  $\sim 1.4 \times 10^{10} \text{ cm}^{-2}$  and the average dots height was  $1.2 \pm 0.5 \text{ nm}$  with a base width of about  $15 \pm 10 \text{ nm}$  estimated from the cross-section scan of dots area. Compared with the AFM image taken from sample A1.5 which was 1.5ML InSb grown at 320 °C, the surface of sample B1.5 consisted of more isolated small islands than those on sample A1.5, the surface morphology was not as smooth as that of sample A1.5. It was suspected that the critical layer thickness under a lower growth

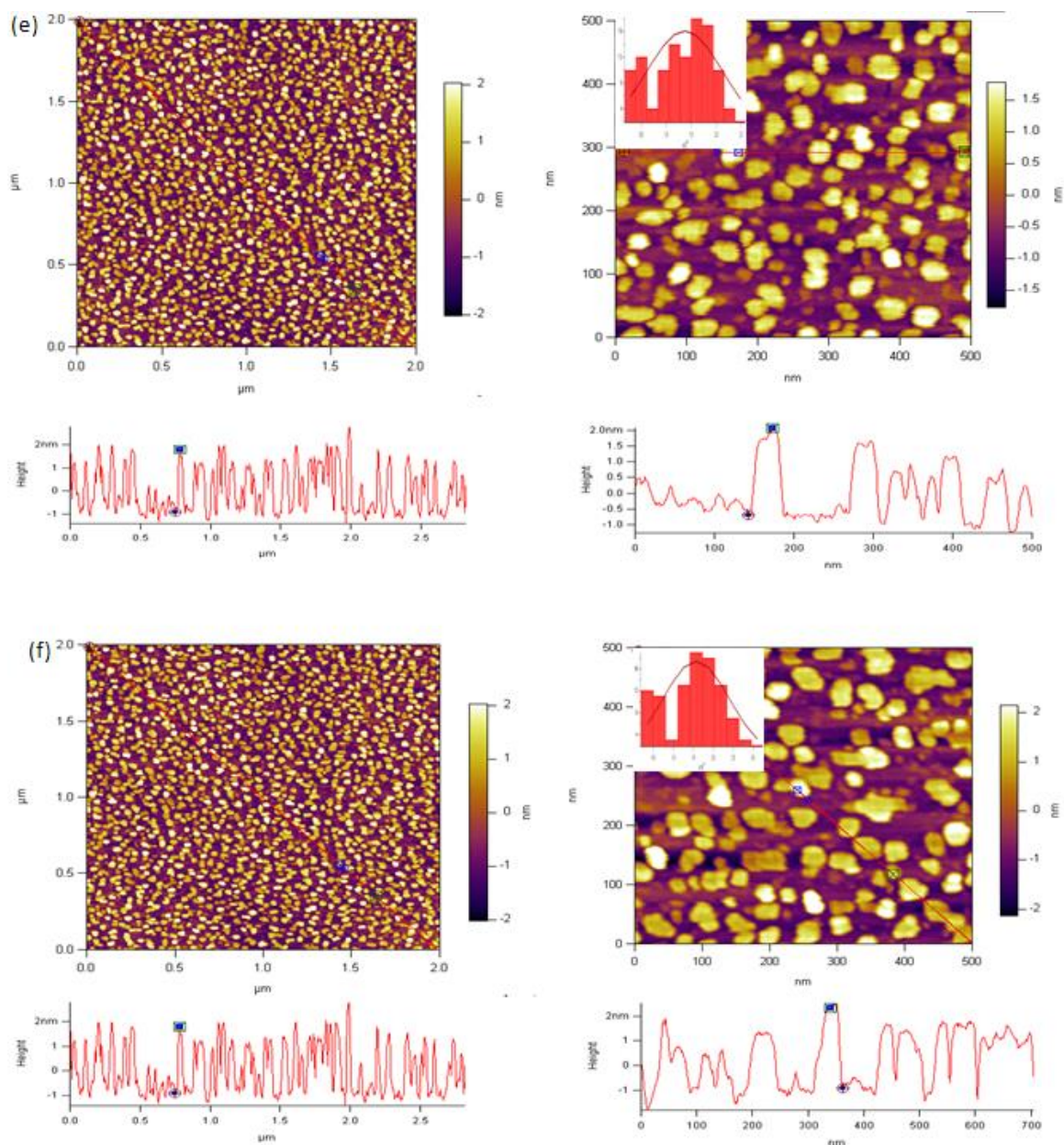


temperature may be lower than that under growth temperature of 320 °C (~1.7 ML) and some strong correlations must exist between the QDs formation and the nature of the wetting layer.









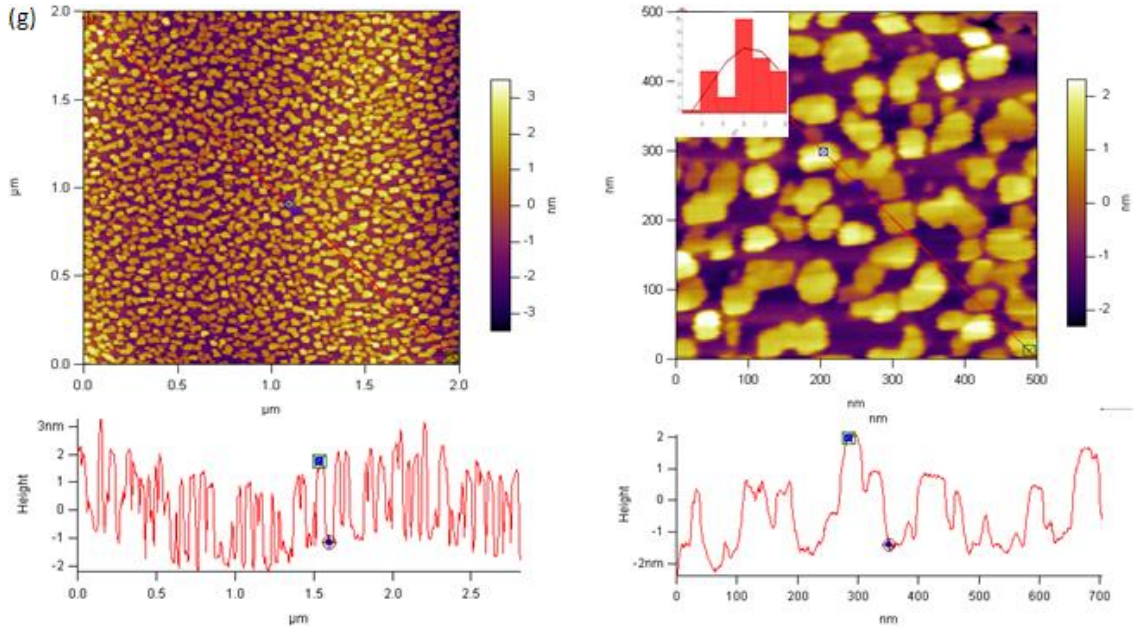


Fig.3.8(a-g) A set of AFM images and cross-section scan of a range of InSb coverage from 2ML upto 5ML grown at 275 °C.

Figure 3.8 shows a set of 2  $\mu\text{m} \times 2 \mu\text{m}$  (left) and 500 nm  $\times$  500 nm (right) AFM images taken from sample B, where the InSb coverage was in the range from 2 to 5ML. A large number of nanoscale dots were observed from the AFM images taken from surface of corresponding samples above the coverage of 2ML. At the coverage of 2ML, small QDs with a very high dot density of  $\sim 11 \times 10^{10} \text{ cm}^{-2}$  were observed from the AFM image. The average dots height was 1 nm and the base diameter was 15 nm investigated by the cross section scan of dots area in figure 3.8 (a). It was likely that above the coverage of 1.5ML, the strain induced by the added amount of InSb resulted in a larger population of the QD nucleation and QDs size both in the height and base diameter didn't change a lot. After analysis the change of total volume of QDs, it was noticable that 19 % of added InSb was incorporated into the formation of QDs. This result has a great discrepancy with that in section 3.1.2 (the increase in dot density was in expense of the reduction in dots size). And it seemed at a lower growth temperature more deposited InSb was involved in the formation of quantum dots. For further deposition of 2ML to 3.0ML InSb, an increase in the size

of dots both in height and lateral width was associated with a reduction in dot density with coverage. At the coverage of 3ML, the dot density was  $\sim 5.1 \times 10^{10} \text{ cm}^{-2}$  and the average dots height was 2 nm with a base diameter of  $20 \pm 10$  nm. Between the coverage of 3ML and 3.5ML, dot density kept stable and dots size increased with the further deposition of InSb. From data in table 3.2,  $\sim 64\%$  of the added amount of InSb was cooperated into the formation of larger dots. The average dot height was 2.5 nm and the base diameter was  $30 \pm 10$  nm. Above the coverage of 4ML, coalescence between dots was observed from the AFM images as shown in figure 3.11 (f). The dot density at this coverage was  $\sim 4.3 \times 10^{10} \text{ cm}^{-2}$ , as the coalescence going on, the dot density would decrease further. The selection of QDs' nucleation sites could be observed directly from AFM images and monolayer steps were observed from the  $2 \mu\text{m} \times 2 \mu\text{m}$  AFM image in figure 3.8 (a, b). That indicated the preferential QDs nucleation sites would be the step edges. And the insets in the  $500 \text{ nm} \times 500 \text{ nm}$  AFM images from figure 3.8 (a) to (g) illustrated the dots height distribution of sample B2 to B5, respectively. The monomodal size distribution indicated a relatively uniform distribution of dots.

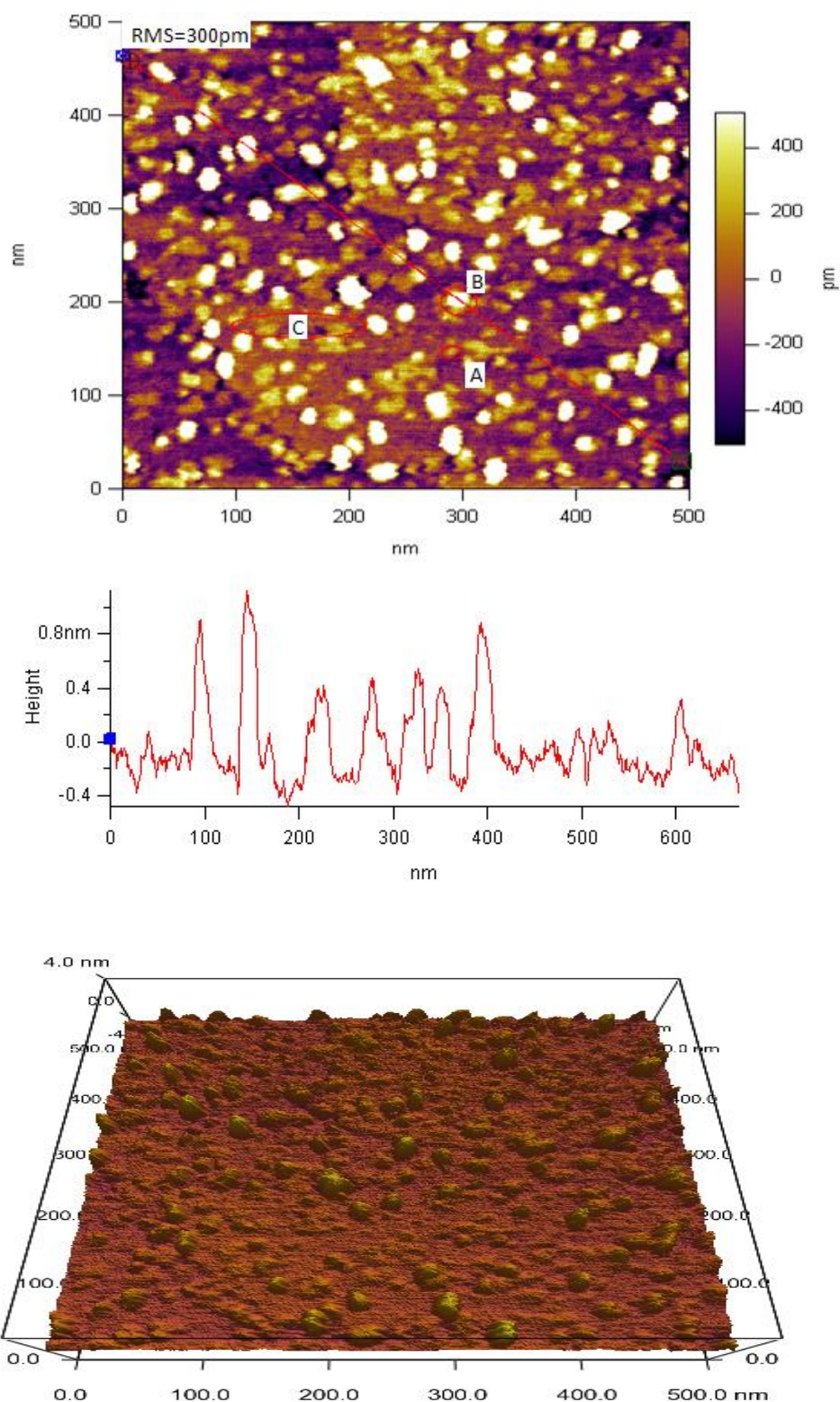


Fig.3.9 AFM topograph of 2.5 ML InSb on GaSb(001) with insertion of a 0.1 μm GaSb buffer layer, growth temperature of 275 °C, growth rate of 0.11 ML/s. Terraces with monolayer height step were observed. Several typical morphologies emerged on



surface, there were small 3D dots with height below 1ML (marked as A), large 3D dots with height above 1ML (marked as B), only these two types of fully strained dots can be considered to be QDs. In addition, large 2D islands were observed on the surface (marked as C).

Figure 3.9 illustrated the surface morphology of 2.5 InSb on GaSb (001) with a 0.1  $\mu$ m GaSb buffer layer. The growth temperature was 275 °C and the growth rate was 0.11 ML/s. A great number of large dots were formed above the coverage of 1.5ML InSb. Compared with morphology of sample A2.5 (Figure 3.2a), more dots were formed above the coverage of 2.5ML InSb. This indicated the reduced 55 °C growth temperature may make more small condensation of Sb which was benefit for more nucleation of QDs.

Table 3.2 Dots volume versus total amount of deposited InSb.

InSb coverage (ML)	Dot density ( $10^{10}\text{cm}^{-2}$ )	$\frac{\Delta V_{\text{Dots}}}{\Delta V_{\text{Deposited InSb}}}$
1.5	1.4	/
2	11	0.21
2.5	8.5	0.12
2.8	9.2	0.40
3	6.0	1
3.5	5.0	0.64
4	4.3	0.74
5	1.9	0.43

Table 3.2 exhibited the dot density and the total volume of dots at different InSb coverage. It was noticeable that from the coverage of 1.5ML to 2ML, dot density increased from  $1.4 \times 10^{10} \text{ cm}^{-2}$  to  $11 \times 10^{10} \text{ cm}^{-2}$ . An increase in the dot density was associated with the reduction on the average size of dots

In order to get a quantitative analysis of the QDs morphology, the statistical measurements of the dots density and size have been presented.

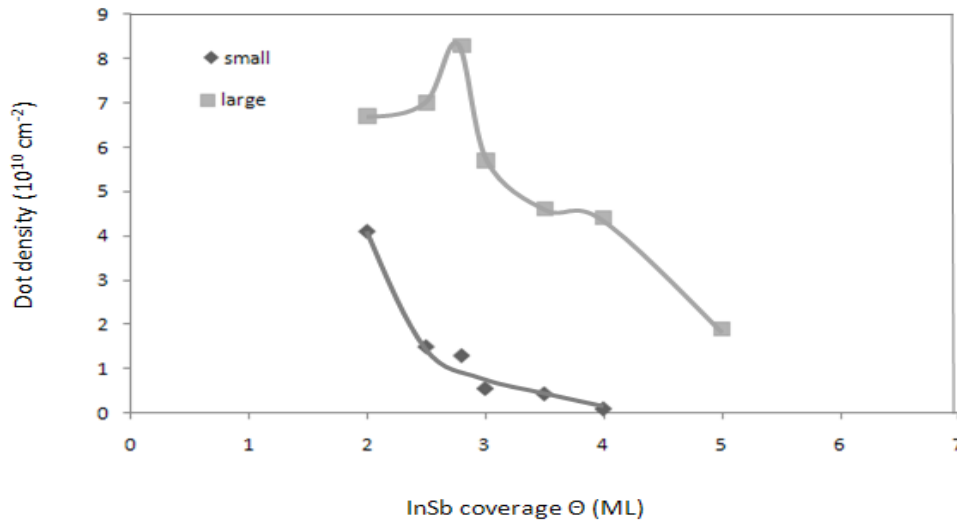


Fig. 3.10 Number densities of small and large dots as a function of InSb coverage ( $\Theta$ ) at a temperature of 275 °C. The full lines join the data for an eye guide.

Figure 3.10 illustrated the number densities of small dots and large dots as a function of InSb coverage. 2 to 4 ML InSb were deposited on GaSb (001) with a prior insertion of 0.1  $\mu\text{m}$  GaSb buffer layer. The epilayer growth temperature was 275 °C and the growth rate was 0.11 ML/s. At the coverage of 2ML, the number density of small dots (height < 1ML) and large dots (height > 1ML) was  $\sim 4.2 \times 10^{10} \text{ cm}^{-2}$  and  $\sim 6.8 \times 10^{10} \text{ cm}^{-2}$ , respectively. The average height of small dots was  $\sim 0.3 \text{ nm}$  with lateral diameter of 6 nm. For the large dots, the average height was  $\sim 1.5 \text{ nm}$  with lateral diameter of 12 nm. As increasing deposition of InSb, the number density of small dots dropped to  $1.5 \times 10^{10} \text{ cm}^{-2}$  and the number of large dots increased until to a maximum density of  $7.0 \times 10^{10} \text{ cm}^{-2}$  at the coverage of 2.5ML. The size of large



dots at this coverage was  $\sim 2.5$  nm of height and  $\sim 18$  nm of base diameter with a aspect ratio (dot height divided by base diameter) of  $\sim 0.13$ . During the deposition of 2.5 to 3.5 ML InSb, the number density of small dots dropped to  $0.45 \times 10^{10} \text{ cm}^{-2}$  and the large dots also decreased to  $4.6 \times 10^{10} \text{ cm}^{-2}$ . For the further deposition of 3.5 to 4 ML InSb, the number densities of large dots and small dots got slightly decreased. The average size of dots became large both in height and lateral width as increasing deposition of InSb.

### 3.3.3 Analysis of samples grown at 250 °C

To assess the effect of further dropping growth temperature on the dots properties, a set of sample with 1.5 to 4 ML InSb were deposited on GaSb(001) at 250 °C.

#### 3.3.3.1 RHEED patterns

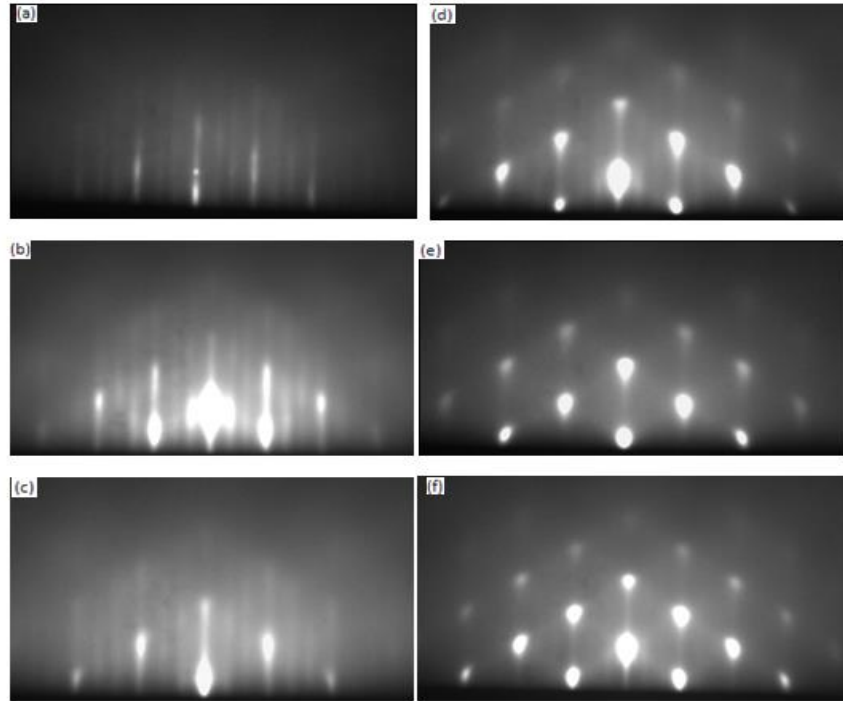
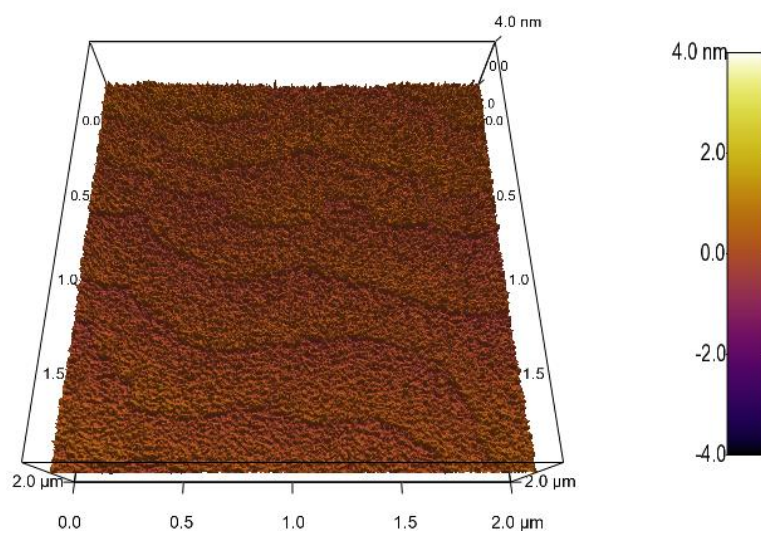
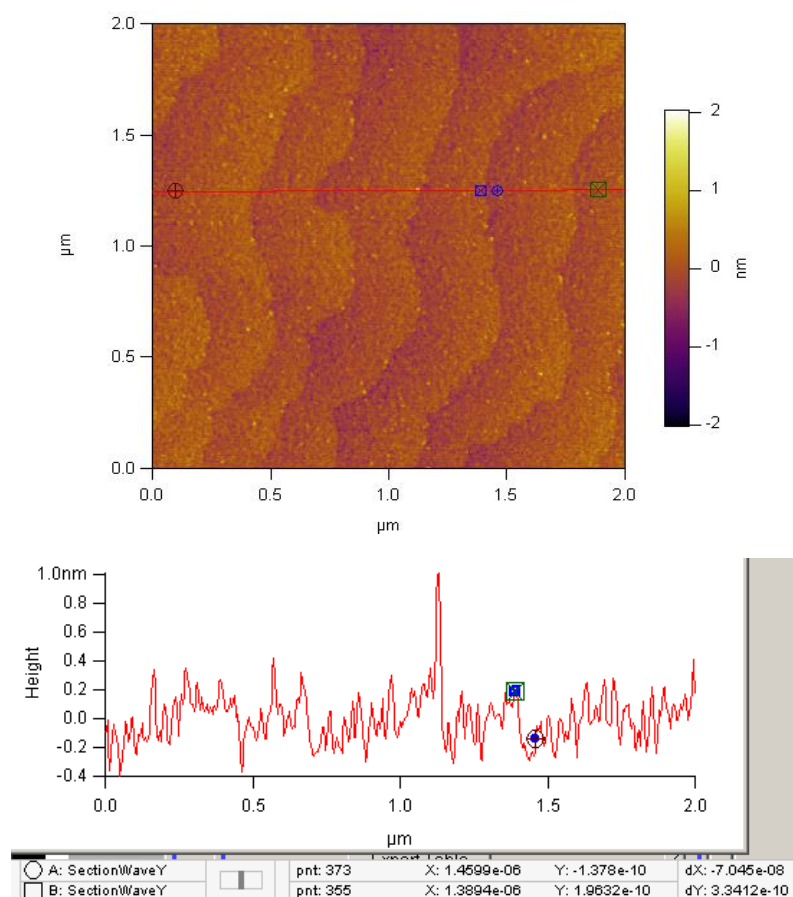


Fig.3.11 RHEED patterns (a)–(f) taken after deposition of 1.5 ML, 2 ML, 2.5 ML, 3 ML, 3.5 ML and 4 ML of InSb at 250 °C, in the [110] azimuthal, respectively,.

Fig.3.11 (a to f) were RHEED patterns taken after depositing of 1.5ML, 2ML, 2.5ML, 3ML, 3.5ML and 4ML of InSb at 250 °C, respectively. The x3 streaky patterns in figure 3.11 (a) indicated a flat surface after the deposition of 1.5ML InSb. And this demonstrated the 2D growth mode dominating the initial growth of InSb wetting layer on GaSb even at the temperature as low as 250 °C. As the growth temperature dropped below 250 °C, surface reconstructions during the InSb growth exhibited different from the  $c(4\times4)$  to  $(\times3)$  transition, the RHEED patterns got simultaneously changed along all the three azimuths. Above the InSb coverage of 2ML, a Sb-rich  $c(1\times1)$  surface emerged from a  $c(4\times4)$  less Sb-rich surface which was consistent with the previous research of InSb surface reconstruction at low temperature[67]. At the temperature of  $\sim 230$  °C, the limited diffusion length of In-atom and the volatility of Sb were not able to sustain 2D layer growth and the phase segregation may occur. It was suspected that the growth mode at temperature of about 250 °C may not strictly obey the S-K growth mode. The morphology of the wetting layer may be more complex than those grown at temperature above 275 °C. Spotty-like patterns as shown in Figure 3.14 (c, d, e and f) indicated the formation of 3D features after depositing more than 2ML InSb.

### 3.3.3.2 AFM analysis



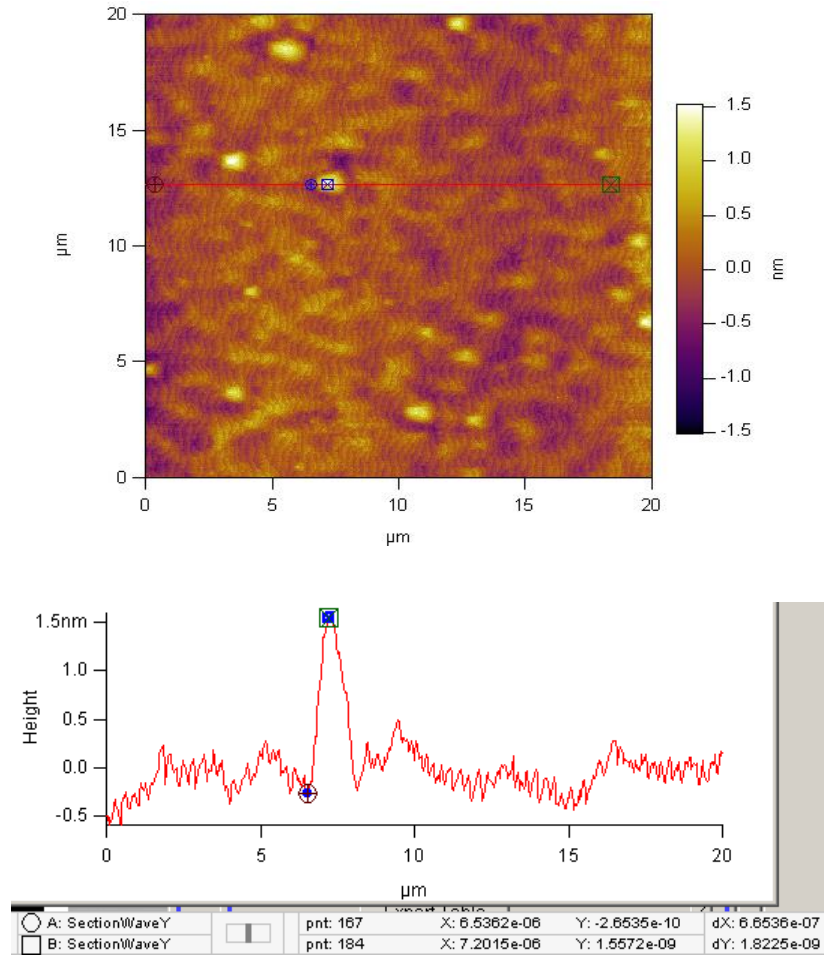


Fig.3.12 AFM images of 1.5ML InSb on GaSb (001) with a 0.1  $\mu\text{m}$  GaSb buffer layer. The epilayer growth temperature was 250  $^{\circ}\text{C}$  and the growth rate was 0.11ML/s.

Figure 3.12 illustrated the surface morphology of 1.5ML InSb on GaSb (001) at the a growth temperature of  $\sim 250^{\circ}\text{C}$  and a growth rate of  $\sim 0.11\text{ML/s}$ . Large terraces were observed on the surface. The average terrace height was about 1ML and the average lateral space was about  $0.3\mu\text{m}$ . Step edges were still clearly observed. The hint of a large number of small QDs have been observed on the AFM topography of 1.5ML InSb grown on GaSb (001) at 250  $^{\circ}\text{C}$ .

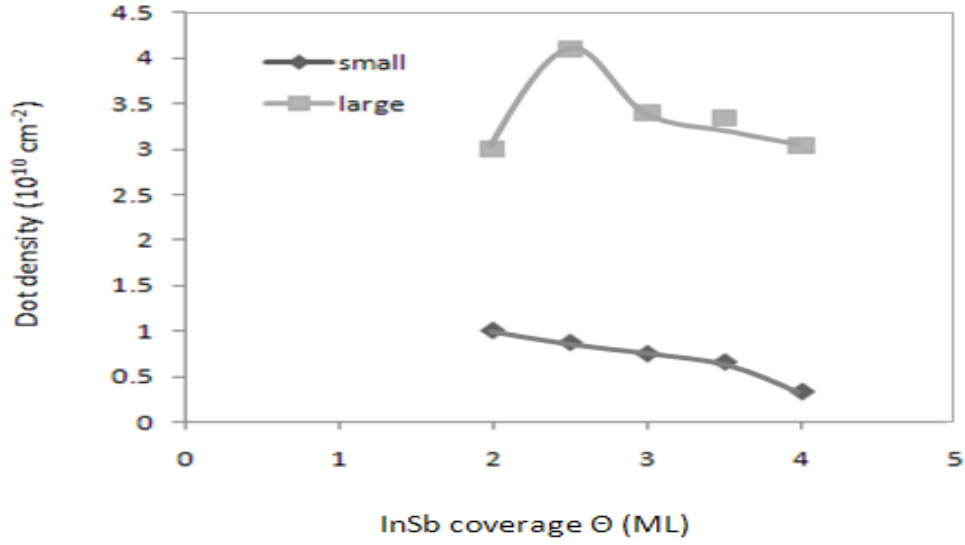


Fig.3.13 Densities of small and large dots as a function of InSb coverage ( $\Theta$ ) at a temperature of 250 °C. The full lines join the data for an eye guide.

For the last set of samples C grown at 250 °C, a great number of dots were also observed after deposition of 2ML InSb. Figure 3.13 illustrated the number densities of small dots and large dots as a function of InSb coverage. 2 to 4 ML InSb were deposited on GaSb (001) with a prior insertion of 0.1  $\mu\text{m}$  GaSb buffer layer. The epilayer growth temperature is 250 °C and the growth rate is 0.11 ML/s. At the coverage of 2ML, the number density of small dots (height <1ML) and large dots (height > 1ML) was  $\sim 1 \times 10^{10} \text{ cm}^{-2}$  and  $\sim 3 \times 10^{10} \text{ cm}^{-2}$ , respectively. The average height of small dots was  $\sim 0.4 \pm 0.1 \text{ nm}$  with lateral diameter of 8 nm. For the large dots, the average height was  $\sim 1.2 \pm 0.4 \text{ nm}$  with lateral diameter of 14 nm. As increasing deposition of InSb, the number density of small dots slightly reduced to  $0.9 \times 10^{10} \text{ cm}^{-2}$  and the number of large dots increased to a maximum number density of  $4.1 \times 10^{10} \text{ cm}^{-2}$  at the coverage of 2.5ML. The average size of large dots at this coverage was  $\sim 1.5 \pm 0.5 \text{ nm}$  of height and  $\sim 16 \pm 4 \text{ nm}$  of base diameter with an aspect ratio (dot height divided by base diameter) of  $\sim 0.1$ . During the deposition of 2.5 to 3 ML InSb, the number density of small dots dropped to  $0.5 \times 10^{10} \text{ cm}^{-2}$  and the large dots decreased to  $3.4 \times 10^{10} \text{ cm}^{-2}$ . For the further deposition of 3 to 4ML

InSb, the number densities of large dots and small dots was decreased. Large dots with oriented side facets and flat top were observed and the dot density dropped to  $3.5 \times 10^{10} \text{ cm}^{-2}$ .

### 3.3.4 Comparison of dots properties for three sets of samples

Reviewing the previous research in growth of InSb on GaSb, growth of high-density and uniform InSb/GaSb QDs both in MBE and MOCVD encountered difficulties. The reported studies of MBE growth of InSb/GaSb(001) QDs have obtained low dot densities between  $10^9$  to  $10^{10} \text{ cm}^{-2}$  with a typical dots height of 8-35 nm and lateral diameter of 50-400 nm [61, 68-70]. The results obtained from MOCVD of InSb/GaSb also exhibited dot density below  $10^{10} \text{ cm}^{-2}$  with a typical dots height of 3-5 nm and lateral diameter of 20-30 nm [71, 72]. Recently, N. Deguffroy. et al reported a typical MBE method by using post-growth annealing, dot density as high as  $7.4 \times 10^{10} \text{ cm}^{-2}$  have been reported [66]. Although it seemed the properties of the QDs can be hardly affected by as growth method, rarely studies have been executed on the as-growth of InSb/GaSb (001) at low temperatures. The related studies of InSb/GaSb have been summerised in table 3.5.

Table 3.5 Comparison of properties of InSb/GaSb QDs grown under different techniques.

<b>Growth method</b>	<b>InSb coverage (ML)</b>	<b>Temperature ( °C)</b>	<b>Growth rate (ML/s)</b>	<b>Dos features</b>
MBE as growth InSb on GaSb(100) [61, 68, 69]	1.8-2.6	365-450	0.3-1.2	Density of $2 \times 10^9 \text{ cm}^{-2}$ with lateral width and height of 50 and 8

				nm, respectively
MBE as growth InSb on GaSb (001) [70]	3.8	455	0.185	Low Density with lateral width and height of 400 and 35 nm, respectively
MOCVD [71]	3	480	1.0	Density of $10^9\text{cm}^{-2}$ with lateral width and height of 20-25 and 3 nm, respectively
MOCVD [72]	4-8	480-500	1-2ML/s	Density of $5\times 10^9\text{cm}^{-2}$ with lateral width and height of 30 and 4 nm, respectively
MBE growth InSb on GaSb(100) with post-growth annealing [73]	2.5	Growth at 300 °C, Annealing at 390 °C	1.5ML/s	Density of $7.4\times 10^{10}\text{cm}^{-2}$ with lateral width and height of $20\pm 10$ and $1.7\pm 0.5$ nm, respectively

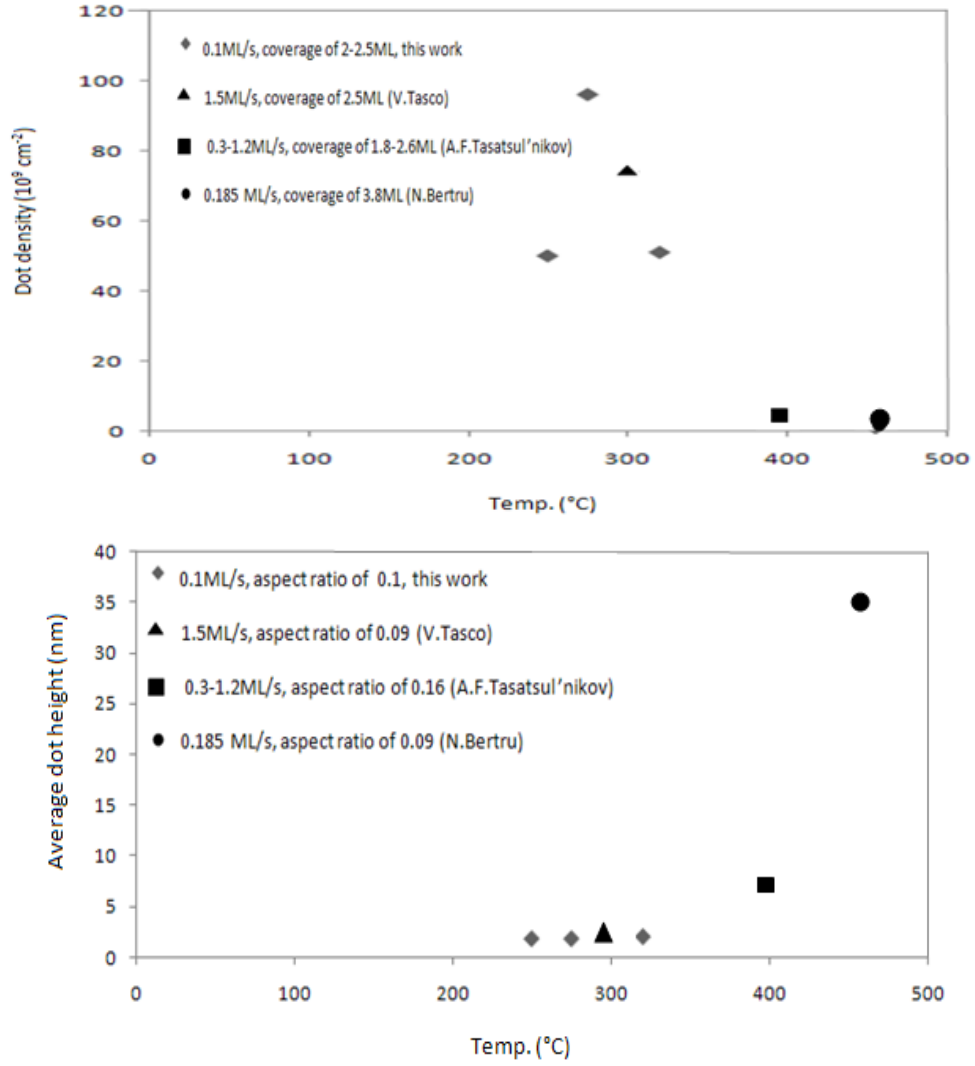


Fig.3.14 Average dot height (up) and density (bottom) shown as a function of temperature for different growth rate, InSb coverage, and aspect ratio. The symbols represented experimental data: part from this work, part from Refs [61, 68, 69].

Figure 3.14 illustrated the average dot height and density as a function of temperature for different growth rate, InSb coverage, and aspect ratio. In the case of properties of dots obtained from the previous research and this work, the number densities of QDs in this work were at least one order of magnitude higher than those depositing InSb on GaSb at high temperature. And the dots size was greatly smaller than the results in refers [68, 69]. In particular, compared with the reported growth of high-density InSb/GaSb QDs with a particular post-annealing method [61], the



as-grown dots at low temperatures in this work had comparable number densities and relatively narrow size distributions.

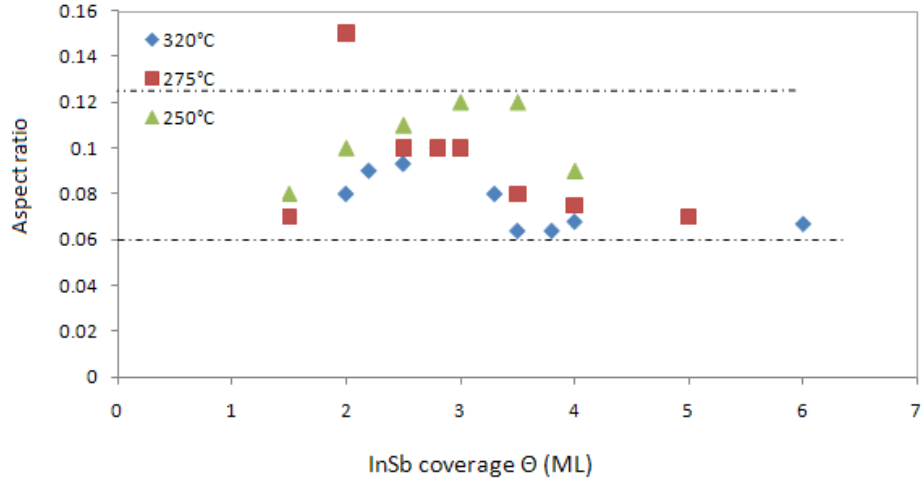


Fig.3.15 The aspect ratio of dots as a function of deposited InSb amount. The symbols represented the experimental aspect ratio data of dots grown at 320 °C (rhombus), 275 °C (square) and 250 °C (triangle).

The aspect ratio of dots was between 0.06 and 0.12, with a relatively higher aspect ratio of 0.15 at the growth temperature of 275 °C and the coverage of 2 ML.

### 3.3.5 Analysis of the material balance

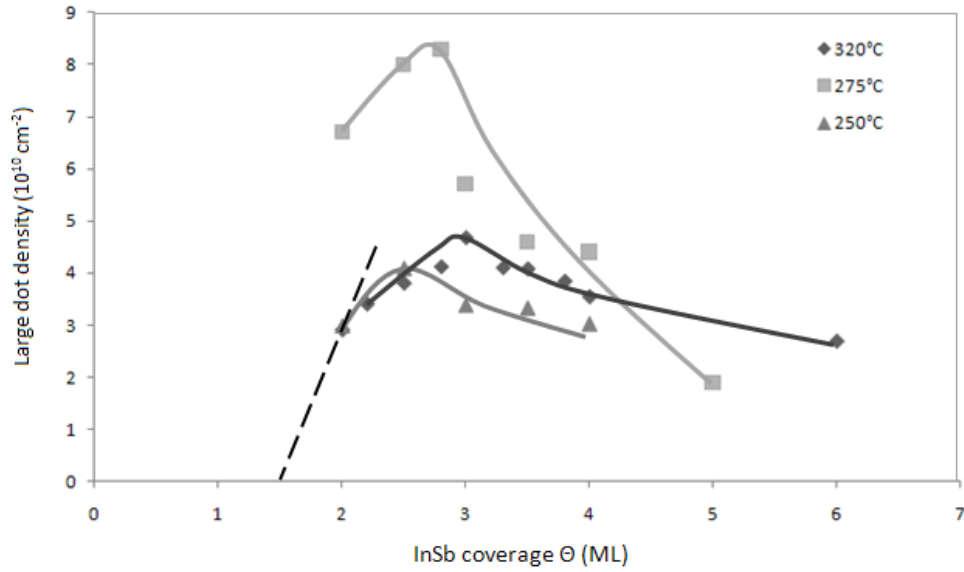


Fig. 3.16 Number densities of dots with height above 1ML as a function of InSb coverage. The symbols corresponded to the experimental number density data of InSb/GaSb (001) QDs grown at 320 °C (rhombus), 275 °C (square) and 250 °C (triangle).

Considering the difficulty in distinguishing the small QDs (height below 1ML) and the monolayer-high 2D islands, the properties of large dots (height above 1ML) were analysed in this study. Different from the evolution of InAs/GaAs QDs, number density decreased as increasing deposition of InAs amount, the trends in the experimental number density of large InSb/GaSb (001) QDs evolved increasing to a maximum value, then decreasing as the further deposition of InSb. The maximum value of large dot densities were  $4.7 \times 10^{10} \text{ cm}^{-2}$  for 3ML InSb grown at 320 °C,  $8.4 \times 10^{10} \text{ cm}^{-2}$  for 2.5ML InSb grown at 275 °C, and  $4.1 \times 10^{10} \text{ cm}^{-2}$  for 2.5ML InSb grown at 250 °C. Compared with the previous results of MBE growth of InSb/GaSb at high temperatures [68-70], dots with number density one order of magnitude higher than the reported as-growth QDs were obtained. The data points in figure 3.19 illustrated that InSb/GaSb QDs grown at 275 °C had higher number densities than those grown at 320 °C. This indicated that reducing the growth temperature below the condensation temperature of antimony reduced the In-adatoms diffusion length. In

particular, the small condensations of Sb may further increase the density of InSb nucleations. When the growth temperature was further decreased to 250 °C, surface reconstructions during the InSb growth exhibited different from the  $c(4 \times 4)$  to  $(\times 3)$  transition, the RHEED patterns got simultaneously changed along all the three azimuths. Above the coverage of 2ML InSb, a Sb-rich  $c(1 \times 1)$  surface emerged from a  $c(4 \times 4)$  less Sb-rich surface which was consistent with the previous research of InSb surface reconstruction at low temperature[66]. At the temperature of  $\sim 230$  °C, the limited diffusion length of In-adatom and the volatility of Sb were not able to sustain 2D layer growth and the phase segregation may occur. Compared with the results of InSb/GaSb(001) QDs grown at 275 °C, It was notable that the number densities of QDs grown at a lower temperature (250 °C) was smaller than those grown at 275 °C as shown in figure 3.16. The unique surface reconstruction at the temperature of 250 °C may suppress the nucleation of InSb, and the limited volatility of Sb and diffusion length of In-adatom may trigger the occurrence of phase segregation.

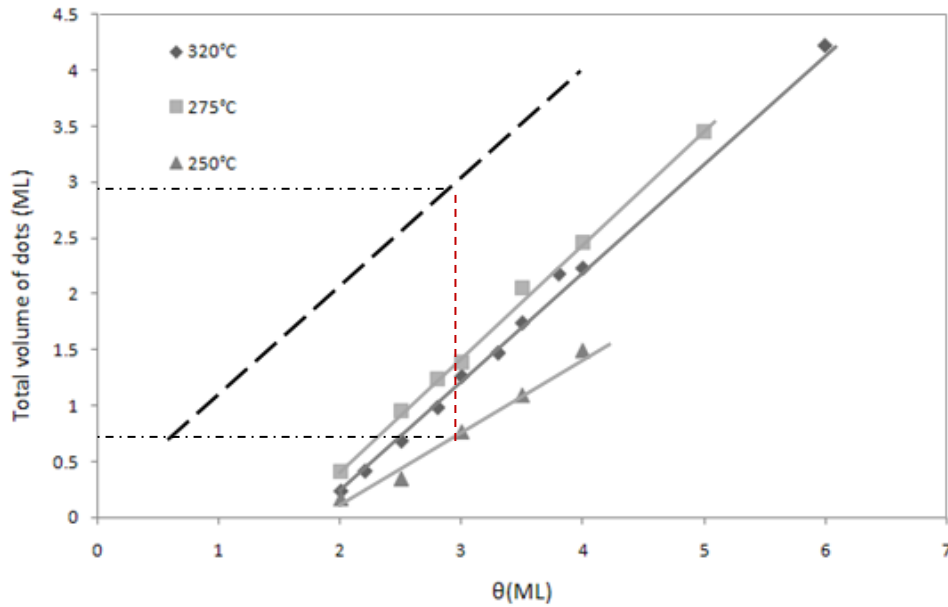


Fig. 3.17 Total volume of 3D dots and thick islands as a function of InSb coverage per unit surface. Three sets of samples were grown at 320 °C, 275 °C and 250 °C,

respectively, with a same growth rate of 0.11ML/s. The dashed line (black) corresponds to the deposited amount of InSb. The dash line (red) indicates the thickness of the wetting layer beneath the 3D features. All the data obtained from AFM particle analysing program. The full lines join the data for an eye guide.

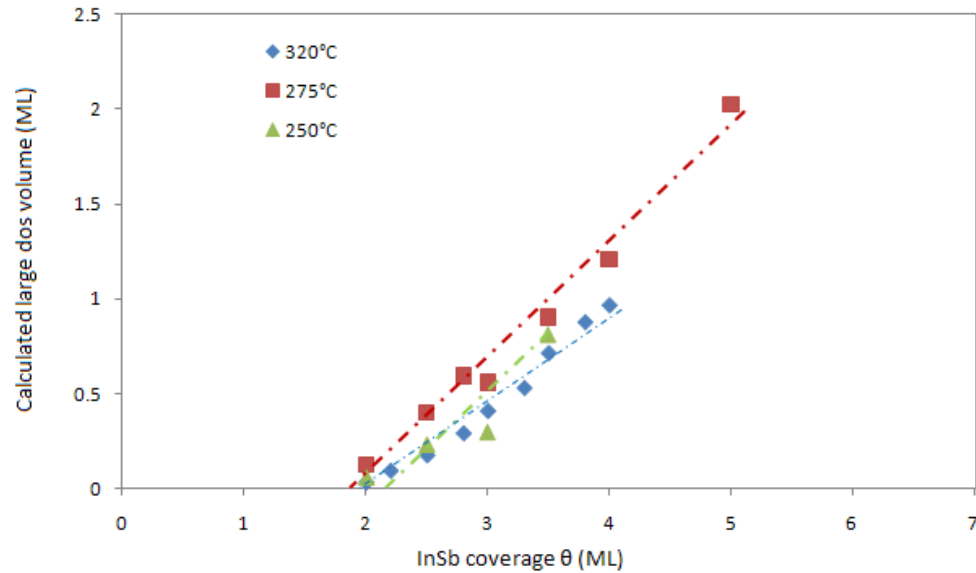


Fig.3.18 The calculated large 3D dots volume according the segment of sphere model as a function of InSb coverage per unit surface. Three sets of samples were grown at 320 °C (rhombus), 275 °C (square) and 250 °C(triangle), respectively, with a same growth rate of 0.11ML/s. The interpolations of dots volume data indicate the estimated thickness of wetting layer of sample grown at 320 °C, 275 °C and 250 °C is about 1.9 ML, 1.8ML and 2.2ML, respectively. All the data obtained from calculation of large 3D dots volume according the segment of sphere model.

To assess the wetting layer of InSb/GaSb (001) grown at low temperature, the experimental total volume data of dots was plotted as a function of deposited InSb amount as shown in figure 3.20 and figure 3.21. It is notable that the guided lines join the data from samples grown at 320 °C and 275 °C were parallel to the black dashed line. This indicated the initial 2D layer by layer growth was sustained during the growth at the temperature between 320 °C and 275 °C. And the assessed thickness

of wetting layers for samples grown at 320 °C and 275 °C was about 1.9ML and 1.7ML, respectively. For the growth temperature of 250 °C, it seemed the wetting layer was thicker than those grown at temperature above 275 °C. Considering that 2D layer growth regime may give way to 3D island growth, when further reducing the growth temperature below 230 °C [67], it was suspected that the growth mode at temperature of about 250 °C may not strictly obey the S-K growth mode. The morphology of the wetting layer may be more complex than those grown at temperature above 275 °C. The data in figure 3.21 were calculated 3D dots volume according the segment of sphere model as a function of InSb coverage per unit surface. The interpolations of dots volume data indicated the estimated thickness of wetting layer of sample grown at 320 °C, 275 °C and 250 °C is about 1.9 ML, 1.8ML and 2.2ML, respectively. This estimated value of wetting layer thickness was basically consistent with the values obtained from the experimental data in figure 3.18.

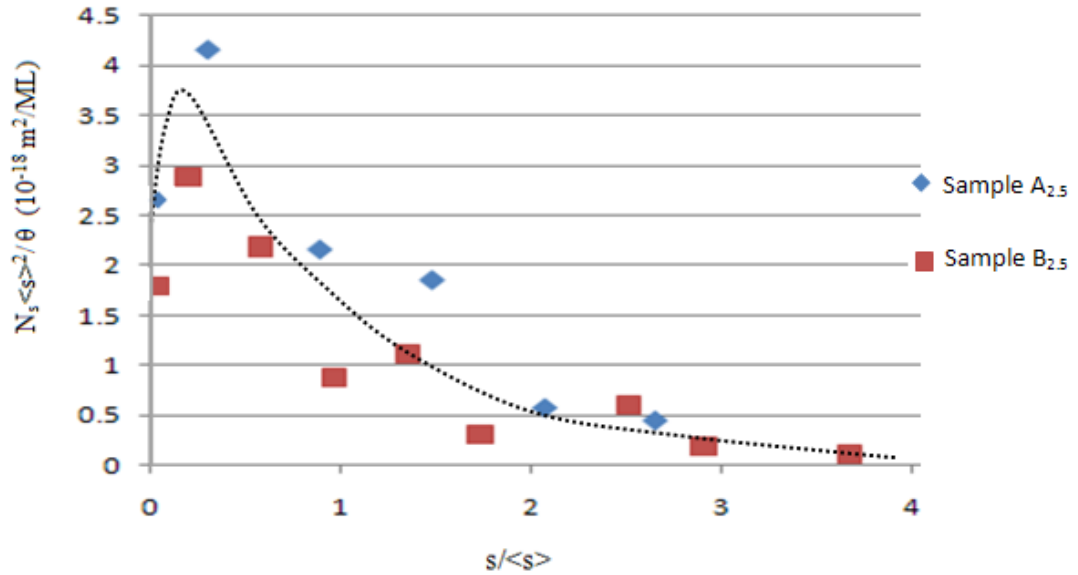
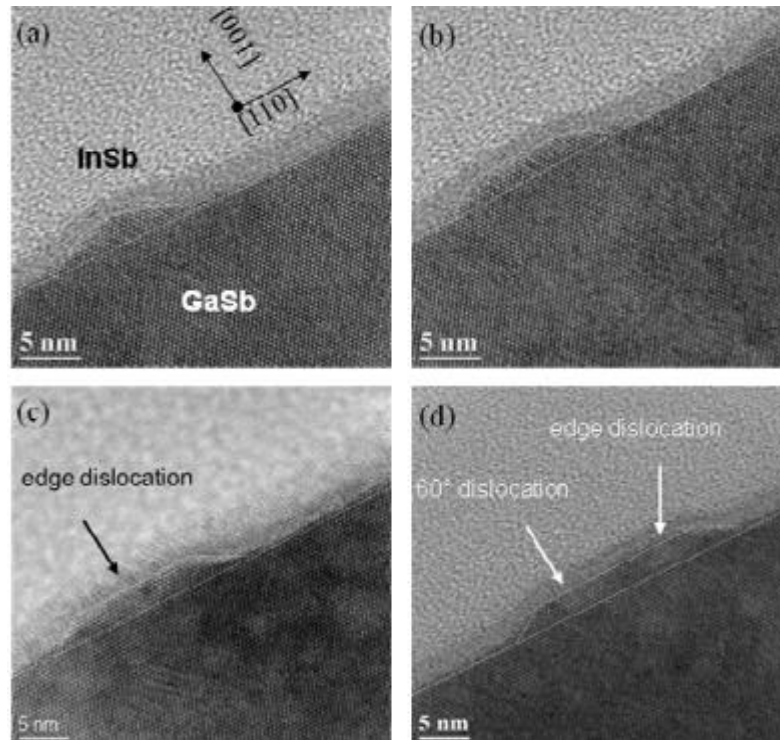


Fig.3.19 Dots size distribution of sample A2.5 and B2.5 for 2.5ML InSb grown at 320 °C and 275 °C, respectively. The dash line is a smooth fit to guide the eye.

Figure 3.19 illustrated dots size distribution of sample A2.5 and B2.5 for 2.5ML InSb grown at 320 °C and 275 °C, respectively. The data were conventionally normalized and based on counts of 100-280 dots. The parameter  $s$  was the dot area and  $\langle s \rangle$  was the mean dot area for the corresponding sample,  $N_s$  was the dot density and  $\theta$  was the coverage of InSb. The dash line was a smooth fit to guide the eye, and it seemed that the two sets of points in figure 3.19 roughly fell onto a single curve. The distributions of both samples displayed that their peaks were located well below the point of  $s/\langle s \rangle = 1$  and the number of dots with very low size was not zero.

### 3.3.6 Analysis the critical size and relaxation mechanism of InSb/GaSb QDs

NDeguffroy, et al. successfully grew high-density InSb QDs by special annealing step at a typical temperature [66]. They suspected the transition from 2D to 3D growth occurs at the InSb coverage of 1.7 ML, after deposition of the wetting layer, a great number of large 3D islands with planar tops are formed. All of the large 3D islands were demonstrated plastically relaxed by the formation of edge dislocations at interface.



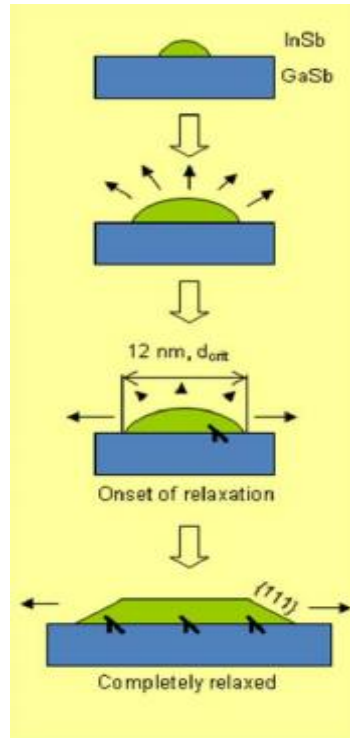


Fig.3.20 Size and shape evolution of the InSb/GaSb QD ensemble, left images are obtained by cross-section HRTEM and right figure was a schematic representation of the Size and shape evolution of the QD [66].

Figure 3.20 illustrated the size and shape evolution of InSb QDs from coherently strain to plastically relax. The QDs relaxation started at the lateral width of  $\sim 12$  nm as shown in figure 3.20 (right). For further estimation the critical size of coherent InSb/GaSb QDs, Han Ye, et al. [74], constructed a model to calculate the strain field in InSb/GaSb QDs using finite element method. The edge misfit dislocation favored to form at the center of the QD and the  $60^\circ$  dislocations were more likely to form at the position of 30% the base lateral width from the island edge [74]. The strain energy of dislocation at the center of QD had the maximum value and dropped as increasing the distance from the QD center. The strain at the edge of QDs was minimum. The result indicated the edge dislocation allowed a strong reduction in compression in the QDs at the center of the dislocations. Their observation demonstrates the position near the core of dislocation was in tension. In particular, the initial dislocation in the QD would not be delaying in formation by larger activation energies at higher growth temperatures [75, 76]. It was not clear whether

the lower activation energy would trigger the formation of dislocation in advance, however, the MBE deposition of InSb directly of GaSb (001) at lower temperatures made the growth of high density and narrow size distribution QDs possible.

Although the previous studies indicated the only route to obtain coherent strained QDs was the specific annealing steps at typical temperatures. The work in this study presented a new method of the growth InSb/GaSb QDs with high number density and narrow size distribution.

To assess the strain relaxation mechanism of the InSb/GaSb heterostructures grown in this study, a capped 3 ML InSb was grown at the growth rate of 0.1  $\mu\text{m}/\text{h}$  at 320  $^{\circ}\text{C}$  on GaSb (001) substrate. A 0.1  $\mu\text{m}$  GaSb buffer layer was directly deposited on the substrates prior to the InSb epilayer deposition at 500  $^{\circ}\text{C}$ . After the growth of 3 ML InSb, the epilayer was capped with a 0.1  $\mu\text{m}$  GaSb layer. The sample was thinned to a [110] section to be inspected in a JEOL 2100 TEM.

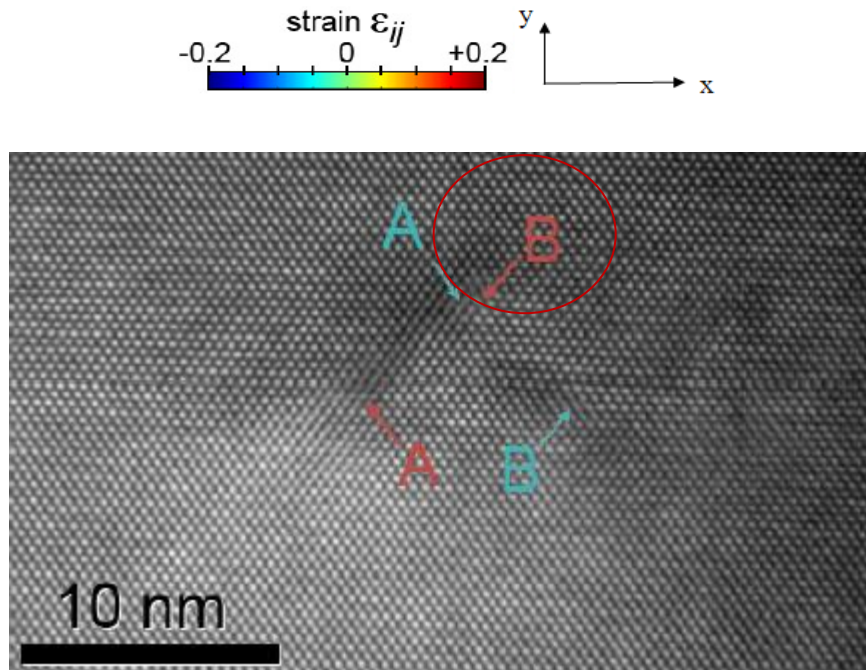


Fig.3.21 High-resolution TEM image of 2.5 ML buried InSb QDs in a GaSb matrix. Two pairs of 60  $^{\circ}$  dislocations were marked as A and B, respectively.



Figure 3.21 illustrated a HRTEM image of 2.5 ML buried InSb QDs in a GaSb matrix. Dislocations marked as arrow A and B were observed after careful inspection of the high resolution TEM image. In particular, they were usually formed in pairs of opposite Burgers vectors cites as A-A and B-B as shown in figure 3.30. Each pair of dislocations lay on the  $\{111\}$  plane which was consistent with the glissile  $\frac{1}{2}\langle 101 \rangle$  dislocation loops. These glissile dislocation loops made the relaxed QDs by the formation of  $60^\circ$  dislocations at the top and bottom interfaces of the QDs. Some coordination in the QDs strain relaxation may exist between the two adjacent dislocation loops such as loop A and B. Although, the small separation between the dislocation A and B (in the red circle) prevented their recombination to a sessile  $\frac{1}{2} [110]$  edge dislocation [77].

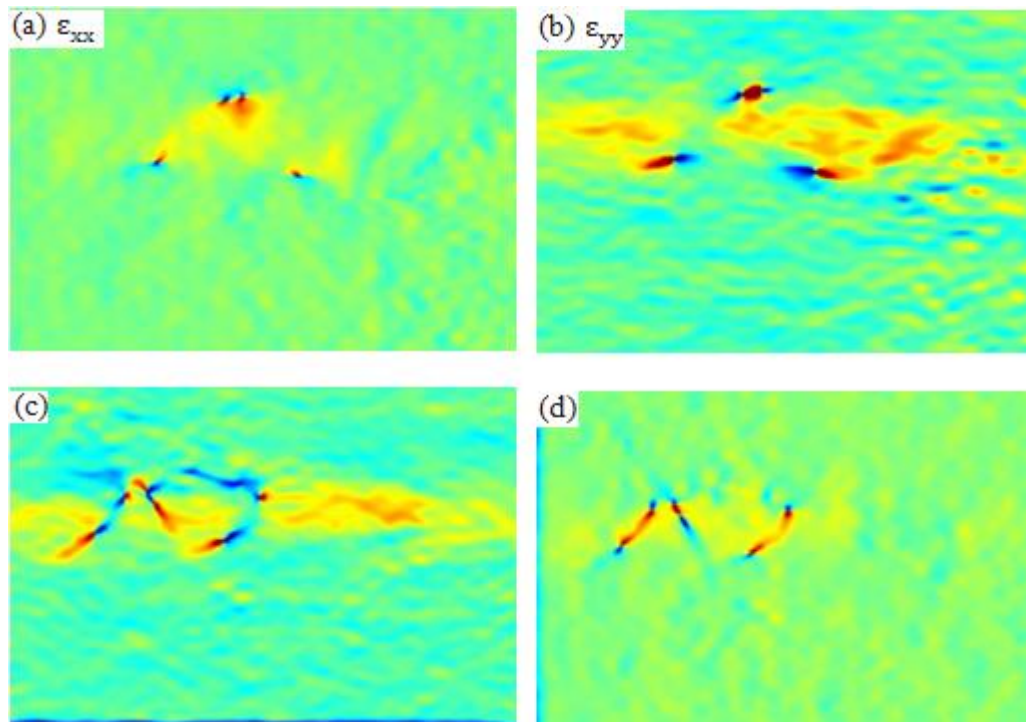


Fig.3.22 The strain components in the x (a) and y (b) axis direction, a hint of  $\sqrt{\epsilon_{xx}^2 + \epsilon_{yy}^2}$  (c), and  $\sqrt{\epsilon_{xx}^2 + \epsilon_{yy}^2}$  (d) structured long chain of loops using peak-pairs algorithm.

Figure 3.22 (a) and (b) illustrated the strain in QDs and dislocations by the peak pairs analysis [78, 79]. The strain in the QD's diffusion region along the growth

direction  $\varepsilon_{yy}$  is  $\sim 0.05$  that makes the QD visible. Figure 3.22 (c) illustrated the QD has nucleated to form a hint of  $\vee\vee$  structure and figure 3.22 (d) exhibited the QD produced a  $\wedge\wedge$  structure. The observation of longer chain loops along QDs indicated the formation of more QDs. Dislocations in the  $[110]$  direction may also exist since the intensity contrast was invisible if the dislocations were perpendicular to the electron beam.

The observation of QDs from the HRTEM examination demonstrated the formation of InSb/GaSb QD ensemble. The strain analysis using the peak pairs algorithm allowed the clear observation of the QD and dislocations. Due to the lattice mismatch between InSb and GaSb is close to the InAs/GaAs ensemble, it was generally assumed their strain relaxation manner would be similar to each other. In this study, the strain in InSb/GaSb QDs exhibited a more regular relaxation manner compared with the mechanism in InAs/GaAs QD ensemble. The suspected reason was the different stacking fault energy between InAs and InSb [79].

### 3.3.7 The properties of InSb/GaSb QDs

The studies in the previous sessions illustrated the growth of InSb/GaSb dots under low temperatures ( $< 320^\circ\text{C}$ ) and a low growth rate ( $\sim 0.11\text{ML/s}$ ). The sample with highest number density ( $\sim 10^{11}\text{ cm}^{-2}$ ) of dots was obtained at the growth temperature of  $275^\circ\text{C}$  at the InSb coverage of 2.5 ML. Although, the observation from the HRTEM image demonstrated the formation of InSb/GaSb QDs, it also proved the existence of misfit dislocations in the center of the dots. To prevent the dots dissolution, sample tmw05066 was 2.5 ML InSb grown on GaSb (001) immediately capping with 100 ML GaSb. The epilayer growth temperature was  $275^\circ\text{C}$  and the GaSb capping layers were grown at the same temperature. The photoluminescence (PL) properties of the capped InSb QDs were investigated by the standard PL apparatus. A diode laser emitted at 800 nm was utilized for optical pumping and the PL spectra was measured upto 4.6  $\mu\text{m}$  at 10 K by a Fourier transform infrared spectrometer using a liquid nitrogen cooled InSb detector. A PL intensity peak

around 1.73  $\mu\text{m}$  (0.72 eV) was detected at 10 K as shown in figure 3.23.

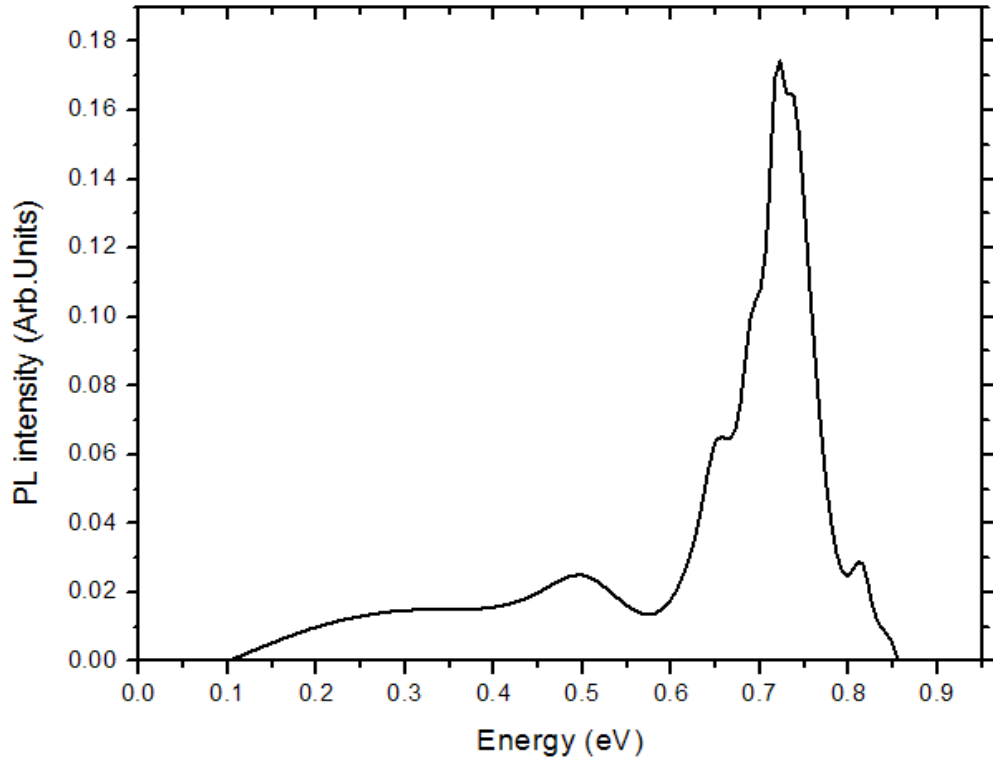


Fig. 3.23 Photoluminescence spectra recorded at 10 K from (sample tmw05066) 2.5 ML InSb capped with 100 ML GaSb. The laser excitation density taken for this measurement was 3 W/cm<sup>2</sup>.

The preliminary investigations of photoluminescence performance of capped InSb dots have been conducted in this session. A PL peak at 1.72  $\mu\text{m}$  (0.72 eV) in the high energy region was detected which was attributed to the wetting layer and the bulk GaSb [80]. The other transition was detected at 0.49 eV which was considered arising from the QDs first excited state transition. Due to the long carrier lifetime and wide spectral spreading of the optical transitions induced by the dots size distribution, the PL intensity from QDs was very low even under a relatively high laser excitation power. It was still not clear whether these dots were nonradiative due to the plastic relaxation or the experimental set up results in the QD related PL signal undetectable. Further study in the electrical properties of buried InSb QDs should be processed in next chapter.

### 3.4 Conclusions

InSb as a narrow band gap III-V compound semiconductor has attracted sustained interest for mid-infrared optical applications. Heteroepitaxial growth of the InSb on GaSb (001) exhibits a Stranski-Krastanow (2D-3D) growth mode. In particular, InSb nano-scale dots have potential applications in fundamental research of quantum confinement and are appealing candidates for the fabrication of high-performance electronic and nanophotonic devices. InSb/GaSb has a lattice mismatch of ~6.3% which is similar to the extensively studied InAs/GaAs system and, in principle, the direct deposition of InSb would form 3D islands via the Stranski-Krastanov growth mode. However, reports in the literature have indicated that direct deposition leads to a low density of dots ( $\sim 4 \times 10^9 \text{ cm}^{-2}$ ) of low aspect ratio, results in the development of methods to create quantum dots to circumvent this problem. For this research perspective, a method of direct depositing 1 to 6 ML of InSb onto GaSb (001) at low temperatures has been investigated. The growth was conducted at GEN II MBE system. The surface evolution during the growth was monitored by in-situ RHEED and surface morphology of sample after removal from MBE chamber was investigated by AFM in tapping mode. Dots number density volume, and size distribution on surface with different InSb coverage were comparatively analysed. Through tracing the transition from wetting layer to initial formation of QDs and the evolution of QDs from coherent to partially relaxed and fully relaxed, the critical size of the coherent InSb QDs has been assessed, in particular, the kinetic mechanisms which mainly drive the nucleation of QDs have been studied. The main results of the studies on the directly deposition of InSb on GaSb (001) have been presented. For the growth of 2.5ML InSb on GaSb (001) at 275 °C, a number density of  $\sim 10^{11} \text{ cm}^{-2}$  with size aspect ratio of ~0.15 has been obtained. After the initial 1 to 2ML planar growth, 3D islands gradually emerge on the surface of growth system. In this sense, growth of coherent 3D dots (self-assembling QDs) can take advantage of the initial formation of 3D dots. It has been demonstrated that the initial driven force of the nucleation of the QDs is the strain accumulated in the wetting layer. Although the systematic control of the number density, size distribution and lateral

position of QDs demands more knowledge of mechanisms far beyond the self-assembling. The conclusion could be drawn as the role of the wetting layer at the 2D - 3D growth mode transition. The sudden nucleation of  $10^{11} \text{ cm}^{-2}$  QDs occurring within 0.5 ML of InSb deposition at the 2D- 3D growth transition of the critical thickness. In aim of obtain self-assembled QDs with optimum optical and electrical properties, the issues including dot number density, dots location on the surface, dots scale and uniformity are crucial. In this study, the effect of growth parameters including growth temperature and deposited amount of InSb onto QDs scale and number density has been assessed. The formation of QDs is dependent on substrate morphology, the strain beneath the surface and kinetics of growth. The number density of QDs is a direct function of the deposited volume of InSb and the growth temperature. A capped 2.5 ML InSb on GaSb was investigated by TEM. The observation from the HRTEM examination demonstrates the formation of InSb/GaSb QDs, it also proved the existence of misfit dislocations in the center of the dots.

Due to the material intermixture between the InSb dots and the strained GaSb layer, the InSb QDs could hardly be clearly distinguished by TEM investigation. A capped single layer InSb was investigated by photoluminescence measurement. A PL peak at  $1.72 \text{ } \mu\text{m}$  (0.72 eV) was detected which was attributed to the wetting layer and the bulk GaSb. Although the QD related PL intensity was weak and may hardly be detected from the single InSb plane dots, the observation in size difference between the uncapped and capped InSb dots indicated the possibility of growth strained QDs. Based on the optimized growth parameters in growing single layer InSb, it is worth to further investigate the growth and characterization of buried InSb on GaSb at low temperatures.

## Chapter 4 MBE growth and characterization of buried InSb dots

Based on the study of surface quantum dots in last chapter, the optimal growth condition of InSb/GaSb ensemble has been obtained. In this chapter, one set of buried 2.5 ML InSb/GaSb (001) were grown by MBE at 275 °C. The structural morphology of both SQDs and BQDs were investigated by AFM and TEM. The electrical properties of QDs were measured by PL apparatus.

### 4.1 Introduction

Growth of high density with high-quality InSb QDs especially on GaSb has encountered great difficulties because the weaker In-Sb binding energy compared with other In-V compounds which, in turn, leads to the longer Indium adatoms' diffusion lengths on Sb-terminated surfaces [61, 64, 66]. Some groups grew InSb on group-V materials such as As-terminated surfaces, dots with high nucleation density has been obtained successfully [80,81]. The heterostructures with InSb QDs buried into the GaSb matrix were obtained by using MOCVP and MBE[81-83]. The average size of the surface quantum dots was ~30 nm in base width and ~3 nm in height, with a density of  $\sim 1 \times 10^{10} \text{ cm}^{-2}$ . Unfortunately, strong pumping was often needed to get any reasonable PL signals especially at low growth temperatures.

In this work, we aim to grow the coherent InSb QDs in SK mode. Based on the surface quantum dots studies in chapter 3, in this chapter, research was focused on the growth and characterization of buried InSb dots on GaSb (001) substrates. The effect of growth temperature and technique such as rotation during the growth onto QDs scale and number density has been investigated in advance. The sample with 2.5 ML InSb buried in GaSb exhibited relatively strong PL intensities and was thought to be originating from the QDs emission. One set of sample grown by GEN II MBE. The growth was monitored by RHEED and the surface morphology of uncapped InSb layer was examined by AFM.

Although the morphology of the top-uncapped dots was significantly different from the buried dots, research the morphology evolution of the uncapped dots by AFM gave the information about the corresponding buried dots properties. High-resolution TEM was utilized to scan the morphologies of dots and the cross-section of heterointerfaces. The temperature dependent PL measurements have been conducted on the initial sample. In order to illustrate the different properties of the SQDs and BQDs, InSb surface was wet etched in an aqueous solution. TEM and PL were conducted on the sample after removal of SQDs. The structural and electrical properties of both SQDs and BQDs were illustrated in this chapter.

## 4.2 Experimental

One set of sample was grown by GEN II molecular beam epitaxy (MBE) by depositing 2.5ML of buried InSb on GaSb (001) substrate at 275 °C. The growth process was monitored by the reflection high energy electron diffraction (RHEED). GaSb substrates deoxydation under stabilizing Sb flux occurred at a pyrometer reading of 540-560 °C. After removal of oxide, a 0.1  $\mu$ m GaSb buffer layer was grown on the substrates in advance of the InSb epilayer deposition. During the growth, good  $\sqrt{3} \times \sqrt{3}$  surface reconstruction was observed by the clear  $\sqrt{3} \times \sqrt{3}$  RHEED pattern. And during the cooling down process,  $\sqrt{3} \times \sqrt{3}$  surface reconstruction gradually gave way to  $\sqrt{5} \times \sqrt{5}$  reconstruction which was clearly indicated by the RHEED patterns. And it fitted for the previous research of surface reconstruction of InSb [83-96]. After buffer layer growth, 2.5ML of InSb was deposited directly on the GaSb buffer layer at growth temperature of 275 °C. After the deposition of InSb epilayer, GaSb spacer layers with thickness of 0.1  $\mu$ m was deposited onto the dots. Followed by deposition of the corresponding same thickness of InSb epilayer onto the GaSb spacer layer. The growth rate was set to 0.11ML/s which was a relatively lower value compared with other InSb/GaSb research groups' growth rates [61, 64, 81, 97]. The reason for doing that is because MBE growth is a kinetic dynamic process and in order to emulate the equilibrium conditions of the surface, the optimum growth

conditions should be explored. The beam flux was monitored by beam ion gauge. Morphology of the top layer uncapped dots was examined by AFM in tapping mode. To avoid the variation introduced by the difference in InSb coverage, AFM images were taken from the areas around the center of samples. Dot density and size were statistically analysed by the AFM particle analysing program. Transmission electron microscopy (TEM) study was operated in a JEM-2010F microscope at an accelerating voltage of 200 kV. Both high-resolution imaging and diffraction contrast modes were exploited. The electrical properties of samples were investigated by the standard PL apparatus. A laser diode emitted at 800 nm was utilized for optical pumping and the laser excitation density was  $\sim 5 \text{ W/cm}^2$ . The PL spectra was measured by a Fourier transform infrared spectrometer using a liquid nitrogen cooled InSb detector. For the removal of InSb SQDs, the InSb surface has been etched in the  $\text{H}_3\text{PO}_4/\text{H}_2\text{O}_2/\text{C}_6\text{H}_8\text{O}_7$  solution for  $\sim 30$  sec. The chemical solution of Hydrobromic acid (46%), orthophosphoric acid (80%), and hydrogen peroxide (35%) were purchased from China-Chemical institution.

#### 4.3 Results and analysis

##### 4.3.1 Structural properties of the InSb SQDs



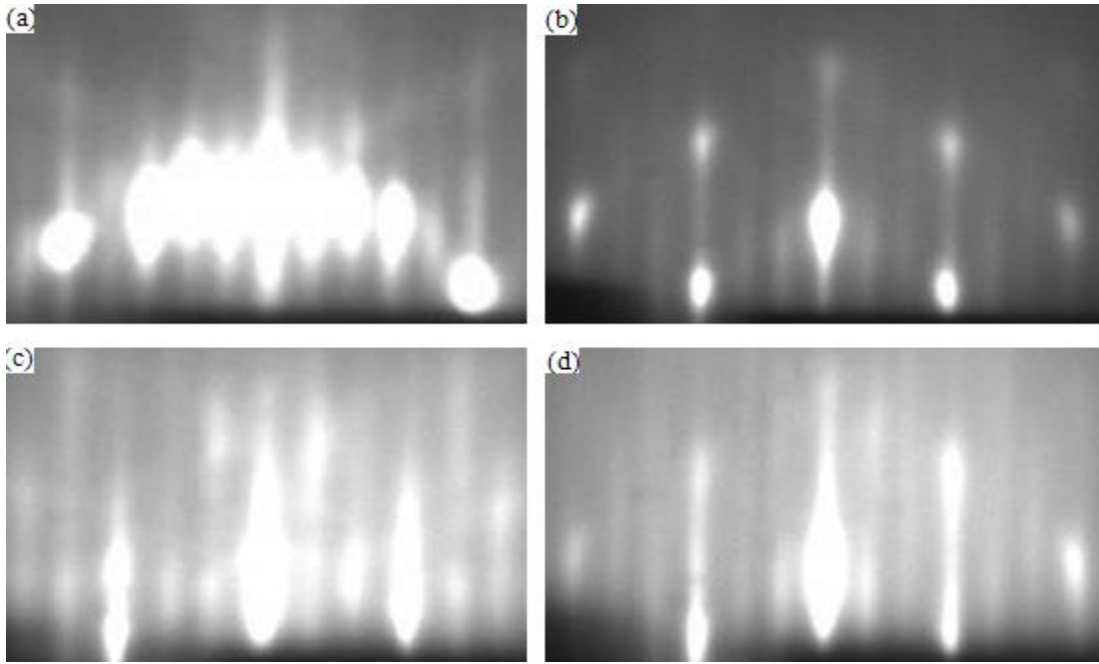


Fig.4.1 RHEED pattern (a) taken prior to initial deposition of InSb in  $[110]$  azimuthal, (b) taken after deposition of 2.5 ML InSb on GaSb (001) wafer in  $[1\bar{1}0]$  azimuthal, (c) taken after deposition of the 0.1  $\mu\text{m}$  GaSb spacer layer, (d) taken after the final 2.5 ML InSb on GaSb spacer layer in  $[110]$  azimuthal. All the samples were grown with rotation only during the growth of spacer and buffer, the growth temperature was  $275\text{ }^{\circ}\text{C}$ , the growth rate was  $0.11\text{ ML/s}$  and rotation rate was  $13.0\text{ rpm}$ .

RHEED pattern in figure 4.1(a) was taken after a  $0.1\text{ }\mu\text{m}$  GaSb buffer layer grown on the GaSb (001) substrate prior to the InSb epilayer deposition. Streaky pattern indicated a flat surface after the growth of  $0.1\text{ }\mu\text{m}$  GaSb buffer layer. Good  $\times 3$  surface reconstruction was observed by the clear  $\times 3$  symmetry RHEED pattern after the  $0.1\text{ }\mu\text{m}$  GaSb spacer layer growth as shown in figure 4.1 (c). Spotty RHEED patterns taken after the initial and final deposition of 2.5 ML InSb were clearly observed as shown in figure 4.1(b) and (d), respectively. That indicated a great number of 3D islands were formed on the surface of initial buried 2.5 ML InSb surface and final 2.5 ML InSb surface. A hint of  $\times 3$  surface reconstruction was also

observed after the initial and final deposition of 2.5 ML InSb. The surface morphologies of InSb SQDs were inspected by AFM.

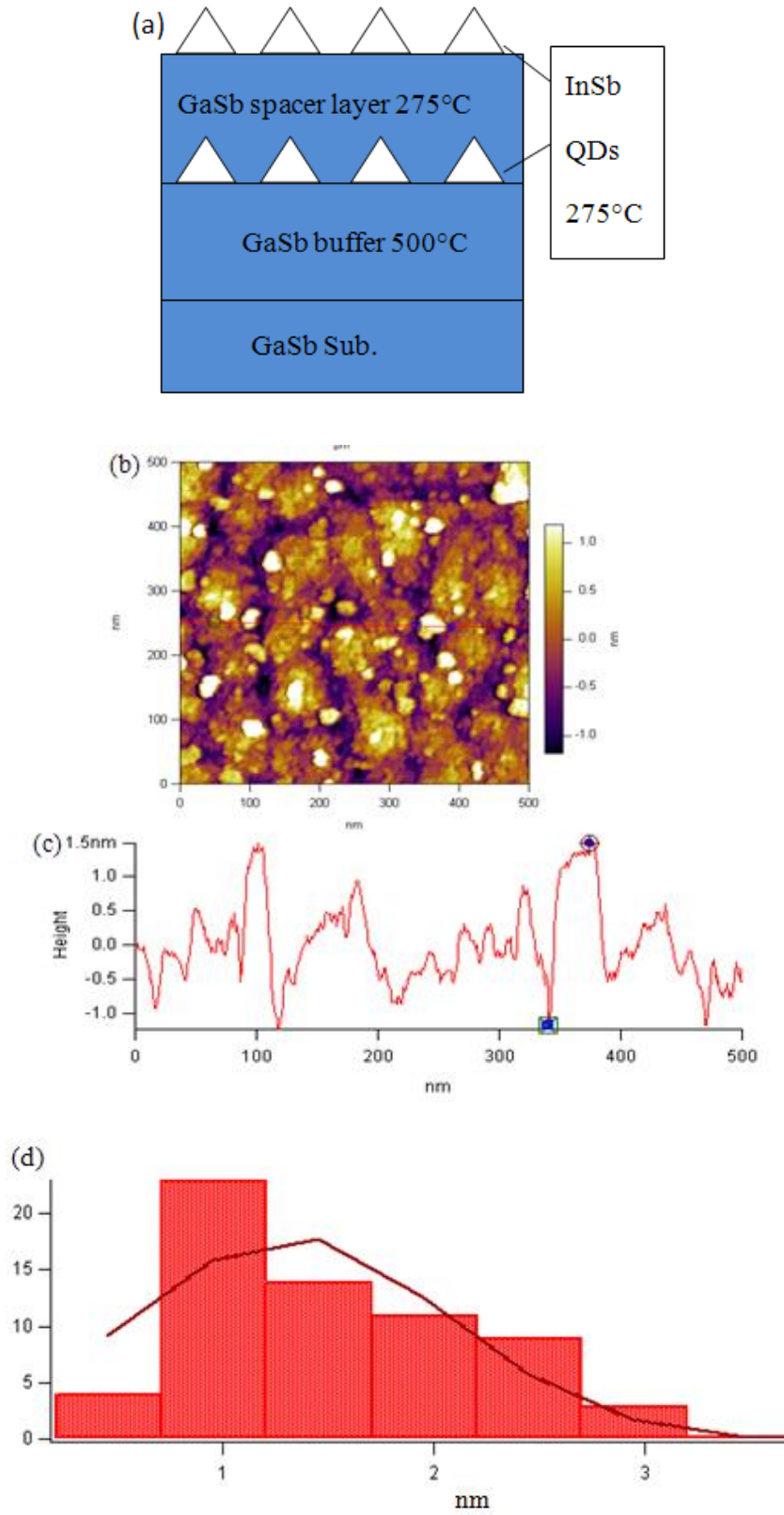
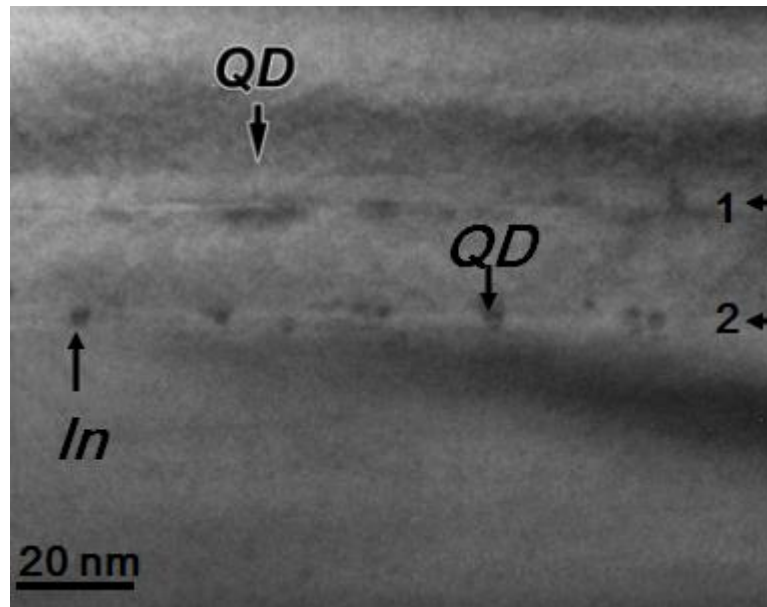


Fig.4.2 (a) growth structure, (b) 500nm  $\times$  500 nm AFM images, (c) cross-section of surface QDs, (d) height histogram of InSb SQDs.

Figure 4.2 illustrated a growth structure and a 500 nm×500 nm AFM image taken from the surface of sample with InSb coverage of 2.5 ML buried under a 0.1μm GaSb spacer layer on GaSb (001) substrate. The growth temperature was 275 °C, the growth rate was 0.11 ML/s and rotation rate was 13.0 rpm. The surface morphology of the sample was relatively smooth after inspection of the background of large AFM image. The quantitative data obtained by AFM analysing illustrated that the RMS over an 500nm × 500nm area was about 600pm. No large bumps were observed from the large AFM image. Clear 3D dots were observed from the 500nm × 500nm images as shown in figure 4.2(b). After checking the cross-section of dots area, the average dot size was about 3 nm high with a lateral width of 30 nm. Dot density was about  $1.1 \times 10^{10} \text{ cm}^{-2}$  estimated by the AFM particle analysing program.

#### 4.3.2 TEM images of sample (before etching)

Transmission electron microscopy was operated in a JEM-2010F microscope at the voltage of 200 kV. The sample was prepared by grinding, dimpling and milling. Both high-resolution imaging and diffraction contrast modes were displayed.



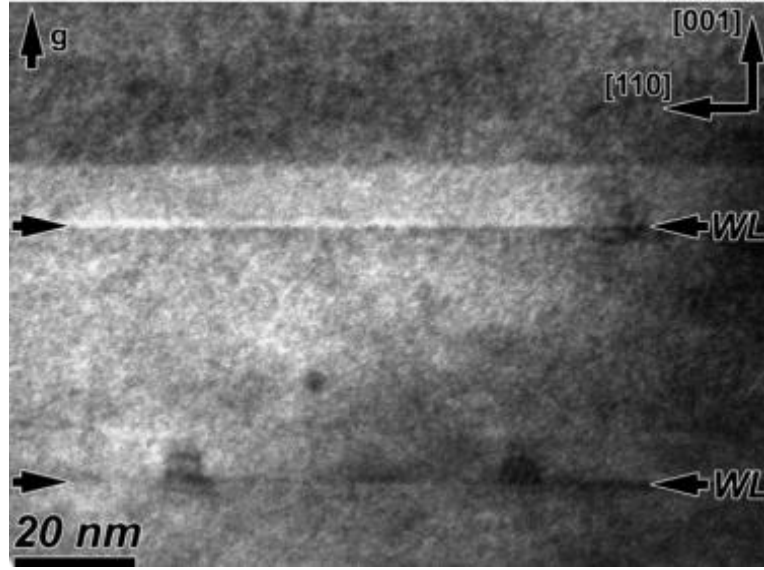


Fig.4.3 (top) Bright-field TEM image of the InSb (QDs)/ GaSb/InSb(QDs)/GaSb heterostructure, obtained under actual diffraction vector  $g(002)$  in two-ray conditions. Dark spots were suspected to be drops of atomic Indium at the InSb/GaSb interface. Arrows near the position 1 indicated InSb QDs/GaSb (spacer) interface and arrow 2 illustrated the InSb QDs/ GaSb (buffer) interface, (bottom) dark field TEM image of the InSb(QDs)/ GaSb and InSb(QDs)/GaSb interfaces, obtained under actual diffraction vector  $g(002)$ , in two-ray conditions, dark arrows indicated the existence of the wetting layers.

It was remarkable that the density of surface QDs was dramatically decreased compared with the single layer 2.5 ML InSb grown on GaSb. Due to the decreasing surface density of the SQDs, it was hard to get a focus of a single quantum dot in the scale of a few nanometers. The enlarged bright-field image (figure 4.3 top) made it possible to reveal the QD locations because of the strain contrast. The estimated size of SQDs was  $\sim 26$  nm (base width) and 3 nm (height). The SQDs lateral width estimated by TEM was slightly larger than the size obtained by AFM. The estimated sheet density of SQDs was  $\sim 1.2 \times 10^{10} \text{ cm}^{-2}$  which was slightly greater than that obtained by AFM. At the InSb/GaSb interface 2, some droplets around the size of 5 nm were observed on both sides of the heterointerface, based on the bright contrast,

these drops were suspected to be indium droplets due to the excess of In which was decomposed from gas phase onto the GaSb substrate at the very early stage of deposition. For the bottom dark field TEM image of the InSb (QDs)/ GaSb and InSb(QDs)/GaSb heterostructures, the dark arrows indicated the sites of the wetting layer which were slightly above the GaSb matrix.

#### 4.3.3 Electrical properties of sample (before etching)

The photoluminescence intensity of the sample (before etching) was performed by a standard PL device. A diode laser emitted at 800 nm solid state laser was utilized for optical pumping. A Fourier transform infrared spectrometer using a liquid nitrogen cooled InSb detector. The cryostat is in the temperature range from 10K to 300K.

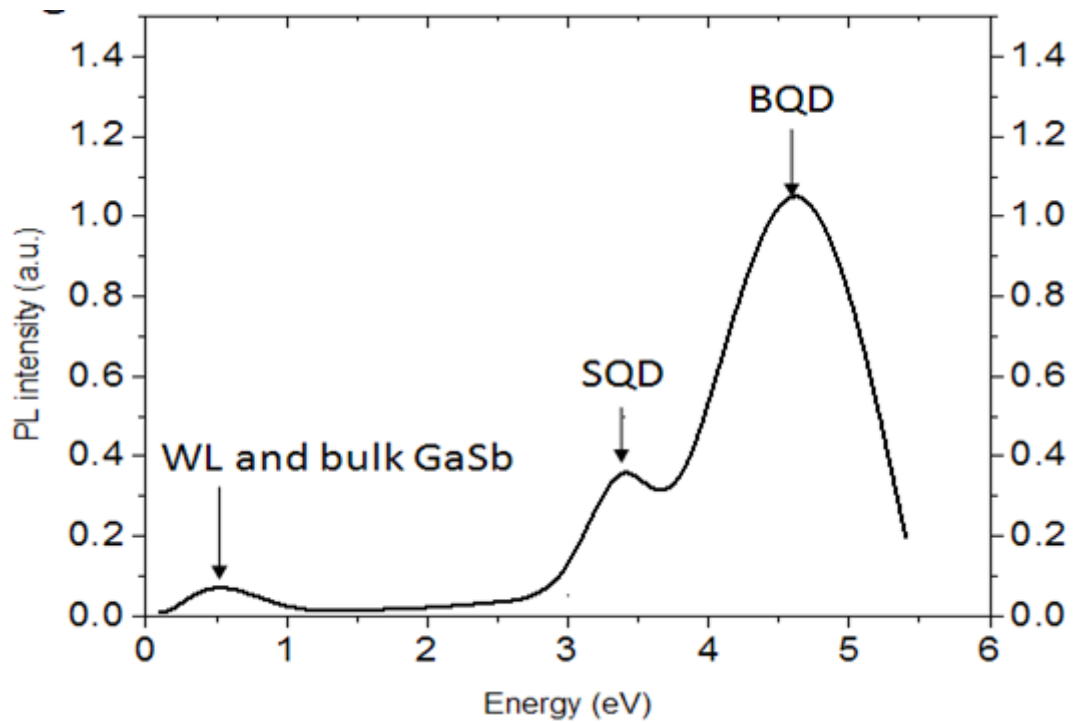
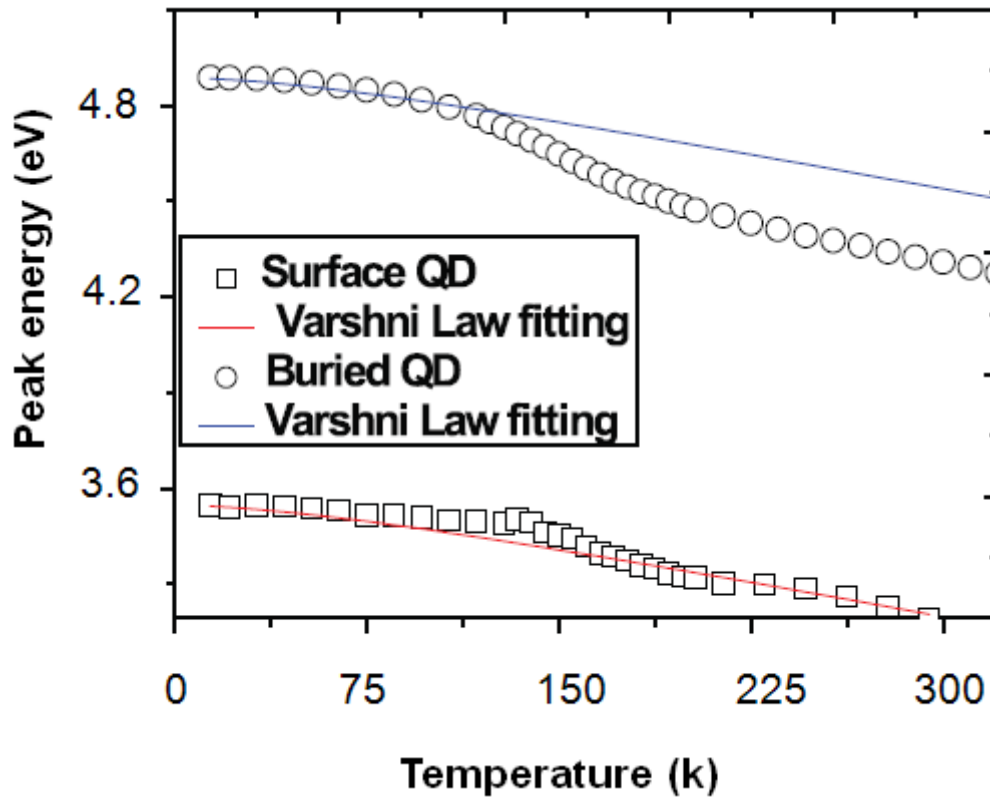


Fig.4.4 PL intensity measured at sample before etching, the operating temperature was 300 K.

The Photoluminescence (PL) intensity operated at 300 K was exhibited in figure 4.4. It was remarkable that there plotted three peaks: the first one was situated at 0.65 eV

with an FWHM of 65 meV, the second one was concentrated at 3.4eV with an FWHM of 78 meV, and the last one was placed at 4.6eV with an FWHM of 132meV. It was notable that the first peak's intensity was the weakest. According the study in section 3.39, it was suspected that this spectra was originated from the wetting layer and the bulk GaSb. For the other two peaks, the intensity of the relatively low peak is about one-third of the other peak. It was nearly impossible for the high peak originating from the excited states. The weaker energy peak was always caused by the fast carrier relaxation between the confined sublevels. The energy difference between the two peaks was about 1.2 eV which was much higher than the energy difference between the ground states and excited states. In addition, the possibility of peak which originated from the QDs could also be excluded based on the nearly-Gaussian height distribution diagram. So here it was suspected that the higher energy peak originated from the ground states of the BQDs, and the lower one was come from the emission of SQDs.



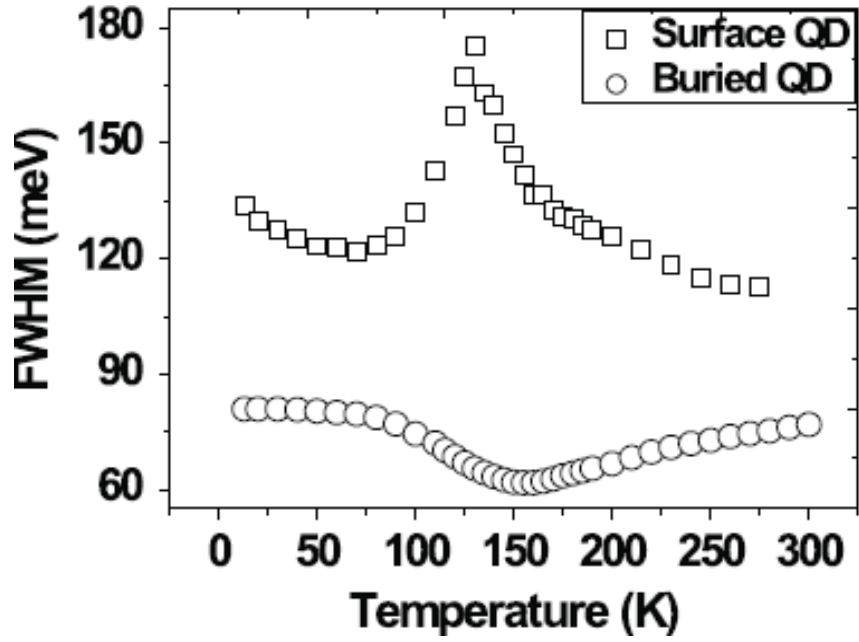


Fig.4.5 Temperature dependence of (top) peak energy and (bottom) FWHM of surface QDs and buried QDs, square represented SQDs and circle represented BQDs.

The poorer PL emissive intensity of the surface QDs than the buried QDs was caused by the large number of surface states originating from the dangling bonds. In that case, most carriers could not be injected into the QDs and also meant they could be dissipated non-radiatively. A few number of small size QDs were observed on the surface of the sample as shown in the AFM image (figure 4.2b). The small size represented poor overlapping of hole and electron wave-functions which further enhanced the weak radiative recombination strength rather than emission. Besides, almost no confined level was left inside the small dots with height below 1 ML. In this study, the energy peak from SQDs was suspected arising from the relatively high surface density which gave energy states for most carriers. In addition, the direct carrier capture into SQDs might be the dominant mechanism for the high density sample by reducing the non-radiative loss in wetting layer or interface defects.



According to the previous studies, another possible reason could be the In/Ga atom inter-diffusing at a higher temperature impeding the material distribution between QDs and increasing their bandgaps[67,79].

A rapid quenching of surface QDs was observed during the emissive process. Although it was shown that abnormal temperature dependence was similar to the disordered group-III nitride ensemble, that exhibited a W-shaped line width and S-shaped energy dependence. It could be caused by thermal assistance of the exciton motion by hopping the localized states through the hetero-interface[98]. In this case, the localized states could also exist because the surface QDs were uncapped. The dangling bond, surface fluctuation, defects and dislocations could be viewed as localized centers for carriers' capture.

From the height histogram in figure 4.2d, there were many quantum dots with height below 1 nm, that could be treated as QD precursors. Those small QDs were hardly to capture carriers for radiative recombination because of without the confined levels. However, it could be treated as a shallow localized center for carrier trapping[99].

There were a few localized centers in the neighborhood of QDs with a relatively high energy level compared with the QDs ground states. When the operating temperature was low, most of carriers could be trapped by those localized centers rather than the QDs. As the temperature increasing from 10 K to 75 K, the carrier thermal diffusion was promoted as well as their hopping through the localized centers. Consequently, this process increased the possibility of the carrier trapping. For further enhance the operating temperature, the carrier could be triggered out of the localized centers because of the weak quantum confinement, thus it was trapped by the QDs nearby. This was the reason why the initial dropping and then rising of both the PL intensity and FWHM from 10 K to 130 K as shown in figure 4.5. The peak blue shift indicated that process was more remarkable in those quantum dots owing high energy levels. It could draw the conclusion that the immature precursors were more

likely to surround the small size dots rather than the large dots. This result was conformed with the previous result for those large QDs were formed by the consumption of their neighboring small dots. Additionally, more localized centers locatted in the neighbourhood of the small size QDs indicated the increased carrier exchange between them, and enhanced the carrier population of small QDs as the operating temperature rising. Based on the theory of different size of QDs owing different carrier capture capabilities. It also indicated that large QDs always won larger capture cross-section area than those smaller dots[100].

When the temperature increased from 130 K to 300 K, both the peak energy of SQDs and FWHM dropped, as well as quenched of the PL intensity. The quenching regime could be fitted by the Arrhenius relation. After the calculation, the activation energies were 75 meV and 166 meV for SQDs and BQDs, respectively. The smaller activation energy of SQDs could be induced by the nonradiative properties of the surface defects.

#### 4.3.4 Etching of InSb surface

To further investigate the electrical difference between the BQDs and SQDs, the sample has been etched in the  $\text{H}_3\text{PO}_4/\text{H}_2\text{O}_2/\text{C}_6\text{H}_8\text{O}_7$  solution for removing the surface InSb dots. The chemical solution of Hydrobromic acid (46%), orthophosphoric acid (80%), and hydrogen peroxide (35%) were bought from China-Chemical institution.

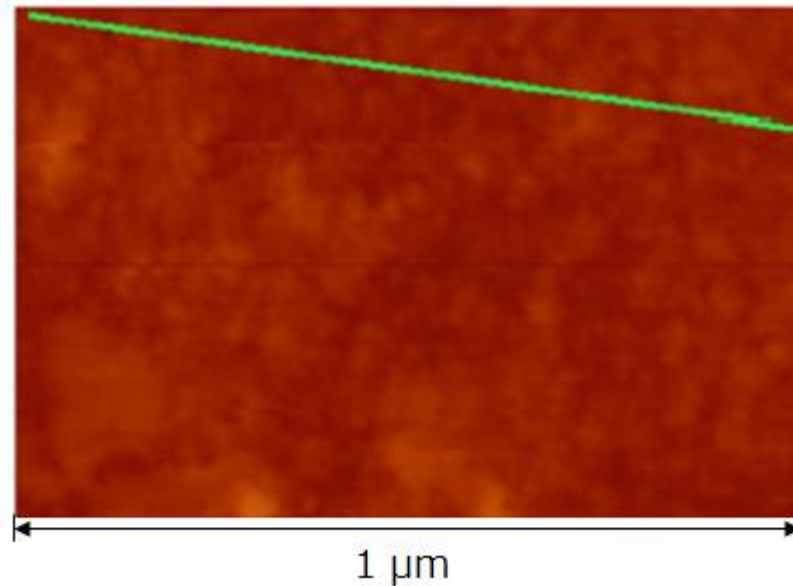
The sample was cut into 1 cm×1 cm wafer. After that, the surface of the sample was rinsed in a methanol solution at 320 K to get rid of the adhered organic contaminants. Then the sample was cleaned with deionized water and dried in nitrogen. The dry sample was placed in the typical etching solution with the front facet facing to the bottom of the Bunsen beaker. The sample was adhered onto a rotating holder by a carbon tape to make sure the regular stirring providing a diffusion configuration when the etchant supplied.

The etching solutions were collected during various etching time. Indium dosages were measured by a Thermo fisher Graphite Furnace Atomic Absorption Spectrometer (GFAAS).

The collected etching solution was initially diluted two hundred times in acidified solutions to stabilize those metals ions. Indium dosages were measured by the graphite furnace GFAAS configuration. Calibration solutions were made in a reconstituted matrix. Palladium nitrate solution (0.6 g/L) was prepared as modifier and added to the solution by the auto-sampler. The dissolved InSb dosage were calculated from the obtained In mass according equation(4.1)

$$e = \frac{m}{d \times s} \times 100 \quad (4.1)$$

where e was the dissolved InSb thickness (mm), m was the dissolved mass (g), d was the InSb density , and S was the InSb surface which was 1 cm<sup>2</sup>. The calculated etching time for the removal of 2.5 ML InSb was 25 seconds. During the etching process, the investigated etching time was in the range from 20 to 40 sec. AFM was used to scan the surface morphology of wafers after etching.



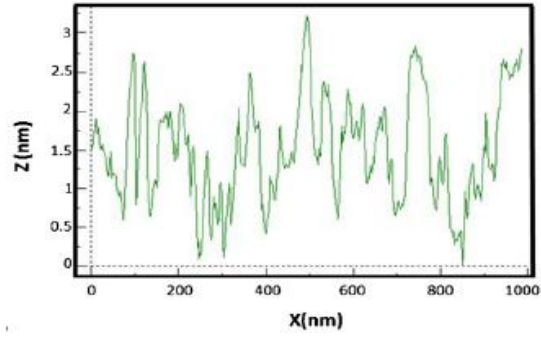
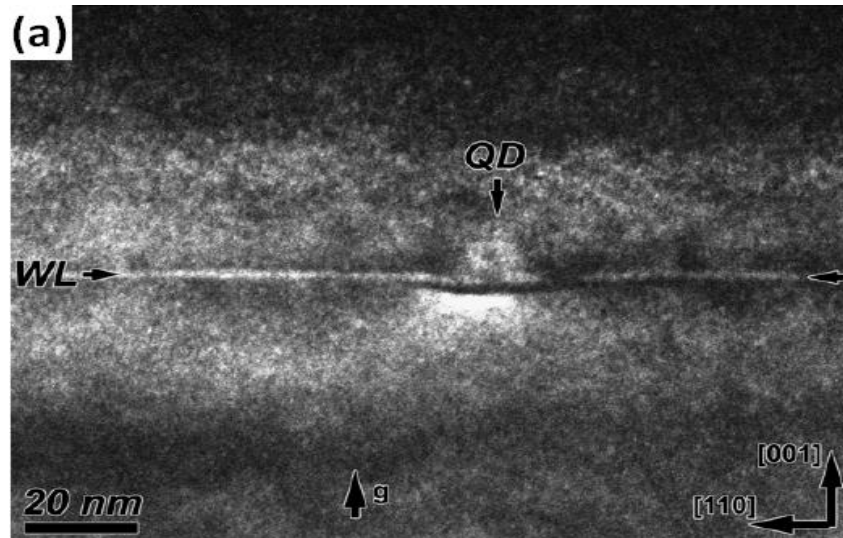


Fig.4.6 AFM image and cross section of the surface after 30 Sec etching in the  $\text{H}_3\text{PO}_4/\text{H}_2\text{O}_2/\text{C}_6\text{H}_8\text{O}_7$  (2 M/0.5 M/0.5 M) solution.

The AFM image in figure 4.6 was collected from the surface after 30 sec etching. After 30 seconds etching in the  $\text{H}_3\text{PO}_4/\text{H}_2\text{O}_2/\text{C}_6\text{H}_8\text{O}_7$  (2 M/0.5 M/0.5 M) solution followed by 1 min in water, no 3D dots were observed from the AFM image which indicated the completely removal of the InSb QDs from the surface.

#### 4.3.5 Structural and electrical properties of BQDs

For further investigate the bulk material and the buried dots beneath, transmission electron microscopy (TEM) was utilized.



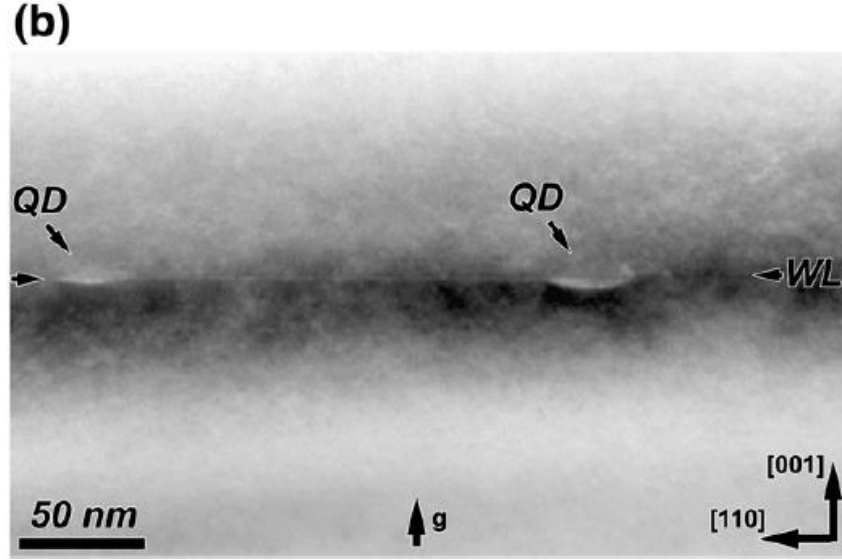


Fig.4.7(a) Dark-field TEM image of the GaSb/InSb (QDs layer)/GaSb heterostructure with diffraction vector  $g$  (002). Dark arrow indicated the existence of a wetting layer at the interface. (b) bright-field TEM image of the GaSb/InSb (QDs layer)/GaSb heterostructure with diffraction vectors  $g$  (004) and  $g$  (002).

The dark lens-shape contrasts in the GaSb matrix marked as QD indicated the existence of buried quantum dots (figure 4.7 a). The average size of the BQDs was slightly smaller in size ( $\sim 22$  nm in lateral width and  $\sim 2.5$  nm in height) and greater in sheet density ( $\sim 4 \times 10^{10} \text{ cm}^{-2}$ ). The experiment illustrated the possibility of the formation of InSb QDs on the GaSb matrix in SK mode. The estimated wetting layer thickness was  $\sim 0.6$  nm ( $\sim 1.7$  ML). The lateral size of this contrast at the interface was estimated to be 22 nm which was close to the value of the diameter of the coherent InSb QD grown by typical annealing process [67]. On the other hand, the bright-field TEM image fig 4.7(b) demonstrated the coherent InSb QDs as defects free particles. Bright lens-shape contrasts were around the GaSb matrix under QD base. The lateral size of these contrasts has been estimated to be 30 nm which was larger than that obtained from the dark-field contrast. It was suspected that the image widening was caused by strain. In addition, in order to be lattice-matched to the GaSb substrate, the coherent InSb QD was compressive strained around its bottom.

Thus the small QD was mainly indicated by strain contrast. It was notable that the strain field was largely extended to the GaSb substrate. Compared with the QD, the substrate was larger, those sites directly surrounded by the QDs were in tension. The obtained experimental data were conformed well with the exited results for the coherent QDs[101], and that was coincident with our previous conclusion that SK growth mode was the dominant mechanism during the formation of InSb QDs.

Besides, coherent InSb quantum dots' formation indicated that there existed an anion-exchange process between InSb and GaSb layer. That process was on the dependence of the elastic coefficients and surface free energy of the adjacent layers.

The electrical properties of the buried QDs were investigated by photoluminescence apparatus.

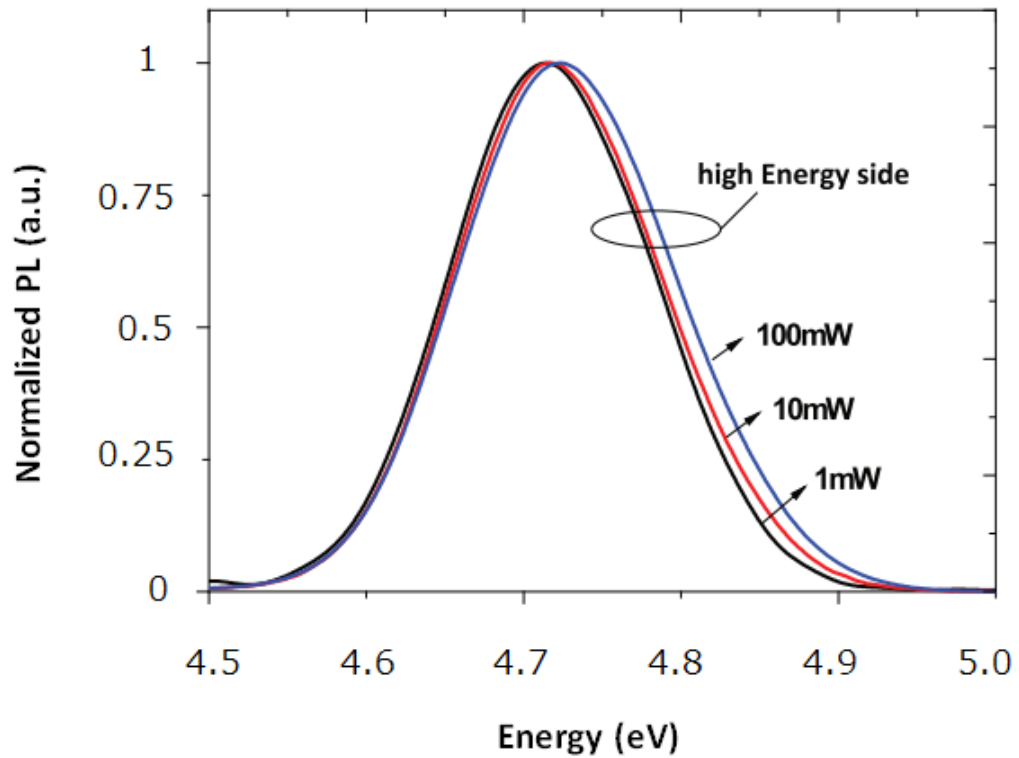


Fig.4.8 Normalized PL intensity of InSb BQDs at the excitation power of 1, 10 and 100 mW under the temperature of 10 K.

The PL intensities of the InSb BQDs at the excitation power of 1, 10 and 100 mW were illustrated in figure 4.8. Since large size quantum dots were more easily populated than smaller QDs at a low temperature, the operating temperature was set at a low value of 10 K. When the temperature increased, the population increment of small QDs was expected to be prominent by the gradual saturating of large QDs. When the excitation power varied from 1 to 100 mW, there appeared a blue shift of  $\sim 6$  meV. The observation indicated that the carrier capture efficiency was lower for small QDs than for large ones in the condition of low excitation power. In consequence, the power induced population was more remarkable for small QDs due to their small initial population. It has to be illustrated that such size dependent capture differences were due to high sheet density, which provided enough energy difference caused by the PL spectra.

#### 4.4 Conclusions

The sample with 2.5 ML buried InSb QDs with density (up to  $4 \times 10^{10} \text{ cm}^{-2}$ ) were obtained on the GaSb (001) by MBE. HRTEM cross-section images of the coherent and defect free InSb QDs buried into the GaSb spacer were observed. The estimated size of SQDs was  $\sim 26$  nm (base width) and 3 nm (height). The estimated sheet density of SQDs was  $\sim 1.2 \times 10^{10} \text{ cm}^{-2}$ . The average size of the BQDs was slightly smaller ( $\sim 22$  nm in lateral width and  $\sim 2.5$  nm in height). The experiment illustrated the possibility of the formation of InSb QDs on the GaSb matrix in SK mode. The estimated wetting layer thickness was  $\sim 0.6$  nm ( $\sim 1.7$  ML). The electrical properties of the sample were measured by PL. The PL spectras indicated there were two energy peaks which related to the QDs. We suspected that the RT peaks at 3.4 eV and 4.6 eV were related to the SQDs and BQDs, respectively. The surface QDs emission could even be sustained at 300 K and was comparable with the spectra from buried QDs. In the low temperature interval, a redshift of energy peak was observed due to the thermal transfer between the SQDs and the localized states. The temperature dependent PL of SQDs exhibited an abnormal transformation compared

with the BQDs. To further assess the different properties of SQDs and BQDs, wet etching of the InSb surface was conducted. After removal of the InSb SQDs, the surface morphology was investigated by AFM. The structures of the BQDs were scanned by HRTEM. The estimated sheet density of BQDs was  $\sim 4 \times 10^{10} \text{cm}^{-2}$ . The low temperature PL spectra indicated a blue shift of BQDs energy peak during enhancing the excitation power from 1 mW to 100 mW. In summary, this work demonstrated the formation of SQDs without capping layers and relatively high-density BQDs. The carrier processes between the SQDs and the localized states could be exploited by temperature dependent PL. Further research was needed to illustrate the effect of surface states on the carrier transfer between BQDs and SQDs in a vertically coupled ensemble.



## **Chapter 5 Investigation the growth of III-Sb on GaAs (001)**

In this chapter, most of work was focused on the deposition of III-Sb on undoped (001) GaAs substrates. Involve the manipulation of growth parameters, such as deposition temperatures, growth rates, V/III ratios. Analysis of the layers was carried out by using RHEED, AFM, TEM and Hall measurement. The growth process and surface reconstruction were monitored by in-situ RHEED. The surface morphology of post-growth samples was investigated by AFM. For the case of heterostructures, the features of surface and interface are of the most importance. The effects related to interface and surface largely determine the optical and electrical properties of the heterostructures. TEM was employed to analyse the interface and bulk features especially for the defects introduced by lattice mismatch. The electrical behaviours of the heterostructures were assessed by Hall measurement. In most of heteroepitaxy systems including GaSb/GaAs, InSb/GaAs and AlSb/GaSb, threading dislocations are inevitable. S. H. Huang, etc. used high-resolution TEM to analyse misfit array at the GaSb/GaAs interface, and the propagated threading dislocations. The results could be concluded as the density of threading dislocations almost remains constant after the GaSb coverage of 0.2  $\mu\text{m}$  which is different from the result obtained in this study.

Growth parameters including temperature, V-III ratio, and the choice of growth technique such as annealing or inserting buffer layers have significant effects on the density of threading dislocations.

### **5.1 Analysis of the deposition of GaSb on GaAs (001)**

#### **5.1.1 Introduction**

Narrow band gap III-V semiconductors including GaSb and InSb have attracted intense research interest for the application of optoelectronics, high-frequency electronic devices and magnetic field sensors for read head applications [102-106].

InAs is a small band gap and electron effective mass semiconductor ( $E_g = 0.36\text{eV}$  and  $m_e = 0.023m_0$  at  $T = 300\text{K}$ ) with a large mobility electrons ( $\sim 30,000\text{cm}^2\text{V}^{-1}\text{S}^{-1}$ ) at room temperature. The unique properties of InAs make it a promising channel material in the fabrication of novel electrical devices such as high-speed field-effect transistors (FETs). For InAs/GaSb assembly, the conduction band of InAs lies below the valence band gap of GaSb and the band alignment is type -II. Hence, the InAs/GaSb superlattices have small energy gaps and high absorption coefficients. These short-period superlattices are potential utilized in active regions for long-wavelength infrared detectors. AlSb is a large band gap ( $E_g = 1.63\text{ eV}$ ) and an indirect-gap semiconductor. In addition, the conduction band offset between InAs and AlSb is  $\sim 1.35\text{ eV}$ . Consequently, AlSb becomes a promising barrier for FETs [105].

The investigation of these binary antimony compounds is important to the further research of ternary and quaternary  $6.1\text{ \AA}$  materials. In this chapter, research was focused on the growth of single layers of InSb, GaSb and AlSb on GaAs substrates. In particular, the issues of surface morphology, reconstruction, dislocations and electrical properties for InSb/GaAs, GaSb/GaAs and AlSb/GaAs systems were highlighted.

For the ternary  $6.1\text{ \AA}$  semiconductor, primary study of the surface morphology and defects engineering of  $\text{Al}_{1-x}\text{Ga}_x\text{Sb}/\text{GaSb}$  system has been processed. All the growth was conducted in the GEN II MBE apparatus.

Semiconductors GaSb, AlSb and InAs are nearly lattice matched ( $a_{\text{GaSb}} = 6.095\text{ \AA}$ ,  $a_{\text{AlSb}} = 6.136\text{ \AA}$  and  $a_{\text{InAs}} = 6.058\text{ \AA}$ ). Ternaries such as  $\text{Al}_{1-x}\text{Ga}_x\text{Sb}$  and  $\text{In}_{1-x}\text{Ga}_x\text{Sb}$  also have lattice constant approximately to  $6.1\text{ \AA}$ . Those semiconductors with lattice constant close to  $6.1\text{ \AA}$  are refereed as the ‘ $6.1\text{ \AA}$  family’. Recently much of research have been focused on the  $6.1\text{ \AA}$  family materials because of their wide range of band gaps and the ability to band alignment [105]. The unique

optical and electrical properties of 6.1 Å semiconductor make them becoming appealing candidates for the fabrication of devices including field-effect transistors (FETs), infrared detectors as well as resonant tunnelling devices[106-108].

Considering the lattice constant of GaSb ( $\sim 6.095\text{\AA}$ ) is quite close to those ‘6.1Å family’ materials, study of GaSb as a substrate has attracted extended interest. GaSb based substrate were promising in the fabrication of devices operating in the mid and long wavelength region such as infrared sensors [109,110].

Compared with GaSb substrate, semi-insulating GaAs substrate would be more preferable due to its unique properties such as low intrinsic carrier concentration, low absorption profile which is benefit to the accuracy for thermal couple and high transmission in the infrared region. Besides, the GaAs production has high quality and cheap cost. In this section, research would focus on the growth of GaSb on GaAs substrates. High-quality films beneath devices are most important for their optical and electrical performances.

For heteroepitaxial growth of GaSb on GaAs, one main consideration is the propagation of dislocations through the growing layers. The lattice mismatch between GaSb and GaAs is 7% [111].

Dislocations induced by lattice mismatch will be formed in epilayers to relieve the strain. In defect engineering, it is essential to consider the defect propagation through the growing layer and its final result on surface morphology and electrical properties. The purpose of the investigation of GaSb on GaAs was to understand the dependence of film quality on the growth conditions including growth temperature, growth rate, group V-III ratio and the choice of post-growth annealing.

Experimental growth was conducted in GEN II MBE apparatus. The in-situ RHEED was used to examine the oxide removal of GaSb substrate and the deposition process of GaSb on GaAs (001). After the growth, the issue of surface morphology and

dislocations induced by lattice mismatch are investigated. Ex-situ characterization microscopies including AFM and TEM were utilized to assess the properties of samples.

#### 5.1.2 Experimental

Before admission to the growth chamber, cleaved quarter pieces of 2'' undoped GaAs(001) substrate were affixed to an indium-free platen and outgassed for 60-100 mins at 400 °C (Eurotherm's reading). Oxide layers on GaAs substrate were thermally desorbed under a stable antimony flux ( $BMI \approx 6.0 \times 10^{-7} \text{ Torr}$ ) at 550-590 °C (thermal couple's reading). The sequent growth would be conducted at growth temperature ( $T_g$ ) of 400-500 °C and growth ratio of 0.5 to 1  $\mu\text{m/h}$ . Substrate rotation was used during the growth of all sets of samples. First two series of Samples were grown in 5.1.3.1. The first pair is the thermal deoxidation of GaAs (001) substrates. They were grown to assess the effect of annealing technique on the surface morphology of the resultant GaAs substrate. To further study the effect of annealing on the GaSb surface morphology, the other set of samples were 5 nm GaSb on GaAs (001) as grown and post-annealing for 30 mins. In order to assess the effect of growth temperature on the final surface morphology of GaSb, two sets of samples were prepared in section 5.1.3.2. The first pair was 250 and 500nm GaSb grown on GaAs at 400 °C. The other pair was 250 and 500nm GaSb grown on GaAs at 500 °C. Based on the previous research of growth GaSb and the results analysis of section 5.1.3.2, the optimum growth temperature for GaSb on GaAs was 500 °C, which was corresponding to the previous research in our lab. To further assess the effect of annealing on the surface morphology of GaSb, samples in section 5.1.3.3 were 250 and 500nm thick GaSb grown on GaAs under 30 min annealing at 580 °C (the epitaxial growth temperature was 500 °C). In order to assess the effect of buffer layer upon the GaSb surface morphology, samples in 5.1.4 were 0.1  $\mu\text{m}$  GaSb grown on GaAs (001) substrates inserted with AlSb buffer layer of different thickness. The subsequent growth would be substrate cooling under a stable Sb flux

( $BMI \approx 6.0 \times 10^{-7} T_{\text{oor}}$ ) until the Eurotherm reading approached the value of 300 °C. After that, samples were transferred to the buffer chamber, and removed for ex-situ analysis until they were cooling down to the room temperature. Considering the thermal variation over the samples, the centre of each wafer were chosen to do the characterization, to make sure that the chosen area of the wafer was corresponding to the region assessed by the pyrometer. In-situ RHEED was utilized through the entire growth process to assess surface reconstructions and ensure the final stable surfaces. The microstructure of GaSb/GaAs interface and surface morphology were characterized by TEM and AFM. The electrical properties were investigated by Hall measurement.

### 5.1.3 Results and analysis

#### 5.1.3.1 Analysis of 5 nm GaSb on GaAs (001)

To investigate the initial stage of the heteroepitaxial growth of GaSb on GaAs, 5 nm of GaSb was deposited on GaAs (001) substrate. To evaluate the effect of annealing technique on surface morphology, a pair of samples tmw04083 and tmw04085 was produced by deposition of 5 nm GaSb on GaAs(001) substrate with oxide removal unannealed and annealing for 30 mins, respectively.

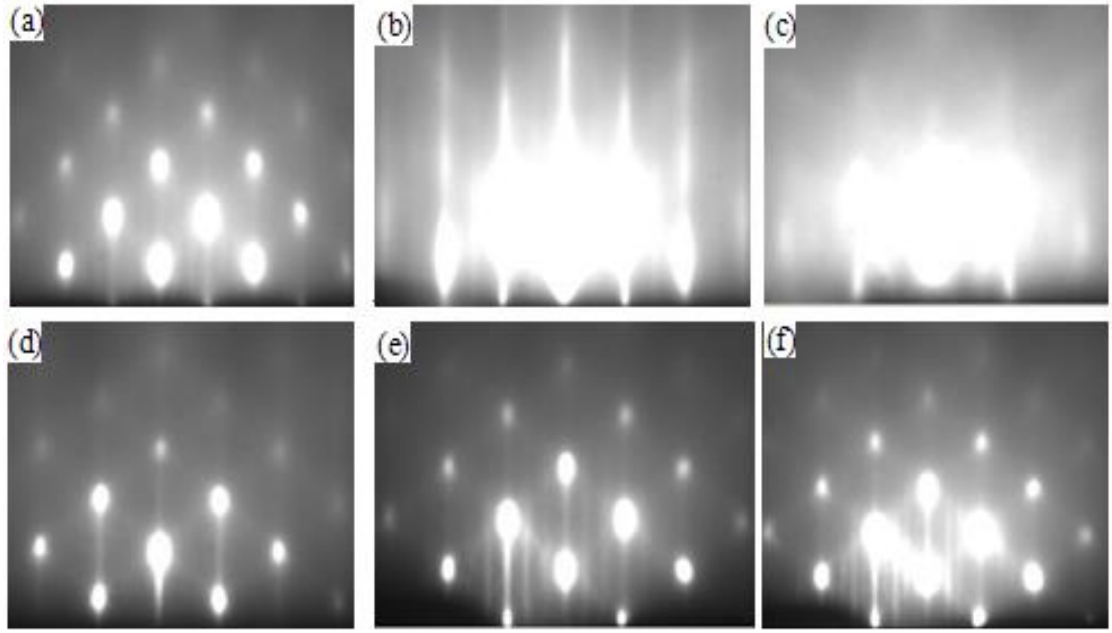
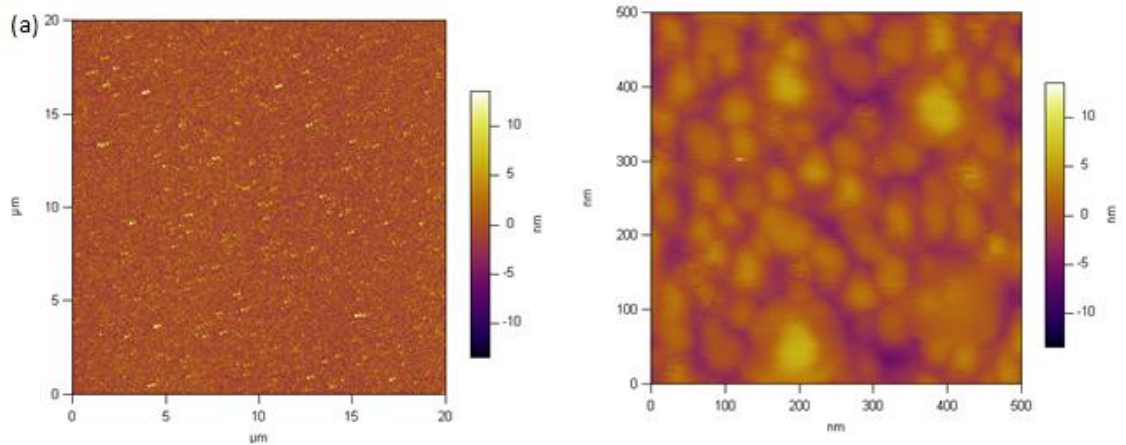


Fig.5.1 RHEED pattern taken (a)after deposition of 5 nm GaSb for sample tmw04083 with the beam incident in the [110] direction (b) during cooling down of sample tmw04083 in with the beam incident in the [110] direction (c) during cooling down of sample tmw04083 in with the beam incident in the  $\bar{1}\bar{1}0$  direction (d) after deposition of 5 nm GaSb for sample tmw04085 with the beam incident in [110] direction (e) for sample tmw04085 with the beam incident in incident in  $\bar{1}\bar{1}0$  direction (f) during cooling down of sample tmw04085 with a bright transition from  $\times 3$  to  $\times 5$  reconstruction.

The growth temperature was 500 °C<sub>p</sub>, BMI was  $\sim 1.2 \times 10^{-6}$  Torr, and the growth rate was  $\sim 0.55$   $\mu\text{m/h}$ . To maintain a specific growth rate, there was a limitation of Sb<sub>2</sub>: Ga flux ratio under a given substrate temperature. The typical RHEED patterns of initial growth of GaSb/GaAs (001) were illustrated in figure 5.1. For sample tmw04083, as the Sb shutter opening, the RHEED pattern changed from ordered streaky to spotty pattern, indicating the transition from 2D planar growth to 3D island growth. The RHEED pattern (a) taken after deposition of 5 nm GaSb on GaAs exhibited bright spots which indicates 3D dots were formed on the surface. During the cooling down process, the RHEED pattern changed from bright spots to ordered

streaky pattern as shown in figure 5.1(b). As for the annealed sample tmw04085, the RHEED pattern taken (d) after the growth of 5nm GaSb on annealed GaAs manifested large and bright spot which indicated large 3D islands were formed on the surface. The RHEED pattern taken from the  $[\bar{1}10]$  direction displayed an ordered streaky pattern with bright spots and a distinct ( $\times 3$ ) reconstruction could be observed in figure 5.1(e). The RHEED pattern in figure 5.1 (f) illustrated a bright transition from  $\times 3$  to  $\times 5$  reconstruction during the cooling down process. Growth of GaSb on GaAs (001) was conducted under excess Sb flux that usually causes antimony rich surface. For Sb-terminated GaSb (001) surface, it generally exhibits  $(1 \times 5)$  and  $(1 \times 3)$  surface reconstruction. The  $(1 \times 3)$  surface reconstruction observed from both of the RHEED patterns taken during cooling down indicated the reconstruction was consistent with a Sb-terminated surface. While the distinct transition from  $(1 \times 3)$  to  $(1 \times 5)$  symmetry observed from sample tmw04085 cooling process indicated that GaSb grown on annealed GaAs(001) substrate had a Sb-terminated surface with a higher concentration of antimony than the  $3 \times$  reconstruction in sample tmw04083[108]. Both of the streaky RHEED patterns observed during cooling down indicated the smooth and flat surface [109]. The surface morphology was investigated by AFM topography.



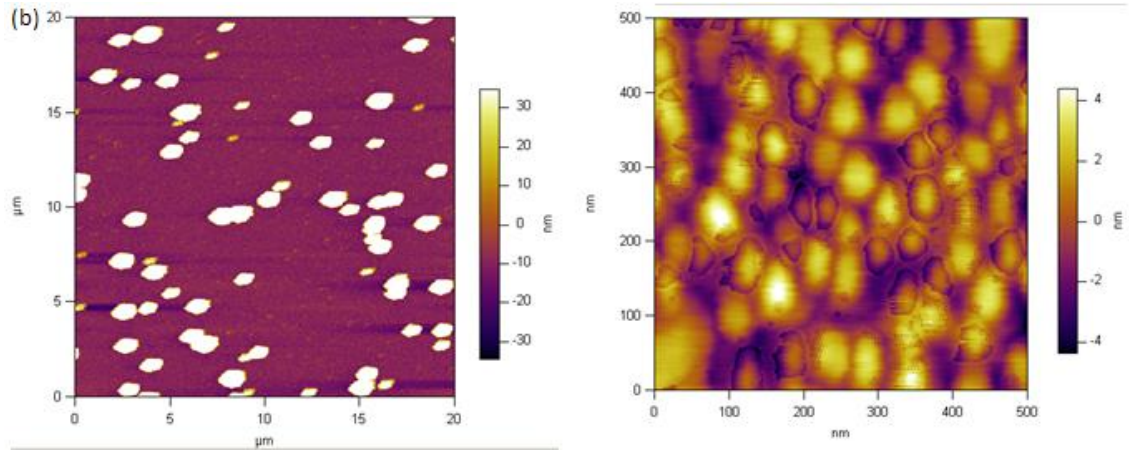


Fig 5.2 AFM images of 5ML GaSb grown on GaAs (001) (a) without annealing, (b) after annealing under Sb flux for 30 mins. The growth temperature was 500 °C and the growth rate was 0.5  $\mu\text{m/h}$ .

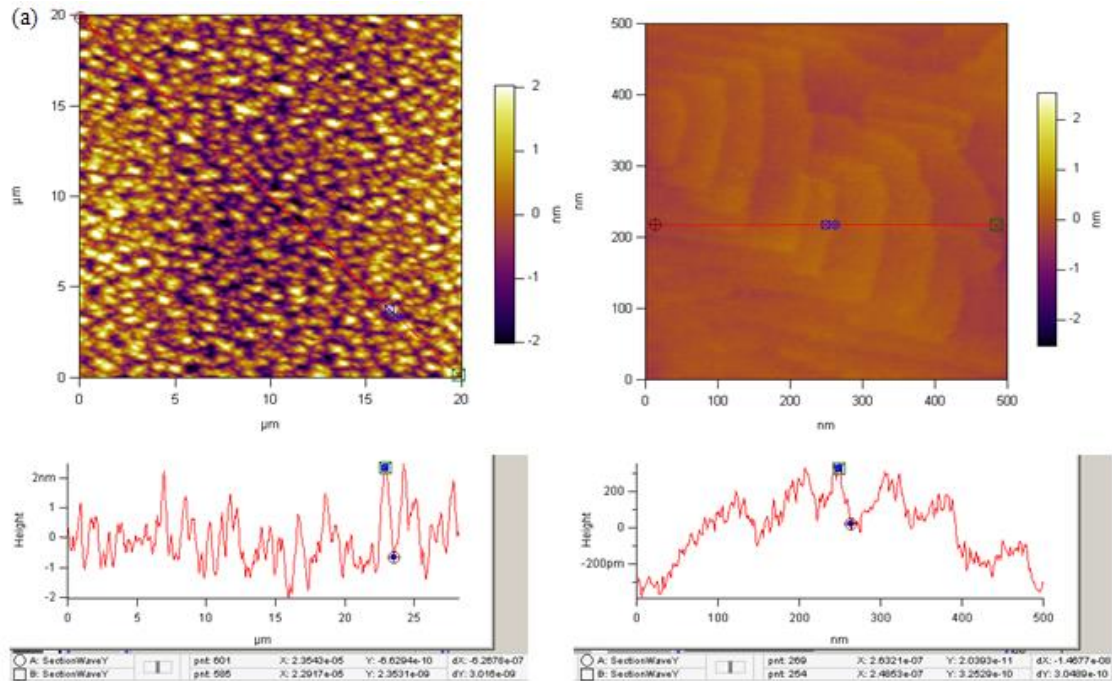
Figure 5.2 illustrated the surface morphologies of 5ML GaSb grown on GaAs (001) substrates. Several small-scaled dots are observed on the unannealed surface, as shown in figure 5.2(a). The dots are of 2 nm high with a width of  $80 \pm 10$  nm. RMS of surface roughness over the  $20 \mu\text{m} \times 20 \mu\text{m}$  area was  $\sim 2.1\text{nm}$ . Several large dots were observed on the annealed surface, as shown in figure 5.4 (b), the dot density was  $\sim 1.5 \times 10^7 \text{cm}^{-2}$  with a dots height of  $170 \pm 10$  nm and width of  $1.7 \mu\text{m}$ . RMS of surface roughness over the  $20 \mu\text{m} \times 20 \mu\text{m}$  area was  $\sim 31\text{nm}$ . Due to the  $\sim 7\%$  lattice mismatch between GaSb and GaAs, after the initial nucleating of GaSb wetting layer on GaAs, 3D island growth was expected during the further deposition of GaSb. Many 3D dots were observed on the surfaces for both unannealed and annealed sample. Based on the preceding analysis surface morphology of GaAs(001) wafer after oxide removal, the 5 nm GaSb grown on annealed GaAs substrate may have a rougher surface which was illustrated from the AFM topography in figure 5.2 (b). The comparison of the surface morphology of sample tmw04083 and tmw04085 indicated the growth of GaSb on GaAs (001) may not need the annealing process and the annealing technique after the oxide removal may cause a rougher surface for the subsequent growth of GaSb. No evidence of threading dislocation was observed on



surface of both of samples. That indicated the spiral growth has not commenced at the GaSb thickness of 5 nm.

#### 5.1.3.2 Analysis of 250 nm GaSb on GaAs (001)

To further evaluate the structural properties of GaSb/GaAs (001) and the effect of post-growth annealing on the GaSb surface, thicker GaSb layers were grown on GaAs (001) substrate. Sample tmw04101 and tmw04102 were 250nm GaSb as grown on GaAs (001) and post-growth annealing at 580 °C for 30 mins, respectively. The growth rate was 0.5um/h and the epilayer temperature was 500 °C<sub>p</sub>. After 2 mins deposition of GaSb, clear  $\times 3$  RHEED patterns were observed for the growth of both samples. And good  $\times 3$  symmetry was observed during the subsequent growth and at the end of growth for both of samples. After the growth of sample tmw04101, the substrate was cooled under a stabilising Sb beam until the temperature dropped below 400 °C. Sample tmw04102 was annealed at 580 °C for 30 mins. After growth, the surface morphology was investigated by AFM.



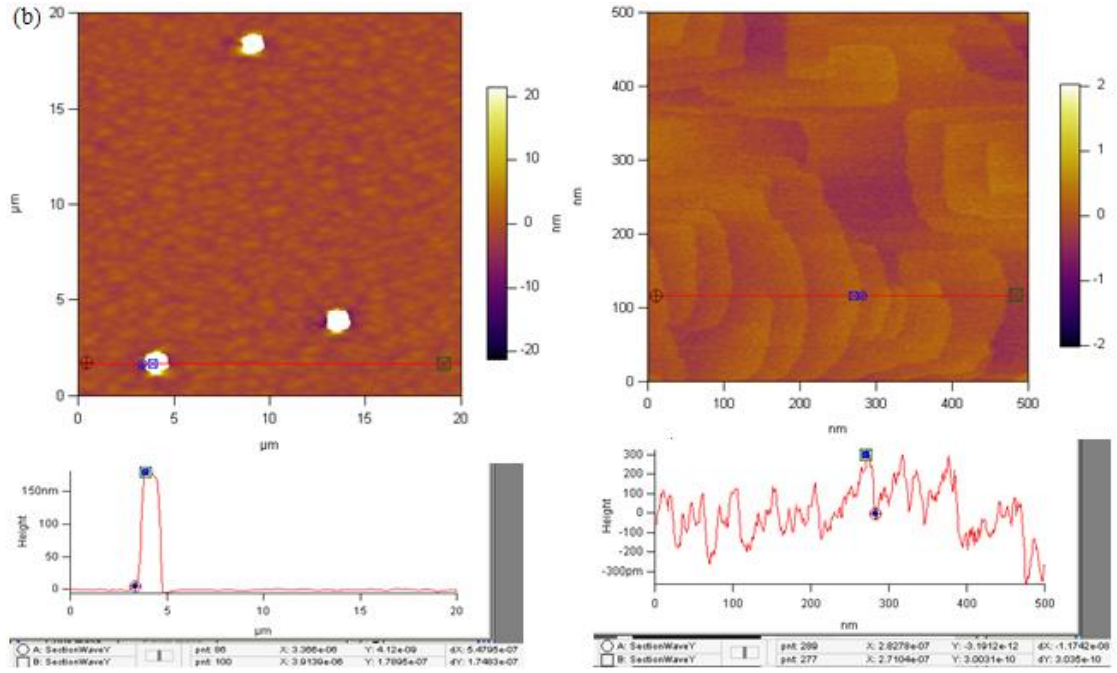


Fig. 5.3 AFM images and cross-section scan of 250 nm GaSb on GaAs(001) grown at 500 °C (a) without annealing, (b) after annealing under Sb flux at 580 °C for 30 mins. The growth temperature was 500 °C and the growth rate was 0.55  $\mu\text{m}/\text{h}$ .

Figure 5.3 (a) illustrated the surface morphologies of 250nm GaSb as-grown on GaAs (001) at 500 °C and (b) with 30 mins post-growth annealing at 580 °C. AFM images provided the direct information about the shape and size of mounds and the spiral step structures on surface. For the as-grown sample, a large number of mounds were observed on the surface from the  $20\mu\text{m} \times 20\mu\text{m}$  AFM image in figure 5.3 (a) left. The typical mound was approximately 4 nm high with a lateral width of 2  $\mu\text{m}$ . The zoom-in  $500\text{nm} \times 500\text{nm}$  AFM image figure 5.3 (a) right illustrated the spiral dislocations on the mound. Spiral steps one monolayer high were observed on the mound. RMS of surface roughness over a  $20\mu\text{m} \times 20\mu\text{m}$  and  $500\text{nm} \times 500\text{nm}$  area was  $\sim 0.83$  nm and 0.2 nm. The number density of threading dislocations was  $\sim 5.1 \times 10^8 \text{cm}^{-2}$ .

A few 3D dots were observed on the surface for annealed sample tmw04102, as shown in  $20\mu\text{m} \times 20\mu\text{m}$  AFM image figure 5.3 (b) left. The largest dot was

approximately 0.25  $\mu\text{m}$  high with width of 2  $\mu\text{m}$ . While the zoom-in of the background area manifested spiral steps with monolayer height (0.3 nm) in the 500 nm  $\times$  500 nm AFM image figure 5.5(b) right. RMS of surface roughness over a 20  $\mu\text{m}$   $\times$  20  $\mu\text{m}$  and 500 nm  $\times$  500 nm area was  $\sim 1.4$  nm and 0.2 nm, respectively. The number density of threading dislocations was about  $4.3 \times 10^8 \text{cm}^{-2}$ . The RMS of surface roughness indicated the surface diffusion length of Ga, the rougher surface of the annealed sample tmw04102 indicated the post-growth annealing resulting in the migration of Ga and Sb species onto the low energy sites such as spiral step edges. Those large 3D dots on the surface could be the Ga accumulations. The Hall measurement using Van der Pauw method was performed in a magnetic field of 0.2 T at room temperature. Both of the samples tmw04101 and tmw04102 exhibited p-type conductivity with RT Hall hole mobility of 135 and 106  $\text{cm}^2/\text{Vs}$ , respectively. The carrier concentrations measured at RT for sample tmw04101 and tmw04102 were  $0.74 \times 10^{20} \text{cm}^{-3}$  and  $1.1 \times 10^{20} \text{cm}^{-3}$ , respectively.

#### 5.1.3.3 Analysis of 500 nm GaSb on GaAs (001)

To evaluate the effect of epilayer thickness on the surface morphology and electrical property, a pair of 500 nm GaSb was grown on GaAs (001) at 500  $^{\circ}\text{C}$ . Sample tmw04104 was 500 nm as-grown GaSb on GaAs (001) and tmw04103 was 500 nm GaSb on GaAs (001) with post-growth annealing at 580  $^{\circ}\text{C}$  for 30 mins. BMI was  $1.2 \times 10^{-6}$  Torr, group V:III flux ratio was 2:1, and the nominal growth rate was 0.5  $\mu\text{m}/\text{h}$ . RHEED patterns taken during the growth of both samples manifested good  $\times 3$  symmetry. Good  $\times 5$  symmetry was observed during cooling down the substrate temperature. Both of the  $\times 3$  and  $\times 5$  symmetry were typical Sb-terminated GaSb surface reconstructions. The transition from  $\times 3$  to  $\times 5$  reconstruction indicated the surface Sb concentration was increased during the substrate temperature cooling down. The reason for that is because of the lower Sb mobility under lower temperature resulting to more accumulation of antimony. For tmw04103, the sample was post- annealing at 580  $^{\circ}\text{C}$  for 30 mins, after that the substrate was cooled down

under a stabilising antimony beam until to the temperature below 400 °C. Good  $\times 3$  streaky RHEED pattern was observed during the growth, annealing, and cooling down process. TEM and AFM were used to investigate the interface and surface morphology of samples after removed from the MBE chamber.

#### 5.1.3.3.1 TEM results

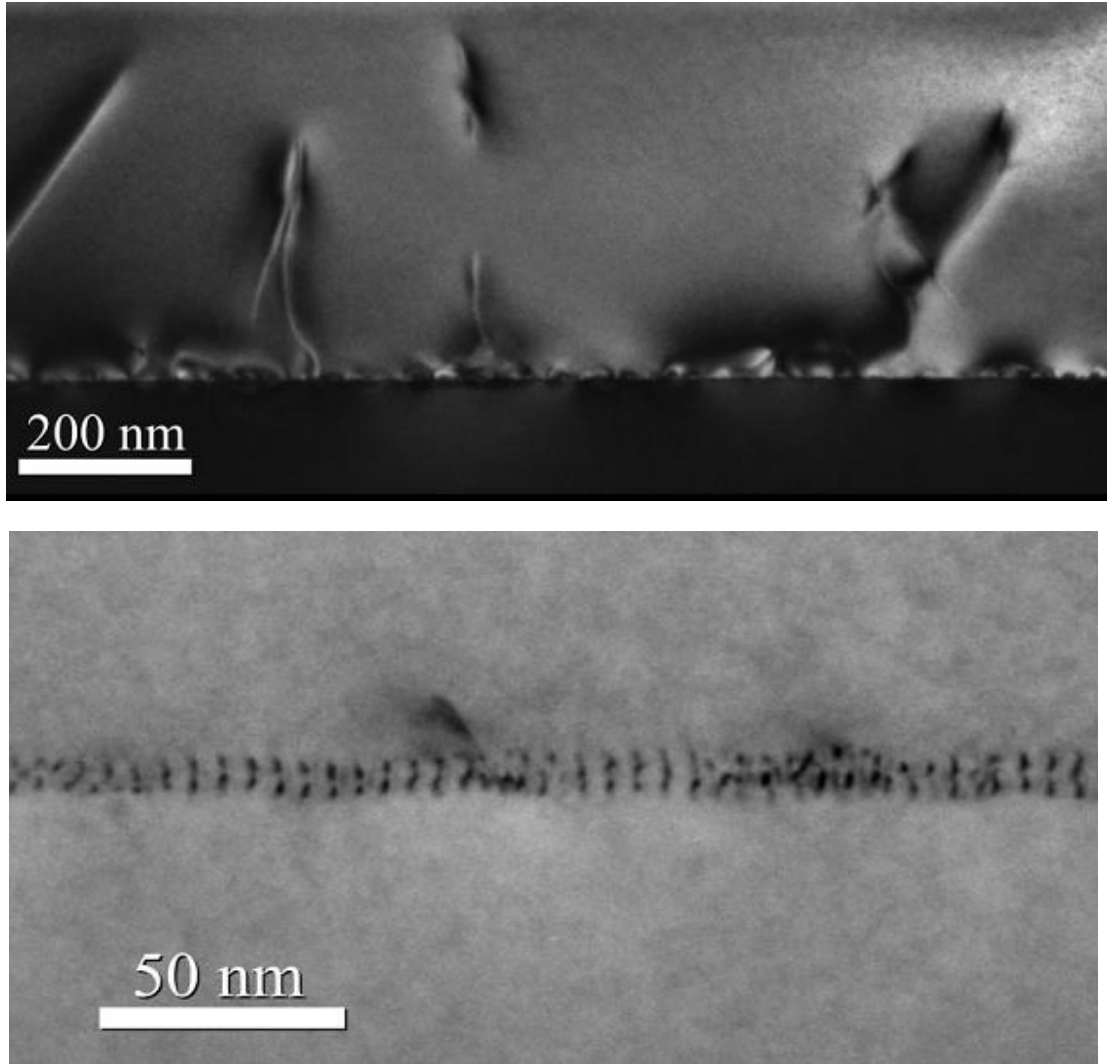


Fig.5.4. Cross-section TEM image of unannealed 500nm GaSb on GaAs showing a highly periodic array of misfit dislocations at the GaSb/GaAs interface. Images measured under bright field 220 conditions. The top (200nm-scale) image manifested that threading dislocations induced by lattice mismatch originated at the GaSb/GaAs interface and propagated through the epitaxial GaSb film. The bottom

(50nm-scale) image clearly illustrated that those threading dislocations arise from the misfit array at the interface and propagated to the GaSb epilayer.

Cross-section TEM image of the unannealed 500nm GaSb on GaAs sample clearly illustrated a highly periodic array of misfit dislocations at the GaSb/GaAs interface (figure 5.6 top), large number of threading defects arising from the misfit arrays and evidently propagating into the grown GaSb layer (figure 5.6 bottom). The higher magnification image clearly manifested that the threading defects were arising from the misfit array rather than directly from the GaSb/GaAs interface. In addition, the RHEED patterns taken from the GaAs deoxidation process involved from halo to spotty to good  $\times 3$  streaky pattern. That may suggest there was no residual oxide layer persisting between the surface of GaSb and GaAs. Further exploration of the oxide removal in interface should be conducted in electrical device such as Auger effect measurement which would not be described here. Additional Cross-section TEM image (figure 5.7) displayed a different region of the sample, and it was observed that the density of threading dislocations changed along with the changing of lateral site. This indicated that the majority of strain caused by lattice mismatch in the area of low- threading dislocation density were relieved into the beneath misfit array. And a low threading dislocations density was a crucial qualification of high quality materials. W.qian .et al investigated the nucleation of GaSb on GaAs (001) substrates, their results indicated that the threading dislocations in GaSb epilayer were originating from the  $60^\circ$  misfit defects propagated in the growing layer, as the increasing deposition of GaSb, part of islands on surface coalesced together which didn't apparently increase the population of  $60^\circ$  misfit defects, the resulting threading dislocation density kept stable as the increasing coverage of GaSb [110][67].

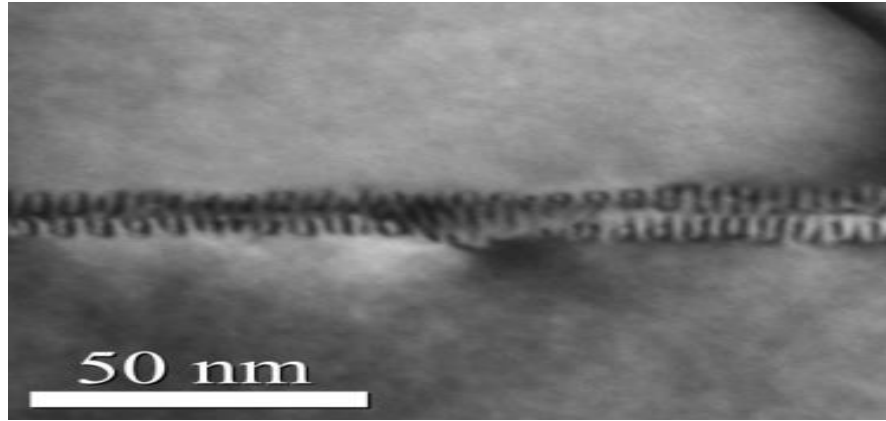


Fig.5.5 Cross-section TEM micrograph taken from different regions from the interface of the unannealed sample1 clearly show a highly periodic array of misfit dislocations at the GaSb/GaAs interface. Images were taken under bright field 220 and dark field 002 conditions.

The imaged region with rare threading dislocations suggested most of mismatch deduced strain were accommodated by the beneath misfit array and that indicated that defects may propagate through the grown film apart from a complete misfit array.

#### 5.1.3.4 Analysis of 0.5 $\mu\text{m}$ GaSb on GaAs (001) grown at 400 $^{\circ}\text{C}$

Based on the research of GaSb/GaAs by Berinder et al.[115], growth temperature and growth rate may have significant effect on the properties of spiral dislocations including size and density. To further investigate the effect of growth temperature and growth rate on the surface morphology of GaSb/GaAs (001) heterostructures, sample tmw05033 and tmw05032 were 0.5 $\mu\text{m}$  GaSb on GaAs (001) grown at 400  $^{\circ}\text{C}$  under the nominal growth rate of 1  $\mu\text{m}/\text{h}$  and 0.5  $\mu\text{m}/\text{h}$ , respectively.

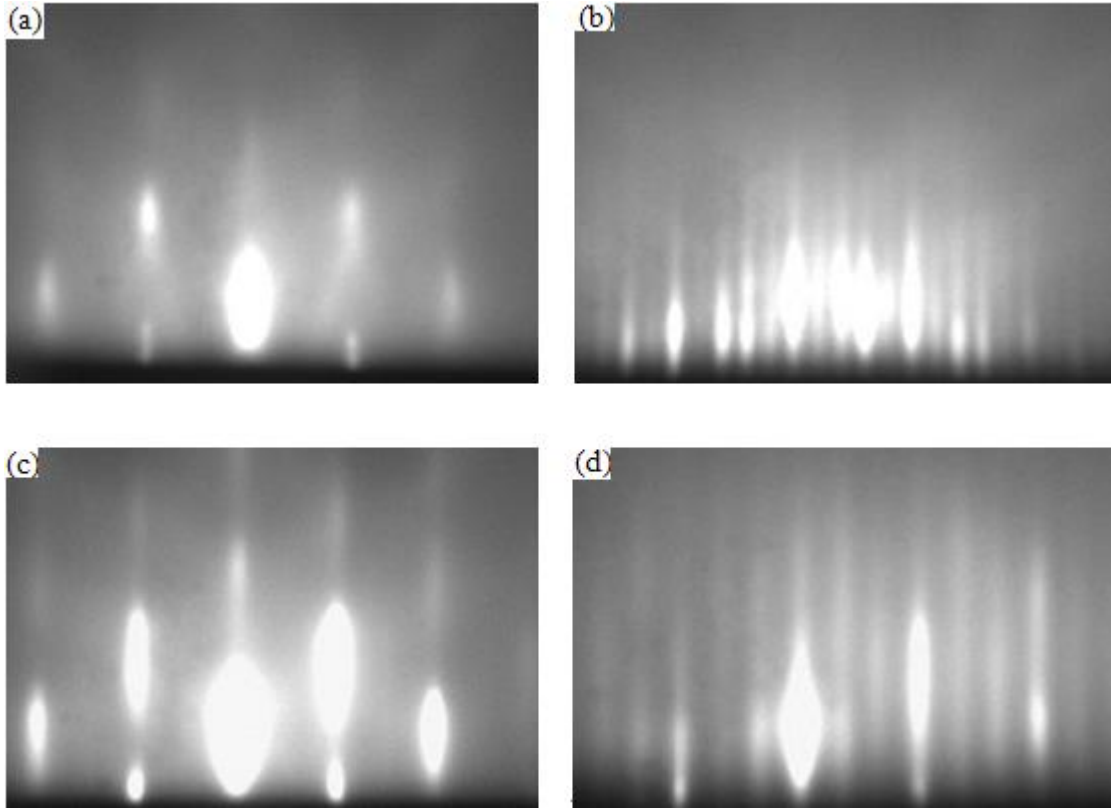


Fig.5.6 RHEED pattern(a) taken after oxide removal, (b) taken after growth of 0.5  $\mu\text{m}$  GaSb on GaAs(001) for sample tmw05033, good  $\times 5$  symmetry observed at the end of growth, (c) taken after oxide removal, (d) taken after growth of 0.5  $\mu\text{m}$  GaSb on GaAs(001) for sample tmw05032,  $\times 3$  symmetry observed at the end of growth. The growth temperature was 400  $^{\circ}\text{C}$  and the growth rate was 0.55  $\mu\text{m}/\text{h}$ .

RHEED patterns taken during the growth of 0.5  $\mu\text{m}$  GaSb on GaAs (001) at 400  $^{\circ}\text{C}$  were illustrated in figure 5.10. The good  $\times 5$  symmetry observed at the end of growth of sample tmw05033 which was produced at the growth rate of 1  $\mu\text{m}/\text{h}$  as shown in figure 5.6(b). While for sample tmw05033 deposited at the growth rate 0.5  $\mu\text{m}/\text{h}$ ,  $\times 3$  surface reconstruction was observed in figure 5.6 (d). This result indicated the higher growth rate ( $\sim 1$   $\mu\text{m}/\text{h}$ ) under the growth condition may lead to the growth of surface with higher antimony concentration. Although, both of samples exhibited Sb-terminated GaSb (001) surface reconstruction. The detailed surface morphology information was provided by AFM characterization.



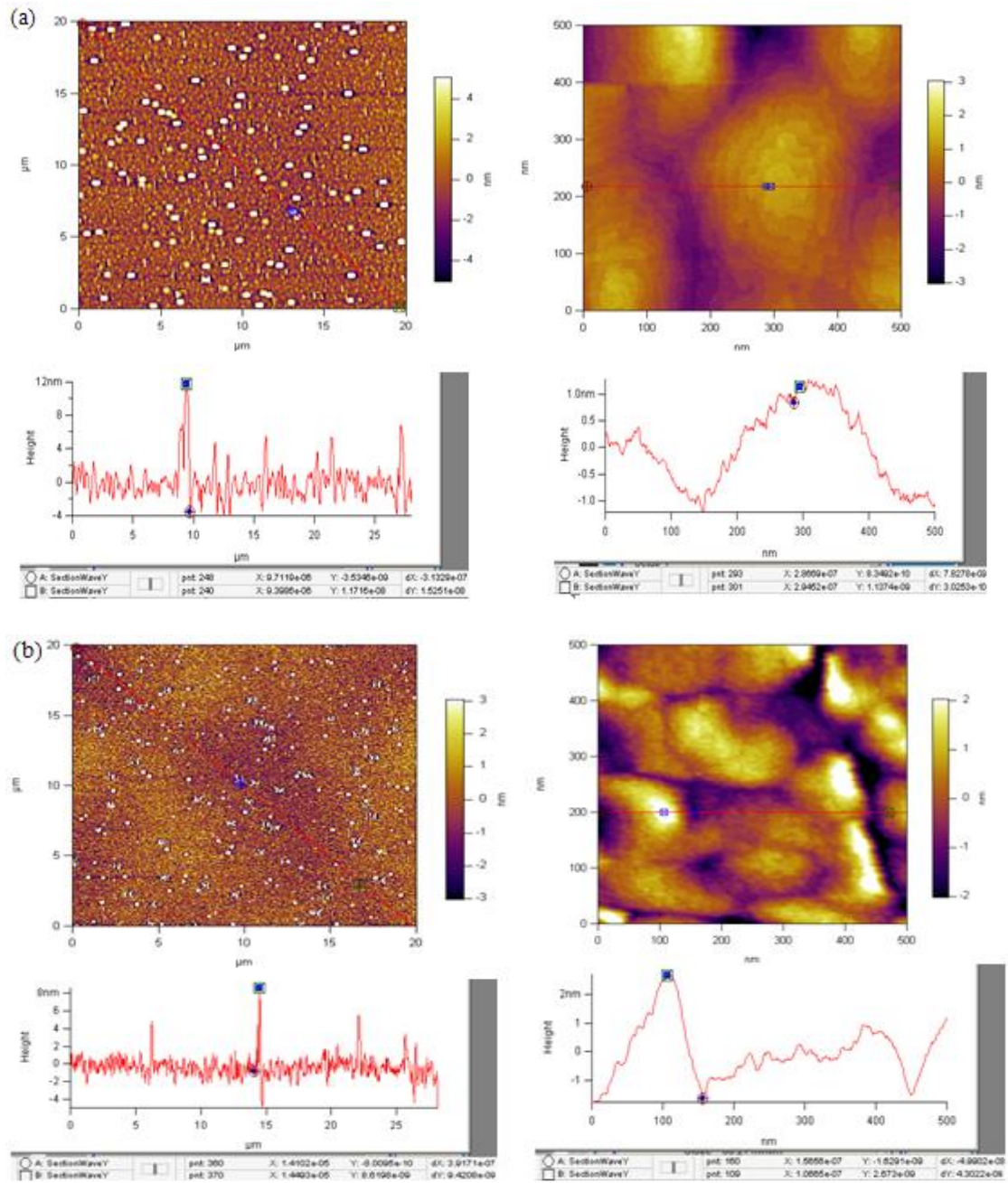


Fig.5.7 AFM images and cross-section scan of 0.5  $\mu\text{m}$  GaSb grown on GaAs (001) at 400  $^{\circ}\text{C}$  under growth rate of (a) 1  $\mu\text{m}/\text{h}$ , sample tmw05033, and (b) 0.5  $\mu\text{m}/\text{h}$ , sample tmw05032.

AFM images provided detailed information about the shape and size of mounds on the surface. The cross-section scan gave information about background morphologies. Many large 3D dots were observed on the surface from the 20  $\mu\text{m} \times 20 \mu\text{m}$  AFM image (figure 5.7 a left). Lower growth temperature may



reduce the surface diffusion length of group-III species. It was suspected these 3D dots were some of the Ga accumulations on the sites of low surface free energy such as step edges. From the zoom-in  $500\text{nm} \times 500\text{nm}$  AFM images, several mounds with spiral dislocations were observed on the surface of sample tmw05033 (figure 5.7 a right). The number density of the spiral dislocations was about  $2 \times 10^9 \text{ cm}^{-2}$  which was almost one order of magnification higher than the value of sample grown at  $500^\circ\text{C}$ . The previous research indicated that the lateral width of the terraces on the singular surface was relevant to surface roughness as well as the diffusion length of the group-III adatoms [116]. The estimated lateral width of terraces on the mounds in sample tmw05033 was  $\sim 30 \text{ nm}$ . And the RMS surface roughness over a  $20 \mu\text{m} \times 20 \mu\text{m}$  and  $500 \text{ nm} \times 500 \text{ nm}$  area was  $\sim 2 \text{ nm}$  and  $0.7 \text{ nm}$ . The Hall measurement result illustrated the sample tmw05033 exhibited p-type conductivity with room-temperature mobility of  $70 \text{ cm}^2/\text{VS}$  and a carrier concentration of  $10^{20} \text{ cm}^{-3}$ .

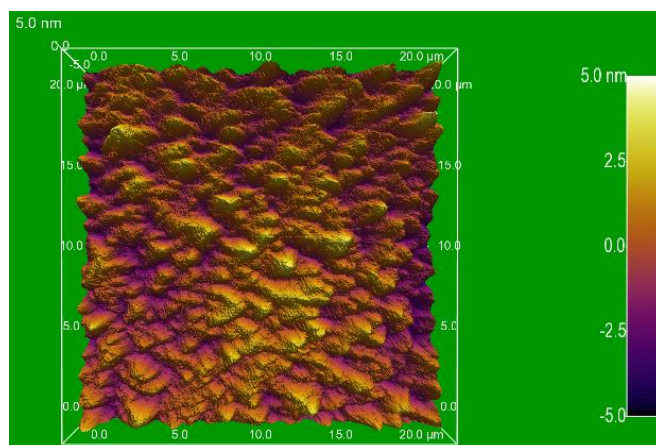
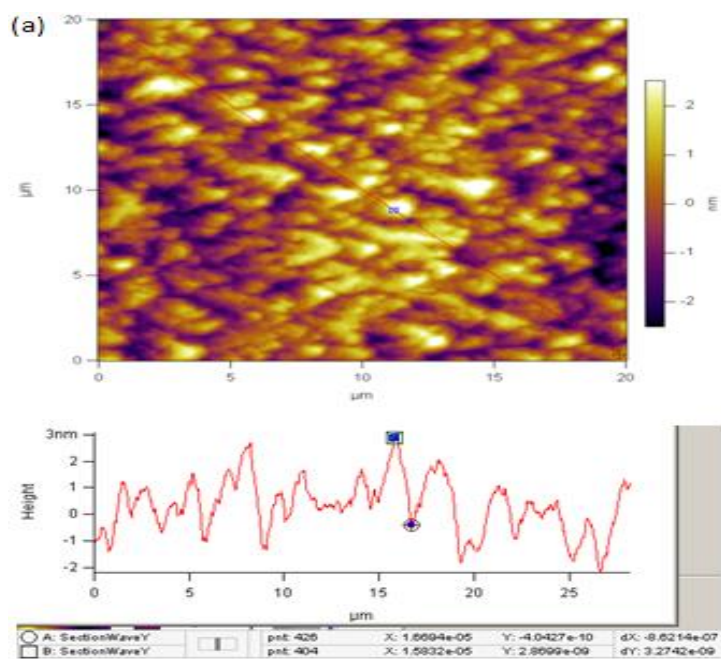
For sample tmw05032,  $0.5 \mu\text{m}$  GaSb on GaAs (001) grown at  $400^\circ\text{C}$  and the growth rate of  $0.5 \mu\text{m/h}$ , many 3D dots were observed on the surface from the  $20\mu\text{m} \times 20\mu\text{m}$  AFM image (figure 5.7 b left). From the high-resolution  $500\text{nm} \times 500\text{nm}$  AFM image (figure 5.7 b right), no evidence of spiral dislocation was observed on the mounds. The RMS surface roughness over a  $20\mu\text{m} \times 20\mu\text{m}$  and  $500\text{nm} \times 500\text{nm}$  area was  $\sim 2.2 \text{ nm}$  and  $0.7 \text{ nm}$ . The Hall measurement result indicated that the sample tmw05032 exhibited p-type conductivity with room-temperature mobility of  $52 \text{ cm}^2/\text{VS}$  and carrier concentration of  $\sim 10^{20} \text{ cm}^{-3}$ . The ultra-low mobilities and high carrier concentrations of both of samples indicated a lower growth temperature ( $400^\circ\text{C}$ ) made the deposited GaSb films exhibit poor structural and electrical performance.

In contrast to the sample grown at  $500^\circ\text{C}$ , the diffusion lengths of Ga adatoms to the step edges at lower temperature were reduced. Many 3D dots were formed on the surface of sample grown at lower temperature. These 3D dots were suspected to be Ga accumulations on the surface of sample grown at lower temperature which was

undesirable to the substrate performance. A large number of mounds were observed on the surface of both samples. No evidence of spiral dislocations was observed on the surface of sample tmw05032. This result was different from the study of 1  $\mu\text{m}$  GaSb grown on GaAs with a insertion of AlSb buffer layer by Berinder et al. [117]. Although the screw dislocations were present on the GaSb/GaAs interface which was demonstrated by the TEM images, this was not a sufficient condition to maintain the spiral growth. To maintain the spiral growth mode, the Ga adatoms must have sufficient surface diffusion length. In consequence, for the purpose of maintaining a 2D layer by layer growth, the growth should be conducted at an appropriate growth rate as well as other growth parameters. Experiments in this section investigated the effect of growth temperature on the structural and electrical properties of GaSb/GaAs heterostructure, the optimal growth conditions in this study was at the temperature of 500  $^{\circ}\text{C}$  and growth rate of 0.5  $\mu\text{m}/\text{h}$ .

#### 5.1.3.5 Analysis of 1 $\mu\text{m}$ GaSb on GaAs (001)

To further study the dependence of Gasb epilayer thickness on the surface morphology and electrical properties of GaSb/GaAs heterostructure. Sample tmw05057, 1  $\mu\text{m}$  GaSb was deposited directly on GaAs (001) substrate at 500  $^{\circ}\text{C}$  with a nominal growth rate of 0.5  $\mu\text{m}/\text{h}$  in the GEN II MBE apparatus. The sample surface morphology was investigated by AFM and the electrical properties are evaluated by Hall measurement performed in the magnetic field of 0.2 T. The experimentally obtained results were compared with the Berinder et al.'s research for GaSb/GaAs heterostructures [117].



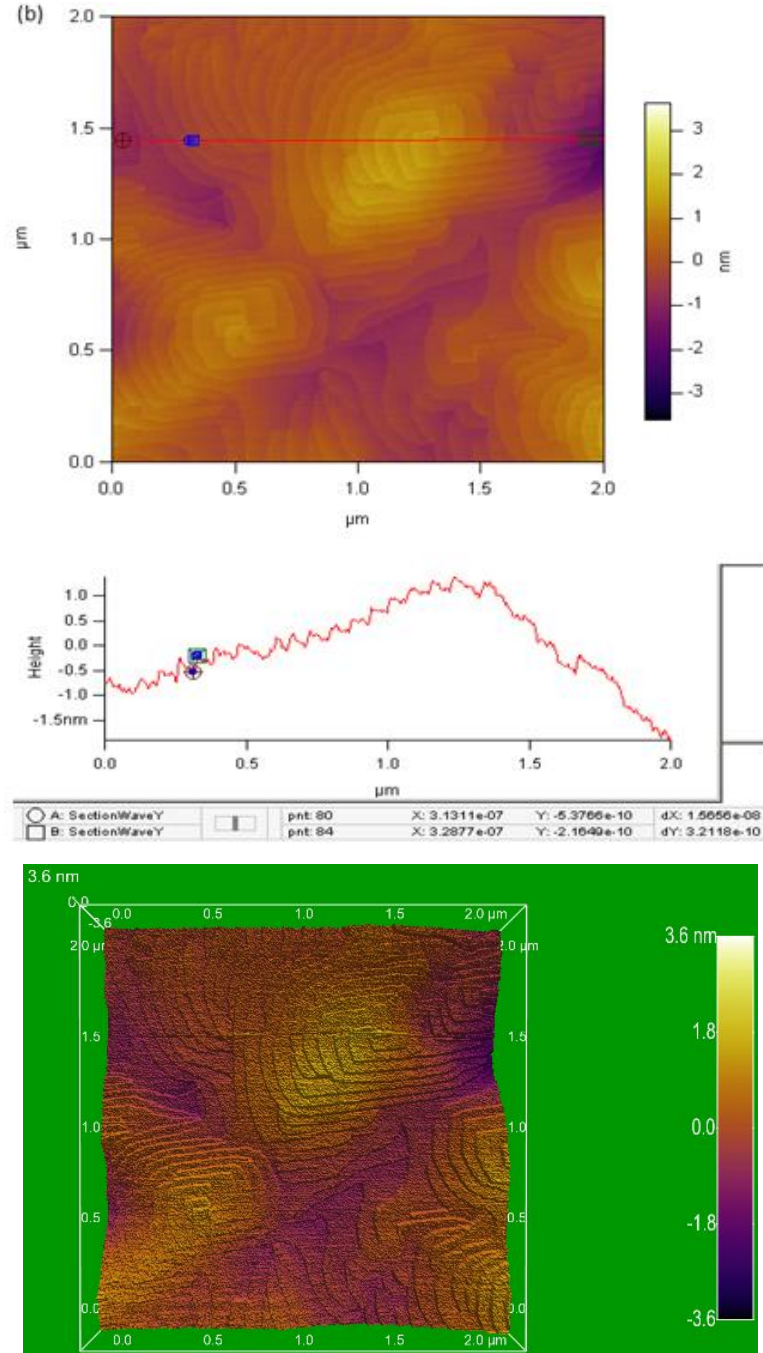


Fig. 5.8 (a)  $20\mu\text{m} \times 20\mu\text{m}$  AFM image (top), cross-section scan (middle ) and 3D-rendering (bottom) (b)  $2\mu\text{m} \times 2\mu\text{m}$  AFM image (top), cross-section scan (middle ) and 3D-rendering (bottom) of 1  $\mu\text{m}$  GaSb on GaAs(001) grown at 500  $^{\circ}\text{C}$  with a nominal growth rate of  $0.5\mu\text{m}/\text{h}$ .

A large number of mounds were observed on the surface from the  $20\mu\text{m} \times 20\mu\text{m}$  AFM image (figure 5.8 a top). The typical mound size was approximately 3.5 nm high with lateral width of  $1.7\mu\text{m}$ . From the  $2\mu\text{m} \times 2\mu\text{m}$  AFM image (figure 5.8 b

top), the spiral dislocations with monolayer-height steps were visible on the mounds and the lateral width between the spiral steps was approximately 40 nm. The 3D renderings in figure 5.8 (a) and (b) bottom illustrated the special morphology of the mounds and the spiral dislocations on the mounds. RMS of surface roughness over  $20\mu\text{m} \times 20\mu\text{m}$  and  $500\text{nm} \times 500\text{nm}$  area was about 1 nm and 0.2 nm, respectively. The number density of threading dislocations was approximately  $1.64 \times 10^8 \text{ cm}^{-2}$  which was half of the value obtained from the sample tmw04014 with GaSb thickness of 500 nm. This figure was comparable to the result obtained by Kyutt et al. [118] Who studied herteroepitaxial of GaSb on GaAs with a initial nucleation of  $10^{10} \text{ cm}^{-2}$  screw dislocations on the GaSb/GaAs interface and after growth of 1  $\mu\text{m}$  GaSb the density of threading dislocation decreased to  $\sim 10^8 \text{ cm}^{-2}$ . The result obtained in this thesis indicated the thickness of GaSb epilayer had a significant impact on the threading dislocation density on surface. The Hall measurement showed the sample exhibited p-type conductivity with room-temperature carrier concentration and mobility at the value of  $3.2 \times 10^{17} \text{ cm}^{-3}$  and  $605 \text{ cm}^2/\text{VS}$ , respectively.

#### 5.1.3.6 Analysis the dependence of the structural and electrical properties of samples on growth temperature

Table 5.1 A summary of growth parameters of samples.

Sample	Growth temperature (°C)	Growth rate (um/h)	Annealing	GaSb thickness (nm)
tmw05033	400	1.0	N	500
tmw05032	400	0.5	N	500
tmw04101	500	0.5	N	250
tmw04102	500	0.5	Y	250
tmw04104	500	0.5	N	500
tmw04103	500	0.5	Y	500
tmw05057	500	0.5	N	1000

Table 5.2 Experimental results of RMS surface roughness, number density of threading dislocation, and mobility.

Sample	RMS over 20 $\mu\text{m} \times 20 \mu\text{m}$ (nm)	Density of threading dislocations ( $10^8 \text{ cm}^{-2}$ )	Hall mobility ( $\text{cm}^2\text{V}^{-1}\text{S}^{-1}$ )
tmw05033	2	20	190
tmw05032	2.2	/	202
tmw04101	0.83	5.1	360
tmw04102	14	4.3	105
tmw04104	1.1	2.3	490
tmw04103	1	3.2	405
tmw05057	1	1.64	605

Sample tmw05032 and tmw04104 were grown under the growth conditions except the growth temperature. To evaluate the effect of growth temperature on the surface roughness and electrical property of sample, figure 5.13 below illustrated the dependence of RMS surface morphology and mobility on the growth temperature.

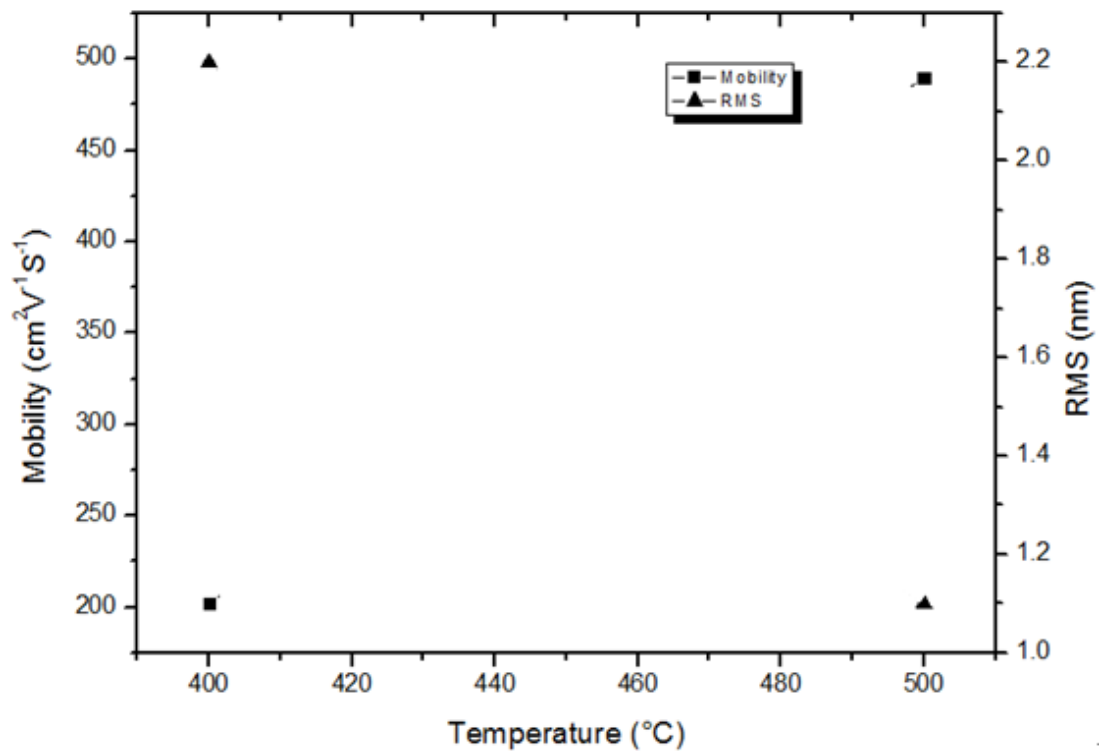


Fig.5.9 The dependence of RMS surface roughness over  $20\mu\text{m} \times 20\mu\text{m}$  area and carrier mobility on the GaSb epilayer thickness.

The results in figure indicated the sample tmw04104 grown at 500 °C exhibited higher mobility at room temperature with a smoother surface than that sample

tmw05032 grown at 400 °C. In that case, the optimal growth temperature in heteroepitaxial GaSb/GaAs (001) in this study was 500 °C. For samples grown at 500 °C, the effects of post-growth annealing technique, growth rate, and GaSb epilayer thickness on the surface morphology and electrical properties were also investigated. Compared with the experimental results of as-grown samples and post-growth annealed samples, the results indicated post-growth annealing technique may result in a large number of 3D Ga accumulations on the surface which resulted in a rougher surface. The mobilities of the as-growth samples tmw04101 and tmw04104 were higher than the corresponding post-growth annealed samples tmw04102 and tmw04103. The surface roughness manifested the surface diffusion length of gallium. The surface diffusion length was given by  $\lambda = \sqrt{2D/r}$ , where D is the coefficient of surface diffusion and r was growth rate. Selection of the appropriate growth rate was decisive to the surface morphology of the growth sample. When the growth rate was too low, the surface diffusion of group III species was long and the group III adatoms may have enough time to immigrate to the place with minimum free energy. All the defects induced by the lattice mismatch strain were those positions with low free energy and some big mounds may be formed by the accumulation of group-III species. Otherwise, if the growth rate was too high, all the surface species would have low mobility and the adatoms would accumulate again on the surface to form mounds in advance of finding the appropriated lattice sites [118]. The sample grown at the growth rate of 0.5  $\mu\text{m/h}$  had a smoother surface and higher mobility than those grown at the growth rate of 1  $\mu\text{m/h}$ . For the purpose of growth of sample with low number density of threading dislocations and high mobility, samples tmw04101, tmw04104, and tmw05057 were 250 nm, 500nm, and 1  $\mu\text{m}$  GaSb grown on GaAs(001) at temperature of 500 °C and growth rate of 0.5  $\mu\text{m/h}$ . The dependence of RMS surface roughness, density of dislocations, and mobility (RT) on epilayer thickness has been plotted in figure 5.10.

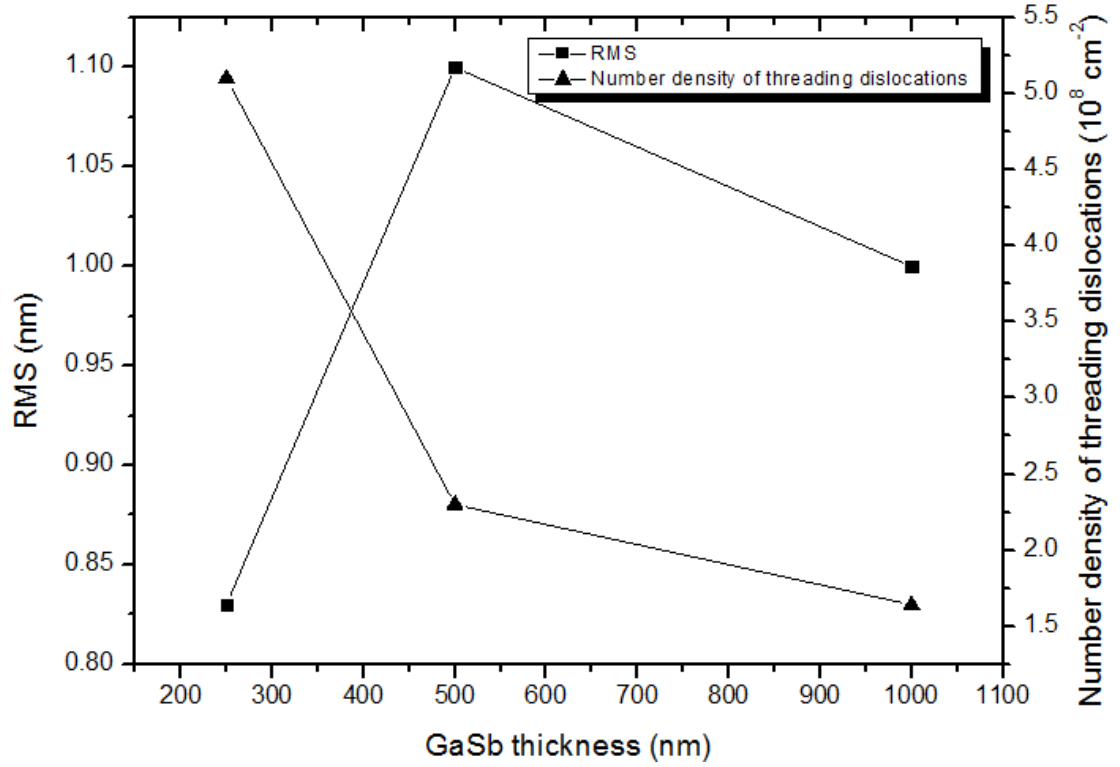


Fig.5.10 The dependence of RMS surface roughness over  $20\mu\text{m} \times 20\mu\text{m}$  area and number density of threading dislocations on the GaSb epilayer thickness. The full lines join the data for an eye guide.

The RMS surface roughness over  $20\mu\text{m} \times 20\mu\text{m}$  area and number density of threading dislocations of sample as a function of GaSb epilayer thickness were shown in figure 5.10. The number density of threading dislocation decreased as increasing epilayer thickness. The minimum density of threading dislocations was obtained at sample with 1  $\mu\text{m}$  GaSb at value of  $1.64 \times 10^8 \text{ cm}^{-2}$ .



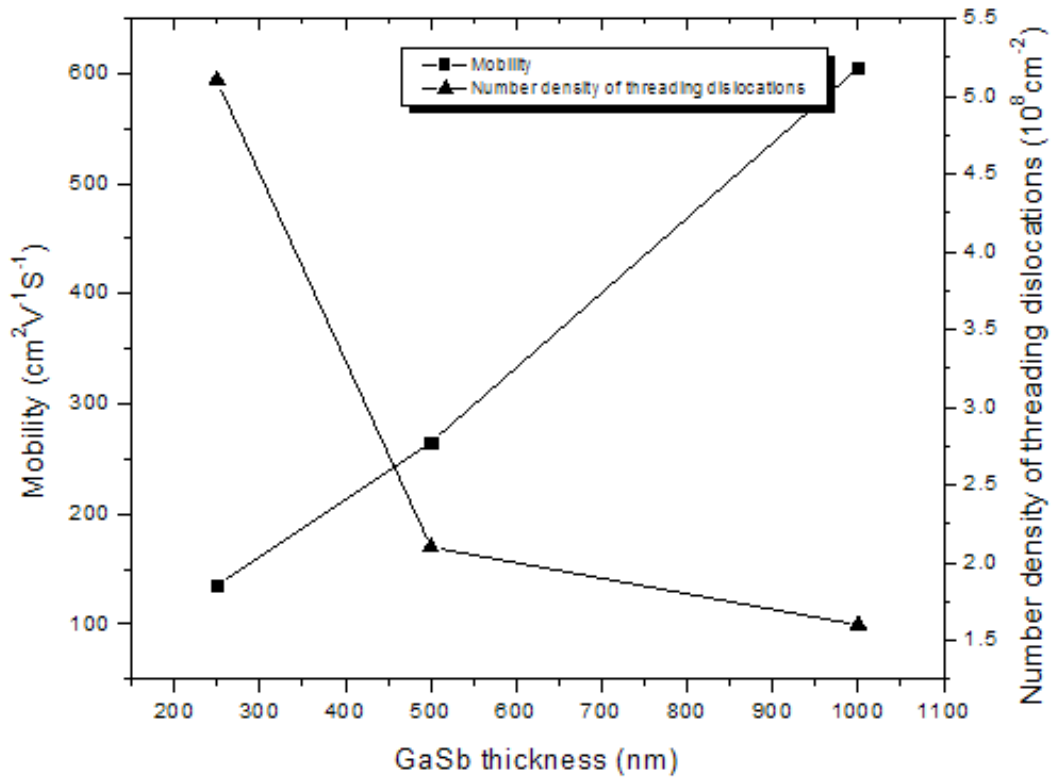


Fig.5.11 The dependence of RT mobility and number density of threading dislocations on the GaSb epilayer thickness for samples deposition at the optimum growth condition, 500 °C and 0.5  $\mu\text{m/h}$ . The full lines join the data for an eye guide. Figure 5.15 also illustrated the relationship between mobility and GaSb epilayer thickness. The mobility increased as the epilayer thickness rised from 250 nm to 1  $\mu\text{m}$ . The sample grown at 500 °C with a GaSb thickness of 1  $\mu\text{m}$  exhibited the highest mobility. The high mobility obtained in this study was  $605\text{cm}^2\text{V}^{-1}\text{S}^{-1}$  which was comparable to the result obtained by ZONG et al. [119]. All of the samples exhibited p-type conductivity, which was consistent with the result of Anayama et al [113]. It was observed that the number of threading dislocations on surface was largely dependent on the GaSb coverage, the number density of apparent threading dislocations decreased with increasing GaSb thickness. When the GaSb thickness was  $\sim 1\text{ }\mu\text{m}$ , the number density of threading dislocations dropped to  $\sim 10^8\text{ cm}^{-2}$ . The mobility increased as the number density of threading dislocations decreased as shown in figure 5.15. As for other GaSb/GaAs (001) samples grown at lower

temperature and higher growth rate, the surface roughness and mobility were much poorer than those grown at 500 °C and 0.5 μm/h. It was evident that the threading dislocations on the surface played an important role in determining the electrical performance of the GaSb/GaAs heterostructures. The research in this study was just the primary investigation the growth of GaSb/GaAs and quantitatively analyzed the dependence of structural and electrical properties on the growth conditions and GaSb coverage. It was more than important to exploit the growth methods to heteroepitaxial the GaSb/GaAs system with low number density of dislocations at interface. The interfacial misfit (IMF) method founded by SH Huang et al. suggested a promising growth mode to fabricate the GaSb/GaAs heterostructures with low interface-originated dislocation [120]. Besides imposing the particular technique onto the interface, another important factor to affect the properties of GaSb/GaAs heterostructure was the choice buffer layers. GaSb and AlSb were almost lattice-matched 6.1 Å family compound semiconductors. Due to the interesting optical and electrical properties GaSb/AlSb superlattice has attracted intensive research of devices such as infrared detectors, resonant tunneling devices, and field-effect transistors [121-123].

#### 5.1.3.7 Analysis GaSb/GaAs with an insertion of AlSb buffer

Using AlSb as a buffer layer to accommodate the lattice mismatch between GaSb and GaAs was not new, the research by Zhou. et al. [120] indicated the optimized thickness and growth temperature of AlSb layers grown on GaAs was around 2.1 nm and 450 °C, respectively.

However, the optimized growth temperature of AlSb was > 450 °C, low AlSb growth temperatures may degrade the crystal quality of AlSb buffer, consequently worsen the epitaxial layers quality. In the section below, 0.1 μm GaSb was grown on GaAs (001) substrate with an insertion of AlSb buffer layer grown at an optimum temperature of 550 °C. In order to investigate the effect of AlSb buffer thickness on

the surface morphology and electrical properties of GaSb layers, sample tmw05079, tmw05081, tmw05080 and tm05075 were 0.1  $\mu\text{m}$  GaSb with different 10 nm, 50 nm, 0.1  $\mu\text{m}$ , and 0.5  $\mu\text{m}$  AlSb buffer layer on GaAs (001) substrate, respectively. AFM was utilized to investigate the effect of buffer layer on the surface morphology of GaSb. Based on the previous study, four samples were grown in our GEN II MBE chambers. The epilayer growth temperature was 550  $^{\circ}\text{C}$ , the nominal growth rate was 1  $\mu\text{m}/\text{h}$  during both of the buffer layer and epilayer growth, BMI was  $\sim 2.2 \times 10^{-6}$  Torr, and the group V:III flux ratio was 2:1. In-situ RHEED was used to monitor the growth process and the surface reconstructions of samples.

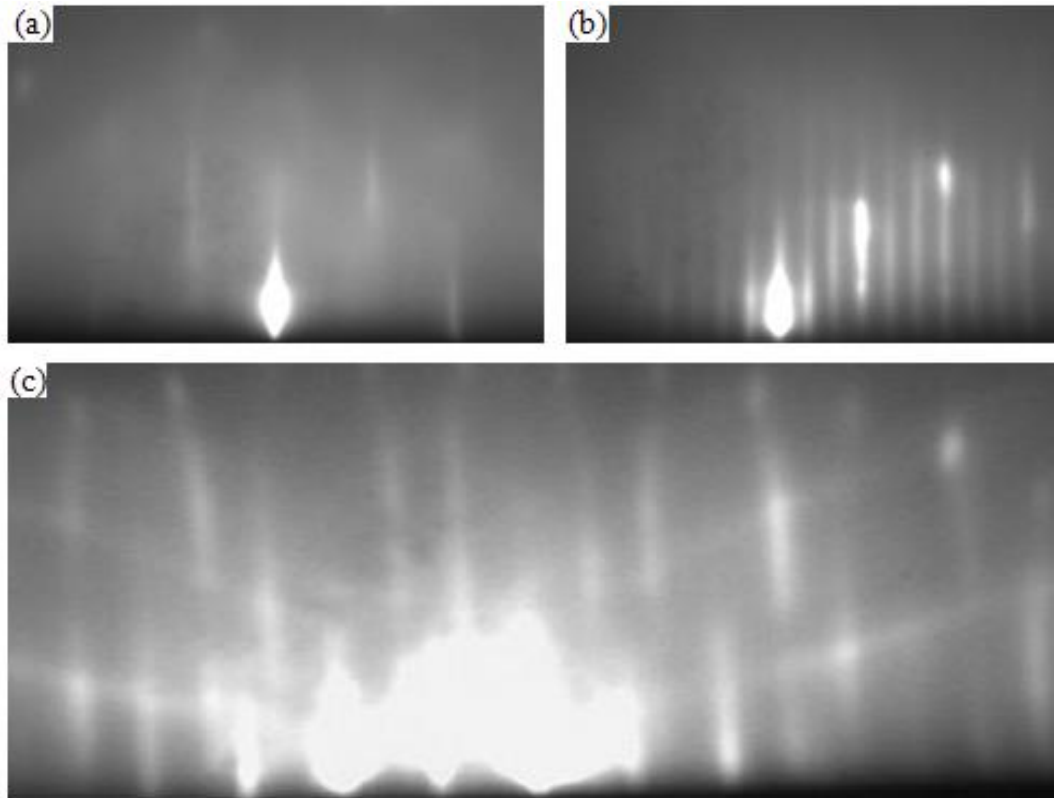
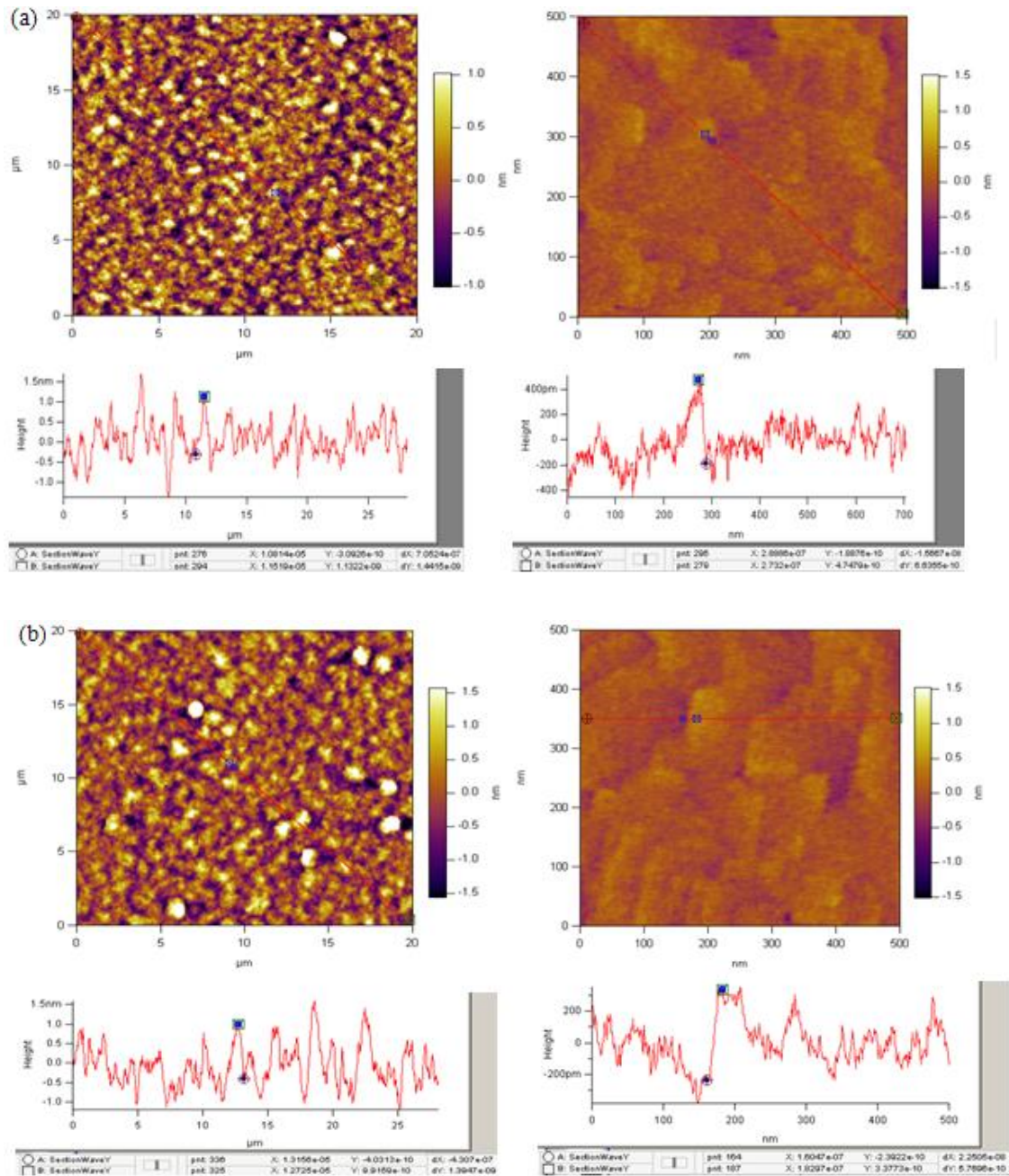


Fig. 5.12 RHEED pattern (a) taken at the initial GaAs surface prior to AlSb deposition, a elongated spotty pattern indicted a rough surface after the removal of oxide, in the [110] azimuthal, (b) taken after 14 -s AlSb deposition, good x3 symmetry streaky pattern indicated a smooth surface at that moment in the [110] azimuthal, (c) taken at the end of GaSb epilayer growth, a mixed 4 x 4 and x 3 surface reconstruction was observed at 305  $^{\circ}$ , in the [110] azimuthal.

RHEED pattern (a) taken after the removal of oxide indicates a rough surface, as the deposition proceeded, Good  $\times 3$  symmetry RHEED pattern was observed in figure 5.16(b) taken after 14 s AlSb buffer deposition, 2D planar growth was expected. At the end of GaSb epilayer growth, a mixed  $4 \times 4$  and  $\times 3$  symmetry was observed in figure 5.16(c). This observation indicated the GaSb surface may exist both  $\times 4$  and  $\times 3$  surface reconstructions. AFM images below provided the direct information of surface morphology to the grower.



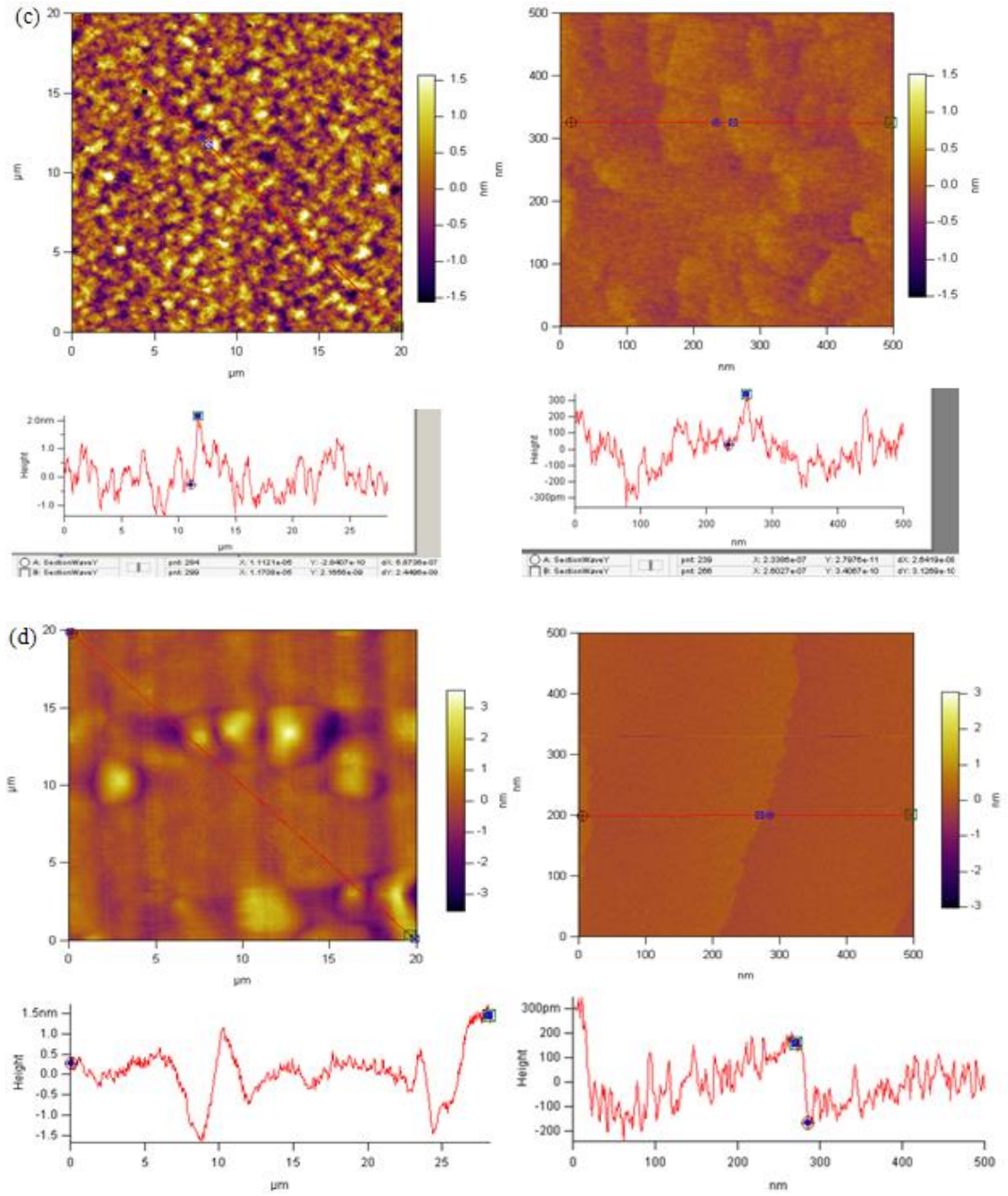


Fig.5.13 AFM images and cross-section scan of 0.1  $\mu\text{m}$  GaSb on GaAs(001) with (a) 10 nm (tmw05079), (b) 50 nm (tmw05081), (c) 0.1  $\mu\text{m}$  (tmw05080) and (d) 0.5  $\mu\text{m}$  (tmw05075) AlSb buffer layer grown at 550  $^{\circ}\text{C}$  with a nominal growth rate of 1  $\mu\text{m}/\text{h}$ .

A large number of mounds were observed from the 20  $\mu\text{m} \times 20 \mu\text{m}$  AFM images for sample tmw05079, tmw05081, and tmw05080 as shown in figure 5.17. The

typical size of the mounds on sample tmw05079, tmw05081, and tmw05080 was ~ 1.5 nm high with a lateral width of 1.4  $\mu\text{m}$ , 2 nm high with a lateral width of 1.8  $\mu\text{m}$ , and 2.5 nm high with a lateral width of 2  $\mu\text{m}$ , respectively. Few mounds were observed on the sample tmw05075 with a 0.5 $\mu\text{m}$  buffer layer. Spiral dislocations were visible on the mounds for sample tmw05079 and tmw05081. In addition, many concentric circles were observed on surface of sample tmw05080 and tmw05075. RMS surface roughness over 20 $\mu\text{m} \times 20\mu\text{m}$  area for sample tmw05079, tmw05081, tmw05080, and tmw05075 was 0.67 nm, 0.55 nm, 0.53 nm and 0.45 nm, respectively. The number density of threading dislocations / concentric rings for sample tmw05079, tmw05081, tmw05080, and tmw05075 was  $3.5 \times 10^8/\text{cm}^2$ ,  $3 \times 10^8/\text{cm}^2$ ,  $2 \times 10^8/\text{cm}^2$ , and  $5 \times 10^6/\text{cm}^2$ . It was possible that thicker buffer layer accommodated the lattice mismatch strain between GaAs and AlSb and made the GaSb surface smoother. The Hall measurement results illustrated that sample tmw05079, tmw05081, tmw05080, and tmw05075 exhibited p-type conductivity with room-temperature mobility of 385, 456, 551 and 724  $\text{cm}^2\text{V}^{-1}\text{S}^{-1}$ , respectively. For the simplicity in calculation, both of the threading dislocations and concentric rings were cited as threading dislocations.

Table 5.3 A summary of sample parameter and experimental results.

Sample	AlSb buffer thickness (nm)	RMS (nm)	Density of threading dislocations ( $10^8 \text{ cm}^{-2}$ )	Mobility ( $\text{cm}^2\text{V}^{-1}\text{S}^{-1}$ )
tmw05079	10	0.67	3.5	385
tmw05081	50	0.55	3	456
tmw05080	100	0.53	2	551
tmw05075	500	0.45	0.05	724

Table 5.3 displayed a summary of experimental results of samples with different AlSb buffer.



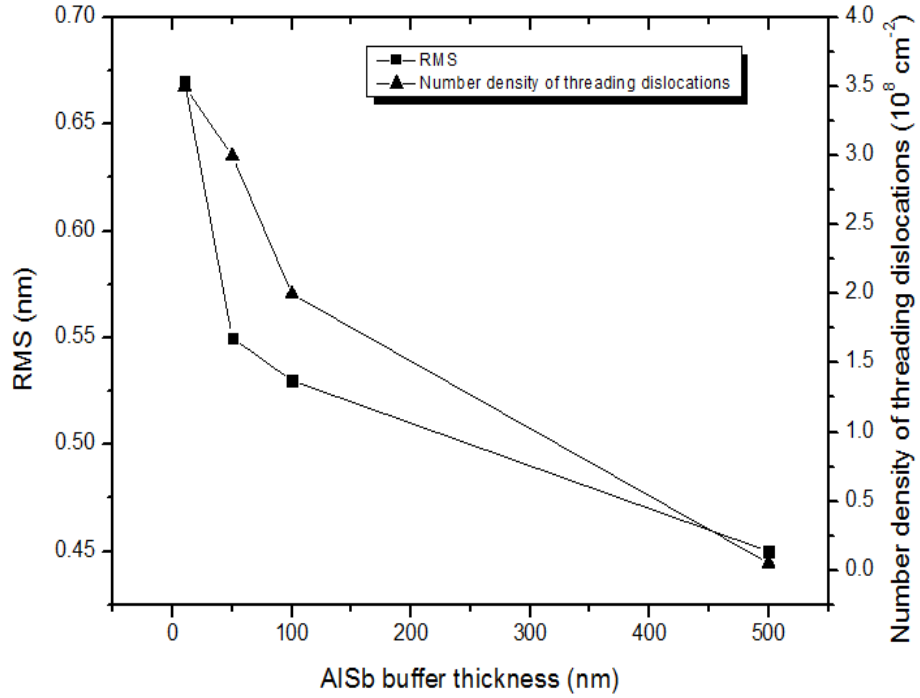


Fig.5.14 The dependence of RMS surface roughness over  $20 \mu\text{m} \times 20 \mu\text{m}$  area and number density of threading dislocations on the AlSb buffer layer thickness. The full lines join the data for an eye guide.

The RMS surface roughness over a  $20 \mu\text{m} \times 20 \mu\text{m}$  area and the number density of threading dislocations as a function of AlSb buffer layer thickness were shown in figure 5.18. Both of the RMS surface roughness and the number density of threading dislocations/ concentric rings decreased with increasing AlSb buffer layer thickness. The minimum RMS surface roughness over  $20 \mu\text{m} \times 20 \mu\text{m}$  area and number density of concentric rings were obtained on sample with 500 nm AlSb buffer at the value of 0.45 nm and  $5 \times 10^6/\text{cm}^2$ . This result indicated the AlSb buffer layer largely accommodated the lattice mismatch between GaSb and GaAs. The surface roughness and number of threading dislocations were dependent on the AlSb buffer thickness. Thicker AlSb made a smoother surface with a lower number density of threading dislocations. In particular, no evidence of spiral growth was observed on the GaSb surface with an insertion of AlSb buffer thicker than  $0.1 \mu\text{m}$ .

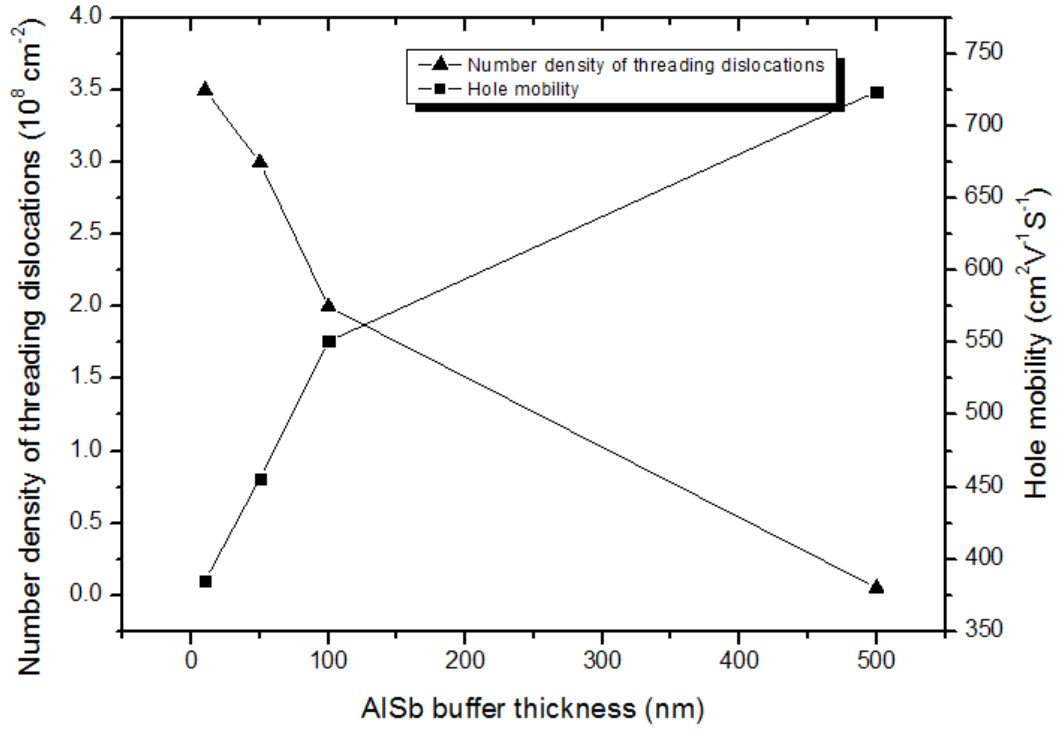


Fig.5.15 The dependence of number density of threading dislocations and mobility (RT) on the AlSb buffer layer thickness. The full lines join the data for an eye guide. Figure 5.19 also illustrated the relation between mobility and the AlSb buffer layer thickness. The mobility increased as the AlSb buffer thickness rised from 10 nm to 500 nm. The sample grown at 550 °C with an AlSb buffer thickness of 500 nm exhibited the highest mobility. The hole mobility at RT obtained in this study was  $724 \text{ cm}^2 \text{ V}^{-1} \text{ S}^{-1}$  which was slightly higher than the value obtained by ZONG et al, they measured the undoped GaSb/AlSb/GaAs was p-type with hole mobility of  $664 \text{ cm}^2 \text{ V}^{-1} \text{ S}^{-1}$  [119].

#### 5.1.4 Analysis the deposition of $\text{Al}_{1-x}\text{Ga}_x\text{Sb}$ on GaAs

In order to overcome the 7% lattice mismatch between GaSb and GaAs, compositionally graded buffer layers have always been utilized. The previous research by Tsang, W.T., et al[121]. manefisted  $\text{Al}_{1-x}\text{Ga}_x\text{Sb}$  with x less than 0.1 had a similar carrier concentration and RT PL intensity to bulk GaSb substrate. In particular, the  $\text{Al}_{0.2}\text{Ga}_{0.8}\text{Sb}/\text{GaSb}$  heterostructure acted as the active region in laser devices operating at wavelength of  $1.78 \text{ } \mu\text{m}$ .



Sample tmw05076 and tmw05076, 0.5 $\mu$ m Al<sub>1-x</sub>Ga<sub>x</sub>Sb with x =0.2 and 0.1 were grown on GaAs (001) substrate. Both shiny mirror-reflecting surfaces were observed after the deposition of 0.5  $\mu$ m Al<sub>1-x</sub>Ga<sub>x</sub>Sb with x=0.2 and x=0.1 buffer layer on GaAs (001) substrate.

The surface morphologies of sample tmw05076 and tmw05076 were investigated by AFM.

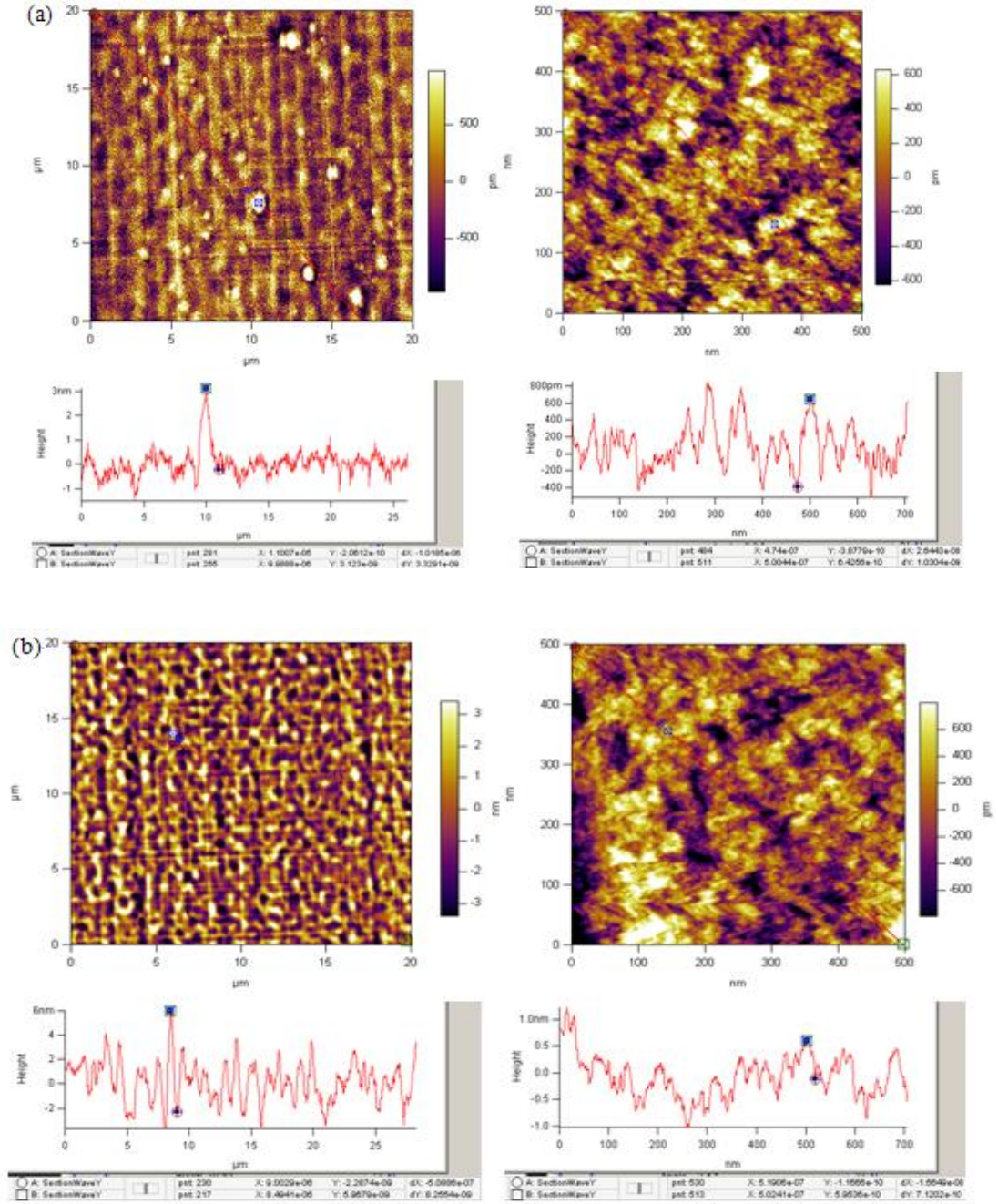
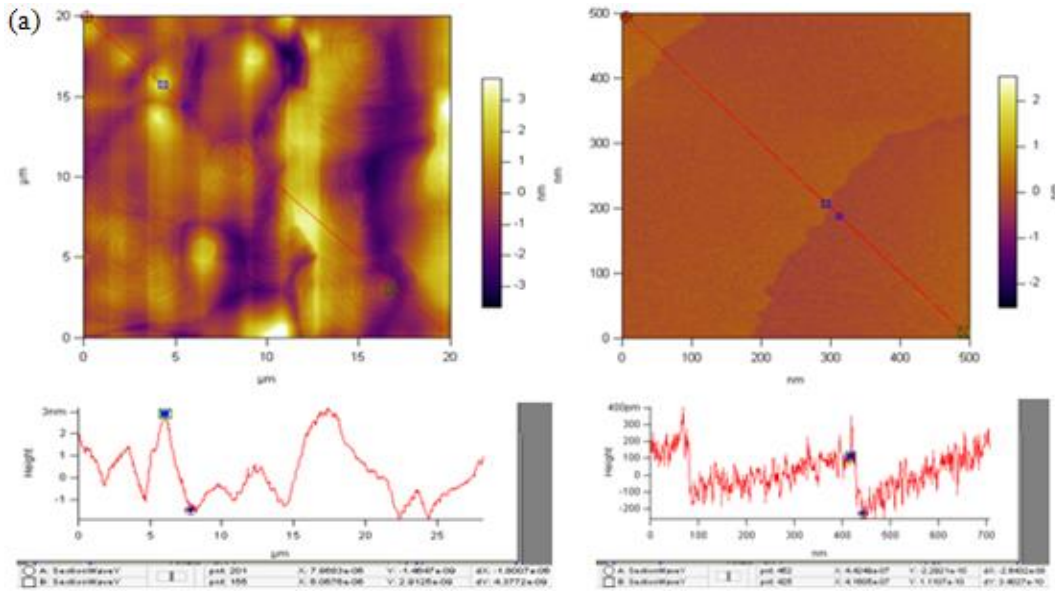


Fig. 5.16  $20 \mu\text{m} \times 20 \mu\text{m}$  and  $500 \text{ nm} \times 500 \text{ nm}$  AFM topographs and cross sections of  $0.5 \mu\text{m}$   $\text{Al}_{1-x}\text{Ga}_x\text{Sb}$  grown on  $\text{GaAs}(001)$  at  $550^\circ\text{C}$ , under the growth rate of  $0.5 \mu\text{m/h}$  (a) sample  $\text{tmw05076}$ ,  $x = 0.2$  and (b)  $\text{tmw05078}$ ,  $x = 0.1$ , respectively.

The  $\sim 14\%$  lattice mismatch between  $\text{Al}_{1-x}\text{Ga}_x\text{Sb}$  (with  $x < 0.2$ ) and  $\text{GaAs}$  resulted in the 3D islanding growth after the initial nucleation of wetting layer. As deposition went on, many 3D islands coalesced after the  $\text{Al}_{1-x}\text{Ga}_x\text{Sb}$  coverage of  $0.5 \mu\text{m}$ ,

connected networks were observed on the surface from the 20  $\mu\text{m}$  x 20  $\mu\text{m}$  AFM topographs in figure 5.16.

For sample tmw05076, RMS surface roughness over an 20 $\mu\text{m}$ ×20 $\mu\text{m}$  and 500nm ×500 nm area was about 460pm and 330pm, respectively. Besides the networks formed on the surface, there were a few large mounds observed from the 20 $\mu\text{m}$  × 20 $\mu\text{m}$  AFM image, the average height of these mounds was about 3nm with lateral width of about 2 $\mu\text{m}$ . No evidence of spiral dislocations was observed from the zoom-in 500 nm × 500 nm AFM topograph. For sample tmw05078, RMS surface roughness over a 20 $\mu\text{m}$  × 20 $\mu\text{m}$  and 500 nm ×500 nm area was about 1.7nm and 520 pm, respectively. More 3D mounds were observed from the 20  $\mu\text{m}$ ×20  $\mu\text{m}$  AFM topograph. The lattice mismatch between Al<sub>0.1</sub>Ga<sub>0.9</sub>Sb and GaAs was larger than that between Al<sub>0.2</sub>Ga<sub>0.8</sub>Sb and GaAs. That may result in a rougher Al<sub>0.1</sub>Ga<sub>0.9</sub>Sb surface. To assess the effect of Al<sub>0.2</sub>Ga<sub>0.8</sub>Sb buffer layer on the surface morphology and electrical mobilities of GaSb layer, 0.1 $\mu\text{m}$  GaSb was grown on GaAs (001) substrate with a insertion of 0.5  $\mu\text{m}$  Al<sub>1-x</sub>Ga<sub>x</sub>Sb (x=0.2) buffer.



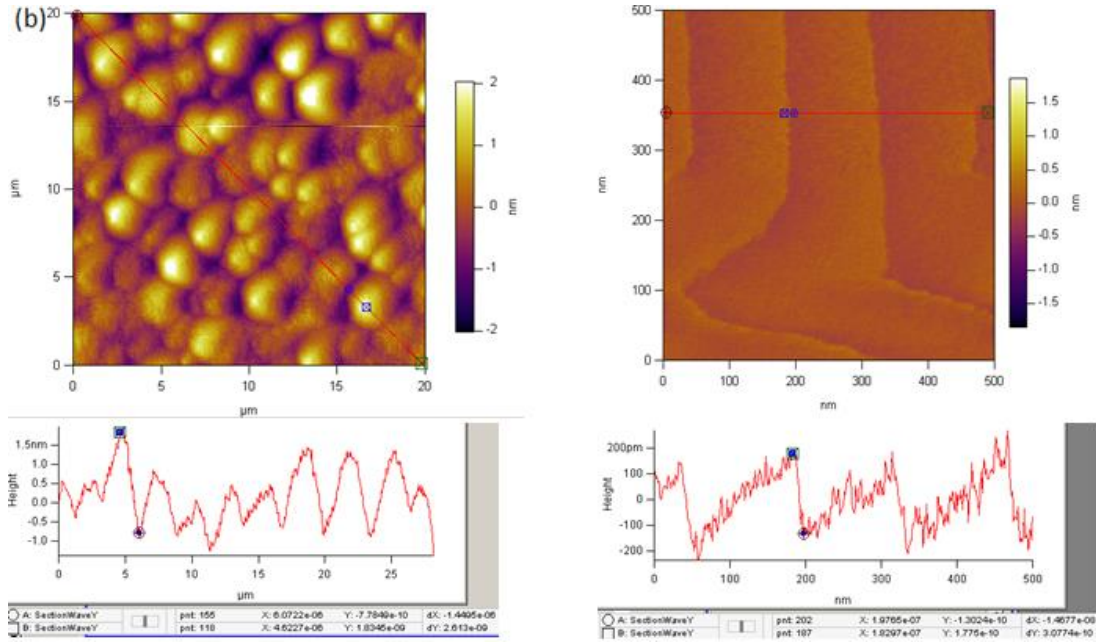


Fig. 5.17 20  $\mu\text{m}$  x 20  $\mu\text{m}$  and 500 nm x 500 nm AFM topographs and cross sections of (a) 0.1 $\mu\text{m}$  GaSb on GaSb (001) substrate with a 0.5 $\mu\text{m}$   $\text{Al}_{1-x}\text{Ga}_x\text{Sb}$  ( $x=0.2$ ) buffer and (b) 0.1 $\mu\text{m}$  GaSb homoepitaxial on GaSb (001) substrate at 520  $^{\circ}\text{C}$ .

RHEED study manifested the abrupt and smooth GaSb/ $\text{Al}_{0.2}\text{Ga}_{0.8}\text{Sb}$  interface. A shiny mirror reflecting surface was obtained after the deposition of 0.1 $\mu\text{m}$  GaSb on 0.5  $\mu\text{m}$   $\text{Al}_{1-x}\text{Ga}_x\text{Sb}$  ( $x=0.2$ ) buffer at GaAs (001) substrate. A few large mounds were formed on the GaSb surface, some concentric rings rather than threading dislocations were observed on these mounds. Compared with the surface morphologies of 0.1 $\mu\text{m}$  GaSb with a 0.5 $\mu\text{m}$   $\text{Al}_{0.2}\text{Ga}_{0.8}\text{Sb}$  and without buffer layer, the GaSb layer with an insertion of buffer had less number of mounds and smoother surface. Monolayer-height terrace steps were observed on the concentric rings from both of the 500 nm  $\times$  500 nm AFM topographs. The Hall measurement results indicated the sample tmw05077 and tmw05048 exhibited p-type conductivity with room-temperature mobility of 795 and 670  $\text{cm}^2\text{V}^{-1}\text{S}^{-1}$ , respectively.

### 5.1.5 Conclusions

Although previous research indicating threading defects significantly propagate through the grown film ( $>1\mu\text{m}$ ), investigations to the effects of growth conditions

including GaSb coverage, growth temperature, V:III flux ratio, and annealing technique onto the final surface morphology are fundamental to the research of GaSb/GaAs heteroepitaxial growth. In the early stages of growth, some 3D islands were formed involving the large lattice mismatch between GaSb and GaAs, as the GaSb growth continues, some of the larger islands coalesce (at the coverage of 0.1-0.25  $\mu\text{m}^2$ ). It was evident that further deposition resulted in a smoother morphology, although the evidence of spiral dislocations could still be observed even on the surface at the coverage of 1.0  $\mu\text{m}^2$ . The spiral defects arise from the misfit array in the GaSb/GaAs interface. The observation of these spiral defects on the surface (figure 5.21) indicate the strain produced by lattice mismatch and the threading dislocation do propagate through the over grown film which was detrimental to the quality of films. And it was demonstrated dislocations at the surface had a mainly screw orientation.

The sample with direct deposition of 1  $\mu\text{m}$  GaSb on GaAs (001) at 500  $^{\circ}\text{C}$  and 0.5 $\mu\text{m}/\text{h}$  exhibited relatively high RT mobility ( $\sim 604 \text{ cm}^2\text{V}^{-1}\text{S}^{-1}$ ) and low number density of threading dislocations at value of  $1.64 \times 10^8/\text{cm}^2$ . Sample with 0.1  $\mu\text{m}$  GaSb grown on GaAs (001) after an insertion of 500 nm AlSb buffer layer exhibited the highest RT mobility of  $\sim 724 \text{ cm}^2\text{V}^{-1}\text{S}^{-1}$  and lowest low number density of threading dislocations at value of  $5 \times 10^6/\text{cm}^2$  among all the samples prepared in this study.

## 5.2 Analysis the deposition of InSb on GaAs (001)

### 5.2.1 Introduction

InSb as the narrowest band gap semiconductor has attracted intensive research interest due to its potential application in macroscopic magnetic sensors [122, 123]. For the fabrication of high-quality magnetic sensors, it is desirable to utilize a semiconductor with high room-temperature mobility. And the superior transport properties of InSb found by Kurtz et al.[124] proved the large potential of InSb in

fabricating low temperature electronic devices. However, InSb can not be employed as substrates due to the large parallel conduction. Consequently, hetero-growth of InSb on semi-insulating GaAs substrate has been widely studied. The main purpose of research heteroepitaxial growth of InSb/GaAs is to obtain high electrical mobility hybrid systems. However, the strain at InSb/GaAs interface induced by lattice mismatch (14.6%) makes it difficult to grow high quality InSb/GaAs hetero-structures. Chyi et al. deposited 5  $\mu\text{m}$  undoped InSb on GaAs and Si, the RT electron mobility was reported at the value to  $57000 \text{ cm}^2\text{V}^{-1}\text{S}^{-1}$ , the electron mobility decreased as decreasing of temperature [125]. And Williams et al. obtained the n-type sample of 10  $\mu\text{m}$  InSb on GaAs with the electron mobility (290 K) of  $66\,000 \text{ cm}^2\text{V}^{-1}\text{S}^{-1}$ . When the temperature dropped the carrier type changed to p-type due to the freeze-out behaviour [126].

Since most devices with narrow band gap materials need to work under cryogenic environment, it is necessary to investigate the degradation behaviour of InSb at low temperatures. Cryostat and room temperature Hall measurement were utilized to investigate the electrical properties of InSb/GaAs samples in this study.

### 5.2.2 Experimental

This section mainly studied the MBE growth and characterization of undoped InSb on GaAs (001) substrate. The growth was undertaken in GEN II MBE apparatus, the growth process was monitored by in-situ RHEED. Electron diffraction patterns and RHEED pattern transitions were observed. Surface morphologies, in particular, threading dislocations were examined by AFM. The electrical properties of residual InSb/GaAs (001) heterostructures were assessed by cryostat and room temperature Hall measurement using Van der Pauw method. There then followed by an analysis of the effect of InSb film thickness and growth rate onto the properties of InSb/GaAs (001) heterostructures. The quantitative analysis of surface roughness and dislocation density of InSb film as a function of film thickness has been addressed. The variation

of mobility and carrier concentration as a function of InSb film thickness and growth rate have been plotted, respectively. In particular, to quantitatively assess the effect of the threading dislocations onto the electrical mobility of InSb films, the variation of mobility as a function of threading dislocation density has been illustrated in this session.

A series of 500 nm, 1  $\mu\text{m}$ , 3  $\mu\text{m}$ , and 5  $\mu\text{m}$  InSb films were deposited on undoped semi-insulating GaAs (001) substrates at different growth rate by MBE. The InSb growth temperature was set around 400  $^{\circ}\text{C}$ . The temperature was evaluated by the InSb surface changing from  $c(4\times 4)$  to  $c(1\times 3)$  reconstruction.

The growth process and the surface reconstructions were monitored by RHEED. The growth rate and III/V flux ratio were calibrated by the RHEED intensity oscillations. The previous studies indicated mirror like InSb was obtained under a low V:III ratio for substrate temperature below 400  $^{\circ}\text{C}$  and the quality of the InSb was determined by the growth rate and the flux ratio of antimony and indium ( $\text{Sb/In}=1\text{-}2.5$ ) [127, 128].

Samples with specular surface have been obtained in this study. The  $\text{Sb}_2\text{:In}$  ratio of 1.1-2 was utilized during the growth. GaAs buffer layer was not employed during the growth of all samples in this session, as the previous research indicated the insertion of GaAs buffer didn't greatly improve the mobility [103].

After removal from the MBE chamber, surface morphologies of samples were examined by AFM. The electrical properties were evaluated by Hall measurement performed in a magnetic field of 0.2T between 77 K and 300 K.

### 5.2.3 Results and analysis

The previous study of the initial deposition of InSb on GaAs (001) revealed the Growth of the InSb started with the formation of 3D rectangular-based islands with sloping sides and flat tops. As deposition went on, islands coalesced and formed a connected network after the approximate coverage of 40 monolayers. After the

equivalent 300 monolayers of deposition, complete InSb layer covered on GaAs substrate was obtained which was evaluated by the previous TEM inspection [129].

#### 5.2.3.1 Analysis of 0.5 $\mu$ m InSb grown on GaAs (001)

To assess the effect of growth rate on the surface morphology and electrical properties of InSb/GaAs (001), thicker InSb were deposited on GaAs (001) substrates. Sample tmw05035 and tmw05034 were 0.5  $\mu$ m InSb grown on GaAs (001) substrate at 400  $^{\circ}$ C under growth rate of 1  $\mu$ m/h and 0.5  $\mu$ m/h, respectively.



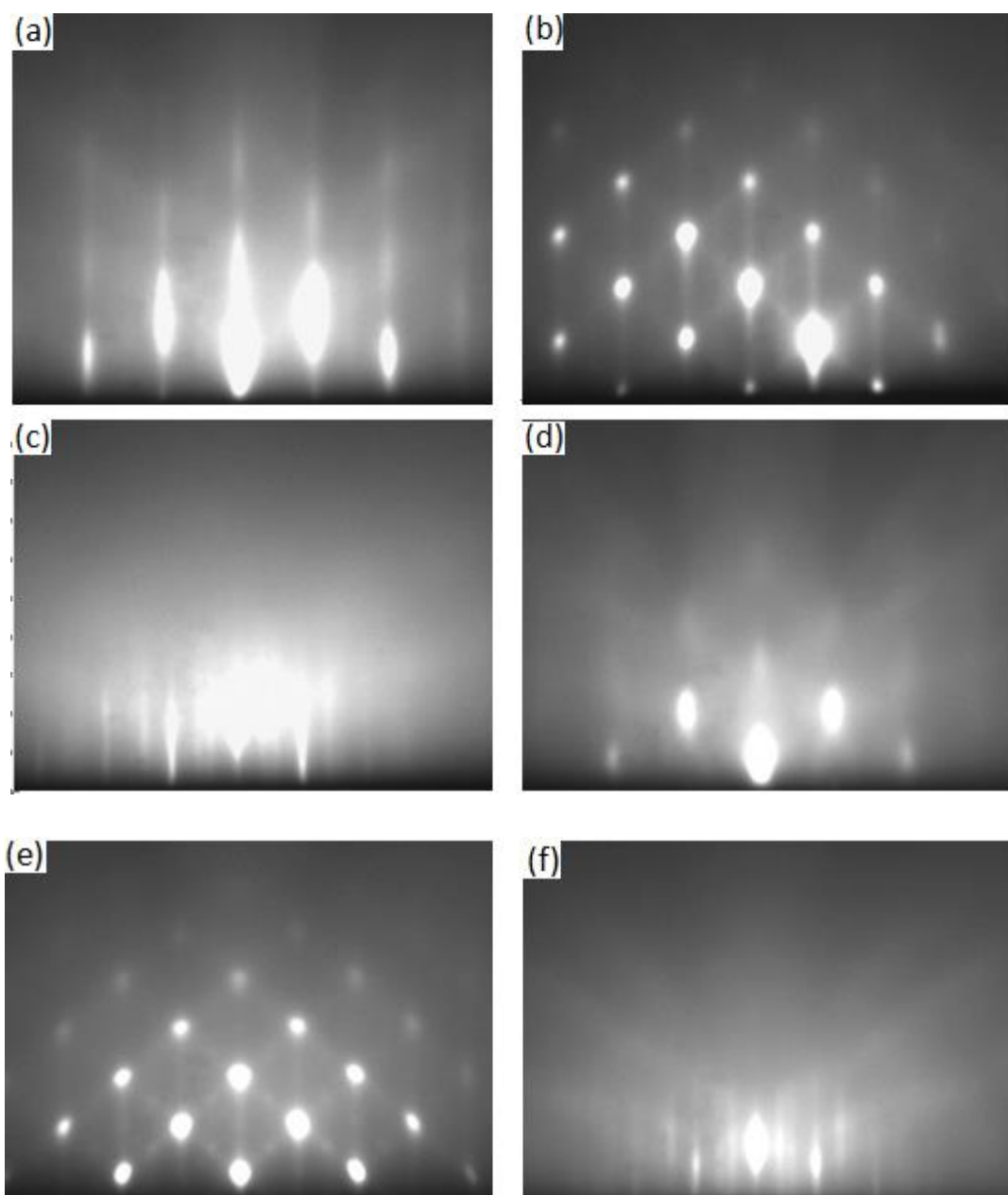
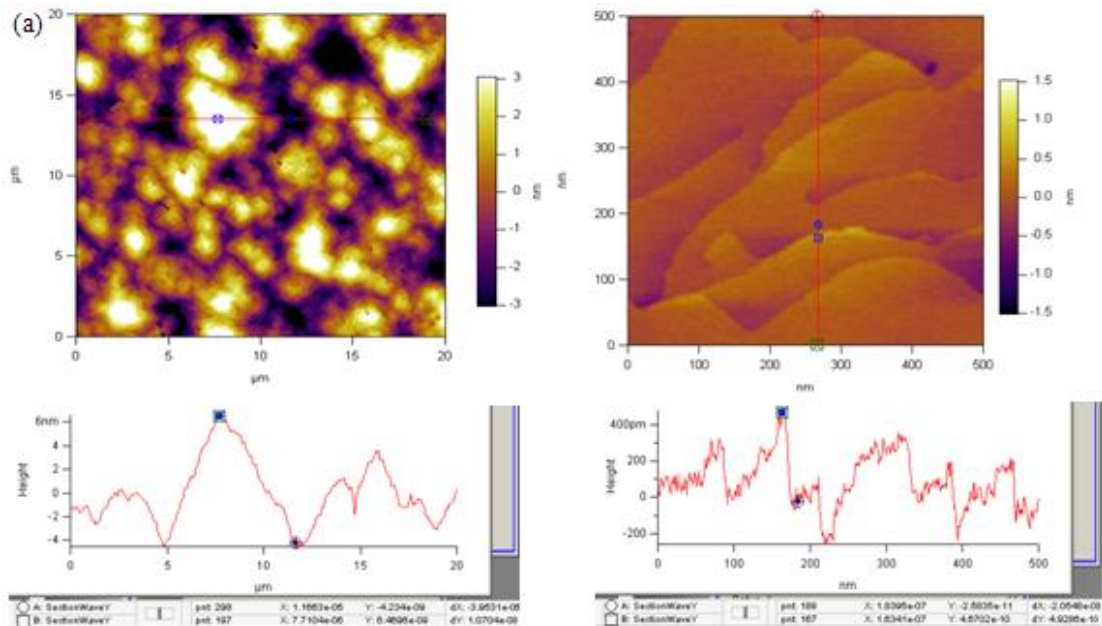


Fig. 5.18 RHEED pattern of sample tmw05035 (a) taken after oxide removal, an elongated spotty pattern indicated rough surface, in the  $[110]$  azimuthal (b) taken after initial 33 s of InSb growth on GaAs (001), spotty pattern indicated large number of 3D dots formed on the surface at that moment, in the  $[110]$  azimuthal (c) after 0.5  $\mu\text{m}$  InSb grown on GaAs(001), good  $\times 3$  symmetry observed at the end of growth, indicated flat surface; RHEED pattern of sample tmw05034 in the  $[1\bar{1}0]$  azimuthal (d) taken after oxide removal, a streaky pattern with elongated spots indicated rough surface in the  $[1\bar{1}0]$  azimuthal (e) taken after initial 33 s of InSb

growth on GaAs (001), spotty pattern indicated large number of 3D dots formed on the surface at that moment in the [110] azimuthal, (f) taken after growth of 0.5  $\mu\text{m}$  GaSb on GaAs(001),  $\times 3$  symmetry observed at the end of growth, indicated flat surface in the [110] azimuthal.

RHEED patterns taken during the growth of 0.5  $\mu\text{m}$  GaSb on GaAs (001) at 400  $^{\circ}\text{C}$  were illustrated in figure 5.22. The elongated spotty patterns obtained after oxide removal indicated rough surfaces for both samples. After the initial 33 s growth of InSb on GaAs (001), a large number of 3D dots were emerged on surfaces of both samples. These 3D dots were induced by the strain of lattice mismatch between InSb and GaAs. The good  $\times 3$  symmetry observed at the end of growth both sample tmw05035 and tmw05034. This indicated a continuous coverage and smooth surface after depositing 0.5  $\mu\text{m}$  InSb on GaAs (001). The detailed surface morphology information was provided by AFM characterization.



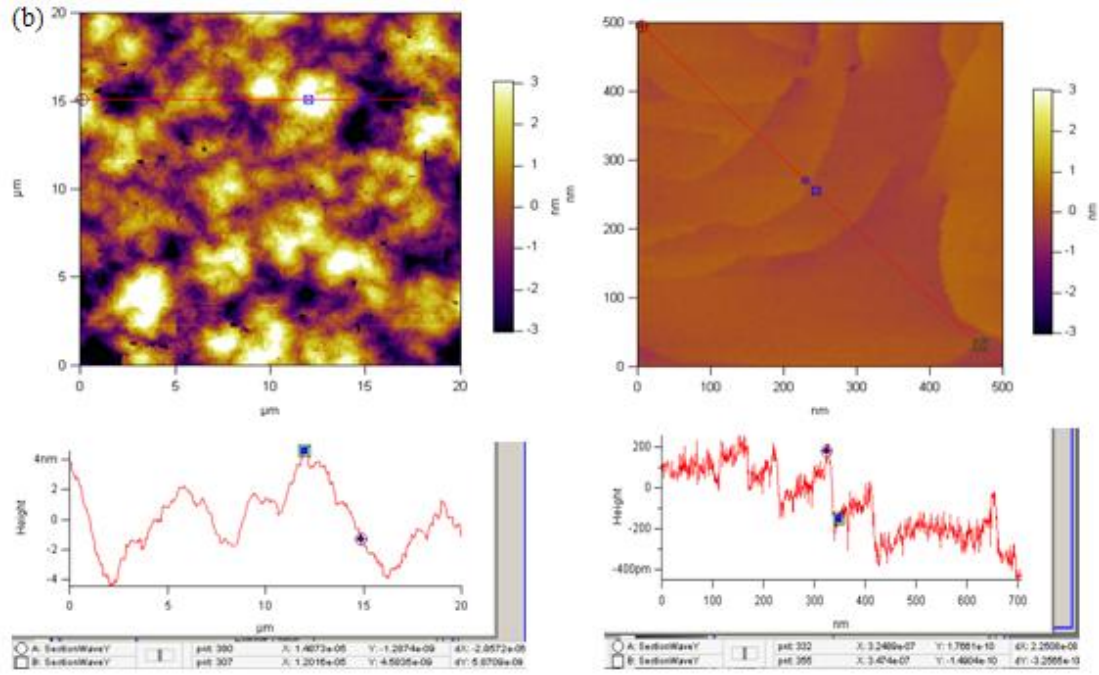


Fig. 5.19 (a) and (b): 20  $\mu\text{m}$  x 20  $\mu\text{m}$  and 500 nm x 500 nm AFM topographs and cross sections of the surfaces of 500 nm InSb hetero-growth at 400  $^{\circ}\text{C}$ , growth rate of 1  $\mu\text{m}/\text{h}$  and 0.5  $\mu\text{m}/\text{h}$ , respectively.

According Zhang, X., et al.'s [120] research about initial stages of InSb deposited on GaAs (001), complete coverage of GaAs substrate was achieved after the equivalent 300 monolayers of deposition. For thicker deposition of InSb epilayer, 2D planar growth was expected. For sample tmw05035 and tmw05034, 0.5  $\mu\text{m}$  InSb was deposited on GaAs (001) substrate at 420  $^{\circ}\text{C}$  under the growth rate of 1  $\mu\text{m}/\text{h}$  and 0.5  $\mu\text{m}/\text{h}$ , respectively. The large lattice mismatch between InSb and GaAs gave rise to defects including micro-pins and threading dislocations on InSb surface, as evidenced by AFM. A large number of mounds were observed on both of the 20  $\mu\text{m}$   $\times$  20  $\mu\text{m}$  AFM topographs (figure 5.23 left). Spiral dislocations were observed on surface with monolayer-height steps visible.

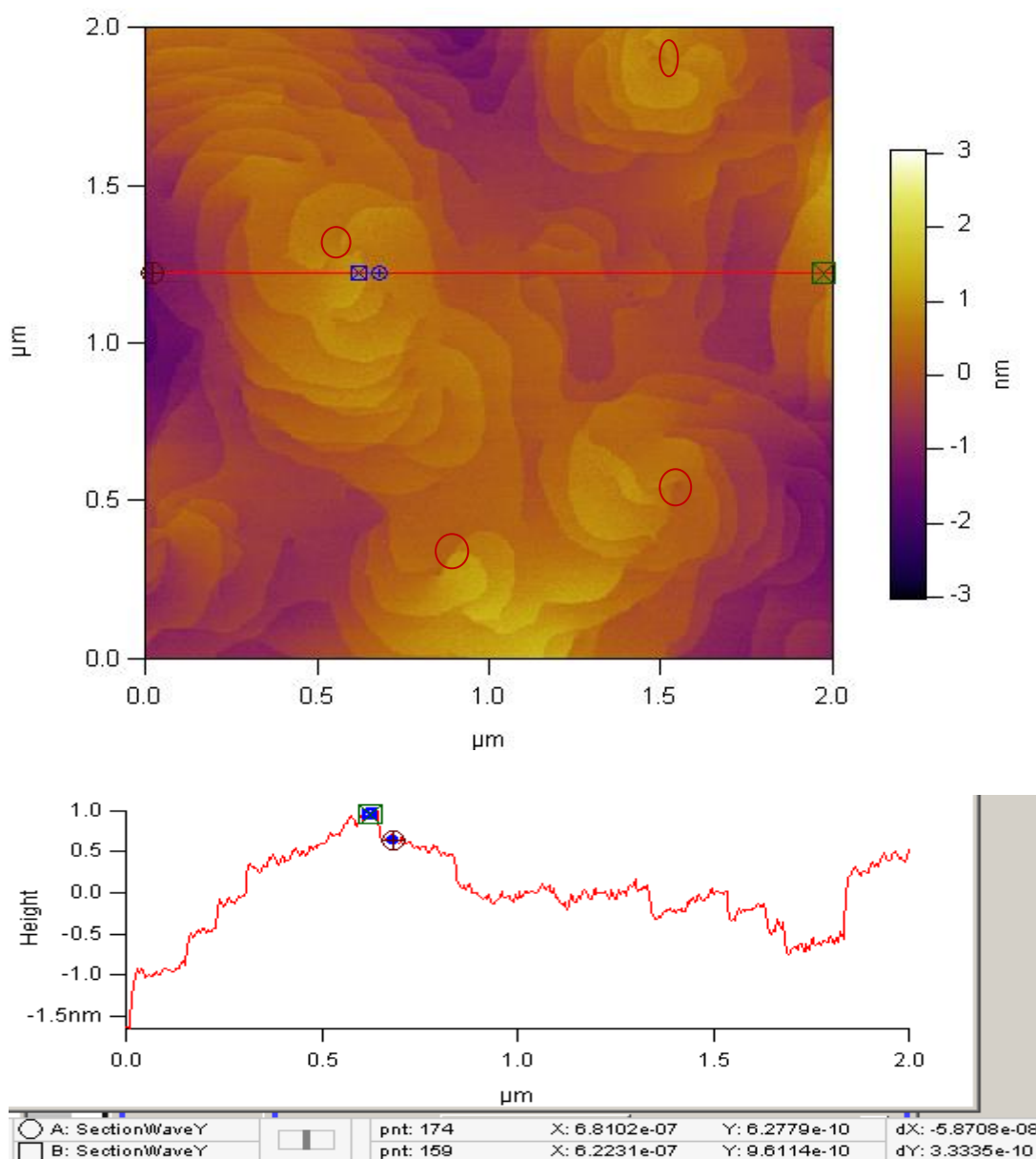


Fig. 5.20 A  $2\mu\text{m} \times 2\mu\text{m}$  zoom-in AFM image and cross sections of the mounds on sample tmw05034. AFM topograph shows a four lobed spiral corresponding to four threading dislocations at the center of the mound and the spiral step edge emanating from a threading dislocation.

From the zoom-in AFM images (figure 5.20), spiral dislocations were observed on the mounds, these spiral dislocations had broad terraces with monolayer-height steps as shown in the  $500\text{ nm} \times 500\text{ nm}$  AFM topographs (figure 5.20 right). Most of spiral dislocations were suspected to be spontaneously generated in InSb/GaAs

interface as soon as the InSb epilayer begins to grow, and most of the defects were  $60^\circ$  type dislocations due to the efficiency of relieving lattice misfit strain as well as allowing more coherent interface area to form[130]. No evidence of indium droplet or antimony condensation was observed on both of the  $20\text{ }\mu\text{m} \times 20\text{ }\mu\text{m}$  AFM topographs. The V:III flux ratio and growth temperature employed in this section were optimized during other study the growth of InSb in our lab. No surface degradation was observed during substrate cooling that indicated the  $\text{Sb}_2$  flux was ceased at the right point during post-growth cooling. For sample tmw05035, the RMS surface roughness over a  $20\text{ }\mu\text{m} \times 20\text{ }\mu\text{m}$  and  $500\text{ nm} \times 500\text{ nm}$  area was 1.7 nm and 0.23 nm, respectively. The number density of threading dislocations is  $\sim 5.4 \times 10^8\text{ cm}^{-2}$ . For sample tmw05034, the RMS surface roughness over a  $20\text{ }\mu\text{m} \times 20\text{ }\mu\text{m}$  and  $500\text{ nm} \times 500\text{ nm}$  area was 1.58 nm and 0.16 nm, respectively. The number density of threading dislocations was  $\sim 4.2 \times 10^8\text{ cm}^{-2}$ . The surface of sample grown at the lower growth rate ( $0.5\text{ }\mu\text{m/h}$ ) was smoother with a lower threading dislocation density than that grown at  $1\text{ }\mu\text{m/h}$ . The temperature-dependent Hall measurements studied the electrical properties of the samples in the temperature range 77-300K and the magnetic field of 0.2 T. All samples exhibited n - type conductivity in the measured temperature range. Figure below illustrated the dependence of carrier density on growth temperature.

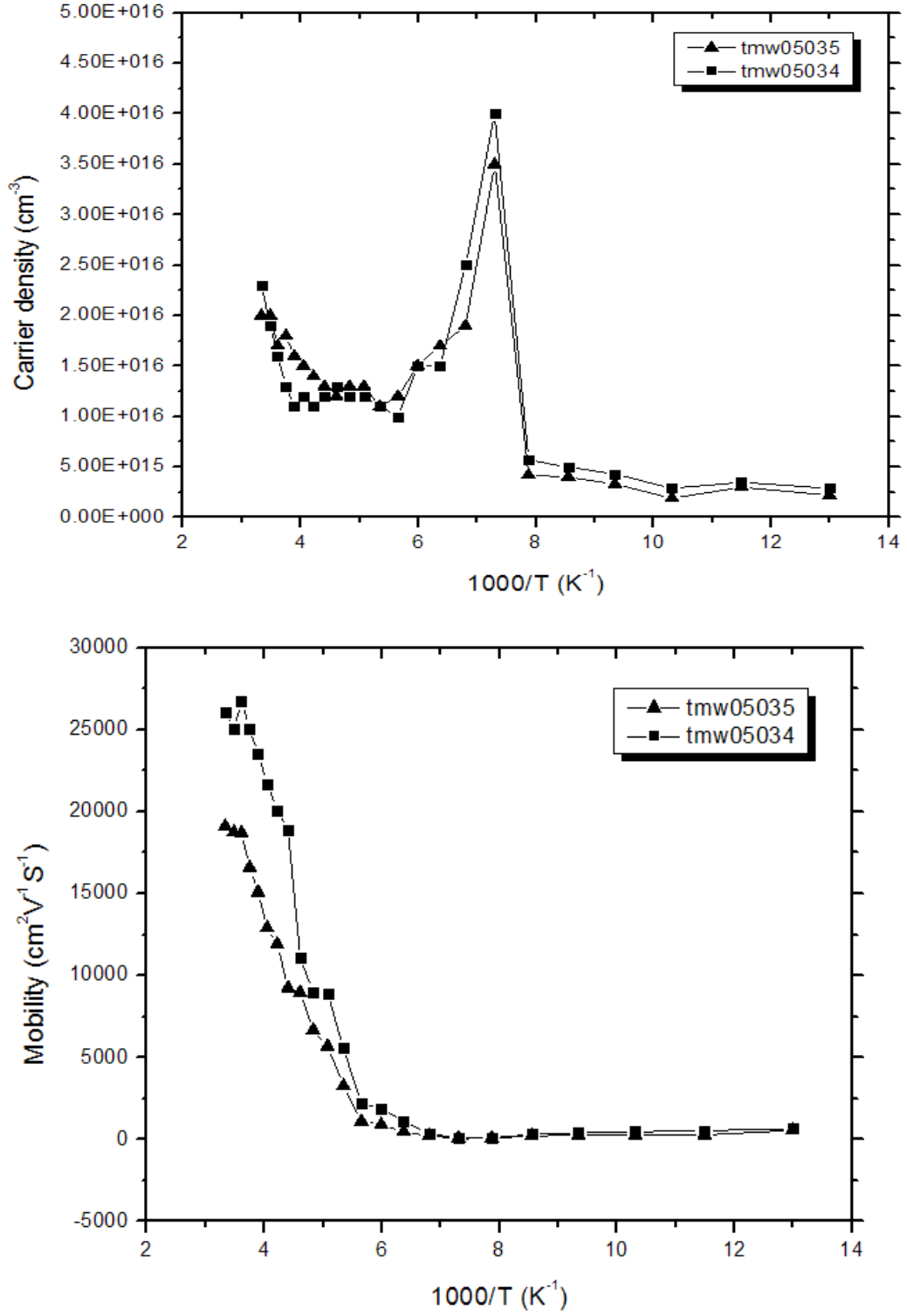


Fig. 5.21 The dependence of Carrier density(top) and mobility (bottom) versus the reciprocal of temperature for sample tmw05035 and tmw05034 with 0.5  $\mu$ m InSb grown on GaAs(001) at 400 pC, under growth rate of 1  $\mu$ m/h and 0.5  $\mu$ m/h, respectively. The full lines join the data for an eye guide.

The growth was under the optimum Sb/In flux ratio of 2, it was demonstrated that deviation from the optimum value of group V:III ratio led to deterioration in the surface morphology and the electrical qualities of the films [131-141]. Undoped InSb layers grown on GaAs (001) under different growth rate usually exhibited n-type conductivity. The relationship between carrier density and temperature was plotted in figure 5.25 (top). The results were calculated by Van der Pauw (VdP) measurements. The overall trend was shown as the universal curve in figures. The InSb layers may exhibit acceptor background. The RT carrier density for sample tmw05035 and tmw05034 was  $1.1 \times 10^{16} \text{ cm}^{-3}$  and  $1.4 \times 10^{16} \text{ cm}^{-3}$ , respectively. Room-temperature mobilities of 19 090 and 26 070  $\text{cm}^2 \text{ V}^{-1}\text{S}^{-1}$  were measured for sample tmw05035 and tmw05034, respectively. Both of the 77 K carrier densities were obtained in the low  $2.5 \times 10^{15} \text{ cm}^{-3}$  range, the electron mobilities (77K) of 550 and 650  $\text{cm}^2 \text{ V}^{-1}\text{S}^{-1}$  were measured for sample tmw05035 and tmw05034, respectively. The mobilities were severely degraded at cryogenic temperatures as shown in figure bottom. In the temperature range 170-300K, the mobility of sample tmw05034 was slightly higher than sample tmw05035, suggesting a lower growth rate may improve the electrical properties of InSb layers. It was suspected dislocations at interface would promote the carrier concentration. The experimentally obtained lower carrier concentration of sample tmw05034 indicated a lower number density of dislocations and a higher mobility for InSb grown at 0.5 $\mu\text{m/h}$ .

One interesting result in this study was the observation of an electron accumulation layer at the InSb surface. This phenomenon was evidenced by the Hall measurement which illustrated one singularity in the carrier concentration versus temperature curve. Due to the Fermi level pin to the valence band edge close the surface of sample, it suggested that surface depletion would play an important role in thin InSb films [99]. Consequently, the carrier concentration would increase while the mobility kept stable.

#### 5.2.3.3 Analysis of 2 $\mu\text{m}$ InSb grown on GaAs (001)

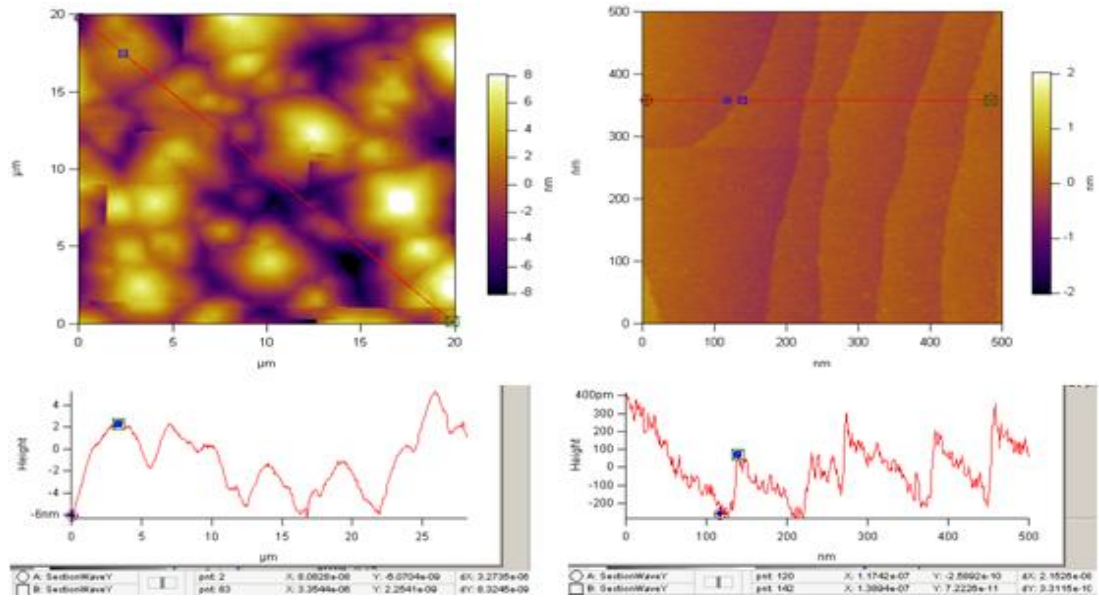


Fig.5.22 20  $\mu\text{m} \times 20 \mu\text{m}$  and 500 nm x 500 nm AFM topographs and cross sections of sample tmw05056, 2 $\mu\text{m}$  InSb grown on GaAs (001) at 420  $^{\circ}\text{C}$ , growth rate of 0.5  $\mu\text{m/h}$ .

Figure 5.26 illustrated two pairs AFM topographs and cross sections of 2 $\mu\text{m}$  InSb grown on GaAs (001) at 420  $^{\circ}\text{C}$ , growth rate of 0.5  $\mu\text{m/h}$ . No large 3D indium droplet or antimony condensation was observed on both of the 20  $\mu\text{m} \times 20 \mu\text{m}$  AFM topographs. A large number of mounds were observed on both of the 20  $\mu\text{m} \times 20 \mu\text{m}$  AFM topographs (figure 5.28 left). Spiral dislocations with monolayer-height steps were also observed on surface. For sample tmw05056, the RMS surface roughness over a 20  $\mu\text{m} \times 20 \mu\text{m}$  and 500 nm  $\times$  500 nm area was 2.8 nm and 0.13 nm, respectively. The number density of threading dislocations was  $\sim 0.25 \times 10^8 \text{ cm}^{-2}$ . The temperature-dependent Hall measurements investigated the electrical properties of the samples in the temperature range 77-300K and in a corrected magnetic field of 0.2 T. Figure 5.27 below illustrated the dependence of carrier density and mobility versus the reciprocal of temperature.



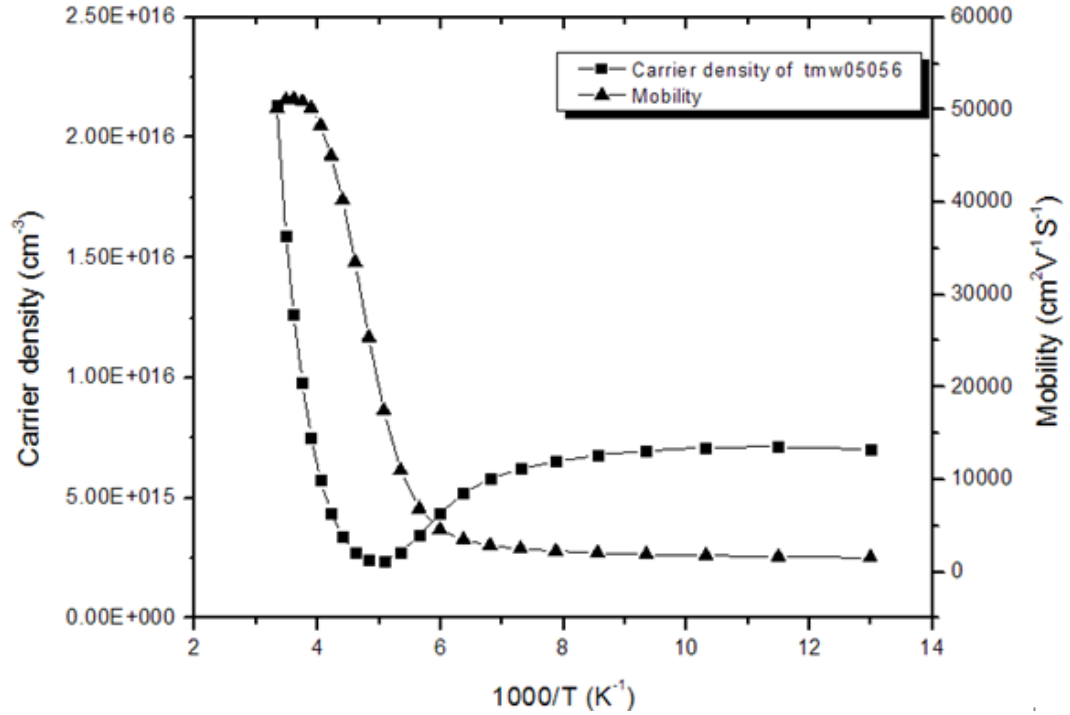


Fig.5.23 Carrier density and mobility versus the reciprocal of temperature for sample tmw05056 with 2 $\mu$ m InSb grown on GaAs(001) under temperature of 420 pC , under growth rate of 0.5 $\mu$ m/h. The full lines join the data for an eye guide.

Room-temperature electron mobilities of 50 130 cm<sup>2</sup> V<sup>-1</sup>S<sup>-1</sup> was obtained for sample tmw05056. The electron mobilities degraded at cryogenic temperatures as shown in figure 5.29 bottom. The electron mobilities (77K) of 1575 cm<sup>2</sup> V<sup>-1</sup>S<sup>-1</sup> was obtained. The 77 K n-type carrier concentration was measured in the low 2 x 10<sup>15</sup> cm<sup>-3</sup> range. Unlike the result of samples in the previous session, no singularity was observed in the temperature-dependent Hall measurement. The 2  $\mu$ m InSb layer grown on GaAs (001) under growth rate of 0.5  $\mu$ m/h exhibited n-type conductivity. It has been demonstrated that above 100 nm from the interface, the carrier density had a value of 2.3 x 10<sup>16</sup> cm<sup>-3</sup> which was comparable to the intrinsic InSb bulk density. The lower carrier concentration suggested a lower number density of threading dislocations as well as a higher mobility, this result indicated the InSb/GaAs (001) interface exhibited donner-like function which was consistent with the result obtained by T. Zhang [120]. The experimentally obtained RT carrier density for sample tmw05056

was  $\sim 2.2 \times 10^{16} \text{ cm}^{-3}$ .

### 5.2.3.3 Analysis of 5 $\mu\text{m}$ InSb grown on GaAs (001)

Further for sample tmw05083, 5  $\mu\text{m}$  InSb was deposited on GaAs (001) substrate at temperature of 420  $^{\circ}\text{C}$ , under growth rate of 0.5  $\mu\text{m/h}$ .

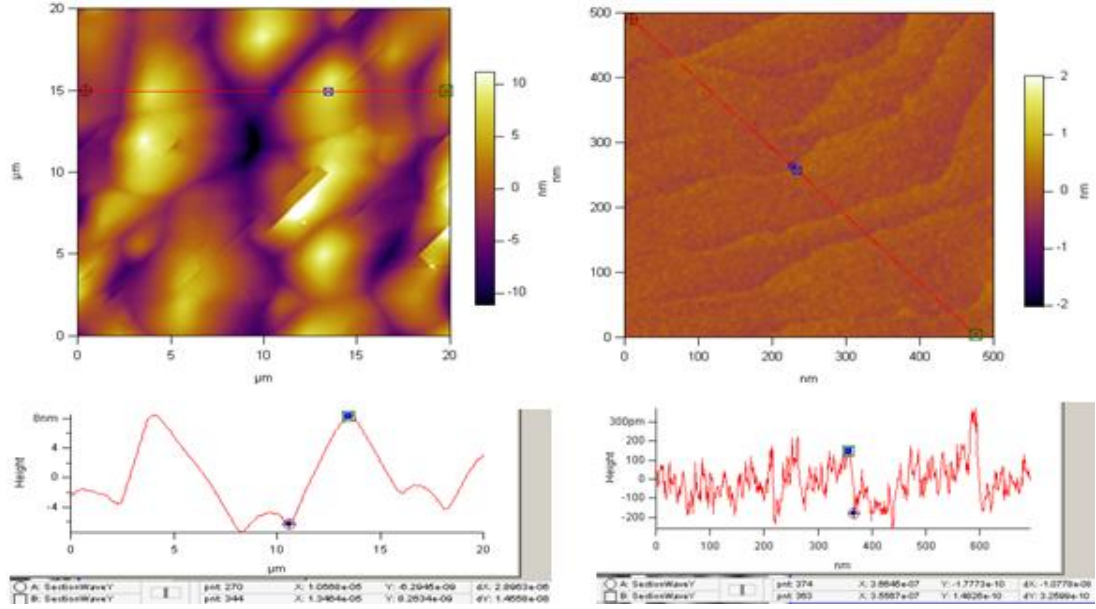


Fig.5.24 A 20  $\mu\text{m} \times 20 \mu\text{m}$  and a 500 nm  $\times$  500 nm AFM topographs and cross sections of the surfaces of 5  $\mu\text{m}$  InSb grown on GaAs(001) at 420  $^{\circ}\text{C}$ , under growth rate of 0.5  $\mu\text{m/h}$ .

Figure 5.28 illustrated the AFM topographs and cross sections of the surfaces of 5  $\mu\text{m}$  InSb grown on GaAs (001) at 420  $^{\circ}\text{C}$ , under growth rate of 0.5  $\mu\text{m/h}$ . No evidence of large 3D islands was observed on the 20  $\mu\text{m} \times 20 \mu\text{m}$  AFM topograph, this proved no 3D antimony condensation was accumulated on the surface under that growth condition. A large number of mounds were observed from the 20  $\mu\text{m} \times 20 \mu\text{m}$  AFM topographs (figure 5.28 left). Spiral dislocations with monolayer-height steps were also observed on surface. For sample tmw05082, the RMS surface roughness over a 20  $\mu\text{m} \times 20 \mu\text{m}$  and 500 nm  $\times$  500 nm area was 1.6 nm and 0.16 nm, respectively. The number density of threading dislocations was  $7.5 \times 10^6 \text{ cm}^{-2}$ . The temperature-dependent Hall measurements study the electrical properties of the

samples in the temperature range 77-300K and in magnetic field of 0.2 T. Figure below illustrated the carrier density and mobility versus the reciprocal of temperature.

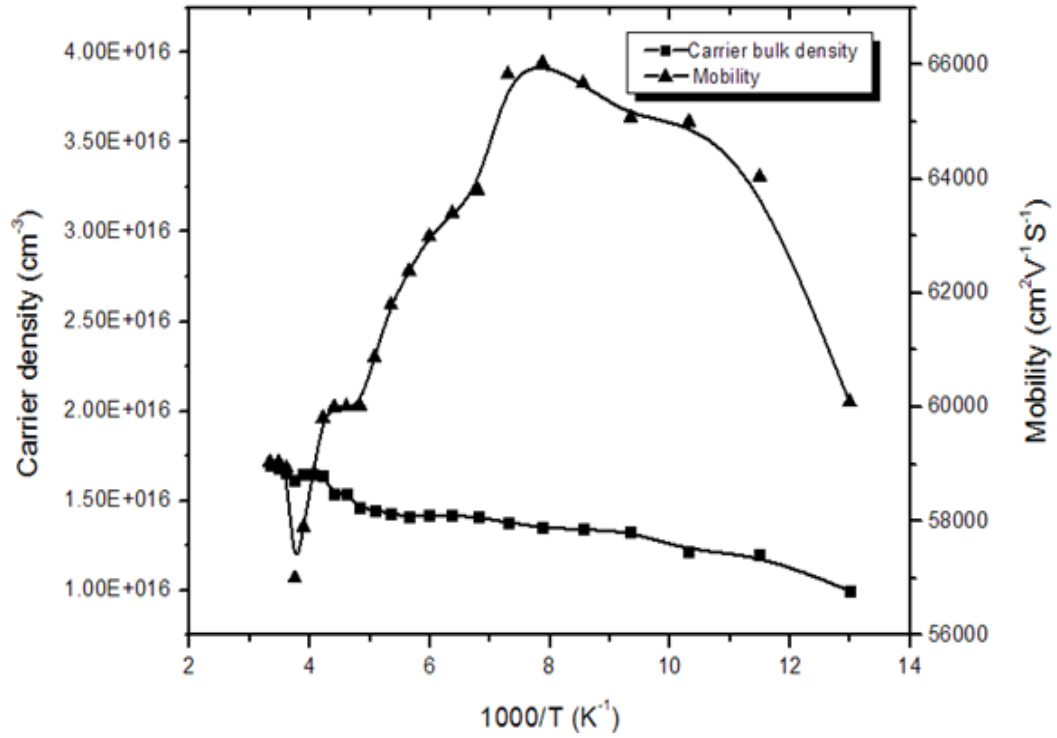


Fig.5.25 Carrier density and mobility versus the reciprocal of temperature for sample tmw05083 with 5  $\mu\text{m}$  InSb grown on GaAs (001) under temperature of 420  $^{\circ}\text{C}$  , under growth rate of 0.5  $\mu\text{m/h}$ . The full lines join the data for an eye guide.

5  $\mu\text{m}$  InSb layers grown on GaAs (001) under growth rate of 0.5  $\mu\text{m/h}$  exhibited n-type conductivity in the temperature range 77-300K. Room-temperature electron mobilities of 59 040  $\text{cm}^2 \text{V}^{-1}\text{S}^{-1}$  was obtained for sample tmw05083. No degradation of the electron mobilities was observed at cryogenic temperatures as shown in figure 5.33 bottom, the electron mobilities (77K) of 60 090  $\text{cm}^2 \text{V}^{-1}\text{S}^{-1}$  was obtained. The RT carrier concentration was  $\sim 1.7 \times 10^{16} \text{ cm}^{-3}$  and the carrier concentration steadily decreased with decreasing temperature to be  $1.0 \times 10^{16} \text{ cm}^{-3}$  at 77 K. Sample tmw05083 exhibited lowest density of threading dislocations and highest electron mobility compared with other InSb/GaAs (001) heterostructures grown in

the previous sessions, and it also suggested its potential application in the electronic devices working at cryogenic temperatures.

#### 5.2.4 Conclusions

This session studied structural and electrical properties of InSb grown on GaAs (001) at the optimum growth conditions. The effects of growth temperature and growth rate on the surface morphology and electrical properties of InSb/GaAs heterostructures have been investigated. It has been demonstrated that samples grown at 420 °C and growth rate of 0.5  $\mu\text{m/h}$  had a considerable improvement in the structural and electrical performances. AFM topographies proved that samples grown at a lower growth rate had smoother surfaces with lower number densities of threading dislocations. The temperature dependent Hall measurements using Van der Pauw method were conducted in the magnetic field of 0.2 T at the temperature from 77 to 300 K. All the samples exhibited n-type conductivity. The Hall measurement results indicate the samples grown at a lower growth rate (0.5  $\mu\text{m/h}$ ) had higher mobilities.

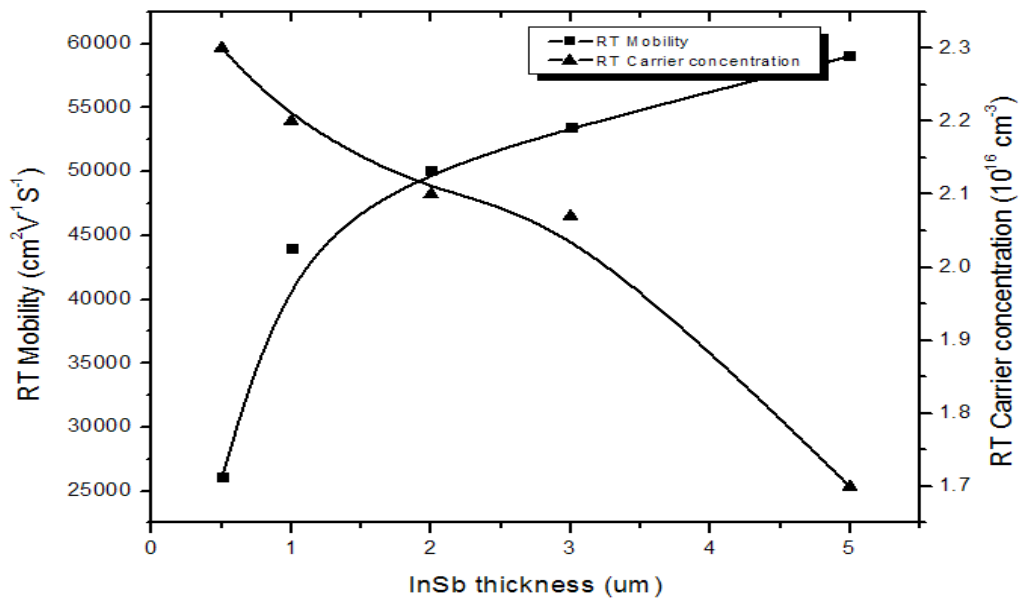


Fig. 5.26 The dependence of RT mobility and carrier density versus InSb thickness for InSb layers with various thickness on GaAs (001) substrates at the optimum

growth temperature of 420 °C and growth rate of 0.5  $\mu\text{m/h}$ . The full lines join the data for an eye guide.

The dependence of RT mobility and carrier density versus insb thickness for InSb layers with various thickness on GaAs (001) substrates at the optimum growth temperature of 420 °C and growth rate of 0.5  $\mu\text{m/h}$  were illustrated in figure 5.34. The RT mobility gradually increased with increasing thickness and the RT carrier densities obtained for samples with InSb thickness between 0.5  $\mu\text{m}$  and 2  $\mu\text{m}$  was close to the intrinsic bulk density of InSb at the value of  $\sim 2.3 \times 10^{16} \text{ cm}^{-3}$ . For further increasing the InSb epilayer thickness, the apparent carrier density got slightly increased. The observation of increasing mobility and decreasing carrier density indicated a donner-like InSb/GaAs interface.

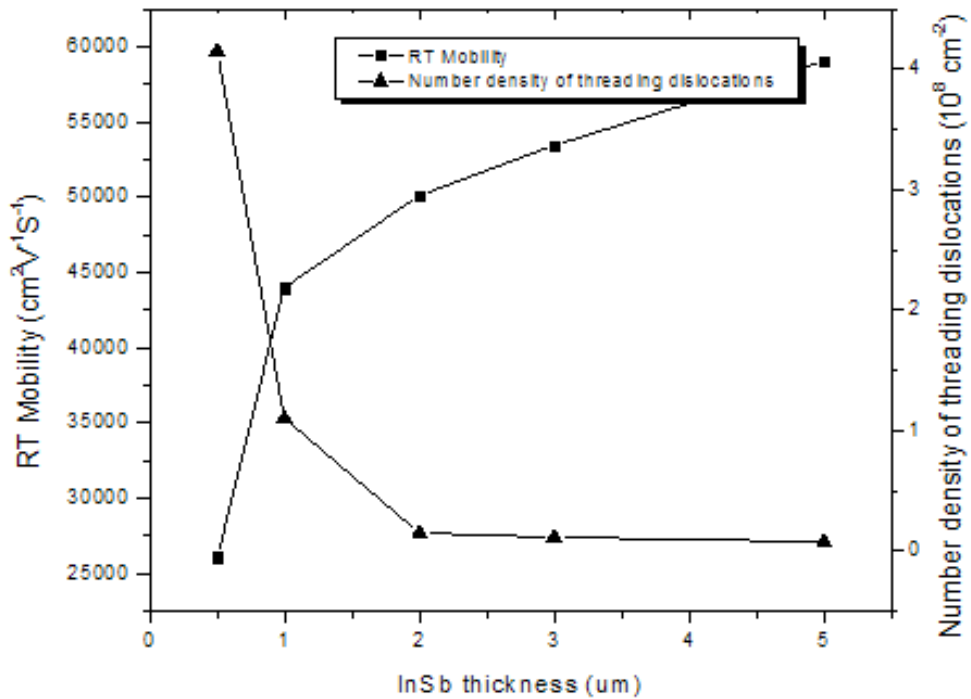


Fig. 5.27 Electron mobility and number density of threading dislocations for InSb layers with various thickness on GaAs (001) substrates grown at 420 °C and 0.5  $\mu\text{m/h}$ . The full lines join the data for an eye guide.

The threading dislocations on the surface play an important role in the electrical performance of the InSb film, the suppression of dislocations decreases the carrier

concentration of InSb which apparently improves the mobility. The InSb/GaAs heterostructures with low number density of dislocation are more than appealing. It has been demonstrated that a lower growth rate (0.5  $\mu\text{m/h}$ ) and thicker InSb epilayers may have positive effects on the surface morphology and electrical properties of InSb/GaAs heterostructures. The optimum substrate temperature for the InSb layer growth is 420  $^{\circ}\text{C}$  with an optimum Sb / In flux ratio of 1.1 and a growth rate of 0.5  $\mu\text{m/h}$ . The best 5  $\mu\text{m}$  thick InSb layer has lowest threading dislocation density of  $\sim 10^6 \text{cm}^{-2}$ , RT electron mobility of 59 040  $\text{cm}^2\text{V}^{-1}\text{S}^{-1}$ , 77 K n-type carrier density of  $\sim 10^{16} \text{cm}^{-3}$ , and 77 K electron mobility of 60 090  $\text{cm}^2\text{V}^{-1}\text{S}^{-1}$ .

## **Chapter 6 Theoretical and experimental analysis the optical properties of III-Sb thin films**

### **6.1 Introduction**

Sb-based semiconductors have great potential in producing infrared devices. In this chapter, both the theoretical and the experimental reflectivity measurements were made on the GaSb and InSb samples. Based on the Kramers-Kronig Transform, the electrical properties could be deduced from the optical parameters [142]. The results obtained from the reflectivity measurements were compared with the Hall measurements.

### **6.2 Theoretical analysis of the optical properties, electrical properties, and their transformation**

Understanding the optical interaction regimes in thin films is the foundation of analysing the optical characteristics of various electrical, optical and photovoltaic devices. A proper numerical model to investigate the reflection, absorption and transmission of light in different nanostructured thin films is crucial to design and optimize a desirable functional structure. Different structures of thin films may exhibit different optical interaction regimes.

For homogeneous thin films, light propagates in a straight line until it reaches an interface, then it gets reflected or transmitted. Extensive researches have been carried out for the optical interactions inside the homogeneous thin films [143-145]. Based on the previous analysis and the subsequent mathematical derivation, the reflection and transmission of light with different wavelengths could be calculated by using Maxwell's equations [146].

#### **6.2.1 Analysis of optical propagation and energy dissipation inside homogeneous structures**

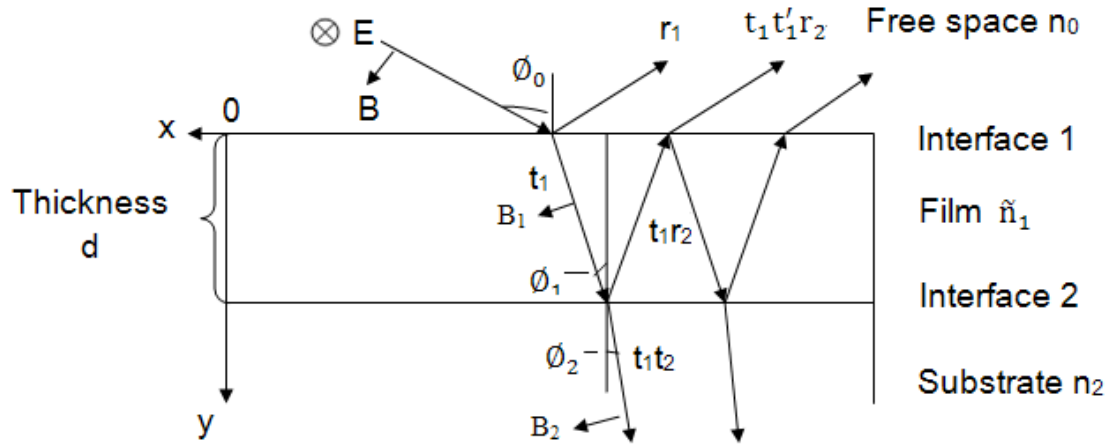


Fig.6.1 Light propagation through a single layer homogeneous film.

Figure 6.1 illustrated a beam of p polarized wave (also known as tangential plane polarized, or said to be the transverse-magnetic wave with the electric vector in the incident plane) propagation through a single layer[147]. The thin film layer was assumed to be homogeneous with the index of refraction  $n_1$  and film thickness of  $d$ . The index of refraction of free space and substrate was  $n_0$  and  $n_2$ , respectively. From the relationship and interaction of electric and magnetic energy of the incident, reflected, and transmitted light, the equations of light energy balance in the interfaces of free space/ film and film/substrate could be derived.

At the interface 1, the boundary conditions of electric and magnetic fields were given as

$$E_1 = E_0 + E_{r1} = E_{t1} + E_{i1} \quad (6.1)$$

$$B_1 = B_0 \cos \phi_0 - B_{r1} \cos \phi_0 = B_{t1} \cos \phi_1 - B_{i1} \cos \phi_1 \quad (6.2)$$

Where  $E$  and  $B$  are the electric field intensity and magnetic field intensity, respectively. The subscript  $r$ ,  $t$  and  $i$  denote the reflected, transmitted and incident part of energy, respectively.  $\phi_0$  is the angle of incident light and  $\phi_1$  is the angle of refraction in the thin film. The Maxwell-Faraday equation  $\nabla \times E = -\frac{\partial B}{\partial t}$  denotes the



interaction of the perpendicular and tangential components of the electric field and the magnetic field. From Maxwell's equations, the relationship between the electric field and magnetic field can be obtained,  $B = n\sqrt{\epsilon_0\mu_0}E$ . Therefore, from the equations (6.1) and (6.2), the relationship between the electric field and magnetic field energy in boundary 1 is given as

$$B_1 = n_0\sqrt{\epsilon_0\mu_0} \cos \phi_0 (E_0 - E_{r1}) = n_1\sqrt{\epsilon_0\mu_0} \cos \phi_1 (E_{t1} - E_{i1}) \quad (6.3)$$

When the light propagates to the interface 2, the balance of electric field and magnetic field energy can be expressed as

$$E_2 = E_{i2} + E_{r2} = E_{t2} \quad (6.4)$$

$$B_2 = B_{i2} \cos \phi_1 - B_{r2} \cos \phi_1 = B_{t2} \cos \phi_2 \quad (6.5)$$

Similarly, from equations (6.4) and (6.5), the following equation can be obtained, as

$$B_2 = n_1\sqrt{\epsilon_0\mu_0} \cos \phi_1 (E_{i2} - E_{r2}) = n_2\sqrt{\epsilon_0\mu_0} \cos \phi_2 E_{t2} \quad (6.6)$$

Where  $\phi_2$  is the angle of emergence in substrate,  $\epsilon_0$  is the permittivity of free space (an electric constant) and  $\mu_0$  is the permeability of free space (a magnetic constant). After light propagating through the thickness  $d$ , there is a phase difference between  $E_{t1}$  and  $E_{i2}$ ,  $E_{r1}$  and  $E_{i1}$ . According to the optical theory [148], the phase difference is given as

$$\delta = \left(\frac{2\pi}{\lambda_0}\right)n_1d \cos \phi_1 \quad (6.7)$$

Substitution of these equations into equation (6.4) and (6.5) at interface 2 can lead to the following formulations for E-field and M-field energy, respectively

$$E_2 = E_{t1}e^{-i\delta} + E_{i1}e^{i\delta} = E_{t2} \quad (6.8)$$

$$B_2 = n_1\sqrt{\varepsilon_0\mu_0}\cos\phi_1(E_{t1}e^{-i\delta} - E_{i1}e^{i\delta}) = n_2\sqrt{\varepsilon_0\mu_0}\cos\phi_2E_{t2} \quad (6.9)$$

Providing  $\chi_0 = n_0\sqrt{\varepsilon_0\mu_0}\cos\theta_0$ ,  $\chi_1 = n_1\sqrt{\varepsilon_0\mu_0}\cos\theta_1$  and  $\chi_2 = n_2\sqrt{\varepsilon_0\mu_0}\cos\theta_2$ , the relation between the electric field energy and magnetic field energy before and after light transport through the thin film can be expressed in a matrix shown as

$$\begin{pmatrix} E_1 \\ B_1 \end{pmatrix} = \begin{pmatrix} \cos\delta & \frac{i\sin\delta}{\chi_1} \\ i\chi_1\sin\delta & \cos\delta \end{pmatrix} \begin{pmatrix} E_2 \\ B_2 \end{pmatrix} \quad (6.10)$$

Matrix  $M_1 = \begin{pmatrix} m_{11} & m_{12} \\ m_{21} & m_{22} \end{pmatrix} = \begin{pmatrix} \cos\delta & \frac{i\sin\delta}{\chi_1} \\ i\chi_1\sin\delta & \cos\delta \end{pmatrix}$  is the transfer matrix of a single layer film.

To realize anti-reflection, it always uses the quarter-wave thick film. When the film thickness  $d = \frac{\lambda_0}{4n_1}$ , then  $\delta = \pi/2$  and  $R = \left( \frac{n_0n_2 - n_1^2}{n_0n_2 + n_1^2} \right)^2$ . Hence, the reflectance is only determined by the material of the film.

If the Fresnel coefficients are small, then their product can be neglected. Also if the absorption in the film is high, the multiple reflection could be neglected. In that case, the expression of transmission and reflection can be simplified as

$$r = \frac{E_{r1}}{E_0} \quad (6.11)$$

$$t = \frac{E_{t2}}{E_0} \quad (6.12)$$

For a multi-layer film, the transfer matrix is given as [145]

$$\begin{pmatrix} E_1 \\ B_1 \end{pmatrix} = \overline{M} \begin{pmatrix} E_N \\ B_N \end{pmatrix} \quad (6.13)$$

And

$$\overline{M} = \prod_{i=1}^N M_i \quad (6.14)$$

### 6.2.2 Relationships between optical and electrical properties

Providing the infrared ray is normally incident to the sample, the reflectivity and reflectivity energy can be expresses as

$$r = \frac{n-ik-1}{n-ik+1} \quad (6.15)$$

$$R = |r|^2 = \frac{(n-1)^2+k^2}{(n+1)^2+k^2} \quad (6.16)$$

Where  $n$  is the refractive index and  $k$  is the absorption index of the substrate, the complex permittivity  $\tilde{\epsilon}(\nu)$  is given by equation

$$\tilde{\epsilon}(\nu) = \tilde{n}^2 = \epsilon_\infty + \frac{(\epsilon_s - \epsilon_\infty)\nu_L^2}{\nu_L^2 - \nu^2 - i\nu\gamma} - \frac{\epsilon_\infty \nu_p^2}{\nu(\nu + i/\tau)} \quad (6.17)$$

Where  $\epsilon_\infty$  is the high frequency dielectric constant,  $\epsilon_s$  is the static dielectric constant,  $\nu_L$  is the LO phonon frequency,  $\nu_p$  is the plasma frequency,  $\gamma$  is the damping constant of phonon, and  $\tau$  is the carrier scattering time. For GaSb,  $\epsilon_\infty$  is 14.45,  $\epsilon_s$  is 15.85, and RT  $\nu_L$  is  $225.5 \text{ cm}^{-1}$ [146]. The plasma frequency  $\nu_p$  can be expressed as follow

$$\nu_p = \sqrt{n_c e^2 / m^* \epsilon_s \epsilon_\infty} \quad (6.18)$$

Where  $n_c$  is the carrier concentration,  $e$  equals  $1.6 \times 10^{-19} \text{ C}$ , and  $m^*$  is the effective carrier mass. In undoped semiconductors, the low carrier concentrations make the lower mode is basically plasma-like and the upper mode is he LO phonon, both of the minima occur near  $\nu_p$  and  $\nu_L$ . The coupling between the plasmas and the LO

phonons won't happen. The two minimum in reflectivity are usually separated by a sharp rise near the LO phonon frequency  $\nu_L$  which is described as reststrahlen peak. These features are known as two-oscillation mode, based on equations 6.16 and 6.17 values of the plasma frequency  $\nu_p$  and the free carrier scattering time  $\tau$  can be calculated. Carrier concentration  $n_c$  can be calculated from equation 6.18.

If  $\delta$  represents the phase change due to reflection, the logarithmic of reflectivity can be expressed as

$$\ln r = \ln \sqrt{R} + i\delta \quad (6.19)$$

Where the absolute value of reflectivity and phase change upon reflection  $\delta$  are mutually dependent, and if the reflectivity at the specific frequency is known, the phase change can be calculated by [149]

$$\delta(\nu_s) = \frac{2\nu_s}{\pi} \int_0^\infty \frac{\ln \sqrt{R(\nu)}}{\nu^2 - \nu_s^2} d\nu \quad (6.20)$$

In the Fourier transform infrared (FTIR) spectrometer, double Fourier transformation has been proposed, the spectra resolution  $h$  is set at the value of  $2 \text{ cm}^{-1}$  and the data interval is  $g$ , then the phase change at any wavenumber can be calculated from the equation [148]

$$\delta(\nu_s) = 4 \int_0^\infty \cos(2\pi\nu g t) dt \int_0^\infty \ln \sqrt{R(\nu)} \sin(2\pi\nu t) d\nu \quad (6.21)$$

Knowing the reflectivity and phase change, the optical constants  $n$  and  $k$  can be obtained as

$$n = \frac{1-R}{1+R-2\sqrt{R}\cos\delta(\nu_s)} \quad (6.22)$$

$$k = \frac{-2\sqrt{R}\sin\delta(\nu_s)}{1+R-2\sqrt{R}\cos\delta(\nu_s)} \quad (6.23)$$

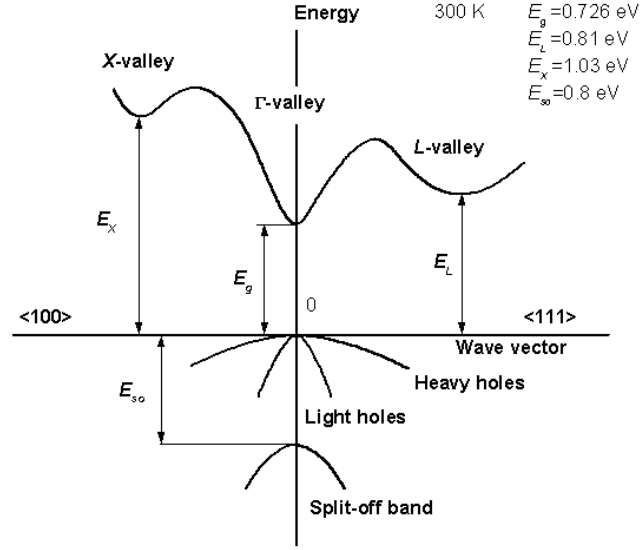


Fig.6.2 RT Band structure and carrier concentration of undoped GaSb [150].

Fourier transform infrared (FTIR) spectrometer is a useful method to investigate the optical properties of the material, applying the relationship between the electrical and optical properties, electrical properties such as carrier concentration and mobility can be obtained. The results from Hall measurement in section 5.1 indicated the p-type conductivity of all the GaSb/GaAs heterostructures. This makes the calculation of carrier density and mobility more convenient than the n-type GaSb. The electrons between the  $\Gamma$ -valley and L-valley in the n-type GaSb are separated by a small energy gap, consequently, it makes difficulty in the measurement of carrier concentration because of the occupation of central  $\Gamma$  minimum and satellite L minimum even at low temperatures [150,151]. In that case, it is inappropriate to analyse the n-type GaSb by direct comparison between the carrier densities obtained from the infrared reflectivity and Hall measurements.

The effective hole mass of GaSb has been derived by the reflectivity measurement to be  $\sim 0.23 m_0$ . Based on Moss's calculation of the effective hole mass by treating the heavy and light hole mass separately, the effective hole mass is given by [152]

$$m^* = \frac{m_{Hh}^{3/2} + m_{Lh}^{3/2}}{m_{Hh}^{1/2} + m_{Lh}^{1/2}} \quad (6.24)$$

Where  $m_{Hh}$  is the mass of heavy hole to be  $0.33 m_0$  and  $m_{Lh}$  is the mass of light hole to be  $0.044 m_0$ [148]. For InSb, the effective electron mass is measured to be  $0.016 m_0$ . The mobility  $\mu$  then can be determined by the equation

$$\mu = e\tau/m^* \quad (6.25)$$

### 6.3 Experimental

Sample tmw05057 was 1  $\mu\text{m}$  GaSb grown on GaAs (001) substrate at temperature of  $500^\circ\text{C}$  and growth rate of  $0.5 \mu\text{m/h}$  by MBE. Sample tmw05083 was 5  $\mu\text{m}$  InSb deposited on GaAs (001) substrate at temperature of  $420^\circ\text{C}$ , under growth rate of  $0.5 \mu\text{m/h}$ . After removal from the MBE chamber, the samples were cleaved to  $1 \text{ cm} \times 1 \text{ cm}$ . The infrared reflectivity measurements have been performed in Fourier transform infrared (FTIR) spectrometer (Perkin Elmer, Frontier) at room temperature. The spectrum frequency ranges from  $20$  to  $250 \text{ cm}^{-1}$  due to the sensitivity to the fitting parameters in this region. The spectrometer was performed in the single beam model.  $10 \text{ line/mm}$  grating was utilized in first order. After the absorption-bands calibration, the reflectivity was compared to the front Al-coated mirror. The spectral resolution is  $\sim 2 \text{ cm}^{-1}$ . Due to the non-destructive of the reflectivity measurement and for the accuracy of the obtained data, RT Hall measurement was performed in the magnetic field of  $0.2 \text{ T}$  on the same sample after the infrared reflectivity measurement.

### 6.4 Results and discussion

#### 6.4.1 Results for GaSb and analysis

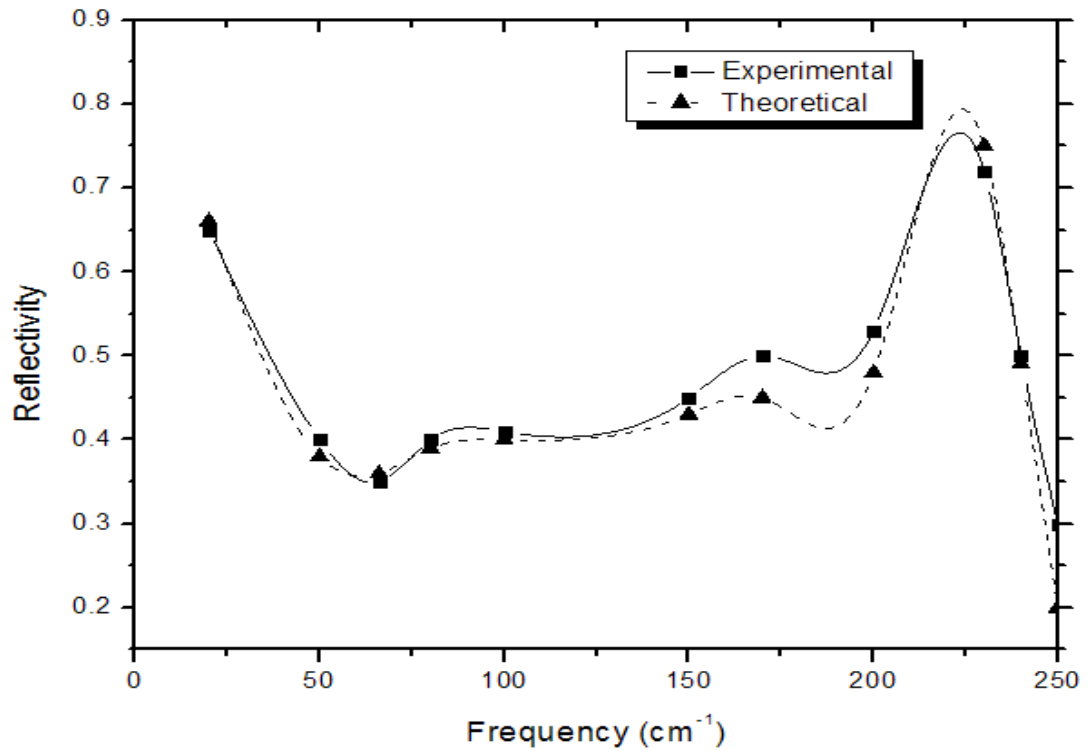


Fig.6.3 Reflectivity of sample tmw05057 at room temperature, experimental (full curve with square symbols) and theoretical (dash curve with triangle symbols). The spectral range 20-250  $\text{cm}^{-1}$ . Sample tmw05057 was 1  $\mu\text{m}$  GaSb on GaAs (001) substrate grown at temperature of 500  $^{\circ}\text{C}$  and growth rate of 0.5  $\mu\text{m/h}$ .

Table 6.1 Parameters obtained from infrared reflectivity (r) and Hall measurements (h) on sample tmw05057.

Sample	$\nu_p(\text{cm}^{-1})$	$n_r (10^{17} \text{ cm}^{-3})$	$n_h (10^{17} \text{ cm}^{-3})$	$\mu_r(\text{cm}^2\text{V}^{-1}\text{S}^{-1})$	$\mu_h(\text{cm}^2\text{V}^{-1}\text{S}^{-1})$
tmw05057	66	3.1	3.2	612	605

Figure 6.3 illustrated the reflectivity of GaSb under the spectral range 20-250  $\text{cm}^{-1}$  at room temperature. Hall measurements were performed at the same sample after the infrared reflectivity measurement. The sample exhibited p-type conductivity. The carrier concentrations and mobilities obtained from Hall measurements, theoretical, and experimental infrared reflectivity measurements were shown in table 6.1. Due to

the purity of the spectrum, the experimental measurement and the theoretical result were consistent well. It could also be founded that the electrical properties obtained from the measurements were fitted well. It should emphasize that the direct comparison of the reflectivity measurement and the Hall measurement was not suitable for the high-carrier-concentration and n-type GaSb due to the simplifying of the optical theory. The plasma-phonon coupling becomes strong and the free carrier scattering time  $\tau$  is reduced in the high-carrier-concentration samples [14].

#### 6.4.2 Results for InSb and analysis

The reflectivity of InSb was measured in spectral range 20-250  $\text{cm}^{-1}$  at room temperature.

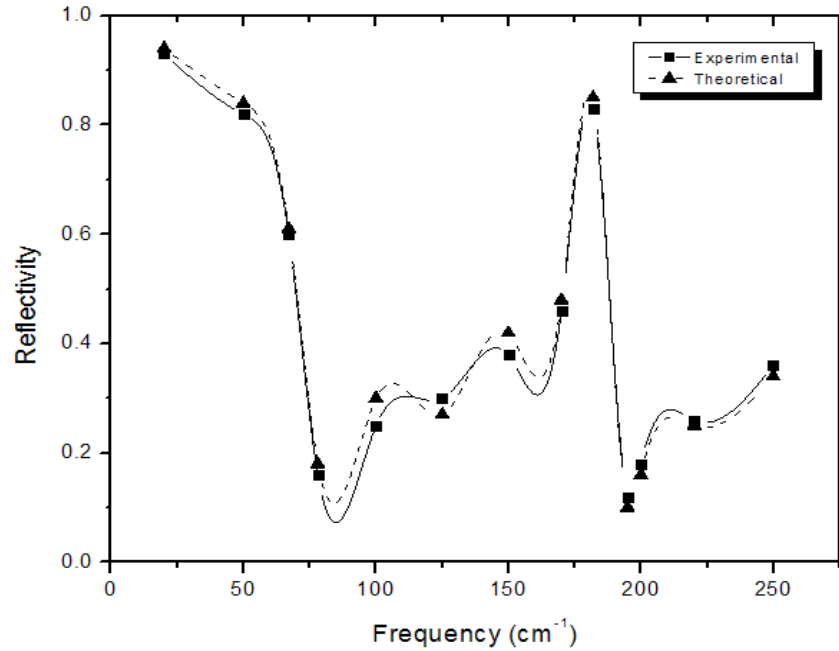


Fig.6.4 Reflectivity of sample tmw05083 at room temperature, experimental (full curve with square symbols) and theoretical (dash curve with triangle symbols). The spectral range 20-250  $\text{cm}^{-1}$ . Sample tmw05083 was 5  $\mu\text{m}$  InSb on GaAs (001) substrate grown at temperature of 420  $^{\circ}\text{C}$  and growth rate of 0.5  $\mu\text{m/h}$ .



Table 6.2 Parameters obtained from infrared reflectivity (r) and Hall measurements (h) on Sample tmw05083.

Sample	$\nu_p(\text{cm}^{-1})$	$n_r(10^{16} \text{ cm}^{-3})$	$n_h(10^{16} \text{ cm}^{-3})$	$\mu_r(\text{cm}^2\text{V}^{-1}\text{S}^{-1})$	$\mu_h(\text{cm}^2\text{V}^{-1}\text{S}^{-1})$
tmw05083	181	1.9	1.7	57085	59040

Figure 6.4 illustrated the reflectivity of InSb in the spectral range 20-250  $\text{cm}^{-1}$  at room temperature. Hall measurements were performed at the same sample after the infrared reflectivity measurement. The InSb sample exhibited n-type conductivity. The carrier concentrations and Hall electron mobilities obtained from Hall measurements, theoretical, and experimental infrared reflectivity measurements were displayed in table 6.2. The good agreement of the experimental and the theoretical measurement were due to the improved spectrum impurity. In particular, the electrical properties obtained from the two types of measurement were almost fitted.

### 6.5 Conclusions

Both theoretical and experimental Infrared reflectivity measurements have been performed on GaSb and InSb, the electrical parameters such as carrier concentrations and mobilities have been calculated by the Kramers-Kronig transform. The reflectivity measurements have been performed in spectral range 20-250  $\text{cm}^{-1}$ . Due to the impure spectrum, the experimental measurement and the theoretical result were consistent well. Direct comparisons of the electrical parameters obtained from reflectivity measurements and Hall measurements were made. Good agreement was obtained from the infrared reflectivity and Hall measurements. The electrical parameters obtained from both types of the measurement were also fitted well. Further more, the electrical parameters obtained from the reflectivity measurements provided a further calibration of the accuracy of the results obtained from Hall measurements and the fitted figures further demonstrated the validation of the Hall results obtained in chapter 5.

## Chapter 7 Conclusions and future work

### 7.1 Conclusions

Investigation of single layers InSb dots has been presented in the thesis. Analysis of trends at 320 °C, 275 °C and 250 °C including dot densities, volumes and estimation of critical thickness have been presented in chapter 3. The characterization techniques are RHEED, AFM, TEM and PL. The single layer InSb/GaSb QDs with high number density of  $10^{11} \text{ cm}^{-2}$  and narrow size distribution have been obtained.

Growth and characterization of buried InSb dots have been presented in chapter 4. The sample with 2.5 ML buried InSb QDs with density (up to  $4 \times 10^{10} \text{ cm}^{-2}$ ) were obtained on the GaSb (001) by MBE. HRTEM cross-section images of the coherent and defect free InSb QDs buried into the GaSb spacer were observed. The estimated size of SQDs was ~26 nm (base width) and 3 nm (height). The estimated sheet density of SQDs was  $\sim 1.2 \times 10^{10} \text{ cm}^{-2}$ . The average size of the BQDs was slightly smaller (~ 22 nm in lateral width and ~ 2.5 nm in height). The experiment illustrated the possibility of the formation of InSb QDs on the GaSb matrix in SK mode. The estimated wetting layer thickness was ~ 0.6 nm (~ 1.7 ML). The electrical properties of the sample were measured by PL. The PL spectras indicated there were two energy peaks which related to the QDs. We suspected that the RT peaks at 3.4 eV and 4.6 eV were related to the SQDs and BQDs, respectively.

Chapter 5 was focused on the heteroepitaxial growth of III-Sb on GaAs substrates. Investigation of the growth of GaSb on GaAs (001) has been present in section 5.1. The effect of growth parameters, such as deposition temperatures, growth rates, V/III ratios on the surface morphology and electrical properties of GaSb has been evaluated. The characterization was carried out by RHEED, AFM, TEM and Hall measurement. Section 5.1.4 provided a primary study the growth of  $\text{Al}_x\text{Ga}_{1-x}\text{Sb}$  on GaAs (001). Growth of AlSb is tricky, and only initial results have been obtained in this work.

In section 5.2, Investigation the growth of InSb on GaAs (001) has been presented. Analysis of the deposition of InSb on GaAs, to involve the effect of growth parameters, such as deposition temperatures, growth rates, V/III ratios on the properties of InSb surface. The characterizations were conducted by RHEED, AFM, and Hall measurement. In this chapter, the dependence of the electrical properties on the surface threading dislocations has been quantitatively evaluated. The electrical results obtained from Hall measurements for both GaSb/GaAs and InSb/GaAs heterostructures were comparable to the results from other groups.

In chapter 6, both theoretical and experimental Infrared reflectivity measurements on GaSb and InSb have been investigated. The electrical parameters such as carrier concentrations and mobilities have been calculated by the Kramers-Kronig transform. Due to the high purity of the spectrum, the experimental measurement and the theoretical result were consistent well. Direct comparisons of the electrical parameters obtained from reflectivity measurements and Hall measurements were made. Good agreement was obtained from the infrared reflectivity and Hall measurements and the electrical parameters obtained from both types of the measurement were also fitted well. The electrical data obtained from the reflectivity measurements further calibrated and improved the accuracy of the results obtained from Hall measurements in chapter 5.

## 7.2 Future work

For InSb/GaSb QDs, although a relatively high density was obtained, the microstructure analysis has shown that a large number of QDs were plastically relaxed. It was well expected QDs capped by another layer as soon as they are formed, a fully-strained QDs may be obtained. While the TEM images illustrated the existence of dislocations which indicated the plastically relaxation of QDs. Such QDs were undesirable for the quantum effect applications. Although further growth of buried 2.5 ML InSb on GaSb (001) under typical kinetic parameters obtained QDs emitted near 3.4  $\mu\text{m}$  at room temperature. The PL measurements taken from the other buried dots manifested low radiative efficiency which were coincided with the

band structure calculations. It is suspected this transition may occur from an indirect transition. The PL measurement is an effective method to assess the electrical properties of QDs, in this thesis, only primary investigations of PL spectrum of QDs samples have been conducted. Studies including using PL to assess the dots size, density, and optimizing the growth conditions to achieve great radiative efficiencies still need to be explored.

For III-Sb/GaAs heterostructures, the defects in the interface and threading dislocations on the surface are difficult to eliminate by direct hetero-epitaxial. The exploration of hybrid systems with high mobility still leaves a lot of work to do.

## References

- [1]E. F.Schubert, Light Emitting Diodes, Cambridge University Press, 2006.
- [2]Bravais, A, J. Ecole Polytech, Crystallographic Society of America, 1949.
- [3]K.Charles, Introduction to Solid State Physics (7 ed.), New York: John Wiley & Sons, p. 10, 2008.
- [4]S.Adachi, Properties of semiconductor alloys: group-IV, III-V and II-VI semiconductors, John Wiley & Sons,2009.
- [5]H. J. Queisser and E. Haller, Science, 281 (1988) 945.
- [6]P. Ehrhart, "Properties and interactions of atomic defects in metals and alloys", volume 25 of Landolt-Börnstein, New Series III, chapter 2, page 88, Springer, Berlin, 1991.
- [7]R. W. Siegel, J. Nucl. Mater. 69 & 70, 117 (1978).
- [8]J. P. Hirth and J. Lothe , Theory of dislocations (2 ed.), Krieger Pub Co. ,1992.
- [9]B. R. Bennett, R. Magno, J.B. Boos, W. Kruppa, and M.G. Ancona, Solid State Electron, 49, 1875 (2005).
- [10]L. M. Fraas, R. Ballantyne, J. Samaras, and M. Seal, AIP Conference Proceedings, First NREL Conference on Thermophotovoltaic Generation of Electricity, 321, 44 (1994).
- [11]D. Bimberg, et al., Semiconductor nanostructures, Springer Berlin Heidelberg New York.
- [12]O. Hipolito, Brazilian Journal of Physics, Vol.22, no. 3, Sept, 1992.
- [13]E. R. Glaser, Applied physics letters, volume:68 issue:25, 1996.

- [14]G. W. Bryant, in interface, quantum wells, and superlattices, Eds. C. R. Leavens and R. Taylor, P. 143, Plenum Press, N. Y., 1988.
- [15]H. T. Chou, D. Goldhaber-Gordon, S. Schmult, M. J. Manfra, A. M. Sergent, and R. J. Molnar, Appl. Phys. Lett. **89**, 033104 (2006).
- [16]R. D. Vispute, V.Talyansky, S. Choopun, and R.P.Sharma, Applied Physics Letters (Volume: 73, Issue: 3).
- [17]M. H. Grabow and G.H. Gilmer, Surf. Sci., 194, 333 (1988).
- [18]J. D. Weeks and G.H. Gilmer, Adv. Chem. Phys., 40,157 (1979).
- [19]C. Ratsch and J.A. Venables, J. Vac. Sci. Technol. A, 21, S96 (2003).
- [20]M. Biehl, W. Kinzel, and S. Schinzer, Europhysics Letters (EPL) 41, 443-448 (1998).
- [21]J. Tersoff, A.W. Denier van der Gon, and R.M. Tromp, Phys. Rev. Lett., 72, 266 (1994).
- [22]Y. Chen and J. Washburn, Phys. Rev. Lett. 77, 4046–4049 (1996).
- [23]H. Brune, Growth modes, in Encyclopedia of Materials: Science and Technology, Elsevier, Amsterdam, 2001.
- [24]I. Daruka and A. L. Barabási, Phys. Rev. Lett., 79, 3708 (1997).
- [25]B. Daudin, F. Widmann, G. Feuillet, Y. Samson, M. Arlery, and J. L. Rouvière, Phys. Rev.B.56. R7069, 1997.
- [26]Tatau Nishinaga and Kyoung-Ik Cho, Jpn. J. Appl. Phys. 27 (1988) pp. L12-L14.
- [27]P. B. Joyce, T. J. Krzyzewski, G. R. Bell, and T. S. Jones, Phys. Rev. B 62, 10891–10895 (2000).

- [28]PB Joyce, TJ Krzyzewski, GR Bell, and T. S. Jones, *Applied Physics Letters* (Volume: 79, Issue: 22).
- [29]A. Cho, *J. Vac. Sci. Technol.* 8, S31 (1971).
- [30]L. Kolodziejcki, R. Gunshor, N. Otsuka, S. Datta, W. Becker, and A. Nurmikko, *IEEE J. Quantum Electron.* 22, 1666 (1986).
- [31]M. B. Nardelli, F. J. Walker, and R. A. McKee, *Phys. Stat. Sol.* 241, 2279 (2004).
- [32]B. A. Joyce, *Rep. Prog. Phys.* 48, 1637-1697 (1985).
- [33]K. Nanbu, J. Saito, T. Ishikawa, K. Kondo, and A. Shibatomi, *J. Electrochem. Soc.* 133, 601 (1986).
- [34]C. T. Lee and Y. C. Chou, *J. Cryst. Growth* 91, 169 (1988).
- [35]T. J. Mattord, M. M. Oye, D. Gotthold, C. Hansing, A. L. Holmes, and B. G. Streetman, *J. Vac. Sci. Technol. A* 22, 735 (2004).
- [36]M. A. Herman, W. Richter, H. Sitter, *Epitaxy: Physical Principles and Technical Implementation*, p. 85, Springer-Verlag, Berlin, 2004.
- [37]G. Lehmpfuhl, A. Ichimiya and H. Nakahara, *Surface Science Letters* 245 L159-L162 (1991).
- [38]Yu. G. Galitsyn, D.V. Dmitriev, V.G. Mansurov, S.P. Moshchenko, and A.I.Toropov, *JETP Lett.*, 81, 629 (2005).
- [39]A.Y. Cho, *J. Appl. Phys.*, 42, 2074 (1971).
- [40]J.S. Harris, R. Kohrbruckr, *Appl. Phys. Lea*, 54023.
- [41]P. A. Maksym a, Z. Mitura b and M.G. Knibb, *Surface Science* 293-298 (1993).
- [42]J. M. VAN HOVE, P.1. COHEN, *Journal of Crystal Growth* 81(1987).

- [43]W. Zhong, G. Overney, D. Tománek, Europhysics Letters (EPL) 15, 49-54 (1991).
- [44]Y. Seo and W. Jhe, Reports on Progress in Physics 71, 016101 (2008).
- [45]K. R. Breen, P.N. Uppal, and J.S. Ahearn, J. Vac. Sci. Technol. B, 7, 758 (1989).
- [46]J. E. Ayers, heteroepitaxy of semiconductors, theory, growth, and characterization, John E. Ayers, 2007.
- [47]M. De Graef, Introduction to Conventional Transmission Electron Microscopy, Cambridge University Press, Cambridge, 2003
- [48]Gfroerer T., H. Photoluminescence in Analysis of Surfaces and Interfaces. In Encyclopaedia of Analytical Chemistry; Meyers, R. A., Ed.; John Wiley and Sons Ltd.: Chichester, pp 9209-9231, (2000).
- [49]M. M. Sayed, C.R. Westgate, Review of Science Instruments, Volume 46, Issue 8.
- [50] A.A. Ramadana, R.D. Gould, Thin Solid Films, V239 I 2, 1994.
- [51]M. Davis, M. Greiner, Optical Engineering 50(6), 061016 (2011).
- [52]H. Z. Chen, X. H. Sun, Lai, K.W.C., M. Meyyappan, and X. Ning, Infrared detection using an InSb nanowire, nanotechnology materials and devices coferece, 2009.
- [53]M. J. Furlong, R. Martinez, S. Amirhaghi, and B. Smith, Antimonide based infrared materials: Developments in InSb and GaSb substrate technologies, Indium Phosphide and Related Materials, 333-338, 2007.
- [54]J. R. Soderstrom, M. M. Cumming, J-Y. Yao, and T. G. Anderson, Semicond. Sci. Technol. 7, 337 (1992).



- [55]D. L. Partin, L. Green, and J. Heremans, J. Electron. Mater. 23, 75 (1994).
- [56]X. Zhang, A. E. Staton-Bevan, D. W. Pashley, S. D. Parker, R. Droopad, R. L. Williams, and R. C. Newman, J. Appl. Phys. 67, 800 (1990).
- [57]K. Anthony, Mid-Infrared Semiconductor Optoelectronics, 2006.
- [58]P. S. Dutta, H. L. Bhat, and Vikram Kumar, J. Appl. Phys. 81, 5821 (1997).
- [59]R. G. van Welzenis, B.K. Ridley, Solid-State Electronics Volume 27, Issue 2, 1984.
- [60]R J Egant, V W L Chin and T L Tansley, Semicond. Sci. Technol. 9 1591, 1994.
- [61]A. Joullie and P. Christol, C.R. Physique 4,621 (2003).
- [62]V. tasco, N. Deguffroy, A. N. Baranov, E. tourie, B. Satpati, and A. Tampert, Phys.Status Solidi B 243, 3959 (2006).
- [63]C. Weisbuch and G. Vinter, Quantum semiconductor structures, Academic, Boston, MA, 1991.
- [64]S. J. Smith, G. R. Nash, M. Fearn, L. Buckle, M. T. Emeny, and T. Ashley, Appl. Phys. Lett. 88, 081909 (2006).
- [65]N. Vukmirović, Z. Ikonić, I. Savić, D .Indjin and P. Harrison , J. Appl. Phys. 100, 074502, 2006.
- [66]D. Leonard, K. Pond, and P. M. Petroff, Physical review B, volume 50, number 16 (1994).
- [67]N. Deguffroy, V. Tasco, A. N. Baranov, E. Tournie, B. Satpati, A. Trampert, M. S. Dunaevskii, A. Titkov, and M. Ramonda, J. Appl. Phys. 101 124309 (2007).
- [68]A. F. Tsatsulnikov, S. V. Ivanov, P. S. Kopev, A. K. Kryganovskii, N. N. Ledenstov, M. V. Maximov, B. Ya. Meltser, P. V. Nekludov, A. A. Suvurova, A. N.

Tiktov, B. V. Volovik, M. Grundman, D. Bimberg, and Zh. I. Alferov, J. Electron. Mater. 27, 414, 1998.

[69]Y. Shusterman, A. Paltiel, V.Sher, Ezersky, and Y. Rosenwaks, J. Cryst. Growth 291, 363, 2006.

[70]N. Bertru, O. Brandt, M. Wassermeier, and K. Ploog, Appl. Phys. Lett. 68, 31, 1996.

[71]E. Alphandéry, R. J. Nicholas, N. J. Mason, B. Zhang, P. Möck, and G. R. Booker, Appl. Phys. Lett. 74, 2041, 1999.

[72]P. Möck, G. R. Booker, N. J. Mason, R. J. Nicholas, E. Alphandéry, T. Topuria, and N. D. Browning, Mater. Sci. Eng. B 80, 112, 2001.

[73]WK. Liu, M.B. Santos. Surface Science 319 (1994).

[74]Han Ye, Pengfei Lu, ZhongyuanYun, BoYongJia, HaoFeng, Yumin Liu, Physica E 42 (2010) 2402–2405.

[75]K.Tillmann, A.Forster, Thin Solid Films 368 (2000).

[76]A. Marzegalli, V.A. Zinovyev, F. Montalenti, A. Rastelli, M. Stoffel, T. Merdzhanova, O.G. Schmidt, Leo Miglio, Phys. Rev. Lett. 99 (2007).

[77]RK Patel, AM Sanchez, MJ Ashwin, TS Jones and R Beanland, Relaxation mechanisms of InSb/GaSb quantum dots, 2012.

[78]PL Galindo, S Kret, AM Sánchez, JY Laval, A Yanez, J Pizarro, E Guerrero, T Ben and SI Molina Ultramicroscopy, 107 (2007).

[79]DB Holt and BG Yacobi in “Extended Defects in Semiconductors”, (Cambridge University Press, Cambridge) p.215.

[80]P. S. Dutta, H. L. Bhat, and V. Kumar, J. Appl. Phys. 81, 5821 (1997).

- [81]A. E. Romanov, P. M. Petroff, and J. S. Spec, Appl. Phys letter, volume 74 number 16, 1999.
- [82]V. tasco, N. Deguffroy, A. N. Baranov, and E.tourie, Applied physics letters 89, 263118 (2006).
- [83]Brain R. Bennett, R.Magno, and B.V.Shanabrook, Appl. Phys. Lett. 68, 505 (1996).
- [84]C. E. C. Wood, L. Rathburn, H. Ohmo, D. DeSimone: J. Cryst. Growth 51, 299 (1981)
- [85]R. M. Biefield and G. A. Hebner, J. Cryst. Growth 109, 272 (1991).
- [86]K. Oura, V. G. Lifshits, A.A. Saranin, A.V. Zotov, and M. Katayama .Surface Science: An Introduction. Berlin: Springer, (2003).
- [87]V. John, Introduction to Surface and Thin Film Processes. Cambridge: Cambridge University Press, (2000).
- [88]A. G. Milnes, A.Y. Polyakov, Solid State Electronics: Volume 36, Issue 6, June 1993.
- [89]Y.Y. Wu and P.D.Yang, Direct Observation of Vapor-Liquid-Solid Nanowire Growth, J. Am. Chem. Soc. 2001.
- [90]W. Lu, T. Rohel, N. Bertru, H. Folliot, et al., Jpn J. Appl. Phys 49 (2010).
- [91]Y.F. Wang, Journal of Infrared, volume 29, number 11, 2008.
- [92]A. F. Tsatsulnikov, S. V. Ivanov, P. S. Kopev, I. L. Krestnikov, A. K. Kryganovskii, N. N. Ledenstov, M. V. Maximov, B. Ya. Meltser, P. V. Nekludov, A. A. Suvurova, A. N. Tiktov, B. V. Volovik, M. Grundman, D. Bimberg, and Zh. I. Alferov, Microelectron. Eng. 43–44, 85 (1998).

- [93]W. K. Liu, M.B.Santos. Surface reconstruction of InSb (001) during molecular beam epitaxy. *Surface Science* 319 (1994).
- [94]S. O. Kasap. *Principles of Electronic Materials and Devices*. McGraw Hill, New York, 2000.
- [95]O. Pierre-Louis, M. R. D Orsogna, and T. L. Einstein, *Physical Review Letters*, Volume 82, Number 18, 1999.
- [96]M. Ivan V. *Crystal Growth for Beginners: Fundamentals of Nucleation, Crystal Growth, and Epitaxy*. Singapore: World Scientific. 1995.
- [97]P. Thompson, J. Villain, *Physics of Crystal Growth*. Cambridge: Cambridge University Press (1998).
- [98]Y.H. Cho, T.J. Schmidt, S. Bidnyk, G.H. Gainer, J.J. Song, S. Keller, U.K. Mishra, S.P. DenBaars, *Phys. Rev. B* 61 (2000).
- [99]T.J. Krzyzewski, P.B. Joyce, G.R. Bell, T.S. Jones, *Phys. Rev. B* 66 (2000).
- [100]F.V. de Sates, J.M.R. Cruz, S.W. de Silva, M.A.G. Soler, P.C. Morais, M.J. da Silva, A. Quivy, J.R. Leite, *J. Appl. Phys.* 94 (2003).
- [101] W.L. Sarney, J.W. Little, S.P. Svensson, *Solid State Electron.* 50 (2006).
- [102]P. E. Thompson, J. L. Davis, J. Waterman, R. J. Wagner, D. Gammon, D. K. Gaskill, and R. Stahlbush, *J. Appl. Phys.* 69, 7166 (1991).
- [103]T. Zhang, S. K. Clowes, M. Debnath, A. Bennett, C. Roberts, J. J. Harris, R. A. Stradling, and L. F. Cohen, *APPLIED PHYSICS LETTERS VOLUME 84*, 22 31, MAY 2004.
- [104]S. A. Solin, T. Thio, D. R. Hines, and J. J. Heremans, *Science* 289, 1530(2000).
- [105]B. Brar, D. Leonard, *Appl. Phys. Lett.* 66 (1995).
- [106]L. Samoska, B. Brar, and H. Kroemer, *Appl. Phys. Lett.* 62, 2539 (1993).

- [107]C. R. Bolognesi, E. J. Caine, and H. Kroemer, IEEE Electron Device Lett. EDL-15, 16 (1994).
- [108]E. R. Brown S. J. Eglash, G. W. Turner C. D. Parker, J. V. Pantano, and D. R. Calawa, IEEE Trans. Electron Devices ED-41, 879 (1994).
- [109]H. Mohseni, J. Wojkowski, M. Razeghi, and W. Mitchel 1999 J. Quantum Elec. 35 1041.
- [110]E H Aifer, J G Tischler, J H Warner, I Vurgafman, J C Kim, R Meyer, B R Bennett, L J Whitman, E M Jackson and Lorentzen, J R 2005 Proc. SPIE 5732 259.
- [111]RT. Hao, YQ. Xu, ZQ. Zhou, J. Phys. D: Appl. Phys. 40 (2007).
- [112]W. Qian, M. Skowronski, R. Kaspi, M. De Graef, and V. P. Dravid. J. Appl. Phys. **81**, 7268 (1997).
- [113]A. S. Bracker, M. J. Yang, B. R. Bennett, J. C. Culbertson, W. J. Moore, Journal of Crystal Growth 220, 384–392 (2000).
- [114]W Qian, M Skowronski, R Kaspi, M De Graef and V P Dravid, J. Appl. Phys. 81 726, 1997.
- [115]B. Brar and D. Leonard, appl. Phys. Lett. 66, 463 (1995).
- [116]C. C. Hsu, Y. C. Lu, J. B. Xu, and I. H. Wilson, Appl. Phys. Lett. 65, 1959 (1994).
- [117]P. Moriarty, P. H. Beton, Y. -R. Ma, and M. Henini, Phys. Rev. B 53, R16148–R16151 (1996).
- [118]R. N. Kyutt, R. Scholz, S. S. Ruvimov, T. S. Argunova, A. A. Budza, S. V. Ivanov, P. S. Kopev, L. M. Sorokin, and M. P. Scheglov, Phys. Solid State 35, 372 (1993).
- [119]Z X Fu, Q S Xiong, Y H Qing, H C He, C J Yi, H Gang, Z C Wu, Acta Physica Sinica, Vol. 39, No. 12, Dec., 1990.

- [120]S. Huang, G. Balakrishnan, and D. L. Huffaker, J. Appl. Phys. 105, 103104 (2009).
- [121]L. Samoska, B. Brar, and H. Kroemer, Appl. Phys. Lett. 62, 2539 (1993).
- [122]E. R. Brown S. J. Eglash, G. W. Turner C. D. Parker, J. V. Pantano, and D.R. Calawa, IEEE Trans. Electron Devices ED-41, 879 (1994).
- [123]C. R. Bolognesi, E. J. Caine, and H. Kroemer, IEEE Electron Device Lett.EDL-15, 16 (1994).
- [124]Z Q. Zhou, Y Q. Xu, et al., CHIN. PHYS. LETT. Vol. 26, No. 1 (2009) 018101.
- [125] W.T .Tsang, N.A.Olsson, Applied physics letters, volume 43, issue 1.
- [126]S. A. Solin, D. R. Hines, A. C. Rowe, J. S. Tsai, Y. A. Pashkin, S. J. Chung, N. Goel, and M. B. Santos, Appl. Phys. Ltee. 80, 4012 (2002).
- [127]G. C. Osbourn, J. Vac. Sci. Technol. B 2, 176 (1984).
- [128]S. R. Kurtz, L. R. Dawson, T. E. Zipperian, and S. R. Lee, Appl. Phys. Lett. 52, 1581 (1998).
- [129]J. I. Chyi, D. Biswas, S. V. Iyer, N. S. Kumar, H. Morkoc, R. Bean, K. Zanio, H. Y. Lee, and H. Chen, Appl. Phys. Lett. 54, 1016 (1986).
- [130]G. M. Williams, C. R. Whitehouse, C. F. Mcconville, A. G. Cullis, T. Ashley, S. J. Coutney, and C. T. Elliot, Appl. Phys. Lett. 53, 1189 (1988).
- [131]J. I. Chyi, S. Kalem, N. S. Kumar, C. W. Litton, and H. Morkoc, Appl. Phys. Lett. 53, 1092 (1988).
- [132]J. E. Oh, P. K. Bhattacharya, Y. C. Chen, and S. Tsukamoto, J. Appl. Phys.66, 3618 (1989).
- [133]X. Zhang, Staton Bevan, A.E. Pashley, D.W. Parker, S. D. Droopad, R. Williams, R. L. Newman, Journal of Applied Physics (Volume:67, Issue: 2).

- [134]C. J. Kiely, J-I. Chyi, A. Rockett and H. Morkoq, MRS Proceedings / Volume 139 / 1989.
- [135]J. E. Oh. P. K. Bhattacharya. Y. C. Chen, and S. Tsukamoto, J. Appl. Phys. 66, 3618 (1989).
- [136]E. Michel, G. Singh, S. Slivken, C. Besikci, P. Bove, I. Ferguson, and M. Razeghi, Appl. Phys. Lett. 65, 3338 (1994).
- [137]K. Kanisawa, H. Yamaguchi, and Y. Kirayama, Appl. Phys. Lett. 76, 589 (2000).
- [138]D. D. Macdonald and Mirna Urquidi-Macdonald, J. Electrochem. Soc. 1985 Volume 132, issue 10, 2316-2319.
- [139]O. S. Heavens, Optical properties of thin solid films, New York: Dover publications, 1991.
- [140]A. Yakimov, et al., J. Appl. Phys. 93 (2003) 3693.
- [141]A. V. Korovin, et al., J. Phys: Conference (2008) Series 100052036.
- [142]J. D.Jackson, et al., Classical Electrodynamics (3<sup>rd</sup> ed), New York: Wiley 1999.
- [143]G. Dennis, et al., Polarized Light (2<sup>nd</sup> ed), 2003.
- [144]R. Jacobsson, Progress in Optics, North-Holland Publishing Co. Amsterdam, 1965.
- [145]H. A. MacLeod, Thin Film Optical Filters, Adam Hilger, London, 1969.
- [146] I V. Skryabinskii and Y I. Ukhonov, Sou. Phys.-Solid St. 14 2838-40, 1973.
- [147]T. S. Moss, optical Properties of Semiconductors, Butterworths, London (1961).
- [148] Y. Liu , YJ. Lee , Cicerone MT, Opt Lett.34(9):1363-5, 2009.
- [149]M. C. Wu and C. C. Chen, J. Appl. Phys. 72, 9 (1992) 4275-4280.
- [150]H. J. Lee and J. C. WooUey, Can. J. Phys. 59, 12 (1981) 1844-1850.
- [151]C Pickering, J. Phys. C: Solid St. Phys., 13 (1980) 2959-68.

[152]A K Walton and U K Mishra, J. Phys. C: Solid St. Phys. 1 533-8, 1968.